Imaging mouse models of neurodegeneration using multi-parametric MRI

A thesis presented in partial fulfilment of the requirements
for the degree of Doctor of Philosophy to
University College London

Holly Elizabeth Holmes

Centre for Advanced Biomedical Imaging

Division of Medicine

University College London

This thesis is dedicated to the memory of Peter Wilfred Bradshaw Holmes.

Declaration

I, Holly Elizabeth Holmes, confirm that the work presented in this thesis is my own. Where information has been derived from other sources, I confirm that this has been indicated in the thesis.

Holly Elizabeth Holmes

Abstract

Alzheimer's disease (AD) is a devastating condition characterised by significant cognitive impairment and memory loss. Transgenic mouse models are increasingly being used to further our knowledge of the cause and progression of AD, and identify new targets for therapeutic intervention. These mice permit the study of specific pathological hallmarks of the disease, including intracellular deposits of hyperphosphorylated tau protein and extracellular amyloid plaques. In order to characterise these transgenic mice, robust biomarkers are required to evaluate neurodegenerative changes and facilitate preclinical evaluation of emerging therapeutics.

In this work, a platform for *in vivo* structural imaging of the rTg4510 mouse model of tauopathy was developed and optimised. This was combined with a range of other clinically relevant magnetic resonance imaging (MRI) biomarkers including: arterial spin labelling, diffusion tensor imaging and chemical exchange saturation transfer. These techniques were applied in a single time-point study of aged rTg4510 mice, as well as a longitudinal study to serially assess neurodegeneration in the same cohort of animals. Doxycycline was administered to a subset of rTg4510 mice to suppress the tau transgene; this novel intervention strategy permitted the evaluation of the sensitivity of MRI biomarkers to the accumulation and suppression of tau. Follow-up *ex vivo* scans were acquired in order to assess the sensitivity of *in vivo* structural MRI to the current preclinical gold standard.

High resolution structural MRI, when used in conjunction with advanced computational analysis, yielded high sensitivity to pathological changes occurring in the rTg4510 mouse. Atrophy was reduced in animals treated with doxycycline. All other MRI biomarkers were able to discriminate between doxycycline-treated and untreated rTg4510 mice as well as wildtype controls, and provided insight into complimentary pathological mechanisms occurring within the disease process.

In addition, this imaging protocol was applied to the J20 mouse model of familial AD. This mouse exhibits widespread plaque formation, enabling the study of amyloid-specific pathological changes. Atrophy and deficits in cerebral blood flow were observed; however, the changes occurring in this model were markedly less than those observed in the rTg4510 mouse. This study was expanded to investigate the early-onset AD observed in individuals with Down's syndrome (DS) by breeding the J20 mouse

with the Tc1 mouse model of DS, permitting the relationship between genetics and neurodegeneration to be dissected.

This thesis demonstrates the application of *in vivo* multi-parametric MRI to mouse models of neurodegeneration. All techniques were sensitive to pathological changes occurring in the models, and may serve as important biomarkers in clinical studies of AD. In addition, *in vivo* multi-parametric MRI permits longitudinal studies of the same animal cohort. This experimental design produces more powerful results, whilst contributing to worldwide efforts to reduce animal usage with respect to the 3Rs principles.

Acknowledgements

This thesis has taken me on an indescribable intellectual journey, and I am in debt to a great many people who have supported me along the way.

Firstly, I would like thank Prof. Mark Lythgoe. Over the past 4 years, Mark has witnessed my transformation from quivering MRes student to competent PhD candidate; this is wholly attributed to his support, motivation and guidance. Mark has also instilled in me a passion for public engagement in the sciences, which I will carry with me in the future. Mark fosters a wonderful environment for learning in CABI, where each and every individual is given space to thrive and flourish. I will forever remain indebted to Mark for pulling me through my PhD.

I am also hugely grateful for the support and supervision of Prof. Elizabeth Fisher and Prof. Sebastian Ourselin; for their guidance and advice throughout this project. I would also like express my sincerest gratitude to Dr. Jack Wells for his encouragement and endless patience.

I would like to thank 'Team Tau' in CABI: Ozama Ismail, Ian Harrison, Niall Colgan and James O'Callaghan; for endless discussion around my research and their inspiring insights. I'd like to extend an extra special thank you to Nick Powell and Ma Da in CMIC, for making my structural scans a million times better with their amazing processing toolkits.

In addition, I am incredibly grateful for the extensive efforts of my collaborators, both at Eli Lilly and The UCL Institute of Neurology: Adrian Isaacs, Emily Collins, Frances Wiseman, Mike O'Neill, Ross Johnson, Susan Noy, Tracey Murray and Zeshan Ahmed.

I would like to thank the whole CABI family, for making the past few years so enjoyable. An extra special mention to: Ben Duffy, Bernard Siow, Daniel Stuckey, Isabel Christie, John Connell, Katy Ordidge, Morium Ali, Niral Patel, Raj Ramasawmy, Rupy Ghatrora, Simon Richardson, Simon Walker-Samuel, Tammy Kalber, Tom Roberts, Val Taylor, Yanan Zhu and Yichao Yu.

I cannot put into words how much my friends mean to me: Dan Jacques, Nisha Mullea, Dora Mortimer, Elisa Johnson, Christina Brown, Rosie Marshall and Nadia

Aoudjane. Their unwavering support and encouragement has been hugely appreciated. A massive thank you to you all.

I owe everything to my parents, Evelyn and David Holmes; for not only encouraging my interest in science during my formative years, but for their continued support and understanding. I would also like to thank my grandma, Maureen Holmes, who has always championed my academic endeavours and ensured I got the best possible education. A special mention to my sister Florence, who has always inspired me with her determination and diligent work ethic. And of course, thanks to my feline friend Tony T; for his companionship and furry cuddles.

And finally, my eternal gratitude to my wonderful boyfriend Rik Lomas; for his endless devotion and for keeping me inspired to be the best I can be.

Publications arising from this thesis

HE Holmes, N Colgan, O Ismail, D. Ma, NM Powell, JM O'Callaghan, IF Harrison, RA Johnson, TK. Murray, Z Ahmed, M Heggenes, A Fisher, MJ Cardoso, M Modat, S Walker-Samuel, EM Fisher, S Ourselin, MJ O'Neill, JA Wells, EC Collins, MF Lythgoe. Imaging the accumulation and suppression of tau pathology using multi-parametric MRI; *Neurobiology of Aging* (in press).

HE Holmes, JM O'Callaghan, N Powell, D Ma, S Noy, S Ourselin, EM Fisher, F Wiseman, MF Lythgoe. Exploring the relationship between chromosome 21 genes and AD neuropathology; manuscript in preparation.

HE Holmes, N Powell, D Ma, O Ismail, N Colgan, JM O'Callaghan, IF Harrison, RA Johnson, TK. Murray, Z Ahmed, M Heggenes, A Fisher, MJ Cardoso, M Modat, MJ O'Neill, EC Collins, EM Fisher, JA Wells, S Ourselin MF Lythgoe. Is alive better than dead when investigating structural changes in transgenic mouse models?; manuscript in preparation.

JA Wells, JM O'Callaghan, **HE Holmes**, N Powell, RA Johnson, B Siow, F Torrealdea, O Ismail, S Walker-Samuel, X Golay, M Rega, S Richardson, M Modat, MJ Cardoso, S Ourselin, A Schwarz, Z Ahmed, TK Murray, MJ O'Neill, EC Collins, N Colgan and MF Lythgoe. *In vivo* imaging of tau pathology using multi-parametric quantitative MRI; *NeuroImage* **111**, 369 (2015).

D Ma, MJ Cardoso, M Modat, N Powell, JA Wells, **HE Holmes**, F Wiseman, V Tybulewicz, EM Fisher and MF Lythgoe. Automatic Structural Parcellation of Mouse Brain MRI Using Multi-Atlas Label Fusion. *PloS one* **9**, e86576 (2014).

JM O'Callaghan, JA Wells, S Richardson, **HE Holmes**, Y Yu, S Walker-Samuel, B Siow and MF Lythgoe. Is Your System Calibrated? MRI Gradient System Calibration for Pre-Clinical, High-Resolution Imaging. *PLoS ONE* **9**, e96568 (2014).

JA. Wells, **HE Holmes**, JM O'Callaghan, N Colgan, O Ismail, EM Fisher, B Siow, TK Murray, AJ Schwarz, MJ O'Neill, EC Collins and MF Lythgoe. Increased cerebral vascular reactivity in the tau expressing rTg4510 mouse: evidence against the role of tau pathology to impair vascular health in Alzheimer's disease. *Journal of Cerebral Blood Flow and Metabolism* **35**, 359–362 (2014).

Selected conference proceedings

2015

HE Holmes, N Powell, JA Wells, N Colgan, O Ismail, JM O'Callaghan, D Ma, MJ O'Neill, EC Collins, MJ Cardoso, M Modat, EM Fisher, S Ourselin, MF Lythgoe. Comparing *in vivo* and *ex vivo* imaging in an Alzheimer's model using tensor-based morphometry. *British Chapter of the International Society for Magnetic resonance in Medicine*, London, UK (2015); Oral presentation **O26**.

HE Holmes, R Ramasawmy, M Da, N Powell, M Cardoso, M Modat, S Walker-Samuel, S Ourselin, B Siow, MF Lythgoe. Is 1T the new 9.4T? A tool for morphological phenotyping and regional brain volume analysis. *British Chapter of the International Society for Magnetic resonance in Medicine*, London, UK (2015); Poster presentation **P18.** Awarded 'Best Poster Pitch'.

HE Holmes, N Powell, JA Wells, N Colgan, O Ismail, JM O'Callaghan, D Ma, MJ O'Neill, EC Collins, MJ Cardoso, M Modat, EM Fisher, S Ourselin, MF Lythgoe. Comparing *in vivo* and *ex vivo* imaging in an Alzheimer's model using tensor-based morphometry. *International Society for Magnetic Resonance in Medicine,* Toronto, Canada (2015); Oral presentation **O394**. Awarded Summa Cum Laude.

HE Holmes, R Ramasawmy, M Da, N Powell, M Cardoso, M Modat, S Walker-Samuel, S Ourselin, B Siow, MF Lythgoe. Is 1T the new 9.4T? A tool for morphological phenotyping and regional brain volume analysis. *International Society for Magnetic Resonance in Medicine,* Toronto, Canada (2015); E-poster presentation **3518**.

HE Holmes, N Colgan, O Ismail, D Ma, JA Wells, N Powell, JM O'Callaghan, I Harrison, MJ Cardoso, M Modat, EM Fisher, S Ourselin, MJ O'Neill, EC Collins, MF Lythgoe. A multi-scale MRI approach to investigate novel drug treatment strategies in mouse models of Alzheimer's disease. *International Society for Magnetic Resonance in Medicine,* Toronto, Canada (2015); Poster presentation **2221**.

HE Holmes, O. Ismail, JA Wells, JM O'Callaghan, N Powell, TK Murray, Z Ahmed, MJ O'Neill, EC Collins, RA Johnson, N Colgan, MF Lythgoe. An imaging strategy to characterise tau pathology in a mouse model of Alzheimer's disease using multi-parametric MRI; *Alzheimer's Association International Conference,* Washington DC, United States of America; Poster presentation **P158**.

2014

HE Holmes, F Wiseman, JM O'Callaghan, JA Wells, VLJ Tybulewicz, EM Fisher, MF Lythgoe. Cerebral Blood Flow Deficits in the Tc1 Mouse Model of Down's Syndrome *International Society for Magnetic Resonance in Medicine,* Milan, Italy (2014); Oral presentation **O222**.

HE Holmes, F Wiseman, JM O'Callaghan, JA Wells, VLJ Tybulewicz, EM Fisher, MF Lythgoe. Investigating cerebral blood flow differences in Alzheimer's disease and Down's syndrome. *British Chapter of the International Society for Magnetic resonance in Medicine*, Edinburgh, United Kingdom (2014); Oral presentation **6D**.

HE Holmes, F Wiseman, JM O'Callaghan, JA Wells, VLJ Tybulewicz, EM Fisher, MF Lythgoe. Investigating cerebral blood flow differences in Alzheimer's disease and Down's syndrome. *British Chapter of the International Society for Magnetic resonance in Medicine: Postgraduate Symposium*, Cardiff, United Kingdom (2014); Poster presentation.

HE Holmes, F Wiseman, JM O'Callaghan, JA Wells, VLJ Tybulewicz, EM Fisher, MF Lythgoe. Hypoperfusion in the absence of *APP* gene triplication in the Tc1 mouse model of Down's syndrome. *Alziemher's Association International Conference,* Copenhagen, Denmark (2014); Poster presentation **P479**.

2013

HE Holmes, JA Wells, JM O'Callaghan, N Powell, B Siow, D Ma, S Richardson, O Ismail, MJ Cardoso, M Modat, EM Fisher, S Ourselin, EC Collins, MJ O'Neill, N Colgan, MF Lythgoe. ASL, DTI and structural MRI: multiparametric biomarkers of Alzheimer's disease neuropathology in the Tg4510 mouse model of tauopathy. *European Society for Magnetic Resonance in Medicine and Biology*, Toulouse, France (2013); Oral presentation **375**.

HE Holmes, N Powell, JA Wells, N Colgan, JM O'Callaghan, D Ma, M Modat, MJ Cardoso, S Richardson, B Siow, MJ O'Neill, EC Collins, EM Fisher, S Ourselin, MF Lythgoe. Tensor-based morphometry as a sensitive biomarker for Alzheimer's disease neuropathology. *International Society for Magnetic Resonance in Medicine,* Salt Lake City, United States of America (2013); E-poster presentation **3679**.

HE Holmes, N Powell, JA Wells, N Colgan, JM O'Callaghan, D Ma, M Modat, MJ Cardoso, S Richardson, B Siow, MJ O'Neill, EC Collins, EM Fisher, S Ourselin, MF Lythgoe. Tensor-based morphometry as a sensitive biomarker for Alzheimer's disease neuropathology. *International Society for Magnetic Resonance in Medicine,* Salt Lake City, United States of America (2013); E-poster presentation **3679**.

HE Holmes, N Powell, JA Wells, N Colgan, JM O'Callaghan, D Ma, M Modat, MJ Cardoso, S Richardson, B Siow, MJ O'Neill, EC Collins, EM Fisher, S Ourselin, MF Lythgoe. Tensor-based morphometry as a sensitive biomarker for Alzheimer's disease neuropathology. *British Chapter of the International Society for Magnetic Resonance in Medicine,* York, United Kingdom (2013); Poster presentation.

HE Holmes, N Powell, JA Wells, N Colgan, JM O'Callaghan, D Ma, M Modat, MJ Cardoso, S Richardson, B Siow, MJ O'Neill, EC Collins, EM Fisher, S Ourselin, MF Lythgoe. Tensor-based morphometry as a sensitive biomarker for Alzheimer's disease neuropathology. *British Chapter of the International Society for Magnetic Resonance in Medicine: Postgraduate Symposium,* London, United Kingdom (2013); Poster presentation **P10.** Awarded 'Best Poster Pitch: 2nd place.

2012

HE Holmes, JA Wells, B Siow, JM O'Callaghan, S Richardson, N Powell, D Ma, EM Fisher, S Ourselin, MF Lythgoe. Optimisation of the *in vivo* sequence for structural imaging of a mouse model of Alzheimer's disease. *British Chapter of the International Society for Magnetic Resonance in Medicine,* Cambridge, United Kingdom (2012); Poster presentation.

HE Holmes, JA Wells, B Siow, JM O'Callaghan, S Richardson, N Powell, D Ma, EM Fisher, S Ourselin, MF Lythgoe. Optimisation of the *in vivo* sequence for structural imaging of a mouse model of Alzheimer's disease. *British Chapter of the International Society for Magnetic Resonance in Medicine: Postgraduate Symposium,* Bristol, United Kingdom (2012); Poster presentation.

I have also spoken at the annual *Laboratory Animal Science Association* in 2013, on preclinical imaging and its 3Rs impact.

Awards and achievements

2015

I received the '*Summa Cum Laude*' honour at the International Society for Magnetic Resonance in Medicine's annual meeting in Toronto, Canada.

I received the '*Best Poster Pitch*' award at the British Chapter of the International Society for Magnetic Medicine in Medicine's annual meeting in London, United Kingdom.

2014

I received the '*Magna Cum Laude*' honour at the International Society for Magnetic Resonance in Medicine's annual meeting in Milan, Italy.

2013

I received the '*Best Poster Pitch: 2nd place*' award at the British Chapter of the International Society for Magnetic Medicine in Medicine's annual Postgraduate Symposium in London, United Kingdom.

Table of contents

Chapter 6:   Application of *in vivo* MRI biomarkers to the J20 mouse model of Alzheimer's disease and the Tc1 mouse model of Down's syndrome: a single timepoint study **170**

Index of figures

*order to extract absolute and normalised volume changes in the high ranked pathology regions. The absolute volume changes within the high ranked pathology regions following (A) early and (C) late intervention are presented. In addition, the absolute volume changes were normalized to the TBV in order to extract the proportional volume changes following (B) early and (D) late intervention. A two-way ANOVA with a post-hoc Sidak multiple comparison was performed to identify significant differences between the groups. Statistically significant groups have been identified and highlighted. Error bars represent the SEM. Wildtype vs. untreated rTg4510s: ** = p≤0.01; *** = p<0.001; **** = p≤0.0001. Wildtype vs. treated rTg4510s: + = p≤0.05; ++++ = p≤0.0001. Treated rTg4510s vs. untreated rTg4510s: -- = p≤0.01; ---- = p≤0.0001.*

Figure 4.9 *TBVs for wildtype, rTg4510 and doxycycline-treated rTg4510 mice across all imaging timepoints. In order to account for the marked differences in brain volume between the mice cohorts, absolute volumes from the atlas-based parcellation were normalized to TBV in order to explore volumetric changes occurring disproportionately to alterations in brain volume. A two-way ANOVA with a post-hoc Sidak multiple comparison was performed to identify significant differences between the groups. Statistically significant groups have been identified and highlighted. Error bars represent the SEM. Wildtype vs. untreated rTg4510s: *** = p<0.001; **** = p≤0.0001. Wildtype vs. treated rTg4510s: ++ = p≤0.01; +++ = p≤0.001; ++++ = p≤0.0001. Treated rTg4510s vs. untreated rTg4510s: - = p≤0.05*

Figure 4.10 *Longitudinal volume changes in the thalamus, extracted from the high resolution structural images, following (A, B) early and (C, D) late doxycycline treatment. Results are shown for (A, C) absolute volume and (B, D) normalised volume. A two-way ANOVA with a post-hoc Sidak multiple comparison was performed to identify significant differences between the groups. Statistically significant groups have been identified and highlighted. Error bars represent the SEM. Wildtype vs. untreated rTg4510s: * = p≤0.05; ** = p≤0.01; **** = p≤0.0001. Wildtype vs. treated rTg4510s: + = p≤ 0.05; ++ = p≤ 0.01 +++ = p≤0.001. Treated rTg4510s vs. untreated rTg4510s: -- = p≤0.01; ---- = p≤0.0001.*

Figure 4.11 *Longitudinal CEST results from the high ranked pathology regions following (A) early and (B) late doxycycline treatment. A two-way ANOVA with a post-hoc Sidak multiple comparison was performed to identify significant differences between the groups. Statistically significant groups have been identified and highlighted. Error bars represent the SEM. Wildtype vs. untreated rTg4510s: * = p≤ 0.05; ** = p≤0.01.Treated rTg4510s vs. untreated rTg4510s: -- = p≤0.01.*

Figure 4.12 *Longitudinal CEST results from the thalamus – a region of low tau burden - following (A) early and (B) late doxycycline treatment. A two-way ANOVA with a post-hoc Sidak multiple*

Index of tables

Index of equations

$$\frac{N_{anti-parallel}}{N_{parallel}} = e^{\left(\frac{-\Delta E}{kT}\right)} \tag{1.1}$$

$$\omega_0 = \frac{\gamma B_0}{2\pi} \tag{1.2}$$

$$E = h\nu = \frac{\gamma h B_o}{2\pi} \tag{1.3}$$

$$M_{xy} = M_z \cdot \left(1 - \exp\left(\frac{-t}{T1}\right)\right) \tag{1.4}$$

$$M_{xy} = M_o \cdot \exp\left(\frac{-t}{T2}\right) \tag{1.5}$$

$$S \propto \rho \times \left[1 - \exp\left(-\frac{TR}{T1}\right) \times \exp\left(-\frac{TE}{T2}\right)\right] \tag{1.6}$$

$$RD = \lambda_1 \tag{1.7}$$

$$AD = \frac{\lambda_2 + \lambda_3}{2} \tag{1.8}$$

$$MD = \frac{\lambda_1 + \lambda_2 + \lambda_3}{3} \tag{1.9}$$

$$FA = \sqrt{\frac{1}{2}} \frac{\sqrt{(\lambda_1 - \lambda_2)^2 + (\lambda_1 - \lambda_3)^2 + (\lambda_2 - \lambda_3)^2}}{\sqrt{\lambda_1^2 + \lambda_2^2 + \lambda_3^2}} \tag{1.10}$$

$$Contrast = Signal_{hippocampus} - Signal_{thalamus} \qquad (3.1)$$

$$SNR = \frac{Mean\ signal}{Noise} \qquad (3.2)$$

$$CNR = \frac{Mean\ signal_A - Mean\ signal_B}{Noise} \qquad (3.3)$$

Abbreviations

^{11}C-PiB	Pittsburgh compound B
^{18}F-FDG	Flurodeoxyglucose
2D	Two dimensional
3D	Three-dimensional
3D	Three-dimensional
ACh	Acetylcholine
ACh	Acetylcholine
AChEI	Acetylcholinesterase inhibitor
AChEIs	Acetylcholinesterase inhibitors
AD	Axial diffusivity
AD	Alzheimer's disease
ADNI	Alzheimer's Disease Neuroimaging Initiative
APOE	Apolipoprotein
APP	Amyloid precursor protein
APT	Amide proton transfer
ASL	Arterial spin labelling
Aβ-42	Amyloid-$\beta_{1\text{-}42}$
CBF	Cerebral blood flow
CEST	Chemical exchange saturation transfer
CNR	Contrast-to-noise ratio
CNS	Central nervous system
CSF	Cerebrospinal fluid
CT	Computer tomography
DNA	Deoxyribonucleic acid
DS	Down's syndrome
DTI	Diffusion tensor imaging
DTPA	Diethylene-triamine-penta-acetic acid
EPI	Echo planar imaging
ETL	Echo train length
FA	Fractional anisotrophy
FAIR	Flow-sensitive alternating inversion recovery
FDG	^{18}F-FDG

FDR	False discovery rate
FID	Free induction decay
FSE	Fast spin echo
FT	Fourier transform
FTD	Frontotemporal dementia
GE	Gradient echo
h*APP*	Human amyloid precursor protein
h*MAPT*	Human microtubule associated protein tau
i.p.	Intraperitoneal
Ind.	Indiana
Lon.	London
LP	Lumbar puncture
MAPT	Microtubule associated protein tau
MCI	Mild cognitive impairment
MD	Mean diffusivity
MIP	Maximum intensity projection
mL	Millilitre
mm	Millimetre
MMSE	Mini mental state examination
MR	Magnetic resonance
MRA	Magnetic resonance angiography
MRH	Magnetic resonance histology
MRI	Magnetic resonance imaging
NFTs	Neurofibrillary tangles
NMDA	N-methyl-D-aspartate
NMR	Nuclear magnetic resonance
NSA	Number of signal averages
PET	Positron emission tomography
PS1	Presenilin 1
PS2	Presenilin 2
P-tau	Phosphorylated tau
RD	Radial diffusivity
RF	Radiofrequency
ROI	Region of interest

SD	Standard deviation
SE	Spin echo
SEM	Standard error of the mean
SNR	Signal-to-noise ratio
SPIO	Superparamagnetic iron oxide
SUV	Standard uptake value
Swe.	Swedish
T	Tesla
T_1	Longitudinal magnetisation relaxation time constant
T_2	Transverse magnetisation relaxation time constant
TBM	Tensor-based morphometry
TBV	Total brain volume
Tc1	Transchromic 1
TE	Echo time
TE_{eff}	Effective echo time
TOF	Time-of-flight
TR	Repetition time
T-tau	Total tau

Chapter 1:   Alzheimer's disease

This chapter gives a broad overview of Alzheimer's disease (AD): from reviewing the existing hypotheses that try and explain the cause of the disease, to describing the current available biomarkers for the diagnosis of AD. A summary of different mouse models of AD is also provided.

1.1   Overview: Alzheimer's disease and the current challenges

In 1906, at the 37th Meeting of the Psychiatrists of South West Germany, Dr. Alois Alzheimer presented the neuropathological and clinical findings of his most recent case. The patient, Auguste D, presented with "a peculiar severe disease of the cerebral cortex," with symptoms including "paranoia, progressive sleep and memory disturbance, aggression, and confusion". Auguste D died of her symptoms at the age of 55.
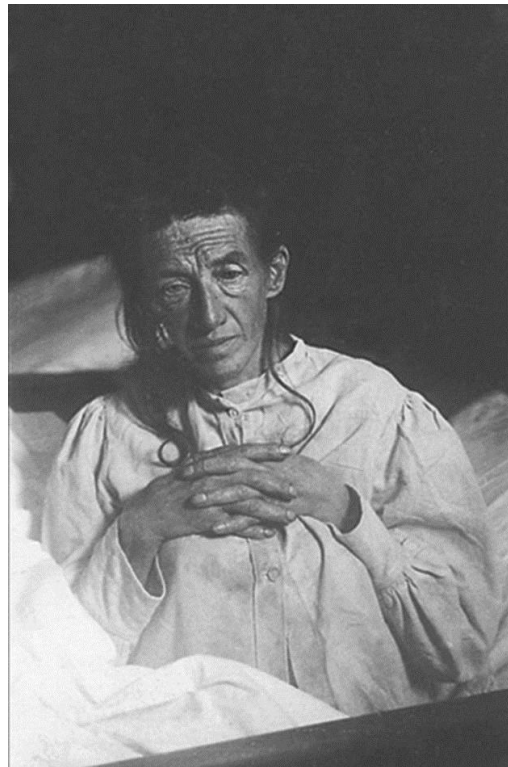
Figure 1.1 *Alois Alzheimer's historical case reported the symptoms of Auguste D, pictured above.*

Alzheimer's subsequent publication in 1911 provided detailed post-mortem analysis of Auguste D's brain, showing various abnormalities including 'senile plaques' – extracellular deposits of amyloid-β – and neurofibrillary tangles of hyperphosphorylated tau (NFTs) (*1, 2*). These discoveries were crucial in uncovering key aspects of the disease, and plaques and tangles are now widely regarded as the histopathological hallmarks of Alzheimer's disease (AD).
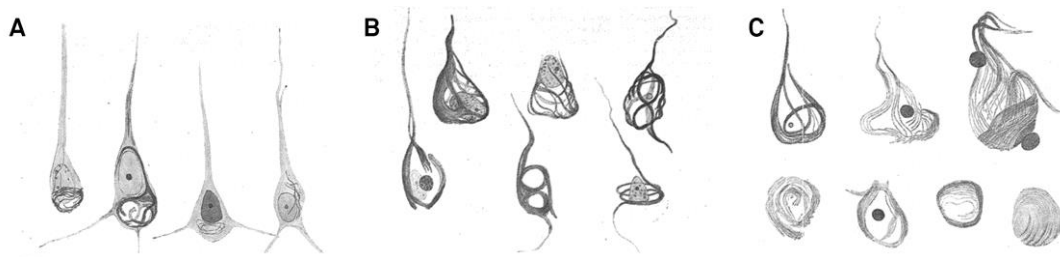
Figure 1.2 *Drawings of histological preparations of postmortem AD brains, taken from Alois Alzheimer's 1911 publication. Alzheimer employed Bielschowsky's silver stain protocol to stain senile plaques and NFTs in the cortex of AD patients. (A) Beginning of the disease; (B) Advanced stage; and (C) Terminal state of the disease.*

It has been over one hundred years since Alois Alzheimer's initial observations of the disease that would come to bear his eponym. Yet, there is still no known cure for this debilitating disease. AD is now known to be the most common form of *dementia*: a broad category of neurodegenerative diseases associated with the progressive decline of brain function. The rest of this chapter will focus on the advancements that have been made in our understanding of AD.

1.2 Causes of Alzheimer's disease

The underlying cause of the vast majority of AD cases is unknown. However, a small proportion of early-onset AD cases are found to cluster in families, and can be attributed to genetic mutations in one of three genes: those encoding amyloid precursor protein (*APP*) (*3*), presenilin 1 (*PS1*) (*4*) and presenilin 2 (*PS2*) (*5*). *APP* mutations cause an increase in amyloid-β production and aggregation, as well as increasing the extracellular concentration of the amyloid-β_{1-42} species, which is believed

to be the initiating molecule in the pathogenesis of AD (*6, 7*). Mutations in the presenilins are linked to abnormal *APP* processing, and are also believed to increase the extracellular concentration of amyloid-β_{1-42} (*8*). Estimates of the prevalence of early-onset forms of AD vary widely, but most recently it has been suggested that 1% - 5% of AD cases are inherited in an autosomal dominant fashion (*9*).

In contrast, the majority of AD cases are late-onset ("sporadic") forms of AD, without obvious familial aggregation. A number of genes have been identified which are associated with a greatly increased risk of developing late-onset AD, without invariably causing it. The ε4 allele of the apolipoprotein ε (*APOE*) gene is the strongest known genetic risk factor for late-onset AD. In comparison to non-carriers, individuals who are heterozygous for one ε4 allele are 3 – 4 times more likely to develop AD; the risk factor for homozygous carriers is even further increased (*10*). In addition, a number of other genetic variants have been associated with increased risk of AD including: CLU and CR1 (*11*); ABCA7, MS4A6A/MS4A4E, EPHA1, CD33 and CD2AP (*12*). It is likely that, over time, more genetic determinants will be implicated in AD (*13*). Other than the age of onset, the clinical and histological features of early-onset AD are indistinguishable from late-onset, sporadic forms of AD (*14*).

With no definitive genetic cause for the majority of sporadic AD cases, a number of hypotheses have been proposed which attempt to outline the cause of the disease.

1.2.1 The cholinergic hypothesis

In an effort to identify a neurochemical abnormality in the brains of AD patients, systematic biochemical evaluation of post-mortem AD brains commenced in the late 1960s (*15*). In 1976, marked deficits of the neurotransmitter acetylcholine (ACh) were identified in AD patients compared to elderly controls (*16, 17*). These findings resulted in the first theory proposed to explain AD: the cholinergic hypothesis of AD. The cholinergic hypothesis proposes that a loss of cholinergic function in the central nervous system (CNS) significantly contributes to cognitive decline in AD patients (*18*). This discovery has led to the development of treatment strategies which aim to increase the levels of ACh, with hope of restoring cognitive function. Acetylcholinesterase inhibitors (AChEIs), which increase neural levels of ACh by inhibiting the acetylcholinesterase enzyme from breaking down acetylcholine, have shown beneficial

effects on cognitive functions and memory in AD patients (*19, 20*). AChEIs currently make up the majority of FDA-approved AD therapies (Table 1.1) (*21*)

Despite these encouraging results, the cholinergic hypothesis is subject to much criticism. Post-mortem analysis of the brains of patients with early stage AD identified no loss in ACh activity (*22*), suggesting that a cholinergic marker would be unsuitable for early detection of AD. These findings also question the therapeutic validity of treating individuals with early stage AD with AChEIs (*23*). In addition, AChEIs only offer mild symptomatic relief of AD, and are not able to reverse or restore neuronal function (*23*). Researchers are now investigating other possible mechanisms which may shed light on the cause of AD.

Table 1.1 *Current FDA-approved drugs for the treatment of AD*

Therapeutic target	Drug	Trade name(s)
AChEIs	Rivastigmine	Exelon
	Galantamine	Razadyne, Reminyl
	Tacrine	Cognex
	Donepezil	Aricept
NMDA-receptor antagonist	Memantine	Namenda

1.2.2 Amyloid cascade hypothesis

With increasing research into the biochemical changes underpinning AD, the amyloid cascade hypothesis emerged in 1992 when Hardy and Higgins proposed that deposits of amyloid-β were the main causative agent in AD. Their hypothesis stipulates that amyloid plaques, formed by aggregates of amyloid-β generated by the proteolytic cleavages of APP, are central to AD pathogenesis (*24*). Once present in the brain, the plaques initiate a succession of neuropathological events including NFTs, neuronal cell loss, and ultimately dementia (Figure 1.3) (*24*).

The amyloid cascade hypothesis emerged after increasing evidence implicated the role of amyloid-β in AD. The discovery that the senile plaques first described by Alois Alzheimer in 1906 contained amyloid-β (*25*) was the first piece of evidence implicating

amyloid-β as a causative agent in AD. It was later shown that the primary constituent of amyloid plaques was amyloid-β_{1-42} – the species believed to initiate the disease (*6, 7*).

The subsequent discovery that mutations in the *APP*, *PS1* and *PS2* genes cause early onset AD provided further proof of amyloid-β's role in the development of AD, as all of these mutations affect the processing and accumulation of amyloid-β (*3*). In addition, the universal occurrence of AD within the Down's syndrome (DS) population has been attributed to triplication of the *APP* gene, which lies on chromosome 21 (*26, 27*). It is believed that the extra copy of the *APP* gene is sufficient to cause the early-onset AD in individuals with DS (*28*). This combination of biochemical, neuropathological and genetic findings provides compelling evidence in support of the amyloid cascade hypothesis, which has been the subject of substantial research in the field over the past two decades. This is reflected in the next generation of disease-modifying AD drugs, the majority of which are targeting the production, aggregation and clearance of amyloid-β (*29*). However, a number of these emerging drugs have since failed to produce a therapeutic effect in clinical trials (*30*). These results suggest that amyloid build-up cannot solely define AD, putting the validity of the amyloid hypothesis into question. Indeed, some people develop amyloid plaques without suffering cognitive impairment; these cases are called 'asymptomatic AD' (*31*).

It is doubtful that the complex pathophysiology of AD can be explained by a simple linear disease model such as the amyloid cascade hypothesis (*32*). It is likely that there are other causative agents besides amyloid-β that are underpinning AD.
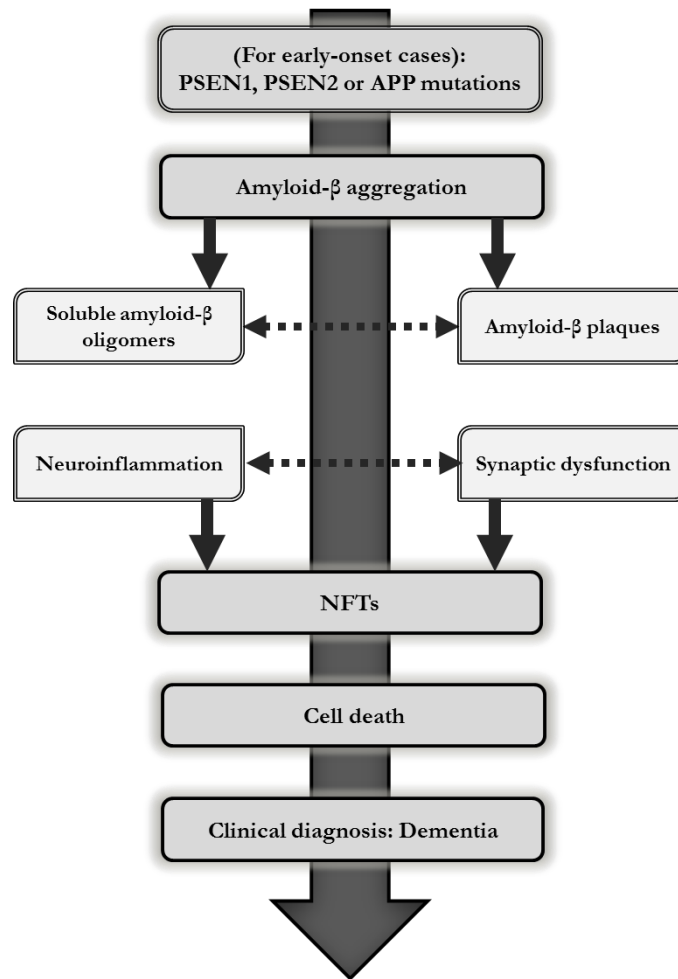
Figure 1.3 *The amyloid cascade hypothesis, adapted from the work by Karran et al. (33)*

1.2.3   The tau hypothesis

One such potentially causative agent is tau, the other major histological hallmark of AD. Tau's inherent role in the human brain is as a cytoplasmic protein that binds to tubulin during its polymerisation, stabilising microtubules and facilitating intracellular transport (*34*). In AD, tau becomes abnormally phosphorylated, forming hyperphosphorylated NFTs. In recent years, tau has been implicated as the major causative agent underpinning cognitive decline in AD (*35*).

The tau hypothesis has a number of advantages over the amyloid hypothesis for defining AD. The work by Braak and Braak identified NFT pathology in post-mortem brains, in the absence of amyloid plaques (*36*); these findings suggest that NFT accumulation is the initiating event in AD (*37*). NFT burden has also been shown to

correlate with the severity of cognitive decline and the duration of dementia (*38, 39*); this correlation is not mimicked with amyloid plaques. In addition to AD, NFTs are also central to a number of other degenerative diseases in the absence of amyloid plaques, such as Pick's disease, frontotemporal dementia (FTD) and progressive supranuclear palsy (*40*). The implication of tau in other dementias strengthens its role as a key pathological agent in AD.

There are no known mutations in the microtubule associated protein tau (*MAPT*) gene that cause early-onset AD; however, a number of mutations in the *MAPT* gene cause other dementias, e.g. autosomal dominant FTD chromosome-17 type (*41*). Individuals with FTD typically exhibit a similar pattern of neuropathological alterations to AD, including cortical atrophy, loss of neuronal cells and behavioural alterations (*42*).

As an AD treatment strategy, there are a number of therapeutic approaches that tau-directed compounds typically target, including: 1) modulating tau phosphorylation by inhibiting tau phosphorylation kinases; 2) stabilization of microtubules, and 3) compounds that prevent tau aggregation (*43, 44*). A number of these tau-mediating therapies have shown promise in preclinical studies, and are currently moving into clinical trials (*45-47*).

In addition to dementias, hyperphosphorylation of tau is observed during hibernation. It has been suggested that tau phosphorylation in the adult mammalian brain may to represent a naturally occurring process that is associated with neuroprotective mechanisms (*48*); hibernating animals may therefore represent an valuable model to study the regulation of tau phosphorylation.

1.2.4 Other hypotheses

Another compelling hypothesis for the cause of AD states that glutamate dysfunction can account for many of the neurochemical and behavioural alterations observed in AD (*49*). Glutamate is the most abundant excitatory neurotransmitter in the CNS which helps regulate synaptic plasticity, neuronal growth, cognition and memory (*50*). Disturbances in the glutamatergic system have been associated with the pathophysiological processes in AD (*51, 52*).

Glutamate activates a number of different receptors in the brain, including the N-methyl-D-aspartate (NMDA) receptors. It is believed that chronic, low-level stimulation

of these NMDA receptors by glutamate leads to neurodegeneration; a phenomenon termed 'excitotoxicity' (*50*). The reason for the increased sensitivity of the glutamatergic system is still unknown, but a number of different mechanisms have been proposed, including: oxidative stress, mitochondrial dysfunction and impaired metabolism, in addition to the presence of amyloid plaques and NFTs (*53-55*).

Therapeutic strategies targeting the glutamatergic system have shown some promise in clinical trials. Memantine, for example, is an FDA-approved NMDA receptor antagonist which addresses the hyperactivity of these receptors (Table 1.1) (*56*). Memantine may delay the deterioration of the patient in mild to moderate cases of AD (*57*).

1.3   Diagnosis of Alzheimer's disease

An accurate and early diagnosis of AD requires careful clinical evaluation, and is crucial for planning treatment strategies and supportive counselling. An initial memory complaint or subtle personality change usually causes a patient to seek medical advice in the first instance.

Typically, a clinician will explore the patient's medical records in order to ascertain whether they have a family history of AD, and therefore may carry an increased risk of developing the disease. For early-onset forms of AD, the increased risk of developing the disease is 50%. It has been estimated that individuals with a family history of late onset ("sporadic") AD carry a 20% chance of developing the disease, compared with 10% across the wider population (*58*). Secondly, a neuropsychological test is employed in order to assess the patient's memory, language and problem solving abilities. The mini mental state examination (MMSE) is the most frequently used, and uses a 30 point questionnaire to measure cognitive function (*59*). As well as helping diagnose AD (and other forms of dementia), the MMSE can indicate the progression and severity of the disease. Patients may undergo additional blood and urine tests, in order to rule out any other cause for their memory problems. Brain imaging techniques may be utilised in order to get a more definitive diagnosis of AD, although these are not routinely employed (*60*).

Often, the current clinical assessment for AD (described in Section 1.3) is inconclusive, resulting in a diagnosis of *mild cognitive impairment* (MCI). MCI can be considered an

intermittent phase between the normal aging process and the earliest features of dementia. MCI patients carry a high risk for developing dementia with over half of those diagnosed converting to AD and other forms of dementia within 5 years (*61*). There are 4 different subgroups of MCI; an algorithm is used by clinicians to aid their classification (Figure 1.4) (*62*). If memory is impaired then the patient is designated as having *amnestic* MCI. A memory component is a strong indicator that the patient will go on to develop AD over other forms of dementia.

In recent years, increasing emphasis is being placed on the development and implementation of *biomarkers of AD*: direct or surrogate measurement of pathophysiological or functional characteristics of the tissue which can be measured *in vivo* (*63, 64*). Biomarkers may offer heightened sensitivity to the early pathological events in AD which precede cognitive impairment, and facilitate early diagnosis of the disease.
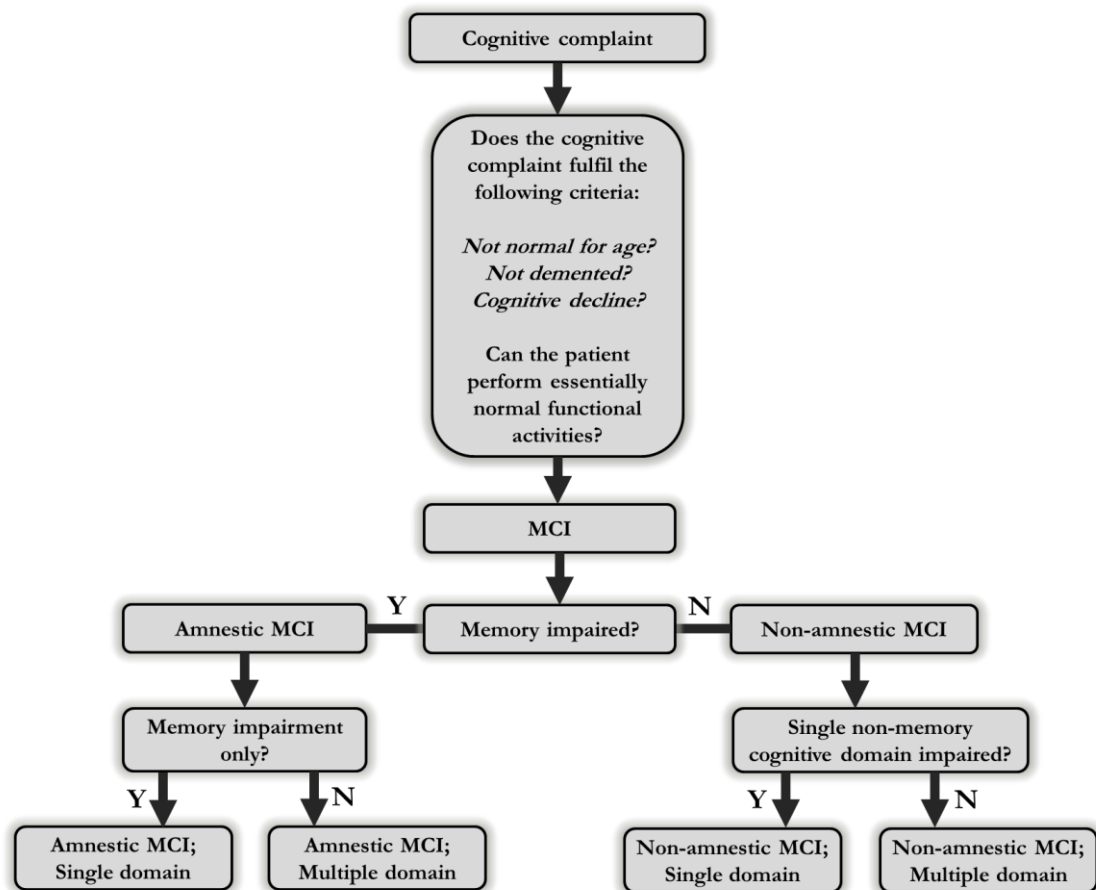
Figure 1.4 *The algorithm used to classify subgroups of MCI, adapted from the work by Petersen et al. (62)*

1.4 Biomarkers of Alzheimer's disease

While the MCI classification is useful for identifying individuals who carry a heightened risk of converting to AD, the diagnostic criteria will ideally move into the asymptomatic stage of the disease. The pathological processes of AD are now believed to begin up to 20 years before the onset of cognitive impairment (*65, 66*). This prolonged prodromal stage of the disease provides a critical opportunity for therapeutic intervention, prior to the irreversible destruction of neuronal tissue (*62, 67*). Thus, the identification and validation of biomarkers of AD is increasingly important, for improving the predictions of those who are at risk of converting from normal cognition to MCI, and finally AD.

Humpel et al. outlined a list of criteria which biomarkers of AD should ideally fulfil (*64*):

1. Reflect physiological aging processes
2. Reflect basic pathophysiological processes of the brain
3. React upon pharmacological intervention
4. Display high sensitivity
5. Display high specificity for the disease as compared with related disorders
6. Allow measurements repeatedly over time
7. Allow reproducibility in laboratories worldwide
8. Should be measurable in non-invasive, easy-to-perform tests
9. Should not cause harm to the individuals being assessed
10. Tests should be inexpensive and rapid
11. Samples should be stable to allow easy and cheap transport
12. Easy collection of fluids not only in hospitals
13. Changes should be at least twofold to allow differentiation of controls
14. Define good cut-off values to distinguish diseases
15. Data published in peer-reviewed journals
16. Data reproduced by at least two independent researchers

While researchers have yet to identify an AD biomarker which satisfies all of the above criteria, several biomarkers have shown sensitivity to early neuropathological changes in AD, and may be useful for the early diagnosis of the disease and evaluating the efficacy of candidate drugs (*63*).

1.4.1 Cerebrospinal fluid

It is now known that molecular changes in the brain can be detected in the cerebrospinal fluid (CSF) (*68*). Candidate CSF biomarkers include: total tau (T-tau) as a marker of neuronal degradation, amyloid-β_{1-42} (Aβ-42), as a marker of amyloid-β metabolism and plaque formation; and phosphorylated tau (P-tau) as a marker for tau phosphorylation and the formation of NFTs (*69*).

A number of studies have reported a marked increase in CSF T-tau and P-tau, alongside decreases in Aβ-42 (*69, 70*). This pattern of changes is unique to AD, and therefore may find relevance in the differential diagnosis of AD over other forms of dementia (*71*). The performance of these biomarkers is high, with reported sensitivity and specificity of CSF biomarkers to discriminate between AD patients from healthy controls of 80 – 90% (*69, 70*). CSF biomarkers are believed by some to be the most sensitive biomarkers of AD neuropathology (*68*).

In order to extract CSF for biomarker analysis, a lumbar puncture (LP) must be performed (*69*). In the clinical scenario, a LP is often avoided due to the post-LP headache, thought to arise due to loss of CSF volume and the leaking of fluid into nearby tissue (*72*). An alternative, non-invasive method for quantifying amyloid-β and tau deposition in the brain is therefore highly desirable.

1.4.2 Positron emission tomography

One such method is positron emission tomography (PET). PET is a nuclear imaging technique which permits the quantification and distribution of a radiolabelled tracer to be assessed *in vivo*. These tracers can be engineered to bind to amyloid plaques and NFTs, which may allow the detection of these causative agents in the brain prior to the onset of cognitive decline (*73, 74*).

The most widely used PET compound for amyloid imaging is the ^{11}C-labelled tracer Pittsburgh compound B (^{11}C-PiB) (*75*). ^{11}C-PiB is a radioactive analogue of thioflavin T; a histological stain which is traditionally used to identify amyloid oligomers – a precursor to amyloid plaques (*76*). It has been demonstrated that the regional uptake of ^{11}C-PiB closely mirrors the post-mortem distribution of amyloid-β, supporting its application as a method for *in vivo* detection of amyloid plaques (*77*). In addition, high

levels of ^{11}C-PiB uptake have been shown to be a strong predictor for conversion from MCI to AD (*78, 79*).
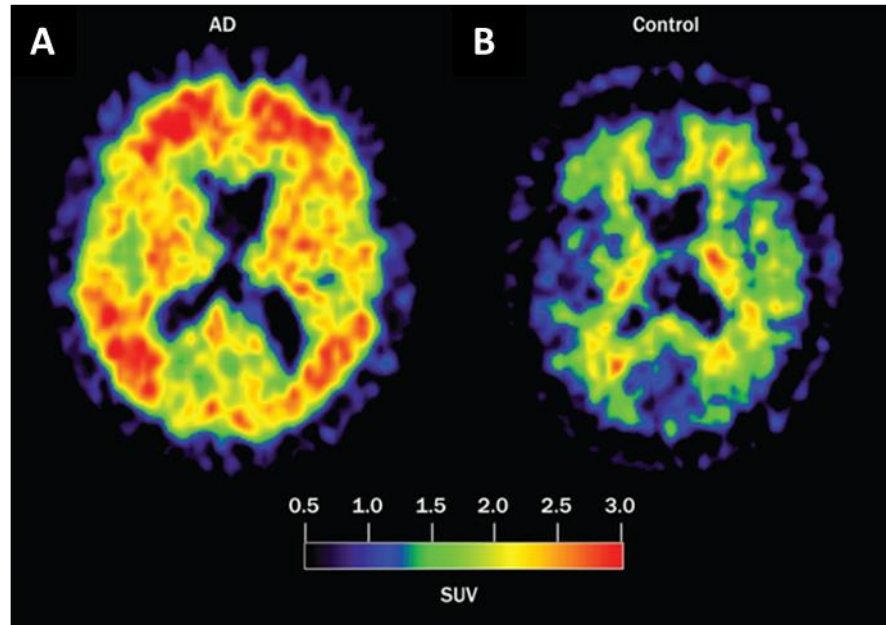
Figure 1.5 *PET scan of an AD patient and healthy control, showing high retention of the tracer in the AD brain. SUV represents the standard uptake value: red = high uptake, blue = low uptake. Reproduced from Nordberg et al. (80)*

However, the very short half-life of ^{11}C (20 minutes) introduces some practical limitations to working with ^{11}C-PiB, as the radioisotope must be produced in close proximity to the PET scanner in order to label the compound and inject the patient in sufficient time (*81*). In order to overcome these difficulties, several other tracers have been developed for *in vivo* amyloid imaging, such as florbetaben, florbetapir and flutemetamol (*81*). These agents are all labelled with the radioisotope ^{18}F, which has a half-life of 110 minutes. Preliminary work using these compounds suggests high sensitivity and specificity to amyloid-β (*81*).

A number of tau radiotracers are currently being developed for *in vivo* tau quantification; these include the compounds ^{18}F-808 (*82*) and ^{18}F-THK-5015 (*83*). As tau burden correlates with cognitive decline in AD (*84*), tracers which permit *in vivo* quantification of the distribution of tau pathology may potentially enable ante-mortem Braak staging

of the disease (*85*). Both of the aforementioned tracers have enabled the differentiation of AD patients from healthy controls, with high uptake in regions vulnerable to NFT deposition (*82, 83*).

Another popular PET tracer for investigating neurodegeneration in AD patients is flurodeoxyglucose (^{18}F-FDG). ^{18}F-FDG is a glucose analogue, and can be used to measure brain metabolism. It is believed that cerebral glucose metabolism measured with ^{18}F-FDG reflects synaptic activity (*86*); in AD, regional reductions in glucose metabolism have therefore been attributed to an impairment in synaptic activity that accompanies neurodegeneration (*63*). Hypometabolism detected using ^{18}F-FDG has a distinct topographical pattern which is distinct from other dementias, enabling the differential diagnosis of AD over other forms of dementia (*87, 88*). It has been shown that ^{18}F-FDG can identify MCI patients who will convert to AD, and may be useful in the early diagnosis of the disease (*89, 90*).
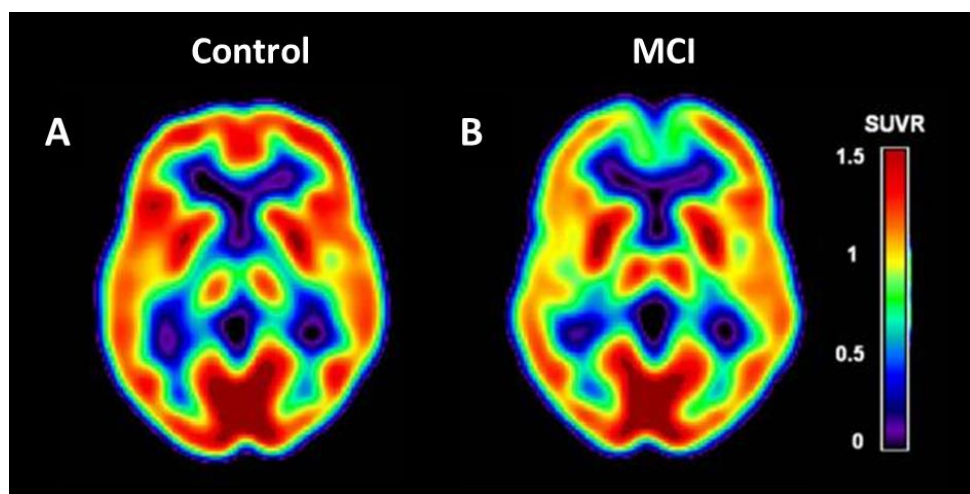
Figure 1.6 *^{18}F-FDG PET scan of (A) a healthy control subject, and (B) a patient with an MCI diagnosis. Regional decreases in ^{18}F-FDG uptake can be observed in the frontal parietal and temporal cortex of the MCI patient. SUV represents the standard uptake value: red = high uptake, blue = low uptake. Reproduced from Mosconi et al. (91).*

However, the short half-life of the PET radioisotopes (both ^{11}C and ^{18}F) has restricted the widespread and routine use of PET for early diagnosis of AD. In addition, the use of PET tracers in longitudinal studies is problematic, owing to the exposure risks

associated with radioactive isotopes; the radiation dose is greatly increased when an anatomical computed tomography (CT) scan is acquired simultaneously, to enable improved localisation of tracer uptake in the brain (*92*).

1.4.3 Magnetic resonance imaging

Structural MRI is an alternative method for assessing AD-related neuropathological changes.

Structural MRI is able to accurately detect grey matter loss in characteristically vulnerable brain regions, such as the hippocampus and entorhinal cortex (*93*). These alterations have been shown to be indicative of progression from MCI to AD and other forms of dementia (*94*). The characteristic topographical pattern of atrophy in the AD brain can also be readily visualised using structural MRI, aiding differential diagnosis of the disease (*93*).
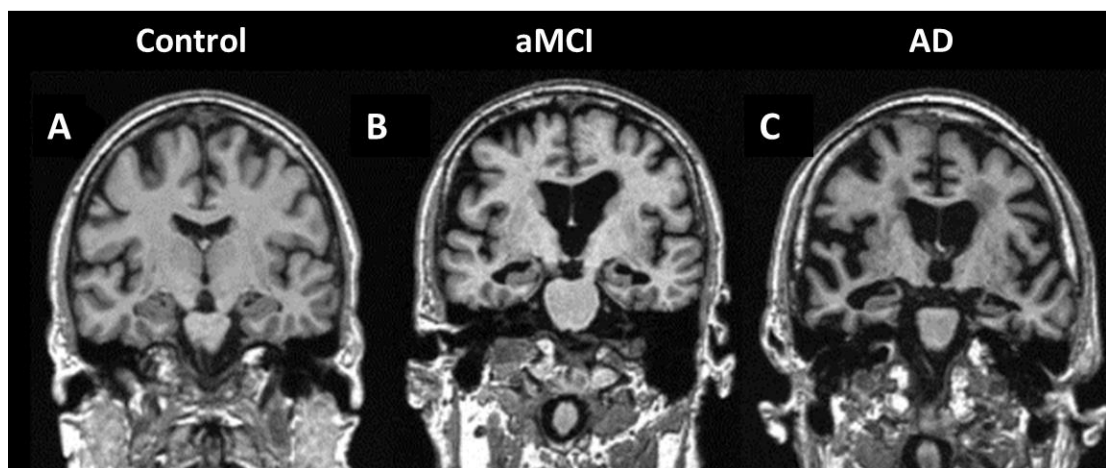
Figure 1.7 *Structural MRI scans of (A) a healthy control subject, (B) a patient diagnosed with amnestic MCI, and (C) and AD patient. Atrophy in the medial temporal lobes can be readily visualized in the aMCI and AD images. Reproduced from Vemuri et al. (95)*

The structural changes which can be visualised using structural MRI have been shown to reflect neuronal loss, decreased synaptic density and cell shrinkage (*96*). As structural changes quantified using MRI correlate well with NFT deposition (*97*), they can be

considered a measure of tau-related neurodegeneration (*98*). It therefore may find clinical relevance in the therapeutic assessment of tau-mediating therapies.

Recently, advanced image processing techniques have been developed to support the analysis of structural MRI datasets, enabling the detection to atrophy in an automated and unbiased fashion (*93*). These techniques have facilitated high throughput analysis of large cohort data sets, such as those generated within the *Alzheimer's Disease Neuroimaging Initiative* (ADNI); a shared resource of AD research data which includes PET and MRI scans, alongside cognitive testing and genetics (*99*). Advanced image processing techniques have also enabled the detection of structural MRI changes up to 10 years prior to the development of AD, in the prodromal phase of the disease (*100*).

Other MRI techniques are increasingly being used to study AD-related changes. Diffusion tensor imaging (DTI), for example, is a technique that has shown sensitivity to microstructural changes in the white matter of the AD brain (*101*). More information about other MRI techniques which may offer sensitivity to neurodegenerative changes can be found in the proceeding chapters.

1.5   The dynamic biomarker model

In 2010, Jack et al. proposed a *dynamic biomarker model* for the AD pathological cascade: a schematic depiction plotting the sensitivity of the aforementioned biomarkers against time (Figure 1.8) (*63, 98*). According to this model, biomarkers of amyloid deposition show the earliest abnormalities prior to tau-related and neurodegenerative changes. This was achieved using measurements of Aβ-42 in the CSF and PET with ^{11}C-PiB, with the former offering the earliest sensitivity to AD-related changes. Biomarkers of neurodegeneration, including CSF measurements of tau, structural MRI and FDG-PET, were abnormal later in the disease.
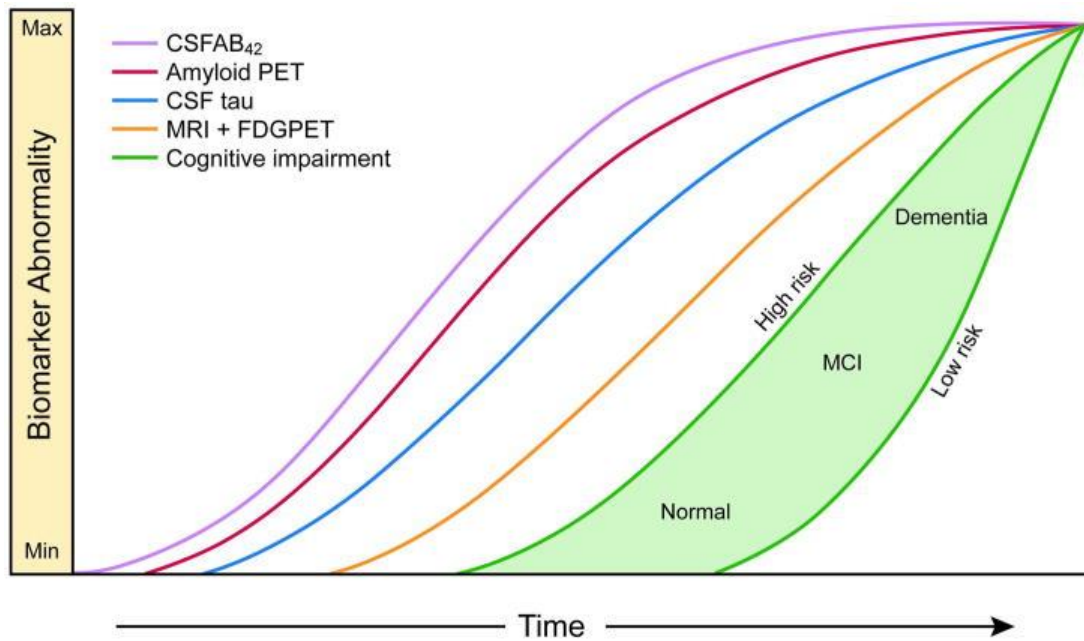
Figure 1.8 *Dynamic biomarkers of the AD pathological cascade model. Amyloid-β is identified by CSF Aβ42 or PET amyloid imaging. Neuronal injury and dysfunction is identified by CSF tau or FDG-PET. Neurodegenerative atrophy is measured by structural MRI. Reproduced from Jack et al. (98)*

Jack et al. acknowledge that the observations made by Braak and Braak, described in Section 1.2.3, do not fit their model. Braak and Braak stated that NFT deposition precedes amyloid-β accumulation in AD -- a finding which is not reflected in the dynamic biomarker model. In defence of their model, Jack et al. stated that the genetic mutations in the *APP*, *PS1* and *PS2* giving rise to early-onset forms of AD are supportive of amyloid disturbances as the initiating event. Alternatively, it is also possible that these early, low levels of tau are below the detection threshold of the current available biomarkers. In support of the latter theory, Jack et al. released another version of their dynamic biomarker model, which acknowledges that tau pathology may be the first pathophysiological process to arise in many AD individuals, although it is below the detection threshold of the currently available biomarkers (Figure 1.9) (*98*).
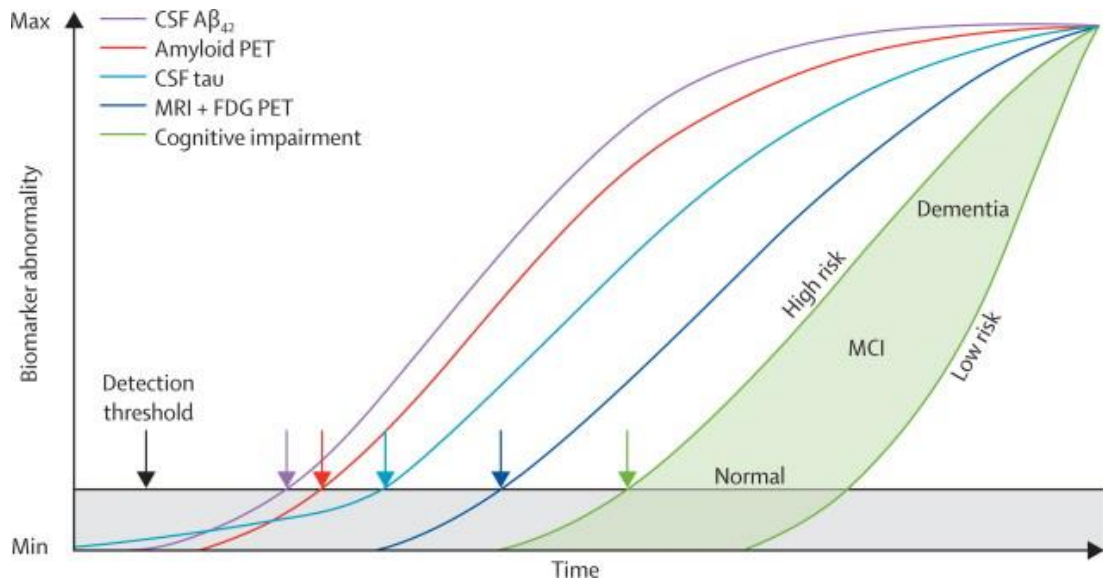
Figure 1.9 *Updated biomarkers of the AD pathological cascade model, which proposes that tau pathology precedes amyloid-β alterations but at a sub-threshold biomarker detection level. Reproduced from Jack et al. (98).*

1.6 Mouse models of Alzheimer's disease

Mouse models of AD are valuable tools for furthering our understanding of the different mechanisms underpinning the human condition. The most commonly used AD mouse models harbour mutations in human transgenes associated with early-onset forms of the human disease: *APP*, *PS1* and *PS2*. Although these mutations are not representative of the majority of sporadic forms of the disease, they enable the replication of AD neuropathology in the mouse.

There are many different mouse models of AD, each exhibiting a unique pattern of AD-related neuropathological changes. Some of the more frequently used models are detailed in Table 1.2.

1.6.1 h*APP* mouse models

The most widely used mouse models of AD are based on transgenic expression of human *APP* (h*APP*) (*102*). There are over 20 known *APP* mutations associated with early-onset AD, each named according to the geographical location from which the

Table 1.2 *Summary of the most commonly used mouse models, adapted from previous work by Hall et al. (102)*

	Mouse model	Genes	Mutations	Plaques (months)	Tangles (months)	Neuronal loss (months)	Synaptic loss (months)	Cognitive impairment (months)	Primary paper
hAPP models	PDAPP	*APP*	Ind.	6			8	3	(*103*)
	J20	*APP*	Ind., Swe.	5		3	8	4	(*104*)
	Tg2576	*APP*	Swe.	11			4 - 5	10	(*105*)
	APP23	*APP*	Swe.	6		14 - 18		3	(*106*)
	TgCRND8	*APP*	Ind., Swe.	3		6	6	3	(*107*)
	R1.40	*APP*	Swe.	13.5					(*108*)
Aβ	BRI-Aβ42	*BRI-A*		3					(*109*)
hAPP/PS1	PS/APP	*APP, PS1*	Swe., *PS1* M146L (A>C)	6		22		3	(*110*)
	APPswe/PS1Δ E9	*APP, PS1*	Swe., *PS1*: Δ E9	6				6	(*111*)
	5XFAD	*APP, PS1*	Swe., Flo., Lon., *PS1* M146L (A<C), *PS1* L26V	1.5		9	9	4 – 5	(*112*)
hTau	Tg2576/Tau(P301L)	*APP, MAPT*	Swe., *MAPT* P301L	6 – 7	3				(*113*)
	rTg4510	*MAPT*	*MAPT* P301L		2.5	5	8	2.5 - 4	(*114*)
	3xTg	*APP, PS1, MAPT*	Swe., *MAPT* P301L, *PS1* M146V	6	12			4	(*115*)
	htau	*MAPT*	-		9	10 - 14		6	(*116*)

affected family originated (*117*). The Swedish (Swe.), London (Lon.) and Indiana (Ind.) are the most frequently replicated in mouse models of AD.

The PDAPP mouse, which was generated by Games et al. in 1995, is considered to be one of the oldest mouse models of AD (*103*). This mouse exhibits a number of cognitive abnormalities which manifest prior to plaque pathology; this includes deficits in spatial working memory from 4 months, followed by a decline in recognition memory from 6 months. Plaque deposition is observed from 6 months. The Tg2576, developed the following year by Hsaio et al., develops a similar pattern of age-related learning defects and plaque formation (*105*).

Unusually, these mice do not typically exhibit significant neuronal loss; a defining feature of the clinical condition (*118, 119*). A number of other h*APP* mouse models have also been unable to replicate the neuronal loss (*120*). Of the h*APP* transgenic mice which do exhibit neuronal loss, such as the APP23 and J20 models, it is marginal and does not reflect the substantial neuronal loss observed in AD patients (*121*). These findings suggest that h*APP* mice may not be the most suitable models for the study of AD.

1.6.2   Amyloid-β mouse models

AD mouse models can also be used to study the pathophysiological effects of different amyloid-β series. McGowan et al. have developed a transgenic mouse (the BRI-Aβ40 mouse) that expresses amyloid-β_{1-42} in the absence of *APP* overexpression, in order to study the neurotoxic effects of amyloid-$\beta_{\beta1-42}$. BRI-Aβ40 mice develop age-related plaque pathology; these findings support the hypothesis that amyloid-β_{1-42} is the initiating molecule in the pathogenesis of AD.

Conversely, mice overexpressing amyloid-β_{1-40} do not develop plaques, providing further proof of amyloid-β_{1-42}'s role in the development of AD (*109*).

1.6.3   Presenilin mice

There are 184 mutation in *PS1*, and 14 mutations in *PS2* that are known to cause early-onset AD (*117*); the former are both more abundant and more severe, making them the focus of AD mouse models (*122*). Transgenic *PS1* mice have been created, which permit the study of the effects of *PS1* on *APP* processing (*102*). These mice exhibit

increased levels of amyloid-β_{1-42}, although they do not develop amyloid plaque pathology or cognitive abnormalities (*123*).

When *PS1* mice are crossed with mice transgenic for h*APP*, however, the development of AD neuropathology is substantially increased, in comparison to the singly transgenic h*APP* mice (*121*). The PS/APP mouse, for example, was generated by crossing the Tg2576 mouse with a mouse expressing mutant *PS1* (*124*). The double transgenic progeny develop plaque pathology from 6 months; a significantly younger age than the single transgenic Tg2576 mice (*124*).

An even more aggressive line is the 5XFAD which encompasses 5 AD-related mutations, including: 3 h*APP* mutations (the Swedish, Florida and London mutations) and 2 mutations in *PS1* (*112*). The 5XFAD mouse rapidly develops amyloid pathology, with plaques detectable from 1.5 months. Unlike the aforementioned mouse models, where neuronal loss is marginal, the 5XFAD also exhibits gross neuronal loss (*112*). These findings suggest that the combination of multiple mutations induces neuronal loss in the mouse that is more representative of the clinical condition (*125*).

1.6.4   Tau mouse models

The models discussed so far faithfully encapsulate the characteristic amyloid plaques in AD. However, they are limited models of AD owing to the absence of tau pathology, and little or no neuronal loss.

In order to model tau pathology in the mouse, transgenic models expressing mutant human *MAPT* (h*MAPT*) have been developed. The rTg4510 is a widely studied mouse model of tauopathy which carries a mutation in h*MAPT* (*114*). This mouse develops robust NFT pathology and exhibits many additional features of AD such as cognitive impairment, synaptic dysfunction and neuronal loss (*114*). It is worth noting that this mouse could arguably be considered a model of FTD; however, the NFT pathology which the rTg4510 mouse exhibits closely mimics that seen in AD patients (*114*). The rTg4510 mouse is therefore widely accepted as a valuable model for dissecting the role of tau in AD (*14*).

An alternative model which is commonly used to study the neuropathological effects of tau is the htau mouse, which develops pathology from the overexpression of non-mutated human tau. Htau mice exhibit AD-like neuropathology including age-related

NFT deposition, cognitive impairment and neuronal loss in a spatiotemporal distribution similar to that found in AD (*116*). These findings suggest that amyloid-β may not necessarily be a prerequisite for tau pathology to develop from wild-type tau, as seen in AD (*116*).

Recently, mice that exhibit amyloid plaques and NFTs have been generated, by combining *APP* mutations (with or without *PS1*) with mutant forms of tau. These mice deliver a combination of plaque and tangle pathology not seen in other lines, permitting the exploration of interactions between amyloid-β and tau (*102*). For instance, the 3xTg line develops age-related AD neuropathology, including cognitive deficits, amyloid plaques and NFTs (*115*).

1.6.5 Promoter sequences

Although many of the models described here exhibit pathological similarities, their temporal profile can differ. This can be due to a number of factors: 1) the different genetic mutation; 2) the genetic background on which the transgene is maintained; and 3) the type of promoter used (*125*).

A promoter is a short construct of deoxyribose nucleic acid (DNA) that initiates the transcription of a gene, and defines where in the body the gene is expressed. Several different promoters are used in mouse models of AD, and outlined in Table 1.3.

Table 1.3 *Commonly used promoters in mouse models of AD; adapted from Hall et al. (102)*

Promoter	Brain region expressed	Cell types	Expression begins by:
PDGF-B	Widespread (*126*)	Neurons (*126*)	E15 (*126*)
Thy-1	Widespread (*127, 128*)	Neurons (*127*)	P7 (*127*)
Prp	Widespread (*129, 130*)	Neurons, astroctyes, oligodendroyctes, microglia (*129*)	E12.5 (*131*)
CaMKII-α	Forebrain (hippocampus, cortex) (*132*)	Neurons, glia, synaptic junction fractions, post-synaptic densities (*132*)	P5 (*133*)

The promoters used are typically not native to the mouse genome, but *heterologous*: that is, taken from another species. They are chosen for their strength or pattern of expression. This often results in expression of the transgenic protein at higher levels than normal, and elevated levels of plaque or NFT deposition (*125*).

1.6.6 Mouse models of Alzheimer's disease: concluding remarks

The ideal mouse model of AD would develop the entire spectrum of clinical and pathophysiological features seen in the human condition, including amyloid plaques and NFTs, neuronal loss, synaptic dysfunction, cognitive deficits and progressive, age-related neurodegeneration. Different mouse lines encapsulate elements of this pathological cascade, and are useful surrogates for patient populations in preclinical drug trials targeting one or more of these features.

While no mouse exists that recapitulates all the aspects of AD, the complementary use of several models will support growing research into the neurobiology of AD.

Chapter 2:   Magnetic Resonance Imaging

In this section, I have provided a brief overview of nuclear magnetic resonance (NMR) physics, and introduced the fundamental MRI pulse sequence and contrast mechanisms. I have also introduced the basic concepts underpinning a number of different imaging techniques that are applied in this thesis.

2.1   Introduction

MRI is a powerful non-invasive imaging technology which utilises strong magnetic fields and radio waves to produce detailed anatomical images of the body. Since its inception in the 1970s, MRI has established itself as one of the most powerful tools for routine clinical diagnosis, as well as a valuable modality in biomedical research.
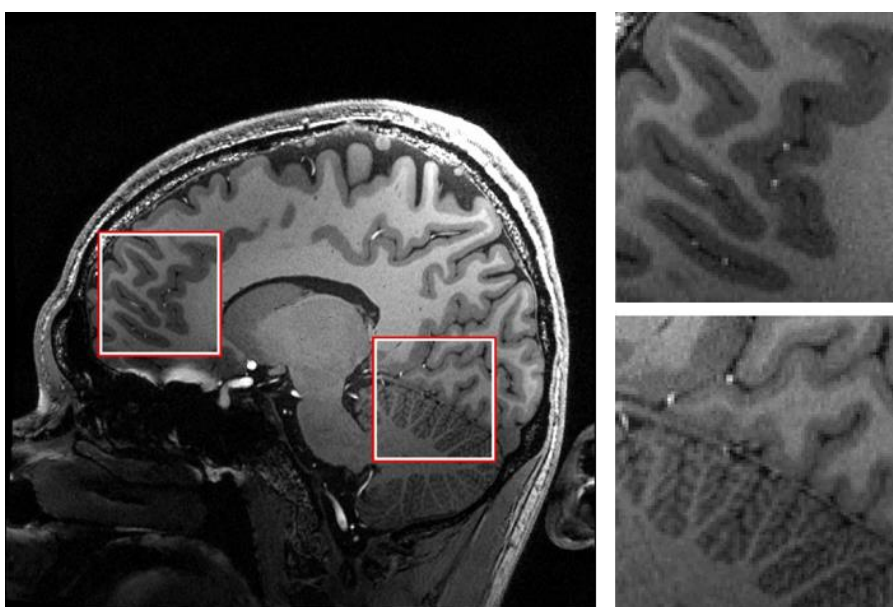
Figure 2.1 *(A) Anatomical scan of the human brain, acquired using a 7 Tesla MRI scanner. This was acquired at 0.44 mm³ isotropic resolution. (B) Magnifications of the marked regions, showing exquisite soft tissue contrast, including the folia in the cerebellum. Adapted from Stucht et al. (134).*

MRI exploits the principles of NMR to produce an image. NMR is a physical phenomenon in which nuclei in a magnetic field absorb and re-emit electromagnetic radiation. It has been known for over 70 years that atomic nuclei which are placed inside a magnetic field and irradiated with radiofrequency (RF) energy of a certain

wavelength will produce a signal (a voltage in a coil); this is due to the interactions of the nuclei with the magnetic field. These early discoveries were unearthed by Felix Block and Edward Purcell, who received the Nobel Prize in 1952 "for their development of new methods for nuclear magnetic precision measurements and discoveries in connection therewith" (*135*).
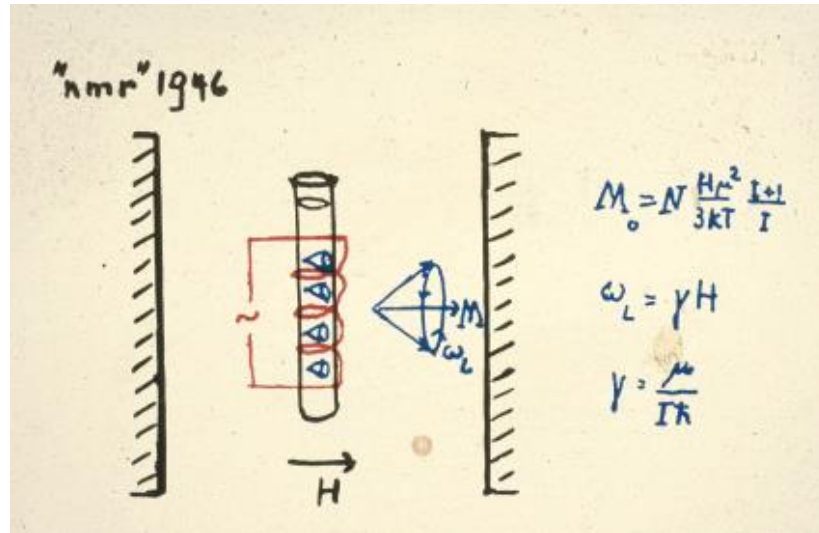
Figure 2.2 *An extract from Felix Bloch's notebook, describing his famous experiment. Here, 1cm³ of water was placed inside a small glass bulb, around which were wrapped an RF transmitter and receiver coil. The bulb was placed inside a magnetic field, before a pulse of RF was delivered to the sample. Image reproduced from 'The discovery of NRM' (136).*

It is now known that atomic nuclei possess their own form of angular momentum called nuclear spin, *I*. This can be visualised as the motion of the nucleus rotating about its axis. The overall spin of an object depends on the number of protons and neutrons it possesses. For atoms with the same proton and neutron number, $I = 0$. Conversely ¹H, the source of signal in most MRI experiments, has no neutrons, thus the proton has two possible spin states: either $+ \frac{1}{2}$ or $- \frac{1}{2}$. These orientations are specified by the quantum number, *m*. When these spin states are placed inside an external magnetic field, B_0, they align either parallel ($m = + \frac{1}{2}$) or antiparallel ($m = - \frac{1}{2}$) to the B_0 field (Figure 2.3). The nuclei of spins in the $m = + \frac{1}{2}$ state have lower energy than spins in the $m = - \frac{1}{2}$ state.
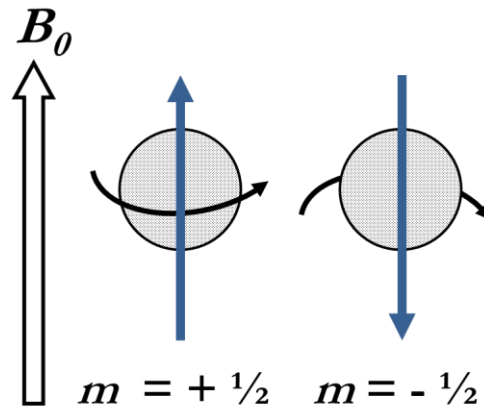
Figure 2.3 *A proton takes two possible orientations when placed in an external magnetic field*

The proportion of spins in the + ½ and – ½ states are determined by the Boltzmann distribution:

$$\frac{N_{anti-parallel}}{N_{parallel}} = e^{\left(\frac{-\Delta E}{kT}\right)} \tag{1.1}$$

ΔE is the energy difference between the two states, k is the Boltzmann constant and T is the temperature in Kelvin. This relation shows that thermal energy will result in the $m = + ½$ state is slightly more populated; in a standard 1.5 T scanner at body temperature of 37°C, this is typically an excess of 4 protons per million in the lower energy state.
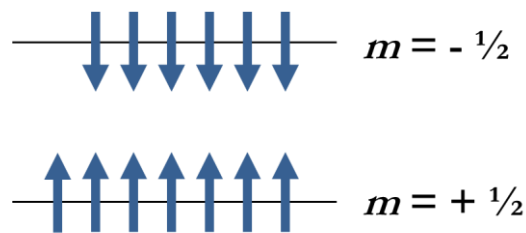
Figure 2.4 *Schematic representation of the imbalance of spins; the lower energy level is slightly more populated.*

This unequal distribution results in a net magnetization, M_0, in the presence of B_0. It is the manipulation of this net magnetization that is the source of signal in all MR

experiments. As B_0 is conventionally defined to be orientated in the z direction of a Cartesian coordinate system, net magnetization is also orientated in the z direction (M_z).
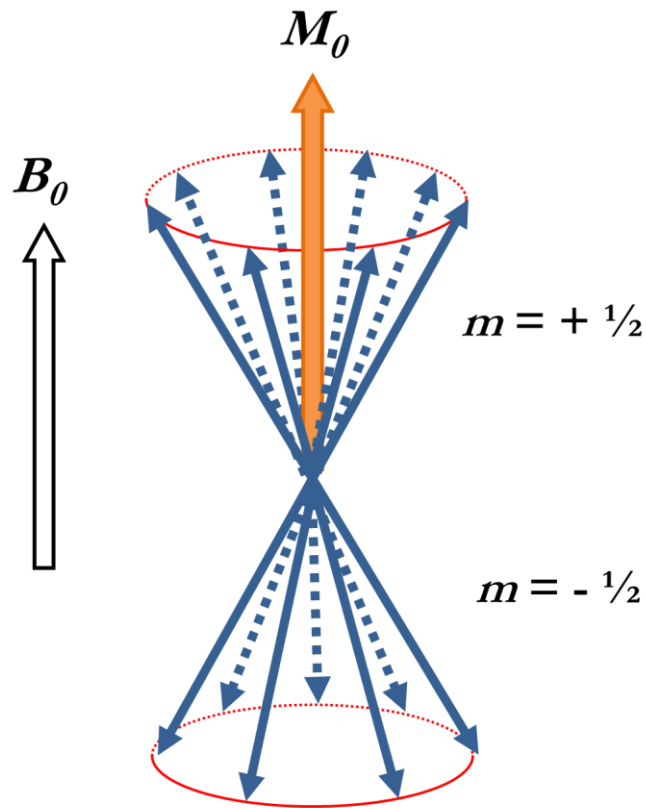
Figure 2.5 *In the presence of the main B₀ field, more spins reside in the m = + ½ there is net magnetization along the z direction.*

Spins will precess when placed in an external magnetic field, due to their angular momentum. The rate of precession is proportionate to the strength of the magnetic field B_0, and expressed by the Larmor equation:

$$\omega_0 = \frac{\gamma B_0}{2\pi} \qquad (1.2)$$

ω_0 is the Larmor frequency and γ is the gyromagnetic ratio – a constant for each nuclei.
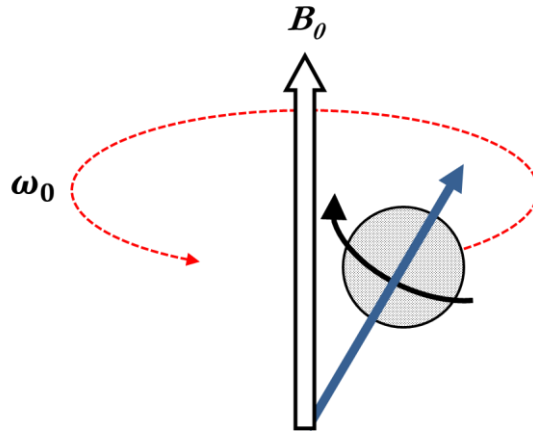
Figure 2.6 *Schematic illustrating the spin precession of a nuclei in the presence of an external magnetic field at the Larmor frequency,* $\boldsymbol{\omega_0}$.

The net tissue magnetisation parallel with B_0 is too small (e.g. 1μT at 1.5T) to be detected whilst at equilibrium. In order to detect the magnetization induced within a sample by the B_0 field, it must be brought out of this alignment using a pulse of energy, which causes protons to transition from the lower energy level to the higher energy level. When M_z is tilted into the xy plane, a signal can be recorded by a receiver coil which only measures magnetization in the xy plane. The energy required for these transitions is defined in Equation 3.

$$E = hv = \frac{\gamma h B_o}{2\pi} \tag{1.3}$$

E is the energy required to excite a proton from the $m = + \frac{1}{2}$ state to the $m = - \frac{1}{2}$ state; h is Plank's constant; B_0 is the external magnetic field strength and γ is the gyromagnetic ratio.

In order for transitions to occur, energy must be applied at the Larmor frequency in order to selectively excite the nuclei under investigation. This energy is supplied in the form of an electromagnetic pulse, which causes the protons to temporarily transition into the higher energy state before returning to ground level. These electromagnetic pulses will typically be in the RF part of the spectrum. This excitation causes the M_0 to move out of the B_0 direction. The extent of deviation from the B_0 field depends on magnitude and duration of the RF pulse. If the RF pulse has exactly enough energy to

63

tilt the magnetization from M_z (parallel to the B_0 field) to M_{xy}, then it is called a 90° RF pulse.

A B_0
Net magnetization M_z
parallel to the B_0 field

B
RF pulse
Magnetization tilted from z direction into the transverse (xy) plane

C
RF pulse
90°
Receiver coil
The magnetization in the xy plane generates a voltage in a receiver coil
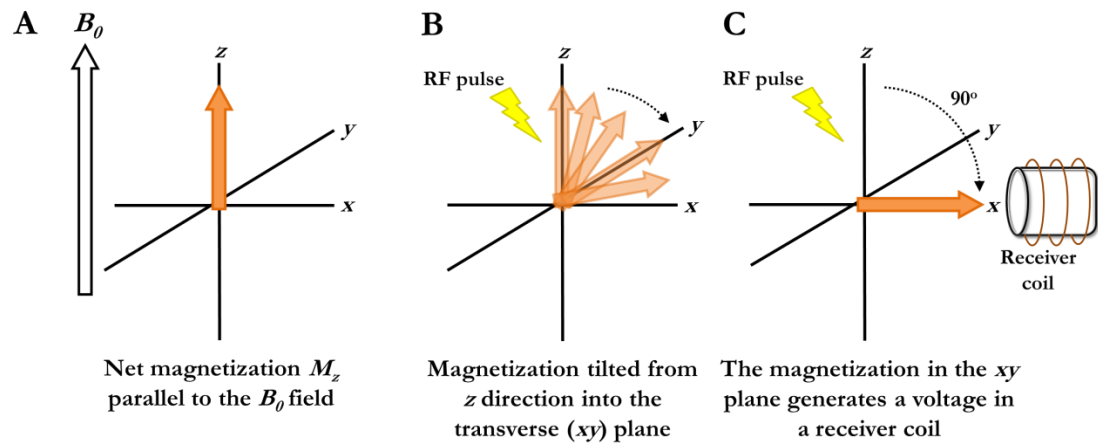
Figure 2.7 *Schematic describing the tilting of net magnetization from the z direction into the transverse (xy) plane, following a 90° RF pulse. (A) In a reference frame rotating at the Lamor frequency, the net magnetization is parallel with the B_0 field in the z direction. (B) An RF pulse is applied, which begins tilting the magnetization into the xy plane. (C) The magnetization has been tilted into the xy plane, where it generates a sinusoidal current in a receiver coil; this coil will detect magnetization which has a component in the xy plane.*

When M_z has been tilted into the *xy* plane, it generates a voltage in a receiver coil, which rapidly decays once the RF pulse has been switched off and the magnetization gradually returns parallel to the B_0 field. The signal that is produced is known as the *free induction decay* (FID) (Figure 2.8A). It is often more convenient to look at the signals in the frequency domain instead of the time domain; so, a Fourier transform (FT) is performed on the time-domain signal, converting it into a frequency domain signal (Figure 2.8B).
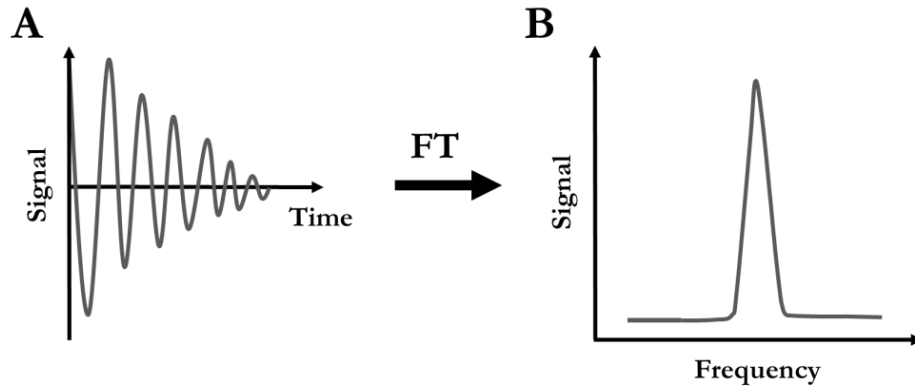
Figure 2.8 *(A) A signal induced in the receiver coil – the free induction decay. Fourier transfer of this time domain signal produces a frequency domain signal, with the peak frequency at the Lamor frequency.*

The loss of net signal, or 'relaxation' has two components: 1) the T_1 or 'spin-lattice' relaxation, and 2) T_2 or 'spin-spin' relaxation; both will be discussed in the next section.

2.2 T_1 Relaxation

T_1, or 'spin-lattice' relaxation, is the rate at which the excited protons return to the equilibrium magnetisation. The term spin-lattice is used as this relaxation mechanism involves an exchange of thermal energy between the excited spins and the lattice: the molecules that make up the surrounding structure. Following exposure to an RF pulse, nuclei dissipate their energy and gradually regain M_0 magnetization; this typically takes 1 – 5 seconds to occur in biological tissue at clinical field strengths. The T_1 time constant is the time it takes for 63% of the M_z magnetization to recover, at a time t, following a 90° RF pulse, and is described by Equation 4.

$$M_{xy} = M_z \cdot \left(1 - \exp\left(\frac{-t}{T1}\right)\right) \tag{1.4}$$

Different tissue types in the body have different T_1 relaxation times. For instance, fats have a very short T_1 (typically 260 ms in a standard 1.5T clinical scanner) whilst fluids such as CSF have a relatively long T_1 (2600 ms). The T_1s of most other tissues in the body fall within the range of fat and fluid. As described earlier, T_1 relaxation occurs when the spins exchange their energy with their surrounding molecular framework.

However, the higher energy state is a relatively stable position for the spins to be in and it does not occur spontaneously. As described earlier, in order for transitions to occur between spin states, energy must be applied at the Larmor frequency. In the absence of a B_1 field (once the RF pulse has been switched off), they must be stimulated to relax by emissions of energy through contact with their neighbouring protons, nuclei or molecules. This contact takes the form of an oscillating magnetic field from the molecular environment in which a spin resides. This oscillating magnetic field refers to the rotation, vibration and translation of the molecules, and is termed *molecular tumbling*.

Water molecules can broadly exist in three states:

1. Free to move (unbound)
2. Bound to a macromolecule by a single bond, which permits rotation (structured)
3. Bound by two bonds, prohibiting movement (tightly bound)

These three different states have a differing range of tumbling frequencies. Free water is evenly likely to tumble at many different frequencies, which makes it very inefficient at T_1 relaxation. The T_1s of free water are therefore very long. In solid structures, the tightly bound water molecules are much more likely to tumble very slowly, producing an oscillating magnetic field which is much *lower* than the Larmor frequency. Equally, they are inefficient at stimulating the transitions and have long T_1s. Incidentally, structured water contained within soft tissues in the body provides the ideal environment for T_1 relaxation: these tissues are most likely produce an oscillating magnetic field at the Larmor frequency, and are efficient at T_1 relaxation.
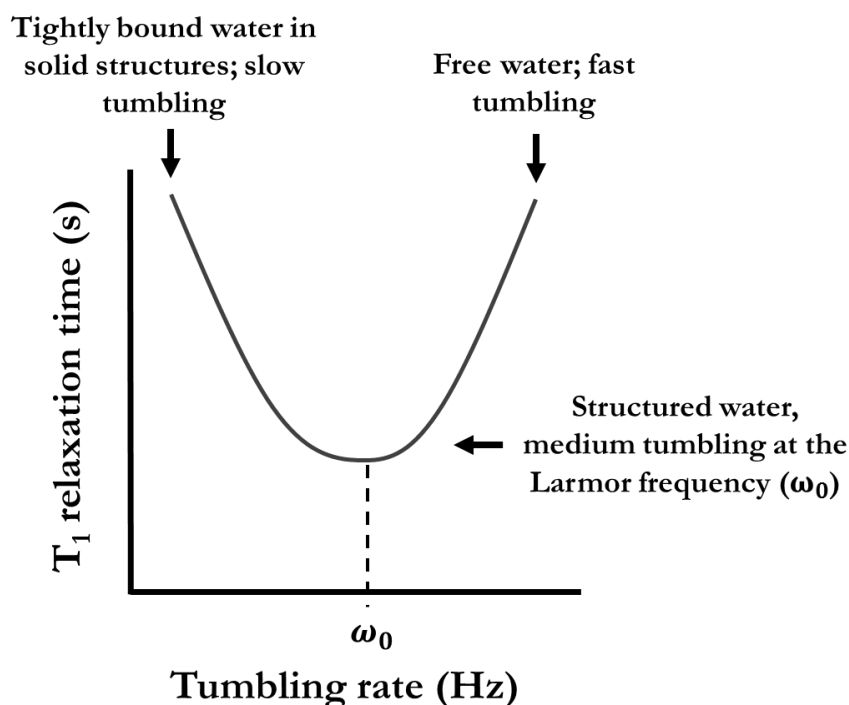
Figure 2.9 *Graph showing the tumbling rates of water in different molecular environments and how it affects the T_1 relaxation time; structured water has the most efficient T_1 relaxation as it tumbles at the Larmor frequency. Adapted from Dowsett et al. (137).*

2.2.1 Measuring T_1 relaxation time

The standard method for measuring T_1 is known as *inversion recovery*. An $180°$ RF pulse is applied, which inverts the M_0 magnetization along the $-z$ axis to give $-M_0$ magnetization immediately after the RF pulse. After a time period, during which $-M_0$ magnetization decays due to spin-lattice relaxation, a second RF pulse is applied at 90^0 and the M_0 magnetization is recorded. This is repeated using different time period delays, which are known as *inversion times* (TIs).

When measuring T_1 relaxation, the delay between successive inversion pulses must be sufficiently long in order for M_z magnetization to completely recover before the next pulse is applied; this delay is called the *repetition time* (TR). TR is typically set to approximately 5 times the T_1 of the tissue under investigation.
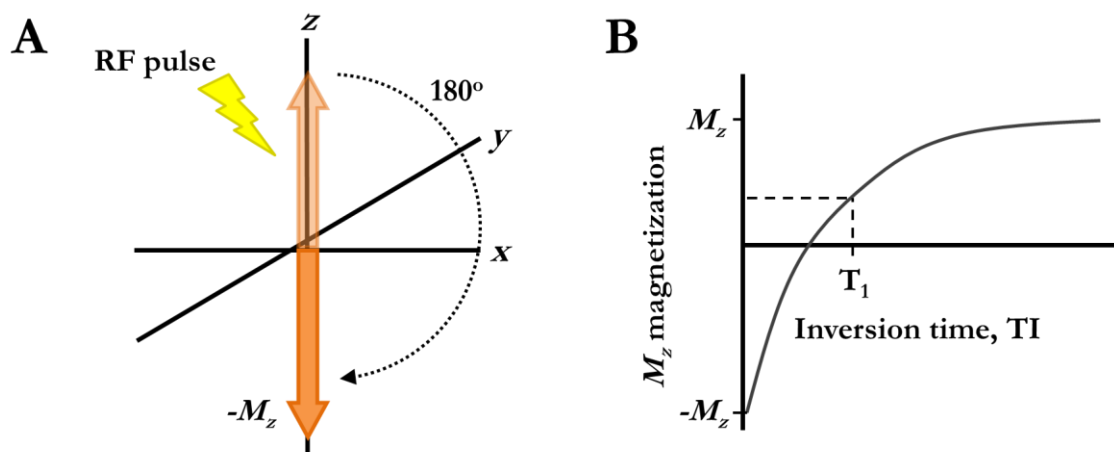
Figure 2.10 *Schematic illustrating the measurement of T_1 relaxation. (A) An 180^0 RF pulse is applied, which inverts M_z magnetization into the $-z$ axis, producing $-M_z$ magnetization. (B) T_1 relaxation is the time it takes for 67% of M_z to recover.*

2.3 T_2 relaxation

T_2, or 'spin-spin' relaxation is the rate at which M_{xy} magnetization returns to a net zero magnetisation following exposure to an RF pulse. The term 'spin-spin' is used because this relaxation mechanism involves interactions between adjacent spins. Immediately after an RF pulse has been applied, the spins are aligned in one direction in the M_{xy} plane. In this state, the spins are said to be phase coherent. However, this coherence is temporary: when two neighbouring protons come together, they begin to interact with each other via their oscillating magnetic fields. These inter- and intra-molecular interactions cause slight changes in the magnetic field that each proton experiences, causing its Larmor frequency to change. This causes the spins to move out of phase, and the M_{xy} magnetization is reduced. The T_2 time constant is the time it takes for 63% of the M_{xy} magnetization to decay, at a time t, following a 90° RF pulse, and is described by Equation 5.

$$M_{xy} \; = \; M_o \cdot \exp\left(\frac{-t}{T2}\right) \tag{1.5}$$

T_2 relaxation typically increases as the molecular tumbling rate increases. Free water molecules that are tumbling very rapidly will be exposed to fluctuating magnetic fields

which averages to zero. This produces a fairly homogeneous local field and little dephasing, resulting in long T_2 relaxation times. Conversely, bound water molecules will experience a static magnetic field inhomogeneity and dephase more rapidly. This will result in shorter T_2 relaxation times.
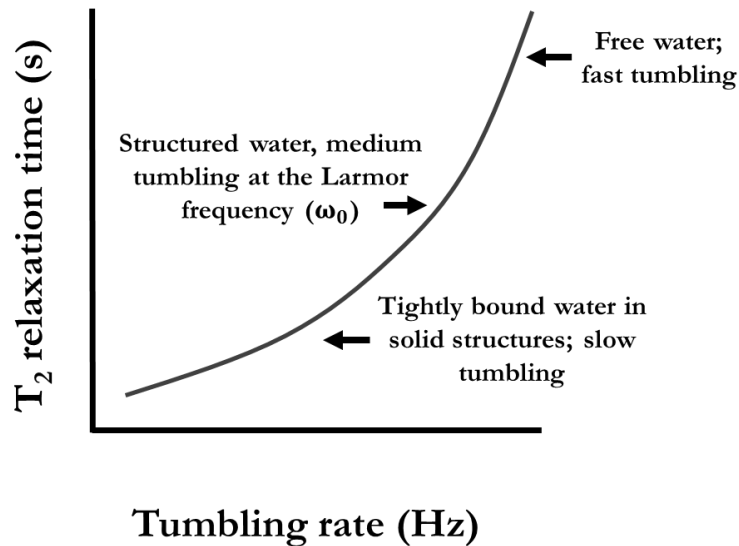
Figure 2.11 *Graph showing the tumbling rates of water in different molecular environments and how it affects the T_2 relaxation time; tightly bound water molecules have the shortest T_2 relaxation times as they behave more like a static magnetic field inhomogeneity. Adapted from Dowsett et al. (137)*

Inhomogeneities in the B_0 magnetic field also cause dephasing of the spins and contribute to the decay of M_{xy} magnetisation. The decay rate constant associated with the combination of spin-spin dephasing and field inhomogeneities is known as T_2^*. However, the T_2 relaxation time only represents the decay rate constant associated with dephasing of the spins due to spin-spin interactions. When measuring T_2 relaxation, the dephasing due to the B_0 field must therefore be taken into account.

2.3.1   Measuring T_2 relaxation time

When measuring T_2 relaxation, a 90° RF pulse is applied which tilts magnetization into the *xy* plane. After a short time, during which M_{xy} magnetization is lost due to spin-spin interactions *and* inhomogeneities in the B_0 field, a 180^0 refocusing pulse is applied. This flips the protons around an axis in the transverse plane; as a result, the slower spins are

now ahead of the faster ones. The spins then begin to regain common alignment and come back into phase at the echo time, TE. The application of the 180° RF pulse effectively causes the dephasing of the spins due to time-invarying field inhomogeneities to be reversed.
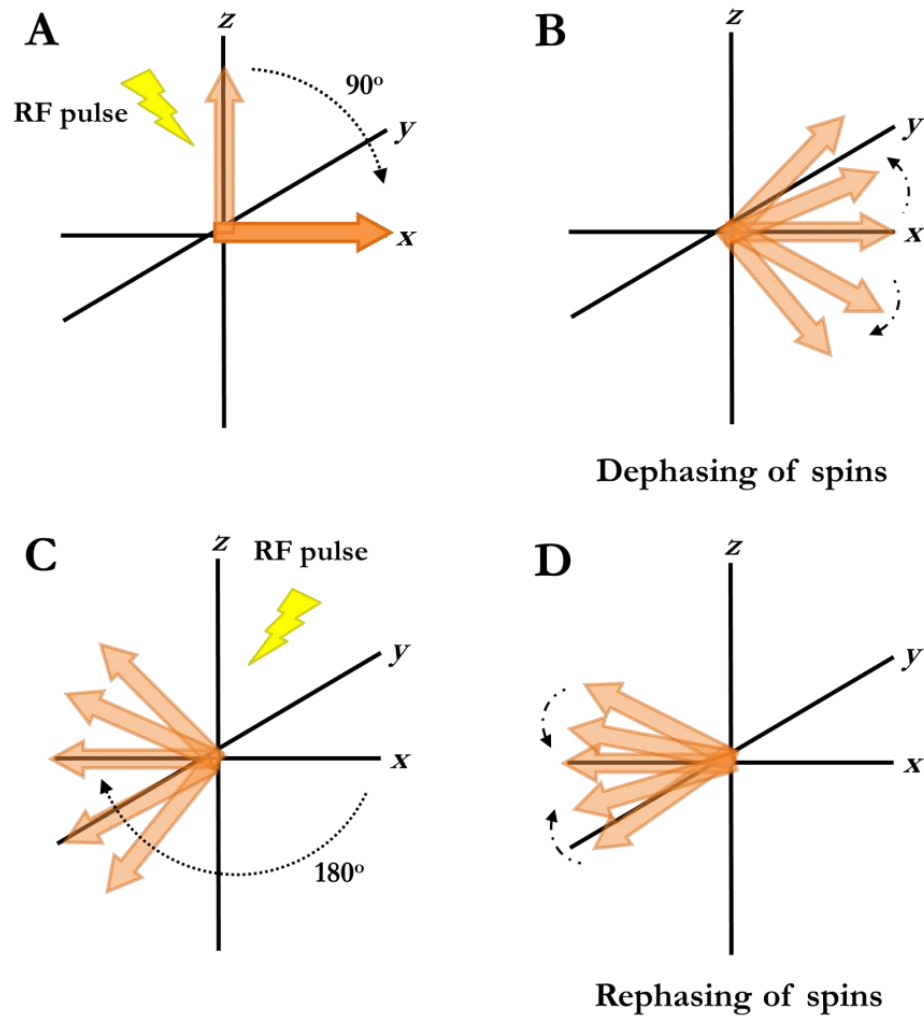
Figure 2.12 *Schematic showing (A) the flipping of magnetization into the xy plane following a 90° RF pulse. (B) The spins rapidly dephase due to spin-spin interactions and B_0 field inhomogeneities. (C) A 180° RF pulse refocuses the spins in the opposite direction, where (D) they gradually regain common alignment and come back into phase.*

This is repeated using different TEs; the time it takes for 63% of M_{xy} to decay is the T_2 relaxation time.
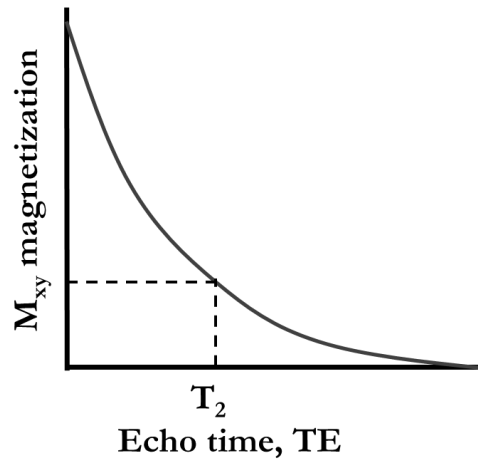
Figure 2.13 *T_2 relaxation is the time is takes for 63% of M_{xy} magnetization to decay.*

2.4 Generating an MRI image

When generating an imaging using MRI, the FID is rarely measured directly. Instead, *echoes* are created and measured. An echo refers to a signal that is formed or regenerated sometime after the initial excitation. As spins begin to dephase following an initial RF pulse, an echo can be generated by bringing the dephasing spins back into alignment.

The two most fundamental imaging pulse sequences in MRI are gradient echo (GE) and spin echo (SE), which will be discussed in this section. But first, a brief description of how spatial information is encoded in an MRI image will be provided.

2.4.1 Spatial encoding

Spatial information is encoded in MRI using a combination of RF pulses and gradient coils. These gradient coils are used to spatially encode the positions of protons by varying the magnetic field linearly across the imaging volume. For instance, a gradient applied along the z axes will cause the magnitude of the B_0 field to increase linearly in

the z direction, from $-z$ to $+z$. At $z = 0$, the field experienced by the nuclei is the B_0 field; these protons will resonate at the Larmor frequency. However, moving along the z direction, the nuclei will experience greater or smaller field strength. This will cause these protons to resonate faster or slower, according to Equation 2. A RF pulse at the Lamor frequency will then only excite the protons resonating at z = 0, enabling selective excitation of this region.

An MR system incorporates three sets of gradients: G_x, G_y and G_z. These are oriented so that gradients can be produced in the x, y and z directions. These three sets of gradients give MRI its three dimensional quality.

2.4.2   Gradient echo

In the GE sequence, a RF pulse is applied with a flip angle α. This is typically between 0° and 90°. A negatively pulsed frequency-encode gradient is immediately applied, which causes rapid dephasing of the spins. A second frequency-encode gradient is then applied with opposite polarity which causes the spins to rephase. A signal is subsequently acquired at a specified TE, when the positive gradient area matches that of the negative gradient area. The time between RF pulses is called the repetition time (TR) and determines how much M_z magnetization recovers before the next excitation. In gradient echo imaging, the consequence of using a low angle excitation pulse is greater M_z magnetization for a given TR.

The positive gradient only compensates for the dephasing caused by the negative gradient, and does not refocus rephasing due to the B_0 field inhomogeneities. Therefore, the decay of transverse magnetization is due to T_2^* relaxation.

Imaging the GE enables the acquisition of an echo in a short timeframe – potentially far quicker than SE, which will be discussed next.
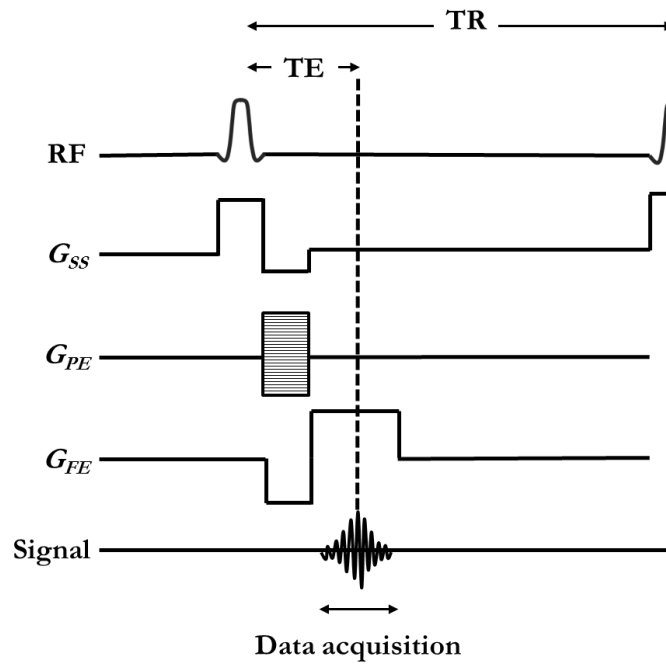
Figure 2.14 *Basic GE pulse sequence. G_{ss} is the slice-selection gradient; G_{PE} is the phase-encoding gradient; G_{FE} is the frequency-encoding gradient. Adapted from McRobbie et al. (138).*

2.4.3   Spin echo

SE imaging was mentioned briefly in Section 2.3.1. This section will provide a more thorough description of this pulse sequence.

The SE sequence employs a 90^0 excitation pulse, which tilts the magnetization into the transverse plane. Immediately following this pulse, all spins are in phase and are precessing together. This phase coherence is temporary, as magnetic field inhomogeneities cause the protons to precess at different rates and fall out of phase with one another. Spins exposed to a lower local magnetic field will slow down, while others will speed up in the presence of a higher local magnetic field. This causes the signal to decay due to T_2^* relaxation.

In order to overcome this rapid dephasing and bring the spins back into alignment, a 180^0 RF pulse is applied at ½ TE. This flips the protons around an axis in the transverse plane, so that the faster protons are now located behind the slower ones. This causes transverse magnetization to reappear, and a T_2 echo can be measured without T_2^* effects. The signal is acquired at the specified TE.

73
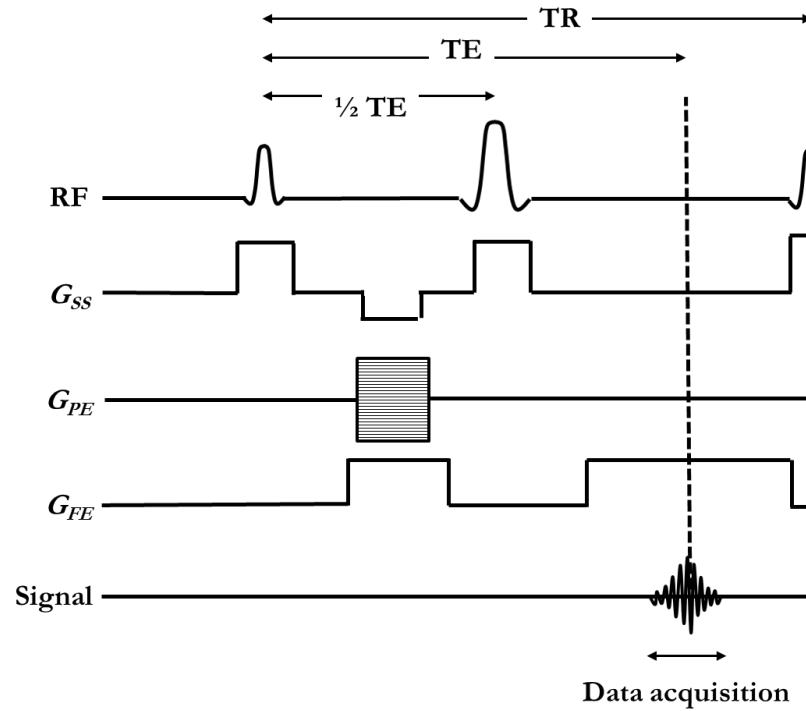
Figure 2.15 *Basic SE pulse sequence. G_{ss} is the slice-selection gradient; G_{PE} is the phase-encoding gradient; G_{FE} is the frequency-encoding gradient. Adapted from McRobbie et al. (138).*

One advantage of SE imaging as opposed to GE imaging is that the B_0 field inhomogeneities are corrected, which produces an echo which follows true T_2 relaxation, not T_2^*. However, SE imaging takes substantially longer, as it employs more than one RF pulse per acquisition, as well as longer TR times.

It is now possible to dramatically speed up SE imaging by applying more than one 180° rephasing pulse after each 90° excitation pulse. The number of successive 180^0 pulses is called the *echo train length* (ETL). Depending on how many rephasing pulses are applied, SE imaging can be made substantially faster. This technique is called *fast spin echo* (FSE).

2.5   Image contrast

When generating an anatomical image using MRI, the scan parameters TR and TE can be manipulated in order to emphasize certain image contrast properties. The signal, *S*, in a SE sequence is influenced by the following properties:

$$S \propto \rho \times \left[1 - \exp\left(-\frac{TR}{T1}\right) \times \exp\left(-\frac{TE}{T2}\right)\right] \qquad (1.6)$$

ρ is the spin density, and represents the number of protons per unit volume. This formula indicates that altering the TR and TE parameters will have a substantial effect on whether the image exhibits T_1- or T_2-weighted contrast.

2.5.1 T_1-weighted images

In T_1-weighted images, contrast is based on the differences in T_1 relaxation time of the different tissues. In order to produce a T_1-weighted image, either a GE or SE sequence can be employed. In both cases, the TR must be kept relatively short to capture the T_1 contrast, which develops during the early growth phase of longitudinal relaxation. The TE must also be kept short in order to limit the amount of T_2 contrast which is allowed to develop, as this can influence image contrast. A short TE value will minimise this effect.

In T_1-weighted (and high proton density) images, fat-containing tissues appear bright owing to their short T_1 relaxations times. White matter has a shorter T_1 relaxation time than grey matter, and so appears brighter in these images. The ventricle containing CSF, however, appear dark owing to the long T_1 relaxation times associated with fluids. T_1-weighted images are known as 'anatomy scans' owing to the range of different contrasts which are exhibited between tissue types.

2.5.2 T_2-weighted images

In T_2-weighted images, contrast is based on the differences in T_2 relaxation time. In order to produce a T_2-weighted image, a SE sequence is employed in order rephase the protons and remove T_2^* effects. A long TR is chosen to minimise T_1 contributions, and a long TE is chosen to allow sufficient time for T_2 contrast to develop.

In T_2-weighted images, fluids such as CSF have a long T_2 and appear bright whilst water- and fat-based tissues are mid-grey. T_2-weighted images are known as 'pathology scans', because most diseased tissues have higher water content than normal; as a result, they appear hyperintense in T_2-weighted images.
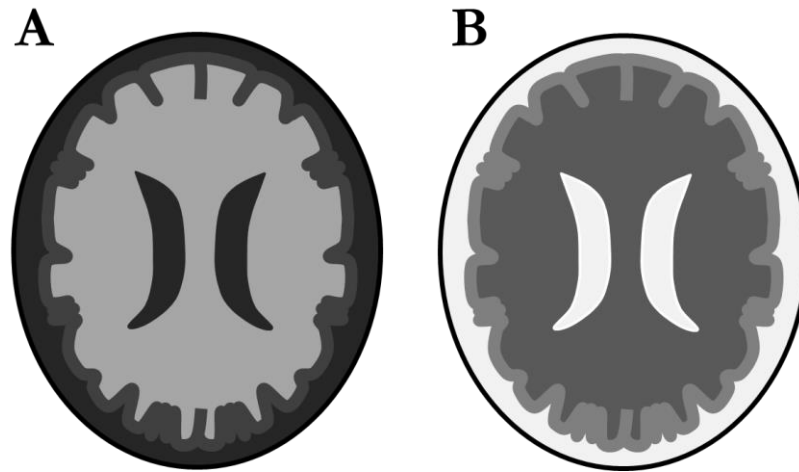
Figure 2.16 *Illustration of different tissue contrast in (A) T_1-weighted images, and (B) T_2-weighted images. Adapted from Dowsett et al. (137)*

More specialised pulse sequences can generate contrast that is sensitive to diffusion and perfusion; however, the precise mechanisms that lead to contrast generated by these sequences are beyond the scope of this thesis.

2.5.3 The effect of contrast agents

Exogenous contrast agents can be introduced in order to improve the visibility of internal structures. The most commonly used MRI contrast agents employ the paramagnetic element gadolinium. When gadolinium is placed inside a magnetic field, it generates a local magnetic field 1000 times that of water protons. This causes magnetic field inhomogeneities, resulting in: a) accentuated transitions between spin states, and shortening of T_1; and b) rapid dephasing of protons, and shortening of T_2 and T_2^*. Gadolinium-based contrast agents have the strongest effect in T_1-weighted images, because the T_1 relaxation time in the tissue is most strongly influenced by the presence of gadolinium.

Gadolinium is highly toxic, so it is introduced to the body in the form of a chelated compound. For instance, the contrast agent Magnevist consists of a gadolinium chelated to a diethylene-triamine-penta-acetic acid (DTPA); this eliminates the toxicity of gadolinium whilst maintaining its paramagnetic properties.

One novel use of gadolinium-based contrast agents proposed by Johnston et al. is as a tissue stain for so-called *magnetic resonance histology* (MRH) *(139)*. The use of contrast agents in such a way reduces the T_1 relaxation time of the tissue under investigation, improving the efficiency of signal available due to faster recovery of M_z magnetization. MRH enables post-mortem tissues to be imaged with enhanced structural detail, which highlights cellular features for investigation of processes involved in development and disease (*140*).

Superparamagnetic iron oxide (SPIO) particles are another class of MRI contrast agents. SPIO particles are a lot larger than gadolinium-based contrast agents, and produce a large magnetic field inhomogeneity when they are introduced into the body. SPIO particles increase the dephasing rate of protons, which decreases the T_2 and T_2^* relaxation time. Therefore, they have the greatest effect in T_2-weighted images, and manifest as tissue signal loss.

2.6 Diffusion, perfusion, chemical exchange and flow

So far, this chapter has provided an overview of the basic imaging sequences, contrast mechanisms, and the physics underpinning MRI. This final section will focus on different ways that MRI is increasingly being used to image specific structural, biochemical or functional properties.

2.6.1 Diffusion tensor imaging

Diffusion tensor imaging (DTI) exploits the intrinsic properties of directionality of water diffusion in the brain in order to examine the tissue microstructure.

The movement of water molecules can be characterized by Brownian motion. When water is unconstrained, the direction of motion of a given molecule is completely random and is said to be isotropic (Figure 2.17A). However, in tissue water, the Brownian motion of water is impeded by cell membranes, resulting in directional anisotropy (Figure 2.17B). DTI provides information about the orientation and anisotropy of the diffusion of water in different tissue types.
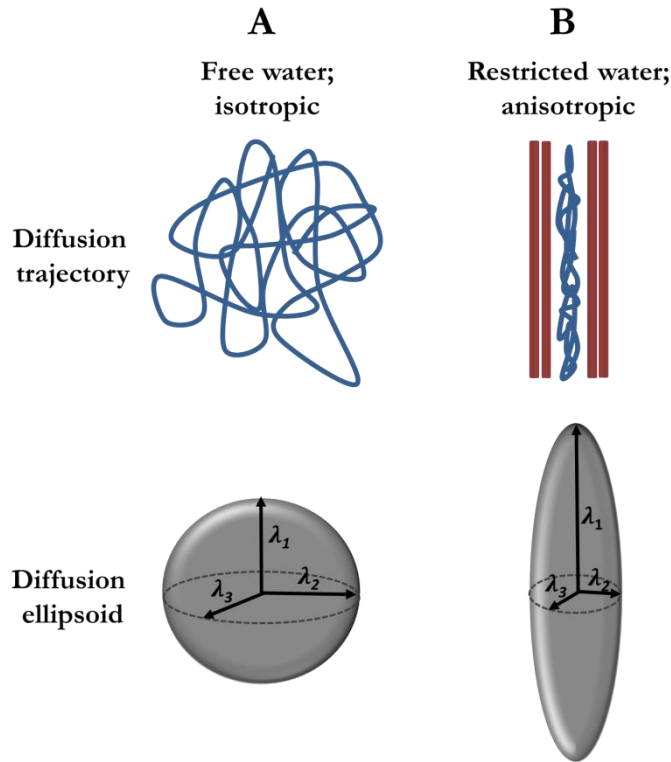
Figure 2.17 *Schematic illustrating (A) isotropic diffusion properties of water and (B) anisotropic diffusion properties of tissue water which is restricted by physical barriers. The eigenvalues λ_1, λ_2, λ_3 are used to characterize the overall directionality of diffusion. Adapted from Alexander et al. (141).*

Water diffusion in tissues is measured using diffusion-sensitized magnetic field gradients applied in multiple directions, to produce images with directional diffusion-weighting. This information can be mathematically modelled to extract the diffusion tensor, which provides quantitative measures of water diffusion for each voxel.

The diffusion tensor is made up of the eigenvalues λ_1, λ_2 and λ_3. Diffusion is considered isotropic when the eigenvalues are nearly equal (e.g. $\lambda_1 \sim \lambda_2 \sim \lambda_3$.). Conversely, the diffusion tensor is anisotropic when the eigenvalues are significantly different in magnitude (e.g., $\lambda_1 > \lambda_2 > \lambda_3$). These eigenvalues, or combinations of them, are used to characterise diffusion measures.

Axial diffusivity (AD) describes the diffusion rate along the main axis of diffusion, and is defined by the largest eigenvalue, λ_1. Radial diffusivity (RD) describes the rate of diffusion in the transverse direction, and is quantified as the mean of λ_2 and λ_3. Mean diffusivity (MD) provides an average of all three eigenvalues (λ_1, λ_2, λ_3) to define the

molecular diffusion rate. Fractional anisotropy (FA) quantifies the fraction of diffusion that is anisotropic by comparing the relative difference between the largest eigenvalue λ_1 to the others. The exact mathematical calculations are shown below:

$$RD = \lambda_1 \tag{1.7}$$

$$AD = \frac{\lambda_2 + \lambda_3}{2} \tag{1.8}$$

$$MD = \frac{\lambda_1 + \lambda_2 + \lambda_3}{3} \tag{1.9}$$

$$FA = \sqrt{\frac{1}{2}} \frac{\sqrt{(\lambda_1 - \lambda_2)^2 + (\lambda_1 - \lambda_3)^2 + (\lambda_2 - \lambda_3)^2}}{\sqrt{\lambda_1^2 + \lambda_2^2 + \lambda_3^2}} \tag{1.10}$$

DTI is particularly useful when studying fibrous tissues such as cerebral white matter. The direction of greatest diffusivity (RD) is assumed to be parallel to the local direction of white matter.

2.6.2   Arterial spin labelling

Arterial spin labelling (ASL) is a non-invasive MRI technique that uses arterial blood as an endogenous tracer to measure cerebral blood flow (CBF). In pulsed ASL (pASL), the arterial blood water is labelled before it enters the tissue of interest using an inversion pulse; which inverts the net magnetization of the blood water protons from M_z to $-M_z$. After a short delay, termed the *inversion time* (TI), the labelled blood flows into the tissues where it exchanges with the bulk tissue water and reduces the tissue magnetization.

A control image is also acquired, with no labelling of the arterial blood water. In the initial application of ASL, the control pulse is applied above the head to account for signal changes caused by the labelling pulse itself (*142*). The control image and the labelled image are subtracted which eliminates signal contributions from the static tissue; the remaining signal reflects perfusion of the tissue of interest.
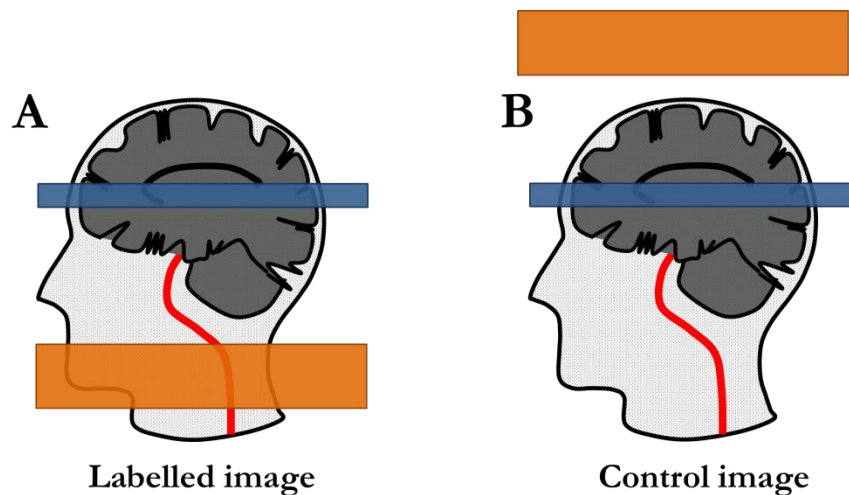
Figure 2.18 *Schematic diagram showing (A) the labelling of the arterial blood with an inversion RF pulse (shown in orange) before an image was acquired of the tissue of interest, and (B) the acquisition of a control image with no labelling of the arterial blood water. Adapted from McRobbie et al. (138).*

2.6.3   Chemical exchange saturation transfer

Chemical exchange saturation transfer (CEST) probes the dynamic relationship between different proton environments. As described in Section 2.2.1, water molecules can exist in bound and free states. In a typical NMR spectrum, bound protons within the macromolecular pool have broad resonance lines (Figure 2.19).

Water protons resonate at a frequency of 4.75 ppm. However, the short T_2 of the bound proton pool means they are off-resonance, and not visible directly with MRI. However, they can influence the signal of the free water pool. This is because the free water protons are in constant exchange with bound protons contained within macromolecules such as lipids, amines, amides and hydroxides (*143*).
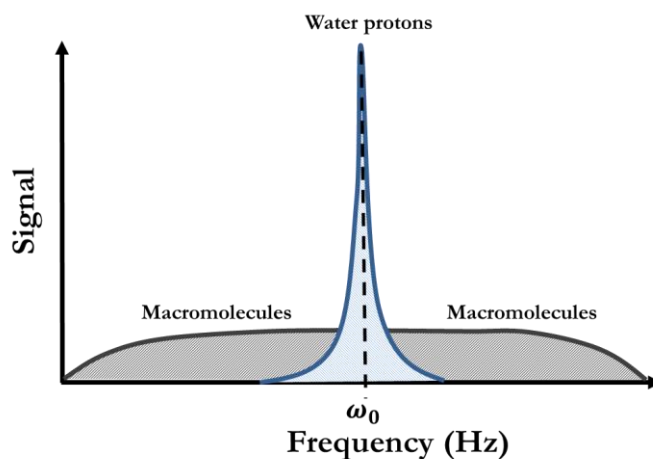
Figure 2.19 *Schematic showing the resonance frequencies of water protons and the macromolecular pool. Water protons (shown in blue) resonate at or near the Larmor frequency (ω_0) while the macromolecular pool (shown in grey) has a much broader resonance spectrum. Adapted from McRobbie et al. (138).*

The bound pool can be selectively excited using an off-resonance RF pulse, with no immediate effect on the free water pool. However, the exchange of protons between the bound and free pool causes the transfer of this saturation into the free water pool, which attenuates the MR signal. For instance, in order to probe the exchange of amide protons to the free water pool, an off-resonance RF pulse is applied at 8.25 ppm. This corresponds to a frequency shift of 3.5 ppm, or 445 Hz at 3T. After a delay termed t_{sat}, this effect is visible in the NMR spectrum (Figure 2.20). This technique is called *amide proton transfer* (APT).
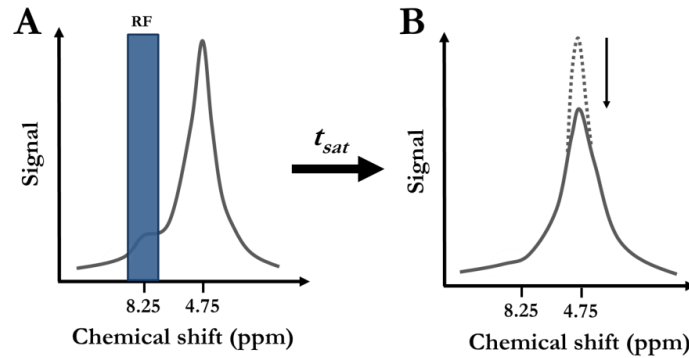
Figure 2.20 *(A) An RF pulse is applied which specifically saturates the amide protons at their resonance frequency (8.25 ppm). (B) Following a time t_{sat} this saturation is transferred to water (4.75 ppm). Adapted from van Zijl et al. (143).*

2.6.4 Magnetic resonance angiography

Magnetic resonance angiography (MRA) exploits the motion sensitivity of certain MRI pulse sequences to illuminate blood flow within vessels. MRA employs short TRs and TEs which saturate the spins from the stationary tissues. Unsaturated spins in the blood move into the imaging slice with full magnetization, producing high contrast. This technique is called time-of-flight (TOF) MRA.
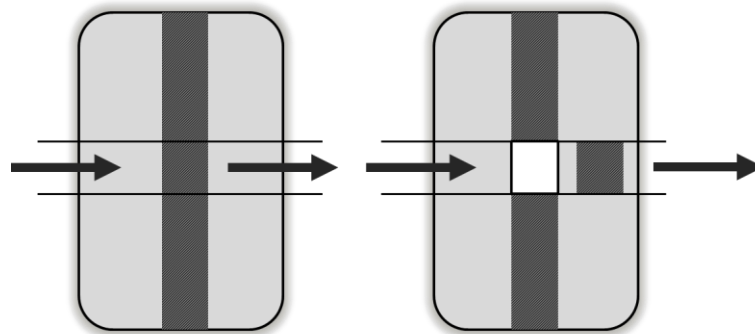
Figure 2.21 *Schematic showing the time-of-flight effect. Following saturation of the stationary tissues, the previously excited blood moves out of the imaging plane and is replaced by blood with full M_z magnetization. Adapted from Gadian et al. (144).*

Alternative MRA methods employ gadolinium-based contrast agents administered intravenously which shorten the T_1 relaxation time of the blood, increasing its signal in T_1-weighted images. These techniques are called contrast-enhanced MRA.

MR angiograms are typically viewed using a *maximum intensity projection* (MIP). A MIP is a volume rendering method for three-dimensional (3D) data, which shows only the brightest voxel along the projection. As the blood vessels appear hyperintense in MRA, a MIP is useful for accentuating this contrast.

This chapter was compiled with the help of the following seminal texts:

D. W. McRobbie et al., *MRI from Picture to Proton* (Cambridge University Press, 2006).

D. Gadian, *NMR and its applications to living systems* (Oxford Science Publications, 1995).

D. J. Dowsett et al., *The Physics of Diagnostic Medicine* (Hodder Arnold, 2006).

Chapter 3: Optimising the *in vivo* structural sequence for high resolution structural mouse brain imaging

3.1 Aims

The overall aim of this thesis is to develop and apply *in vivo* MRI techniques to transgenic mouse models of neurodegeneration, with the intention of characterising pathological changes longitudinally, and uncovering novel phenotypes.

This chapter focuses on optimising a structural MRI sequence for high resolution *in vivo* mouse brain imaging. The suitability of the optimised sequence for tensor-based morphometry (TBM) was then assessed through subsequent application to the rTg4510 mouse model of tauopathy at a single timepoint (8.5 months of age), in order to characterise neurodegenerative changes occurring in this model. The development of this sequence lays the foundations for the proceeding chapters, where *in vivo* structural MRI has been applied in a longitudinal study of neurodegeneration in the rTg4510 mouse with comparisons made to the preclinical gold standard for single timepoint imaging: high resolution *ex vivo* MRI of post-mortem mouse brain using contrast agents.

In this work, I acquired the T2 maps and wrote the two-tier optimisation script in order to calculate optimum scan parameters. I also was involved in the experimental set-up, acquisition of the structural scans of the rTg4510 mice and wildtype controls, and post-processing of the results. Following *in vivo* scanning, I perfuse-fixed all of the mice before dispatching the tissues to my collaborators for histology. I also manually segmented the cortex and hippocampus, in order to investigate correlations between the MR findings and histology.

I would like to acknowledge: Simon Richardson at the UCL Centre for Advanced Biomedical Imaging, for his help producing the 3D printed head holder; and Nick Powell at the UCL Centre for Medical Image Computing, for developing the image processing software.

Sections of this work have been peer-reviewed and published in NeuroImage (*145*).

3.2 Introduction

Alzheimer's disease (AD) is devastating neurodegenerative disease, characterised by progressive memory impairment and cognitive decline. A number of factors have been implicated in the multifaceted pathogenesis, including local inflammation (*146*), protein accumulation (*147*), abnormal mitochondrial function (*148*) and haemodynamic alterations (*149*) with amyloid plaques and NFTs being the classical hallmarks of the post-mortem AD brain. In the past decade, structural MRI has emerged as an integral part of the diagnosis and study of AD, owing to its ability to detect patterns of atrophy in the AD brain (*93*). These changes are now believed to precede the onset of the clinical symptoms of the disease (*98*), strengthening the role of MRI as a valuable tool in AD research, where early detection may increase the success of emerging therapeutics.

Transgenic mouse models are increasingly being used to further our knowledge of the cause and progression of neurodegenerative diseases such as AD. While no mouse recapitulates all characteristics of the human condition, such models do permit the study of specific pathological features in experimentally controlled conditions. This is particularly advantageous in AD where human clinical research can often be confounded by uncontrollable variables such as lifestyle choices and other co-morbidity; mice allow the precise impact of genes and their role in AD to be fully explored.

There are currently over 100 different mouse models of AD (*150*), all which express one of more of the key neuropathological hallmarks of the disease (*14*). Some of the most commonly used mouse models of AD are detailed in Chapter 1.6. As previously described, mice containing mutations in the *APP* gene are the oldest and most widely studied AD models, and are used to investigate the role of *APP*, amyloid-β and amyloidosis in neurodegeneration (*102*). These mice are also valuable tools in preclinical drug discovery, where many emerging therapeutics focus on decreasing amyloid-β production and aggregation. However, the failure of these compounds to produce a therapeutic effect in clinical trials (*30*) has resulted in a shift in interest towards tau-mediating therapies.

Tau is thought to play a critical role in the neurodegenerative process in AD: aggregates of hyperphosphorlylated tau forming NFTs are a major histological hallmark of AD and correlate with clinical disease progression (*151*). In the absence of amyloid-β, NFTs are also implicated in several other neurodegenerative diseases (e.g. FTD), further

supporting the role of tau in the dementing process (*152*). A mouse model of tauopathy (rTg4510) has recently been developed that specifically expresses tau in the forebrain but without amyloid plaques, enabling dissection of the unique role of tau in AD pathology (*114, 153*). Behavioural and histological studies of the rTg4510 mouse have demonstrated cognitive deficits in learning and motor tasks and marked atrophy of brain regions known to be selectively vulnerable to AD such as the hippocampus and frontal cortex(*114*).

Structural MRI, with high spatial resolution, is increasingly being used to study mouse models of AD; however there is limited information on the optimum scan parameters for acquisition of mouse brain structural data sets. In particular, within the discussion and justification of the chosen structural MRI parameters in the relevant literature there is no mention of the specific demands of advanced imaging processing techniques (such as TBM) (*154, 155*). These demands include:

1. High resolution, isotropic voxels to reduce partial volume effects and improve localisation of deformations to sub-regional structures;
2. Whole brain coverage for global morphological analysis and application of existing mouse brain atlases;
3. High contrast between tissue boundaries to enable voxel-wise tests to detect regions of change.

In this chapter, I have developed and implemented a structural MRI sequence for *in vivo* mouse brain imaging, which is suitable for advanced image processing techniques. The sequence permits the acquisition of high resolution, isotropic voxels encompassing the whole mouse brain within a 1 hour 30 minute acquisition time. The demand for isotropic voxels meant that I selected a three-dimensional (3D) rather than two-dimensional (2D) sequence (where artefacts may be introduced by imperfect slice profiles with such thin slices (150μm)). Furthermore, I choose a SE rather than GE sequence in order to avoid artefacts that occur due to signal "drop out" in GE images. Such artefacts are caused by local magnetic field inhomogeneities that occur at boundaries of material with different magnetic susceptibility, and are known to be particularly problematic at the high field strengths employed for rodent imaging (*156*).

The scan parameters within the 3D SE sequence were optimised for high contrast between the hippocampus and its surrounding grey and white matter structures, as the

hippocampus suffers gross atrophy in clinical cases of AD and is frequently compromised in AD mouse models. Importantly, this phenotype appears to present in the rTg4510, where marked atrophy of the hippocampus has been previously reported (*157*).

When planning the 3D structural sequence, the field-of-view (FOV) was first adjusted in order to encompass the whole mouse brain. This would permit global analysis of morphological changes, and facilitate the application of pre-existing mouse brain atlases for future automated parcellation analyses. Hence, a FOV of 19.2 mm × 16.8 mm × 12.0 mm was selected, which was sufficient to avoid aliasing in the images due to the mouse's ears; this can result in undesirable wraparound artefacts. Next, a resolution of $150\mu m^3$ was selected; this was based on previous work by Lau et al. where voxel-wise analysis techniques were successfully applied to *in vivo* mouse brain data sets at $156.25\ \mu m^3$ resolution (*155*). Together, the selected FOV and resolution would permit the acquisition of suitable mouse brain data sets within an imaging time of approximately 30 mins – 90 mins (depending on the TR – see below). With these parameters fixed, I proceeded to optimise the TR and TE in order to yield maximum contrast between the hippocampus and the surrounding tissue by using a "two tiered" optimisation approach; this is detailed in the Methods section.

In this work, I have optimised the TR and TE for optimum contrast to distinguish the hippocampus from its surrounding grey and white matter structures. The optimised sequence was subsequently applied to a cohort of rTg4510 mice and wildtype controls at 8.5 months of age. Previously published *in vivo* structural analysis in the rTg4510 mouse has identified marked atrophy within the hippocampus and cortex, and expansion of the ventricles (*157*). As such, this earlier study provides a comparison through which to validate my imaging and analysis protocol to detect structural differences between cohorts of mice. I sought to verify and expand upon these previous findings, and use TBM to characterise discrete structural changes occurring in this model.

This work demonstrates the suitability of the optimised structural MRI sequence for detecting morphological changes in the rTg4510 using TBM analysis; with scope to apply atlas-based structural parcellation in future studies.

3.3 Methods

3.3.1 Animals

<u>For T_2 mapping</u>

A wildtype C57BL/6J mouse was imaged *in vivo*.

<u>Single time-point imaging study</u>

Generation of homozygous rTg4510 transgenic mice has been reported previously (*153*). Female rTg4510 mice were licensed from the Mayo Clinic (Jacksonville Florida, USA) and bred for Eli Lilly by Taconic (Germantown, USA). Mice were imported to the UK for imaging studies at the Centre for Advanced Biomedical Imaging (CABI), London. All studies were carried out in accordance with the United Kingdom Animals (Scientific Procedures) act of 1986. Prior to imaging, all mice were secured in a cradle under anaesthesia with 1-2% isoflurane in 100% oxygen using a custom-built head holder, which was designed and 3D printed in collaboration with Simon Richardson at the UCL Centre for Advanced Biomedical Imaging (Figure 3.1). Body temperature was maintained at $36 - 37.5^{\circ}$C using a water-heating system and warm air fan. Core body temperature and respiratory rate were monitored using an MR-compatible temperature probe and pressure pad (SA Instruments, NY).
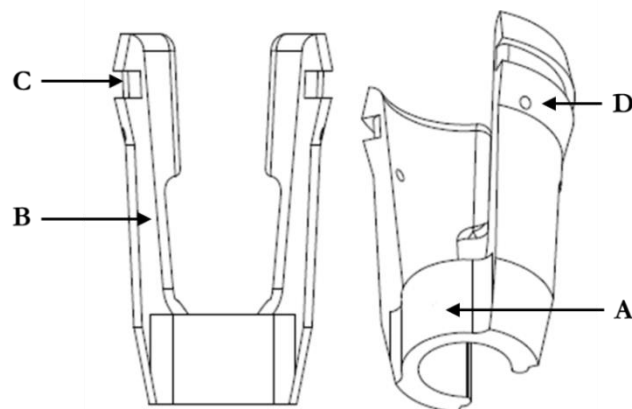
Figure 3.1 *Custom-built mouse brain head holder. (A) It is compatible with the RAPID 4 channel split array mouse head coil, and clips onto the nose cone. (B) The mouse head is stabilized by pressure from the protruding arms. (C) Additional support can be provided using a cable tie which fits into the grooves without applying pressure on the mouse's respiratory tract. (D) Optional ear bars provide further stability.*

3.3.2 Image acquisition

All images were acquired using a 9.4T Agilent MRI scanner. A 120 mm diameter imaging gradient set (SGRAD 205/120/HD/S, Agilent Technologies UK Ltd., Berkshire, UK) was used. A 72 mm birdcage RF coil was employed for RF transmission and a quadrature mouse brain surface coil (RAPID, Germany) was used for signal detection. Tuning and matching of the coil was performed manually. Shimming was performed across the mouse brain prior to image acquisition.

3.3.3 Measurement of tissue parameters

To provide tissue information for the optimisation of the high resolution structural imaging sequence, T_2 maps were acquired with a SE sequence with the following parameters: FOV = 16 × 16 mm; matrix size = 128 × 128; 1 mm slice thickness; TE = 6.3, 10, 15, 20, 25, 30, 35, 40, 50, 60 ms; TR = 2000 ms; number of signal averages (NSA) = 1. A total of 4 slices were obtained.

T_2 relaxation times were calculated by manually selecting and drawing regions of interest (ROIs) on the images using custom software written in MATLAB (The Mathworks Inc., Natick, MA, USA). Measurements were taken and averaged for 3 wildtype mice.
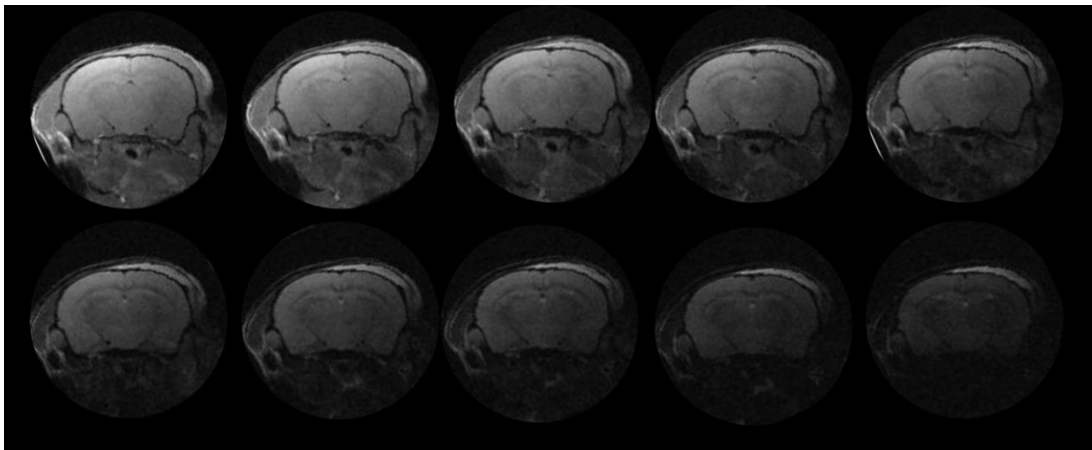
Figure 3.2 *Example SE images of a wildtype mouse at increasing TEs for calculating T_2 relaxation times of the corpus callosum, cortex, hippocampus and thalamus.*

The MATLAB Curve Fitting Toolbox was used to fit T_2 curves to Equation 2.5, which describes the decay of magnetization in the *xy* plane following a 90^0 excitation pulse.

T_2 relaxation times were calculated for the following ROIs: corpus callosum, cortex, hippocampus, and thalamus. Table 3.1 shows the T_2 relaxation fitting results, with 95% confidence bounds for the fitted coefficients.

Table 3.1 *T_2 relaxation times (with 95% confidence bounds) for mouse brain ROIs: the corpus callosum, cortex, hippocampus and thalamus.*

Structure	T_2 relaxation time (ms)
Corpus callosum	31.99 (30.36, 33.62)
Cortex	39.75 (37.86, 41.66)
Hippocampus	38.93 (37.9, 39.93)
Thalamus	34.99 (30.36, 33.62)

T_2 relaxation times were highly consistent with literature values (*158, 159*).

Due to time restrictions, it was not possible to also acquire T_1 maps. Instead, T_1 relaxation times for the scan parameter optimisation were taken from previous work by van de Ven et al. at 9.4T (*160*). As the T_1 relaxation time for the thalamus was not reported in this work, the relaxation time for the periaqueductal gray was presumed to be representative of the thalamus as they are both centrally locate grey matter structures.

Table 3.2 *T_1 relaxation times taken from the literature for mouse brain ROIs: the corpus callosum, cortex, hippocampus and thalamus*

Structure	T_1 relaxation time (ms)
Corpus callosum	1750
Cortex	1890
Hippocampus	1820
Thalamus	1700

3.3.4   Contrast optimisation by computer simulation

To determine optimum scan parameters, the SE signal equation (Equation 2.6) was used to calculate signal intensity for a SE sequence using a 90° excitation pulse and 180°

refocusing pulse (*161*): Signal intensity was simulated for a range of TEs (1 – 100ms) and TRs (1 – 2500ms). TR was limited to 2500 ms which corresponded to an *in vivo* imaging time of 1 hour 30 minutes with the previously determined resolution (150µm) and whole brain FOV (19.2 mm × 16.8 mm × 12.0 mm). This imaging time was chosen as a compromise between resolution and signal-to-noise ratio (SNR), and permits the acquisition of complementary functional data for the remaining duration of the scan.

The SE signal equation was used first to calculate optimum scan parameters for maximum contrast between the hippocampus and thalamus; this was defined as the greatest signal difference between the two tissues occurring over a range of scan parameters (*162*).

$$Contrast = Signal_{hippocampus} - Signal_{thalamus} \qquad (3.1)$$

In the rTg4510 mouse, atrophy is most pronounced in the forebrain regions, with high NFT deposition previously observed in the hippocampus and frontal regions of the cortex (*114*). It was therefore crucial that that these two structures could be readily delineated from their neighbouring grey and white matter structures. The corpus callosum lies between the cortex and the hippocampus within the forebrain regions, providing an inherent white matter barrier between these two ROIs. However, there is no dividing white matter structure between the hippocampus and thalamus. Therefore a two-tier simulation was performed to investigate sequence parameters for optimal contrast between i) the hippocampus and the thalamus and ii) the cortex and the corpus callosum.
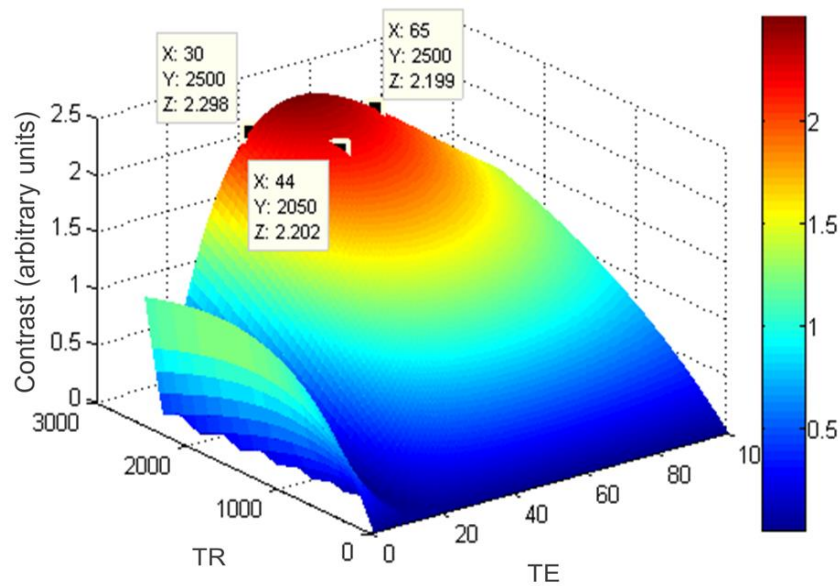
Figure 3.3 *Results from the scan parameter optimisation for maximum contrast between the hippocampus and the thalamus. The simulation identified scan parameters where optimal contrast could be achieved: TR 2050 – 2500 ms; TE 30 – 65 ms.*

The results from the simulation revealed that a T_2-weighted sequence employing a 90° excitation pulse would offer the maximum contrast between the hippocampus and thalamus (Figure 3.3), since long TRs and TEs were found to produce maximal contrast. The simulation identified a range of scan parameters that would produce high contrast (contrast > 2) between the hippocampus and thalamus (Table 3.3) which were then used as constraints in part ii) of the optimisation (optimising contrast between the cortex and corpus callosum).

Table 3.3 *Range of optimum scan parameters identified from the SE signal equation for high contrast between the hippocampus and thalamus.*

TR (ms)		TE (ms)	
Minimum	*Maximum*	*Minimum*	*Maximum*
2050	2500	30	65

In order to enhance contrast between the grey and white matter structures, the SE signal equation was used to calculate optimum scan parameters for maximum CNR between the corpus callosum and cortex using the range of TEs and TRs previously identified in part i) of the simulation (Figure 3.4).
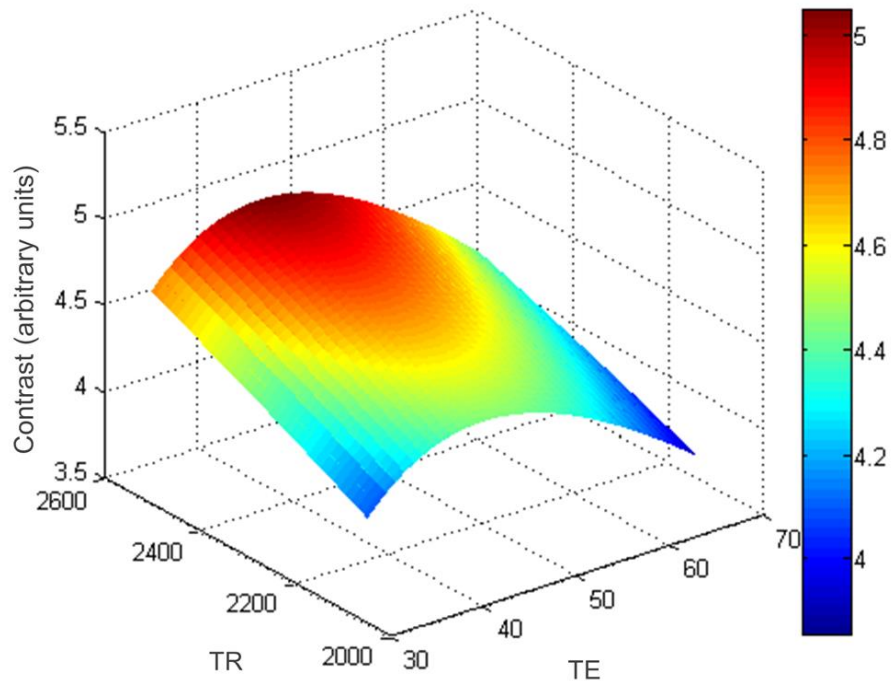
Figure 3.4 *Results from the scan parameter optimisation for maximum contrast between the cortex and the corpus callosum, constrained by the range of parameters for high contrast between the hippocampus and the thalamus.*

The result from this second SE optimisation revealed that maximum contrast between the cortex and corpus callosum would be achieved at a TR of 2500 ms and a TE of 43 ms.

3.3.5 Implementation of optimum scan parameters: single time-point study of neurodegeneration in the rTg4510 mouse model

Female rTg4510 mice (n = 9) and wildtype controls (n = 17) were imaged *in vivo* using a 3D FSE sequence with the following parameters: FOV = 19.2 mm × 16.8 mm × 12.0

mm; resolution = 150 μm × 150 μm × 150 μm; TR = 2500 ms, effective echo time (TE_{eff}) = 43 ms, ETL = 4, NSA = 1. Total imaging time was approx. 1 h and 30 mins.

3.3.6 Perfuse fixation

Following *in vivo* imaging, animals were terminally anaesthetised with Euthanol (1 mL) administered via intraperitoneal (i.p.) injection. The thoracic cavities were opened and the animals perfused through the left ventricle with 15–20 mL of saline (0.9%) followed by 50 mL of buffered formal saline (10%) at a flow rate of 3 mL per minute. Following perfusion, the animal was decapitated, defleshed, and the lower jaw removed. All brains were stored in-skull in buffered formal saline (10%) at 4 °C before being dispatched for histology.

3.3.7 Histology and immunohistochemistry

Histology was performed by my collaborators at Eli Lilly. Brain samples were processed using the Tissue TEK® VIP processor (GMI Inc, MN USA) before being embedded in paraffin wax for coronal brain sectioning. Serial sections (6μm) were taken using HM 200 and HM 355 (Thermo Scientific Microm, Germany) rotary microtomes. Immunohistochemistry (IHC) was performed using a primary antibody for tau phosphorylated at serine 409 (PG-5; 1:500 from Peter Davies, Albert Einstein College of Medicine, NY, USA) as previously described (*163*). Stained sections were digitised using the Scanscope XT slide scanner (Aperio, CA, USA) at 20× magnification. Imagescope software (version 11.1.2.760; Aperio, CA, USA) was used to view the digitised tissue sections and delineate the regions of interest (cortex, hippocampus and thalamus). The number of PG-5 positive neurons was manually counted within a delineated region and expressed as a density (mm^2). Both sides of the brain were analysed and averaged before statistical analysis.

3.3.8 Image analysis

In vivo MR images were reconstructed using custom software written in MATLAB by Nick Powell.

Manual segmentation of the hippocampus was performed using open source software (ITK-SNAP) (*164*) with visual reference to a mouse brain atlas. A previously published calibration protocol (*165*) was used to adjust volume estimates to correct for scaling

94

errors caused by the imaging gradients. Briefly, a 3D grid phantom was imaged in both gradient sets and CT data was used as a ground truth to generate absolute scaling factors that were then applied to the data. This protocol was developed by my collaborator at the UCL Centre for Advanced Biomedical Imaging. The computer-aided design (CAD) drawings for the 3D grid phantom are available online:

http://www.ucl.ac.uk/cabi/publications/open_source

3.3.9 Tensor-based morphometry

For TBM analysis, *in vivo* structural images were automatically oriented to a standard atlas space (Right Antero-Superior), corrected for intensity non-uniformity using the N3 algorithm (*166*), and skull stripped using a STAPLE algorithm (*167*) to combine masks from several prior atlases registered to the data. Intensities were normalised and a multi-iteration group-wise registration, implemented in the open-source *NiftyReg* software (*168*), was performed as follows to align equivalent voxels between subjects. First, all subjects were rigidly aligned to a randomly-chosen target member of the group. This was followed by four iterations of affine registration (12 degrees of freedom), using a block-matching algorithm based upon normalised mutual information, and 20 iterations of non-rigid registration (NRR), based upon symmetric free-form deformation. After each iteration, the intensity average image was found and used as the target for the subsequent registration. Deformation fields were transformed by taking the log of the determinant of the Jacobian matrix calculated at each voxel, to give that voxel's relative expansion or contraction in the final average image compared to each original. These values were smoothed with a 0.2 mm FWHM Gaussian kernel to account for registration error and to render the values closer to a normal distribution, and mass-univariate statistics (two-tailed t-tests) were performed on each voxel, fitting a General Linear model controlling for total brain volume (TBV) based upon the brain masks. The resulting statistical parametric map was corrected for multiple tests using the False Discovery Rate (FDR (*169*), q = 0.05).

3.3.10 Signal-to-noise and contrast-to-noise ratio calculations

SNR was calculated for all brain regions under investigation. Contrast-to-noise ratio (CNR) was calculated for grey and white matter regions; I chose to investigate CNR between the cortex and corpus callosum, following the protocols from previous CNR

measurements in the literature (*140*). SNR and CNR were calculated using the following formulae:

$$SNR = \frac{Mean\ signal}{Noise} \tag{3.2}$$

$$CNR = \frac{Mean\ signal_A - Mean\ signal_B}{Noise} \tag{3.3}$$

Signal was taken from ROIs including: corpus callosum, cortex, hippocampus, and thalamus. The noise ROI was placed in a "ghost-free" region of background signal. Noise was defined as the standard deviation (SD) of the background signal. CNR was calculated between the grey matter (cortex) and white matter (corpus callosum).

3.4 Results

3.4.1 Visual inspection of the data

Figure 3.5 shows coronal and axial slices of a representative wildtype mouse. Visual inspection of the data revealed sufficient contrast to identify many ROIs, including the hippocampus and cortex. These structures are frequently compromised in neurodegenerative disease models, so it was crucial they could be easily identified. Appreciable contrast between the grey and white matter regions enabled the corpus callosum to be readily delineated. The grey-white matter folds of the cerebellum were also noted. Adequate contrast between adjacent grey matter regions, as well as grey-white matter contrast is crucial for the optimal implementation of automated analysis techniques; these require high contrast boundaries between neighbouring structures for the application of pre-existing mouse brain atlases.

Figure 3.6 shows coronal and axial slices of a representative rTg4510 mouse. Shrinkage of the hippocampus and thinning of the cortex was readily observed, in additional to expansion of the ventricles containing CSF which appear hyperintense in the T_2-weighted MRI images.

We observed some artefacts in the coronal FOV which may be due to the spontaneous respiration of the animals in the scanner. However, I do not anticipate this being a
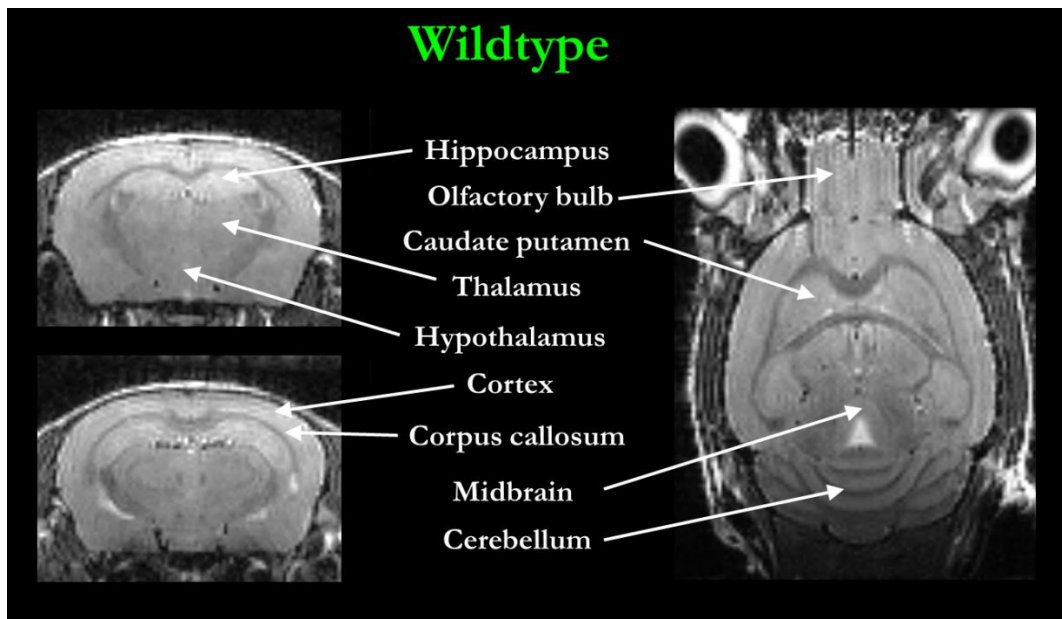
Figure 3.5 *Coronal and axial slices taken from a representative wildtype mouse. Contrast was sufficient to enable visualization of many ROIs.*
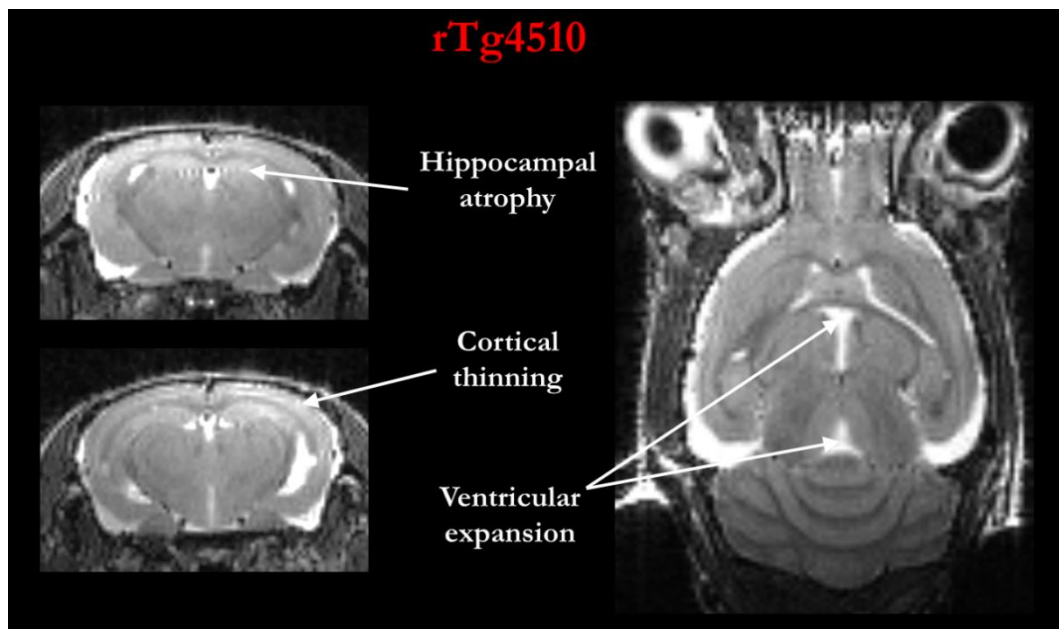
Figure 3.6 *Coronal and axial slices taken from a representative rTg4510 mouse. Visual inspection of the data revealed known morphological changes in this model, including gross hippocampal atrophy, cortical thinning and expansion of the ventricles.*

dramatic confounder in the automated image analysis, which relies on registration algorithms to produce a groupwise average image.

3.4.2 SNR measurements

SNR measurements were taken from all ROIs under investigation in a single, representative, animal in order to quantify image quality (Table 3.4). CNR was calculated between the cortex and corpus callosum, and served as a measure of how well grey and white matter features can be distinguished in the images (*170*).

Table 3.4 *SNR and CNR measurements taken from a representative wildtype mouse in vivo. ROIs were drawn within the corpus callosum, cortex, hippocampus and thalamus. CNR was defined as the absolute difference in SNR between the corpus callosum and the cortex.*

Structure	SNR
Corpus callosum	8.7
Cortex	12.4
Hippocampus	11.8
Thalamus	7.8
CNR (grey-white matter)	3.7

Given the limitations on scan time imposed by *in vivo* imaging, the optimised structural sequence permitted the acquisition of whole brain images at $150\mu m^3$ resolution. CNR of 3.7 proved sufficient to unveil detailed anatomical structures (identified in Figure 3.5), and is in agreement with previously published measurements in the mouse brain (*170*).

3.4.3 Manual segmentation

In this work, the scan parameters were optimised for high contrast between the hippocampus and its neighbouring structures. In order to assess the sensitivity of the structural sequence to neuropathological changes occurring in the hippocampus and to investigate correlations to histological quantification of tau burden, this structure was manually delineated in the wildtype (n=17) and the rTg4510 (n=9) mice at 8.5 months

(Figure 3.7). An entirely female cohort was investigated in order to reduce any gender-related variance in the animals.
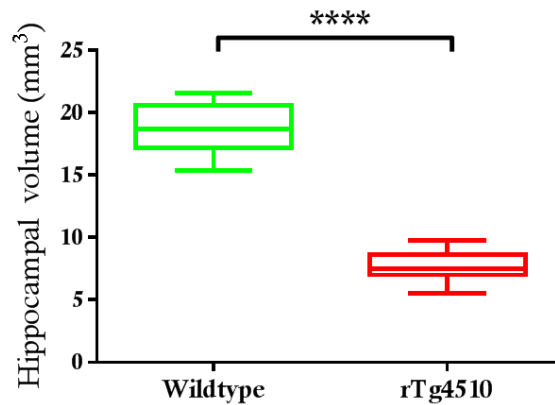
Figure 3.7 *Manual segmentation results from the 9 rTg4510 and 17 wildtype control mice at 8.5 months. A t-test was performed to identify significant differences between the groups. **** = p ≤ 0.001.*

Complete discrimination was observed between the rTg4510 mice and wildtype controls (p<0.0001), with 59.3% difference in hippocampal volume in the rTg4510 mice compared to wildtype controls. Mean hippocampal volume in the rTg4510 mice was 9.268 mm^3 (±1.5 mm^3) compared to 22.78 mm^3 (± 2.3 mm3) in the wildtype controls. Due to the highly laborious and time consuming nature of manual segmentation, only the hippocampus was delineated in both the rTg4510 mice and wildtype controls in order to make this comparison.

3.4.4 Histology and immunohistochemistry

It order to investigate possible correlations between the structural MRI findings with alterations occurring at the cellular level, immunohistochemistry was performed on each of the individual rTg4510 (n = 9) and wildtype (n = 17) mice (Figure 3.9) to estimate the density of NFTs.

The PG-5 antibody was used, which exhibits immunoreactivity with hyperphosphorylated tau. The rTg4510 mice exhibited high PG-5 staining in regions known to be affected in this model: the cortex (mean PG-5 density = 229.3 ± 29.51 mm^2) and hippocampus (mean PG-5 density = 82.92 ± 15.3 mm^2) (Figure 3.9C, D).

Conversely, low levels of PG-5 staining were observed within the thalamus (mean PG-5 density = 2.267 ± 0.81 mm^2) (Figure 3.9D). No PG-5 positive cells were observed in the wildtype controls in any of the regions under investigation (Figure 3.9C-E).

3.4.5 Structural correlations with histology

To further explore the relationship between the hippocampal volumetric estimates and tau pathology, the density of PG-5 positive neurons taken from a single slice in the hippocampus was plotted against the manual segmentation results of the rTg4510 mice.
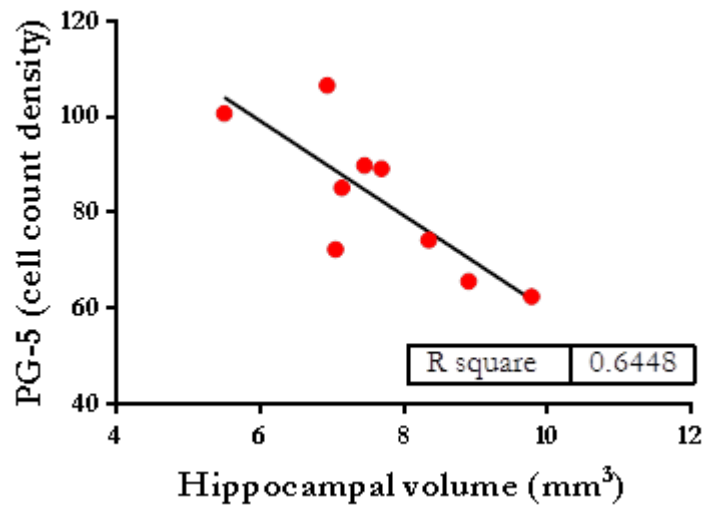
Figure 3.8 *A significant negative correlation was observed between the density of PG-5 positive neurons in the hippocampus, and hippocampal volume (p ≤ 0.01).*

A significant negative correlation between hippocampal volume and PG-5 positive neurons was observed (p≤0.01) (Figure 3.8), suggesting that this optimised structural sequence produces accurate hippocampal volume estimates that correlate to NFT deposition in this model.

I performed additional manual segmentation in the cortex of the rTg4510 mice in order to investigate structural correlations in this structure, which also suffers high NFT deposition. However, no significant correlations were observed between cortical volume and PG-5 positive neurons (Figure 3.10).
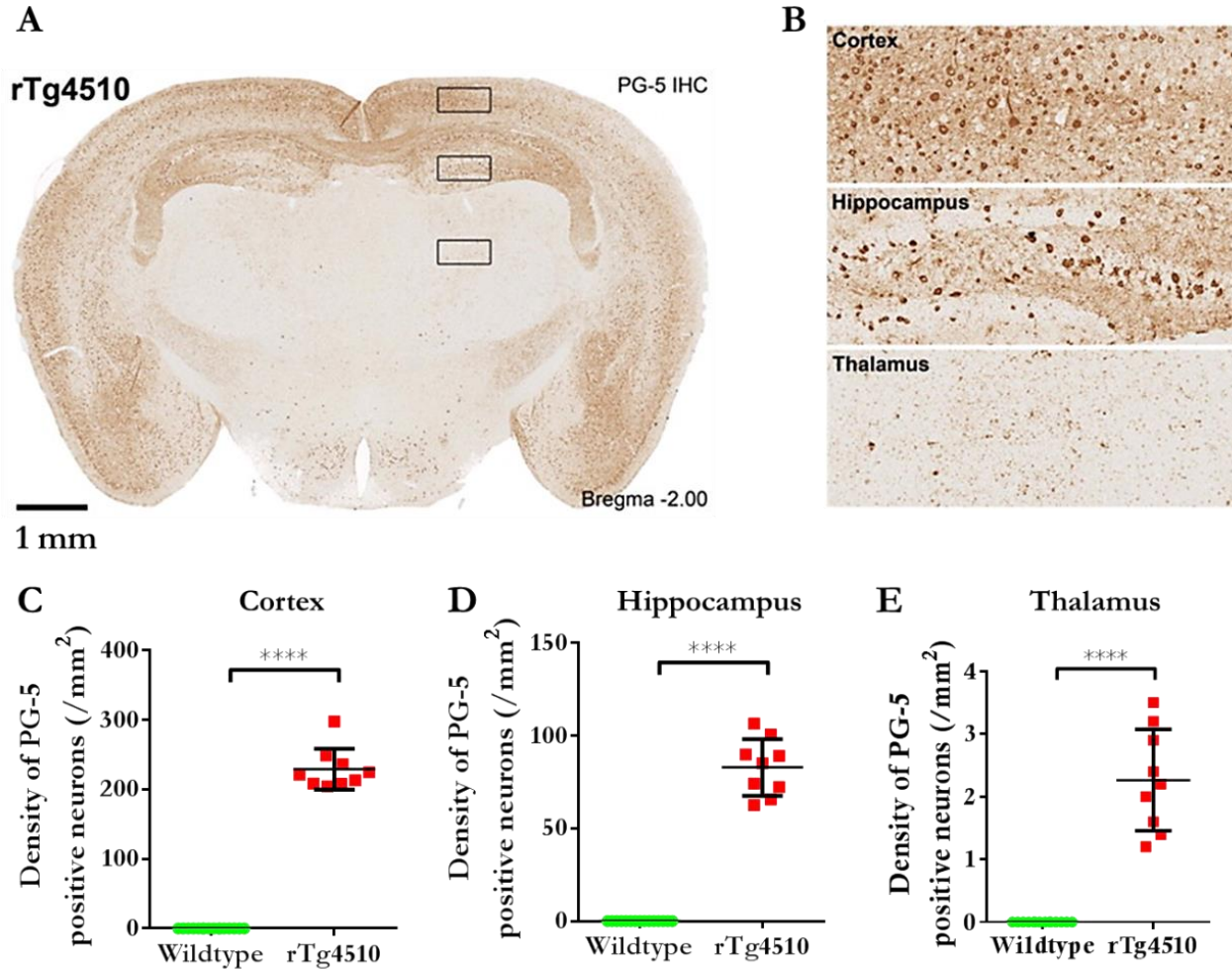
Figure 3.9 *Immunohistochemistry to estimate regional PG-5 positive NFT density. (A) Single slice from a representative rTg4510 mouse with staining for PG-5 positive NFTs. (B) Marked regional dependence of NFT density is observable, with high PG-5 staining in the cortex and hippocampus, and low levels in the thalamus. Quantitative regional estimates of NFT density for each of the 17 wildtype and 9 rTg4510 mice within (C) the cortex, (D) the hippocampus and (E) the thalamus. A t-test was performed to identify significant differences between the groups. **** = p ≤ 0.0001.*
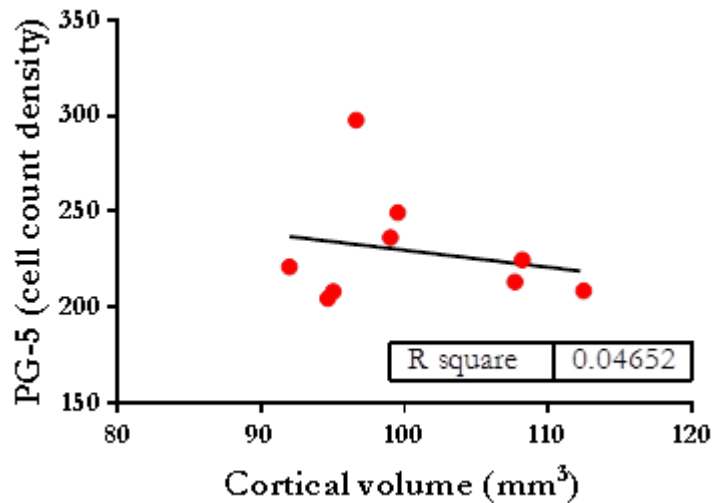
Figure 3.10 *No significant correlations were observed between the density of PG-5 positive neurons in the cortex, and cortical volume.*

3.4.6 Tensor-based morphometry

The manual segmentation of the hippocampus revealed volume loss within this region in the rTg4510 mice compared to wildtype controls. In order to explore morphological changes across the entire brain, TBM was employed.

Figure 3.11A-F shows the group-wise average with TBM statistics overlaid. Extensive bilateral changes throughout the rTg4510 brains relative to the average were observed, including atrophy in the cortex, caudate putamen, hippocampus and olfactory bulbs. Hippocampal atrophy could be localised to the CA1 subfield. TBM also detected expansion of the lateral, third and fourth ventricles. Negligible significant voxels were observed within the thalamus.
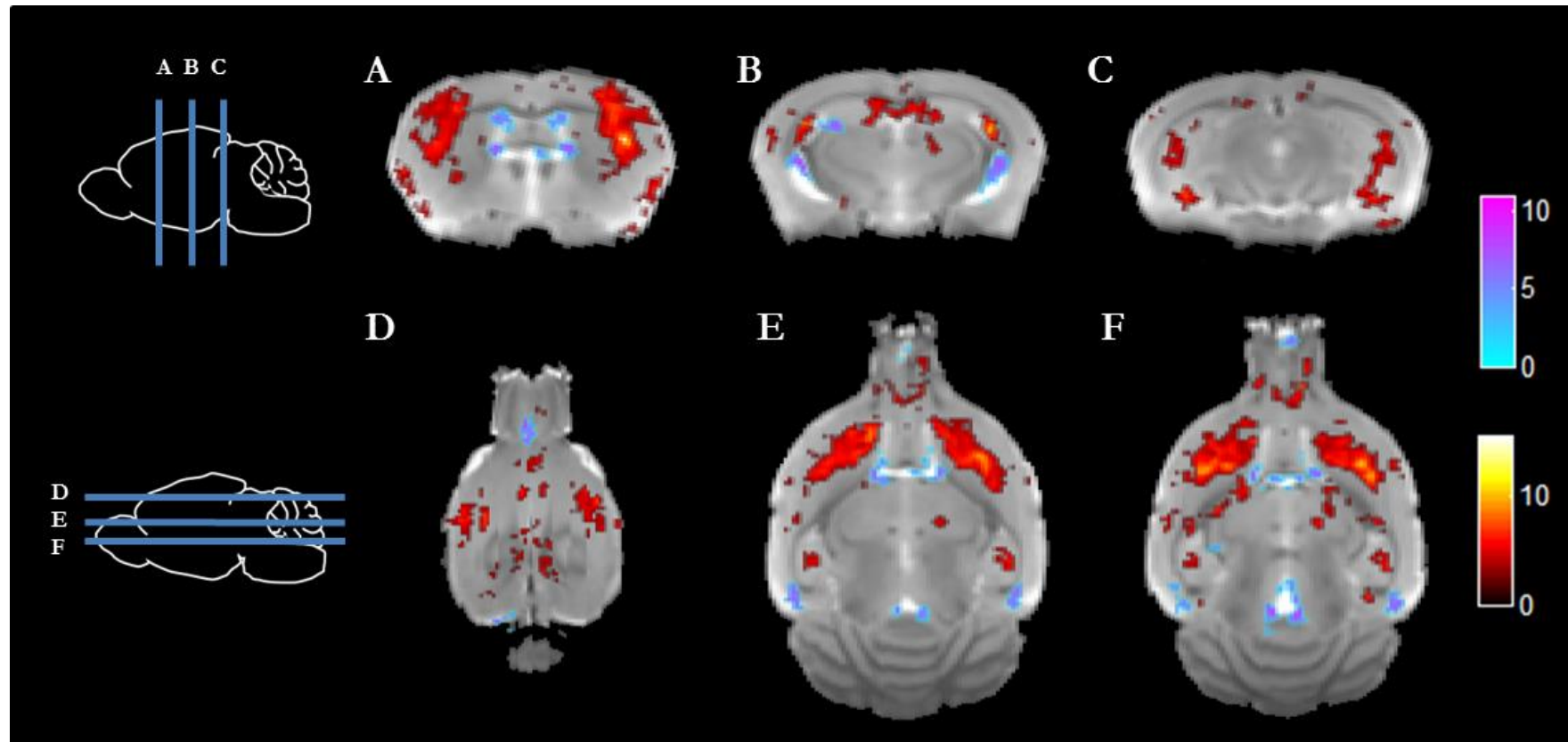
Figure 3.11 *Structural analysis results, showing TBM statistical results through representative (A – C) coronal and (D – F) axial slices of the final average image of all subjects after 20 iterations of NRR (locations indicated on schematic diagram above). Red: regions where the rTg4510 brains are significantly smaller than the average; blue: regions where the rTg4510 brains are significantly larger than the average. Based upon FDR-corrected t-statistics (q = 0.05), controlling for total intracranial volume. Clusters smaller than 20 voxels were removed.*

3.5 Discussion

In this chapter, a structural sequence for *in vivo* mouse brain imaging has been developed. The sequence permits the acquisition of high resolution, isotropic voxels within a feasible *in vivo* imaging time of 1.5 hours. Scan parameters (TR, TE) were optimised for maximum contrast between the hippocampus and thalamus, as well as the cortex and corpus callosum. The first application of TBM to the rTg4510 mouse model of tauopathy is also presented, where marked morphological changes have been identified in this model. This work presents a platform for my subsequent investigations of longitudinal structural changes in the rTg4510 mouse that is presented in this thesis.

Previous *in vivo* structural characterisation of AD mouse models has largely employed 2D sequences, with a range of spatial resolutions: 94 μm × 140 μm × 400 μm (*171*); 62.5 μm × 125 μm × 500 μm (*172*); 78 μm × 78 μm × 500 μm (*173*); 120 μm × 120 μm × 500 μm (*174*). In all these studies, the researchers have favoured high in-plane resolution over slice thickness. Analysis of these data sets has largely been restricted to manual segmentation of ROIs, in order to determine volumetric alterations. However, the thickness of the imaging slice may have introduced partial volume artefacts which would have led to inaccuracies in the volumetric results. When optimising the sequence for high resolution *in vivo* imaging, I selected a 3D sequence in order to minimise this effect.

All of the studies detailed above have employed a SE (T_2-weighted) rather than GE (T_2*-weighted) sequence; this is likely to be due to the susceptibility artefacts which are frequently observed in *in vivo* mouse brain data, and can corrupt GE imaging data. Very few of these papers have reported SNR measurements for their imaging data; however, Natt et al. have previously reported that SNR of 15 – 20 was sufficient to unveil anatomical details in the mouse brain (*175*). In this work, my sequence returned an SNR of between 8 and 12 which appeared suitable for manual delineation of ROIs as well as voxel-wise analysis techniques.

Previously published work in the rTg4510 mouse has reported structural changes in the hippocampus and cerebral cortex, as well as enlargement of the ventricles using manual segmentation of *in vivo* MRI data sets (*157*). Using TBM, we were able to extend these observations and additionally detect local volume reductions in the cortex,

hippocampus, caudate putamen and olfactory bulbs as well as ventricular expansion. At this time point, the transgenic brains have undergone gross atrophy which is noticeable by eye in the *in vivo* structural images. I therefore anticipate that TBM will be most valuable in the detection of subtle structural abnormalities that occur at earlier stages of tauopathy that I investigate in the longitudinal study of the rTg4510 described in Chapter 4.

The hippocampal atrophy observed using TBM was validated by manual delineation of this region, where complete discrimination of the rTg4510 animals and wildtype controls was observed. However, this marked loss in hippocampal volume was not entirely encapsulated in the TBM findings, which only showed a handful of significant voxels in the caudal slices of the hippocampus. According to Lerch et al., image registration works best when the data to be matched is comparable (*176*); that is, when the phenotype to be explored is reasonably subtle. In this work, the transgenic animals had undergone gross atrophy of the forebrain regions, which may have introduced some difficulties when registering these data sets to the wildtype controls. This may have resulted in an underestimation of the hippocampal atrophy in the TBM findings.

The negative correlation that we measured between hippocampal volume and NFT density provides evidence of a direct relationship between NFT pathology and atrophy, whilst highlighting the sensitivity of *in vivo* MRI to subtle volume changes. This correlation was not present in the cortex, despite higher NFT density. This may be because the hippocampus has a more rapid progression of tangle formation and thus the subsequent neurodegeneration is more advanced at 8–9 months of age.

Structural MRI has already established itself as a reliable biomarker in the clinical diagnosis of Alzheimer's disease (*93*) , where characteristic grey matter reduction and ventricular enlargement can be readily visualised using standard structural MRI sequences. Structural MRI has found additional clinical relevance in the differential diagnosis of AD over other forms of dementia (e.g. dementia with Lewy bodies) where neuropsychological testing alone may be insufficient (*177, 178*). Crucially, structural MRI may enable detection of AD prior to the onset of clinical symptoms, making it a valuable biomarker of the disease (*98*). It is currently employed within the ADNI study – a worldwide collaboration between research institutes, with the aim of understanding the physical brain changes that accompany the descent into dementia (*179*).

Advanced image processing techniques are routinely applied to large clinical AD cohort studies (*179*), to identify morphological differences in AD subjects. These techniques include voxel-wise analysis methods e.g. TBM, in addition to atlas-based segmentation techniques (*180-182*). The utility of these techniques has expedited high throughput analysis of large clinical data sets, such as those generated within the ADNI study, enabling automated and unbiased detection of morphometric changes occurring within AD subjects. These methods are being increasingly applied to structural data sets of the AD mouse brain.

Quantification of volumetric alterations in mouse models of AD has traditionally been performed using manual segmentation, which requires a trained user to delineate regions of a target structure in each image slice in order to generate a 3D volume (*183, 184*). Manual analysis methods suffer a number of disadvantages; they are prone to user-bias, are time-consuming, and require a *priori* hypotheses to inform the regional analysis. In order to overcome these limitations, the preclinical MRI community are rapidly adopting advanced image processing techniques to analyse mouse brain MRI data. In particular, atlas-based segmentation techniques have established themselves as robust alternatives to manual segmentation for regional analysis of AD mouse brains (*157, 185*). A number of published pipelines for automatic structural parcellation are now available (*186, 187*), enabling the automatic delineation of mouse brain regions. The application of these pipelines to mouse brain data sets has been facilitated by increasing availability of *in vivo (188)* and *ex vivo (189-192)* mouse brain atlases, to support atlas-based segmentation techniques.

Despite the growth of automated segmentation techniques to characterise structural mouse brain data sets, the translation of voxel-wise analysis methods has been somewhat slower to progress; however, they are gaining popularity due to their ability to detect discrete morphological changes which may be undetected by regional analysis. A number of rodent studies have employed voxel-wise analysis techniques to investigate a range of neurological disorders including: Huntington's disease (*154, 193, 194*), AD (*155, 195-197*), Prader-Willi syndrome (*198*) and neurodevelopmental abnormalities (*199-203*). These techniques have demonstrated enhanced sensitivity to morphological disturbances over manual segmentation in mice, making them an attractive alternative for characterising a mouse model (*204*). However, the vast majority of these studies were performed using *ex vivo* mouse brain data, which involves perfuse-fixation of the

tissues before they are imaged at near-microscopic resolution (*205*). A contrast agent is frequently employed as a tissue-active stain, to highlight detailed anatomical structures (*140*). Although this produces high quality imaging data with exquisite soft tissue contrast, it sacrifices the ability to image the same animal longitudinally.

Only a handful of studies have successfully employed voxel-wise analysis techniques to study *in vivo* AD mouse brains (*155, 197*). This is surprising, given the significance of longitudinal data in characterising neurodegeneration and its modulation by emerging therapeutics. This may be due to inadequacies in the imaging data, as most *in vivo* imaging protocols employ multi-slice 2D sequences with high in-plane resolution at the expense of poor section thickness (*175*). This may render the data unsuitable for TBM analysis, where high resolution isotropic voxels are a requirement. Indeed, previous work by Teipel et al. employed structural MRI in conjunction with voxel-wise analysis techniques to characterise a mouse model of AD (*206*). In this work, no grey matter alterations were observed, despite histological observations of cerebral amyloidosis at this timepoint (*207*). Closer inspection of the imaging parameters employed by Teipel et al. revealed that a 2D sequence was employed; with high in-plane resolution (31.25μm) at the expense of poor slice thickness (600μm). This choice of parameters is likely to be non-optimal for voxel-wise analysis methods, and may have prohibited the detection of morphological changes.

In this work, I have optimised the sequence for high resolution *in vivo* mouse brain imaging, which fulfils the specific requirements for TBM analysis. The application of the optimised sequence to the rTg4510 mouse demonstrated its suitability to detect AD-related changes in this mouse.

3.6   Conclusion

In conclusion, in this chapter I developed a structural MRI sequence designed with consideration of the following factors: i) spatial resolution ii) isotropic imaging voxels iii) contrast between the hippocampus and surrounding tissue iii) SNR iv) spatial distortion due to magnetic field inhomogenities v) imaging time.

Whilst I did not perform an exhaustive exploration all these parameters, I developed a sequence with spatial resolution and SNR aligned with literature values with isotropic voxel size and optimised contrast to delineate the hippocampus (using a T_2-weighted

FSE 3D sequence). Using this sequence, I observed marked atrophy of cortical and hippocampal regions in the rTg4510 mouse model of AD using both manual segmentation and TBM. Importantly, I observed a correlation between hippocampal volume and NFT density in agreement with clinical findings. As such this observation supports the clinical relevance of this model to explore the interaction of tau pathology and tissue atrophy in AD.

Chapter 4: Imaging the accumulation and suppression of tau pathology using multi-parametric MRI

4.1 Aims

In the preceding chapter, a sequence for high resolution *in vivo* structural has been developed. The sensitivity of this sequence to morphological changes in the rTg4510 mouse was assessed in a single time-point study of neurodegeneration, at an age when the mice experience gross atrophy within the forebrain regions.

In this chapter, this sequence has been applied in a longitudinal study of neurodegeneration in the rTg4510 mouse, a subset of which were treated with doxycycline at different timepoints to suppress the tau transgene. Using this paradigm, I investigated the sensitivity of MRI biomarkers to both a) progressive tau-driven neurodegeneration in the rTg4510 mice, and b) the suppression of pathological tau in the doxycycline-treated rTg4510 mice. High resolution structural MRI was employed alongside other MR biomarkers which offer sensitivity to other pathological mechanisms which have been implicated in AD: arterial spin labelling (ASL) to quantify cerebral blood flow (CBF), diffusion tensor imaging (DTI) to explore microstructural changes and chemical exchange saturation transfer (CEST) which is sensitive to the chemical exchange of mobile protons.

In this work, I have been involved in the experimental set-up, acquisition of the imaging data and post-processing of the results. Following *in vivo* scanning, I perfuse-fixed all of the mice before dispatching the tissues to my collaborators for histology. I also investigated and interpreted all MR findings, and performed cross-correlations between the imaging parameters, as well as against histology.

4.2 Introduction

It has been over a century since Alois Alzheimer first described the symptoms of the presenile dementia which would come to bear his name (*208*), but to date there is still no disease-modifying or preventative treatment for this devastating disease. As the incidence of Alzheimer's disease (AD) continues to rise to epidemic proportions (*209*), effective therapies are urgently required to ease both the economic and emotional burdens of this devastating disease.

The two key neuropathological hallmarks of AD are plaques composed of amyloid-β and NFTs of hyperphosphorylated tau. Emerging therapies targeting the production or clearance of these protein aggregates require robust biomarkers to evaluate and quantify therapeutic efficacy. The development of reliable biomarkers in humans, however, is complicated by the length of clinical studies required to follow the evolution of pathology; this is currently believed to occur as much as 30-40 years prior to cognitive deficits (*98*). One approach is to establish and validate biomarkers using mouse models of AD as a surrogate for patient populations.

Tau pathology, not amyloid-β burden, independently predicts cognitive status in patients with AD (*210*). This suggests the potential value of tau-targeted therapies in AD and the requirement for non-invasive biomarkers that are sensitive to the severity of tau pathology. To investigate tau specific biomarkers of pathology I have used the rTg4510 mouse (*153*), which was previously characterised in a single timepoint study using structural MRI in the preceding chapter. This mouse expresses a mutant form of the h*MAPT* human gene under the control of a tetracycline-responsive (*tetO*) CaMKII-α promoter. One advantage of the model is that the expression of mutant tau can be suppressed by the administration of the tetracycline derivative doxycycline (Figure 4.1) (*114*). Longitudinal assessment of this model enables the investigation of biomarkers sensitive to the accumulation of tau pathology and provides a framework to evaluate the efficacy of therapeutic strategies targeted at the suppression or removal of pathological tau.
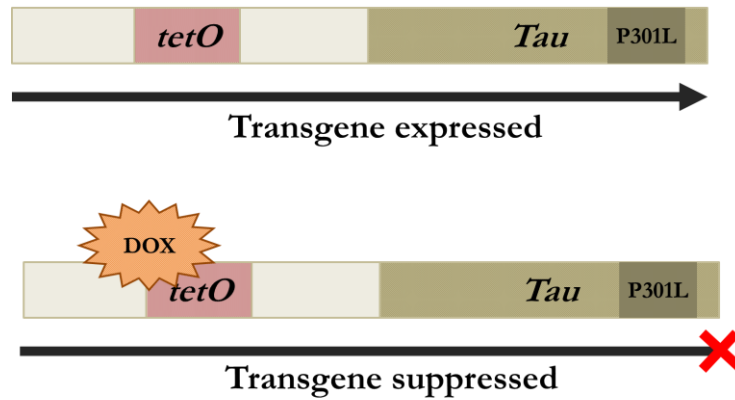
Figure 4.1 *Schematic showing the suppression of the transgene in the presence of doxycycline. Adapted from SantaCruz et al. (114)*

In this work, I have sought to identify specific elements of the pathological cascade, as well as the advancement and inhibition of tau pathology, using multi-parametric MRI measures in the rTg4510 mouse. I explored morphological changes using high resolution structural MRI, the breakdown in chemical exchange of mobile proteins using CEST, microstructural changes in the cytoarchitecture through DTI and alterations in CBF using ASL, over time. To coincide with the development of NFTs from 4 months, I conducted two longitudinal studies: one group received doxycycline from 3.5 months, representing an "early" therapeutic intervention. The second cohort received doxycycline from 4.5 months, representing "late" therapeutic intervention. Utilising these multi-parametric MRI techniques, I demonstrate sensitivity to tau-driven pathological changes as well as tau suppression in the rTg4510 in mice treated at two distinct time points.

4.3   Materials and Methods

4.3.1   Mice

The rTg4510 animal model used in this study was previously described in Chapter 4. For this study, Female rTg4510 mice and litter-matched wildtype controls were bred on a mixed FVB/NCrl + 129S6/SvEvTa background for Eli Lilly and Company by Taconic (Germantown, USA) and received on site 2 weeks prior to the initiation of the studies.

Two doxycycline intervention cohorts are reported in this study and summarized in Figure 4.2: 'early' (3.5 months) and 'late' (4.5 months) intervention. The early intervention cohort consisted of 20 rTg4510 mice with 10 wildtype controls, and the late intervention cohort consisted of 19 rTg4510 mice with 11 wildtype controls. Subsequent to their initial scan, the rTg4510 mice were divided into two subgroups: the treated rTg4510 mice received two boluses of 10mg/kg doxycyline hyclate (Sigma Aldrich; 10mg per kg of body weight) via oral gavage and were maintained on doxycycline-mixed chow diet (Harlan Teklad Rodent Diet; 200mg doxycycline per kg of dietary chow) until the end of the study (Harlan Teklad Rodent Diet); the untreated rTg4510 animals and the wildtype controls received two boluses of a 5% glucose vehicle via oral gavage and were maintained on standard chow. The dietary content of the doxycycline-mixed and standard chow was consistent for each group.

For further evaluation of the rTg4510 mouse's response to increasing concentrations of isoflurane, a separate cohort of female rTg4510 mice and wildtype controls were imaged at 9 months.

All mice were kept in standard size mouse cages ($29 \times 18 \times 13$ cm; up to 5 per same sex groups) at 20°C to 26°C on a daily 12 hour light-dark cycle with *ad libitum* access to food and water. All studies were carried out in accordance with the United Kingdom Mice (Scientific Procedures) act of 1986 and subject to approval by UCL's internal ethical review panel.
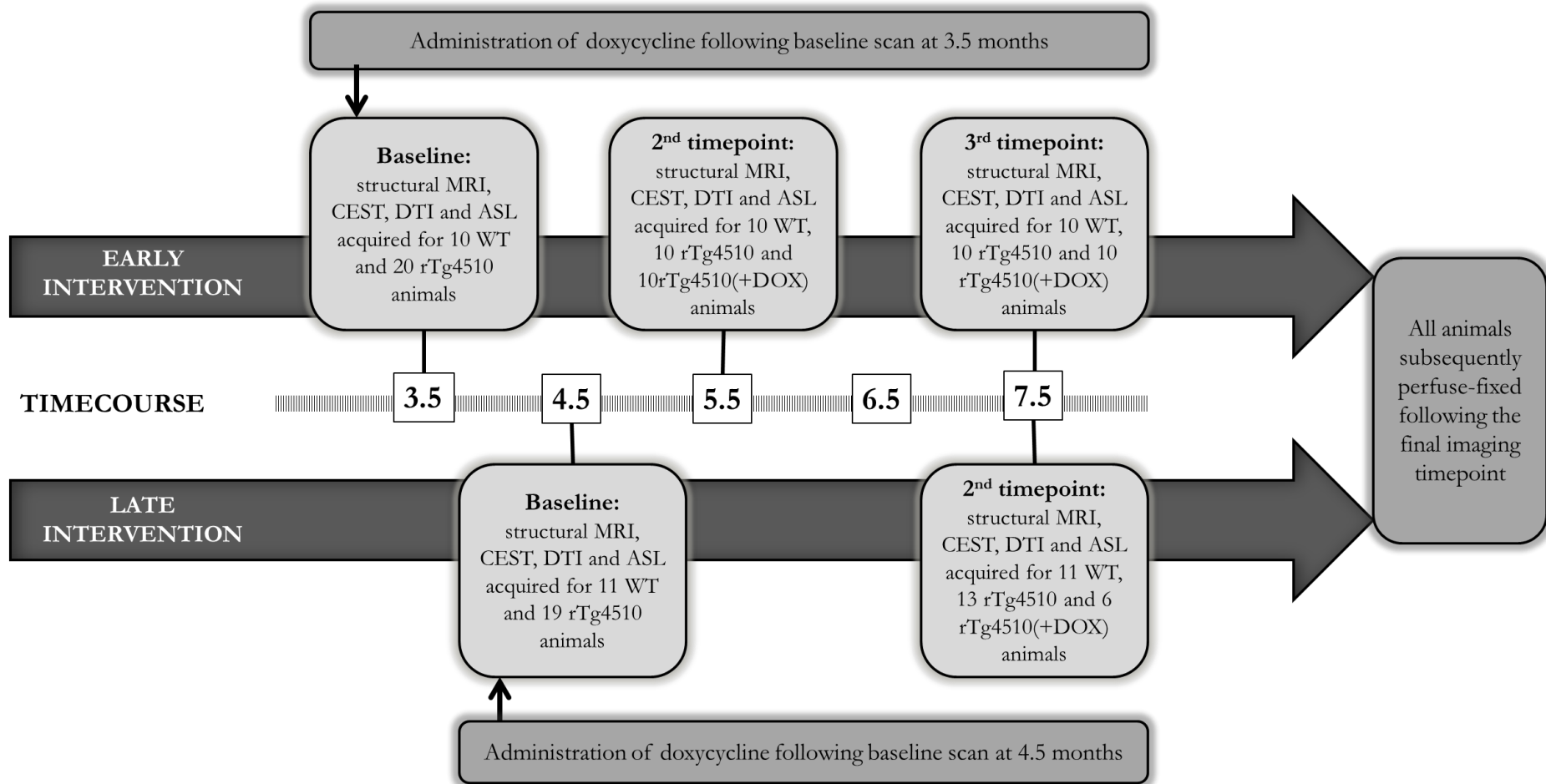
Figure 4.2 *Schematic describing the early and late doxycycline intervention studies. High resolution structural MRI, CEST, DTI and ASL was acquired at all timepoints. Doxycycline was administered to a subset of rTg4510 mice following the baseline scan; all treated rTg4510 mice were maintained on a doxycycline mixed chow diet until the end of each respective study.*

4.3.2 Magnetic resonance imaging

Mice were placed in an induction box before anaesthesia was induced using 2% isoflurane at 1 l/min in 100% O_2. Mice were subsequently positioned in a MRI-compatible head holder to minimise motion artefacts. Anaesthesia was maintained throughout imaging using 1.5% isoflurane at 1 l/min in 100% O_2 delivered via a nose cone g, which permitted spontaneous breathing of the mice. Core temperature and respiratory rate were monitored using a rectal probe and pressure pad respectively (SA instruments). Mice were maintained at ~37°C using heated water tubing and a warm air blower with a feedback system (SA instruments). Scans were performed in the following order: CEST, ASL, DTI and structural imaging. Prior to imaging, shimming was first performed across the CEST imaging slice (3mm slice thickness). Following CEST acquisition, shimming was performed across the whole mouse brain for the structural, ASL and DTI sequences.

I employed high resolution structural MRI, CEST, DTI and ASL at each timepoint to characterise the treated and untreated rTg4510 mice and wildtype controls. The imaging protocol is detailed in Figure 4.2. The mice from the early intervention cohort were perfuse-fixed following the final imaging timepoint before being dispatched for histology. The mice from the late intervention cohort were similarly perfuse-fixed following the final imaging timepoint; however, their brains were retained for high resolution *ex vivo* structural scanning in order to compare the sensitivity of the *in vivo* and *ex vivo* structural sequences. This study is summarised in Chapter 5. Once these extra scans were complete, the brains were dispatched for histology.

4.3.3 High resolution *in vivo* structural MRI

High resolution structural scans were acquired using the sequence parameters previously optimised in Chapter 3. Briefly, a 3D T_2-weighted FSE sequence was employed with the following parameters: FOV = 19.2 mm × 16.8 mm × 12.0mm; resolution = 150 μm × 150 μm × 150 μm; TR = 2500 ms, TE = 43 ms, ETL = 4, NSA = 1. Total imaging time was approx. 1 h and 30 mins.

4.3.4 Tensor-based morphometry

TBM was performed by my collaborators at the UCL Centre for Medical Image Computing, using the methods previously detailed in Chapter 3.3.9. Briefly, the *in vivo*

structural images were automatically oriented to a standard atlas space, non-uniformity corrected, skull-stripped and intensity-standardised at each imaging timepoint. This was followed by 1 iteration of rigid registration, 4 iterations of affine registration and 15 iterations of non-rigid registration, to align equivalent voxels between subjects. The determinant of the Jacobian matrix was calculated at each voxel of the resulting deformation fields which was subsequently smoothed, before statistics were performed at each voxel in order to compare groups. The resulting statistical parametric maps were corrected for multiple tests using the FDR (*169*); q=0.05.

4.3.5 Automatic structural parcellation

Automatic structural parcellation was performed by my collaborators at the UCL Centre for Medical Image Computing. Using a multi-atlas-based structural parcellation framework (*211*), three structures of interest were extracted: the cortex, hippocampus and thalamus for each animal at each timepoint. The brain images were oriented, non-uniformity corrected and skull-stripped as above. Following orientation, non-uniformity correction and skull-stripping as above, my collaborators adopted the publicly available *in vivo* mouse brain MRI atlas previously published by Ma et al. (*188*) for the framework. First, the atlas images were registered affinely to the original MRI image data using a block-matching algorithm (*212*). Once complete, the STAPLE algorithm [17] was applied to fuse the resampled atlas masks together to create a consensus brain mask for each animal's scans. A further non-rigid registration based on fast free-form deformation was then performed to correct any remaining local mis-alignment of the affinely registered atlas to the brain volumes (*168*). The structural labels from the atlas were then resampled to match the resolution of the brain scans and fused using the STEPS algorithm (*167*) to create the final parcellated structures of interest: the cortex, hippocampus and thalamus.

As described in Chapter 3.3.8, a previously published calibration protocol was used to correct gradient scaling errors in the data (*165*).

4.3.6 Chemical exchange saturation transfer

The CEST sequence was independently developed for *in vivo* imaging of the rTg4510 mouse by my collaborator at the UCL Centre for Advanced Biomedical Imaging (*213*). The CEST sequence was acquired using a single slice GE imaging sequence positioned axial using the splenium of the corpus callosum as a landmark for consistency of slice

positioning between subjects (TR = 6.1 ms, TE = 2ms, flip=5°, FOV = 20 mm × 20 mm, slice thickness 3 mm, matrix size = 64 × 64). Saturation pulses were applied at 79 frequency offsets covering ± 6 ppm to encompass APT saturation peaks approximately 3.5 ppm downfield from the water; this corresponds to the 8.25 ppm in the proton resonance spectrum. A reference offset at 200 ppm was also acquired for normalisation. Shimming was performed across the entire imaging slice (3 mm thickness). The APT signal was calculated as the area under the MTRasym curves between 3.3 and 3.7 ppm on a pixel-by-pixel basis by fitting a polynomial function to Z spectra, correcting for off-resonance effects by cubic spline interpolation and subtracting the signal intensities at either side of the direct water saturation peak (*214*). Total imaging time was 5 minutes.

4.3.7   Diffusion tensor imaging

The DTI sequence was independently developed for *in vivo* imaging of the rTg4510 mouse by my collaborators at the UCL Centre for Advanced Biomedical Imaging (*213*). A four shot SE echo planar imaging (EPI) sequence was used to acquire sixteen slices. The fissure between the olfactory bulbs and the cortex was used as an anatomical landmark to maintain consistency in slice positioning between mice. The FOV was 20 × 20mm with a matrix size of 100 × 100 and a slice thickness of 0.5 mm. Diffusion gradients were applied in twenty directions with the following parameters G = 0.25 T/m, Δ = 9.3ms, δ = 5.5 ms, and b = 1050 s/mm^2 to generate diffusion weighted images in addition to a single unweighted B_0 image. Acquisition of 5 averages with a TR of 2000ms gave a total imaging time of 25 minutes. Software written in Matlab was used to construct tensors at each voxel through a least squares solution approach (*215*). The FA, MD and RD were calculated from the tensors following standard methods (*216, 217*). The total imaging time was 25 minutes.

4.3.8   Arterial spin labelling

The ASL sequence was independently developed for *in vivo* imaging of the rTg4510 mouse by my collaborator at the UCL Centre for Advanced Biomedical Imaging (*213*). A flow-sensitive alternating inversion recovery (FAIR) sequence (*218, 219*) with a 4-shot segmented SE EPI readout was impemented with the following parameters: 5 slices, slice thickness = 1 mm, FOV = 20 × 20 mm, matrix size = 64 × 64, slice selective inversion pulse width = 12 mm, inversion time = 1500 ms, TE = 11 ms, TR

= 3500 ms, 20 averages. A hyperbolic secant adiabatic inversion pulse was used with a bandwidth of 20 kHz for the FAIR labelling pulses (*220*). The splenium of the corpus callosum was used as a landmark for consistency of slice positioning between subjects. Total imaging time was 20 minutes. CBF maps were generated using the model described by Buxton *et al.* (*221*).

The total time dedicated to image acquisition was 2 hours 10 minutes. The animal set-up, positioning and shimming took no longer than 30 minutes, which ensured the total time the animal was under isoflurane did not exceed the three hour anaesthesia tolerance, as defined by Lerch et al. (*222*).

4.3.9   Perfuse fixation

The perfusion fixation protocol for preparation of the post-mortem brain samples for histological evaluation was fully described in Chapter 3.3.6. Briefly, mice were terminally anaesthetised before being perfused through the left ventricle with 15 – 20 mL of saline (0.9%) followed by 50 mL of buffered formal saline (10%) at a flow rate of 3 mL per minute. Following perfusion, the animal was decapitated, defleshed, and the lower jaw removed. All brains were stored in-skull at 4 °C before being dispatched for histology.

4.3.10   Histology and immunohistochemistry

Brain samples were processed using the Tissue TEK® VIP processor (GMI Inc, MN USA) before being embedded in paraffin wax for coronal brain sectioning. Serial sections (6μm) were taken using HM 200 and HM 355 (Thermo Scientific Microm, Germany) rotary microtomes. Immunohistochemistry (IHC) was performed using a primary antibody for tau phosphorylated at serine 409 (PG-5; 1:500 from Peter Davies, Albert Einstein College of Medicine, NY, USA) as previously described (*163*). Stained sections were digitised using the Scanscope XT slide scanner (Aperio, CA, USA) at 20× magnification. Imagescope software (version 11.1.2.760; Aperio, CA, USA) was used to view the digitised tissue sections and delineate the regions of interest (cortex, hippocampus and thalamus). The number of PG-5 positive neurons was manually counted within a delineated region and expressed as a density (mm^2). Both sides of the brain were analysed and averaged before statistical analysis.

4.3.11 Statistical analysis

Quantitative data were analysed using a one-way ANOVA to determine whether there were any significant differences between the immunohistochemistry results for the 4 mice cohorts (wildtype controls, early treatment rTg4510 mice, late treatment rTg4510 mice and untreated rTg4510 mice). A two-way ANOVA with a post-hoc Sidak multiple comparison was performed to investigate group differences in the longitudinal imaging studies. GraphPad Prism 5 (version 5.04; GraphPad software Inc., CA, USA) was used to perform statistical tests and to produce graphs, which display mean values ± standard error of the mean (SEM). Statistical significance was set at $p \leq 0.05$.

For the CEST, DTI and ASL analysis, measurements were taken from ROIs drawn in a single slice positioned approximately Bregma -2.3; this was to align our MRI measurements with the histology. ROIs were manually drawn in the cortex, hippocampus, thalamus and corpus callosum (DTI only), as illustrated in Figure 4.2. The results within the hippocampus and cortex were averaged in order to calculate parameters within regions suffering from gross tau pathology.

The structural images were analysed using the automated methods as described in Section 4.3.4 and 4.3.5.
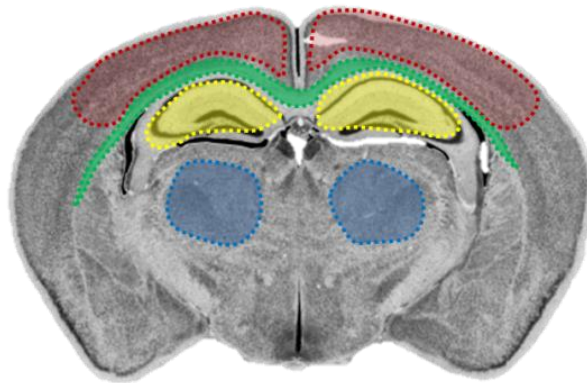
Figure 4.3 *Slice section taken from The Mouse Brain Library's Mouse Brain Atlas showing location of hippocampal (yellow), cortical (red), thalamic (blue) and white matter (green) ROIs for quantitative multi-parametric MRI analysis. The cortical and hippocampal results were averaged to extract parameters within the "high ranked" tau pathology regions.*

4.4 Results

In this work, I have explored the sensitivity of multi-parametric MRI to the accumulation and suppression of pathological tau. A detailed description of the imaging protocol is provided in Figure 4.2, including the "early" and "late" doxycycline intervention strategy.

4.4.1 Histology and immunohistochemistry

To quantify the severity of tau pathology in the treated and untreated rTg4510 groups, all mice (21 wildtype controls; 23 untreated rTg4510 mice, 10 early treatment rTg4510 mice and 6 late treatment rTg4510 mice) were sacrificed following the final imaging timepoint (7.5 months) and prepared for neuropathological assessment. Histology was performed by my collaborators at Eli Lilly. Immunohistochemistry using PG-5 (pS409), a marker of tau hyperphosphorylation, was used to quantify the density of tau-positive neurons in the cortex, hippocampus and thalamus (Figure 4.4).

Consistent with literature data and my previous findings in this model (*114*), untreated rTg4510 mice contained a high density of PG-5 positive neurons in the cortex and hippocampus (mean = 345.2 ± 10.05 and 103.3 ± 7.64 (SEM), respectively; Figure 1A-C). In contrast, the thalamus had a significantly lower density (mean = 5.369 ± 0.64 (SEM); Figure 4.4A, D). For this reason, I classified the cortex and hippocampus as 'high tau burden' regions and the thalamus as a 'low tau burden' region. There was no PG-5 positive staining observed in the wildtype mice. (Figure 4.4B- D).

Following administration of doxycycline to rTg4510 mice, I observed a significant reduction in the number of PG-5 positive neurons in the cortex, hippocampus and thalamus of early ($p<0.0001$) and late ($p<0.001$, $p<0.05$ and $p<0.01$ respectively) treated mice when compared to the untreated group (Figure 4.4A–D). The group treated with doxycycline early (3.5 months) showed the greatest reduction in PG-5 positive neuron density, especially in the hippocampus and thalamus regions, illustrating the effectiveness of early intervention in this model. However, it is worth noting that the thalamus suffers markedly less PG-5 positive neurons in comparison to the hippocampus and cortex, hence its classification as a 'low tau burden' region, as described above.
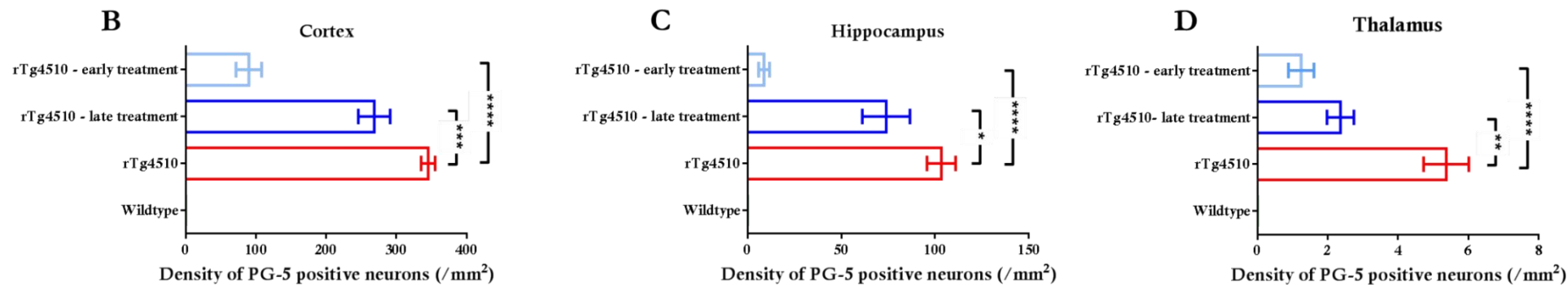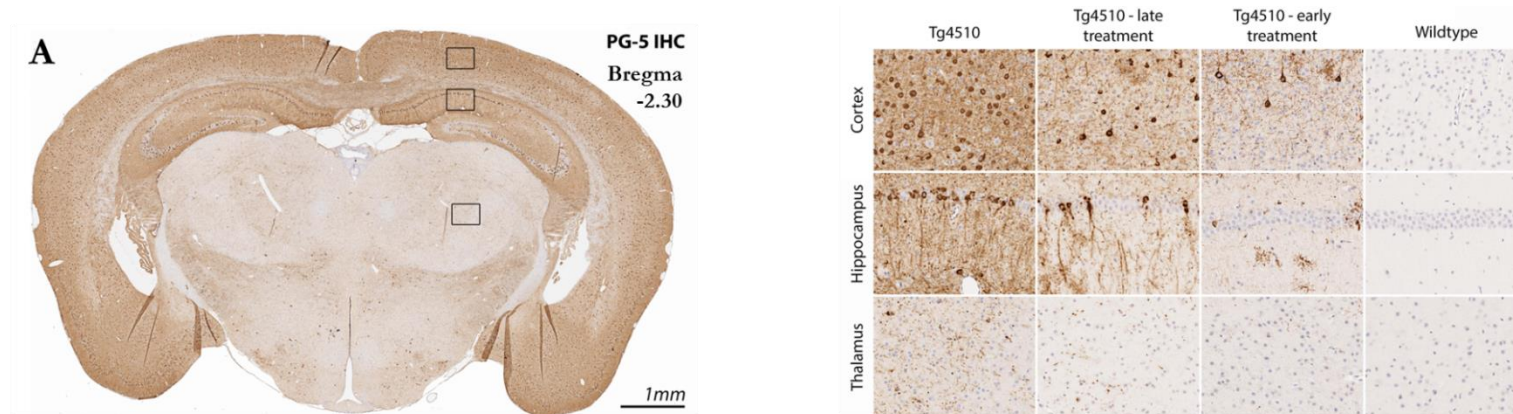
Figure 4.4 *Immunohistochemistry to estimate regional density of tau (PG-5) positive neurons. (A) Representative coronal slice illustrating the distribution of PG-5 positive neurons in the untreated rTg4510. Quantitative estimates of PG-5 neuron density in cortical (B), hippocampal (C) and thalamic (D) regions for wildtype (n=21), untreated rTg4510 mice (n=20), late treated Tg4510s mice (n=6) and early treated rTg4510 mice (n=10) at 7.5 months of age. A one-way ANOVA was performed to identify significant differences between the groups. Statistically significant groups have been identified and highlighted. Error bars represent the SEM. *=p<0.05; ** = p≤0.01; ***=p<0.001; **** = p≤0.0001.*

4.4.2 High resolution structural MRI

To investigate morphometric changes in the rTg4510 mice, I acquired high resolution *in vivo* structural images for the two longitudinal cohorts, using the sequence I optimised in Chapter 3. In both cases, doxycycline was administered to a subset of rTg4510 mice following the baseline scan: at 3.5 months for the early intervention study, and 4.5 months for the late intervention study.

My collaborators at the UCL Centre for Medical Image Computing used TBM to identify local areas of significant brain atrophy or expansion in the rTg4510 mice; the results at 7.5 months are shown in Figure 4.5. For each set of comparisons, three coronal slices with TBM statistics overlaid are presented. Extensive bilateral morphometric changes were detected in the untreated rTg4510 mice compared to wildtype controls, including significant atrophy in the forebrain, cortex, lateral striata and hippocampus as well as expansion of the lateral, third and fourth ventricles (Figure 4.5A). Reductions were also observed in the thalamus; in the absence tau pathology, this is likely to reflect global differences in brain volume of the rTg4510 mice compared to wildtype controls.

To investigate the morphological changes within the doxycycline-treated rTg4510 mice, two comparisons have been made: first, wildtype vs. doxycycline-treated rTg4510 mice (Figure 4.5B, C) and second, untreated rTg4510 vs. the treated rTg4510 mice (Figure 4.5D, E). In mice treated with doxycycline from 3.5 months, TBM detected small discrete structural changes within the caudate putamen and the hippocampus compared to wildtype controls (Figure 4.5B), indicating preservation of cortical regions and ventricular spaces which presented with markedly fewer significant voxels. Figure 4.5D compares early doxycycline-treated rTg4510 mice with untreated rTg4510 mice. Here, TBM detected gross relative expansion of the ventricles and a bilateral pattern of cortical atrophy, highlighting regions preserved due to suppression of the tau transgene. Following administration of doxycycline from 4.5 months (late intervention), a similar yet more marked pattern of changes was observed in comparison to wildtype controls (Figure 4.5C). The comparison between late doxycycline-treated rTg4510 mice and untreated rTg4510 mice revealed a small number of significant voxels within the hippocampus, indicating small differences between the two cohorts (Figure 4.5E); early intervention appeared more successful at limiting atrophy and ventricular expansion.
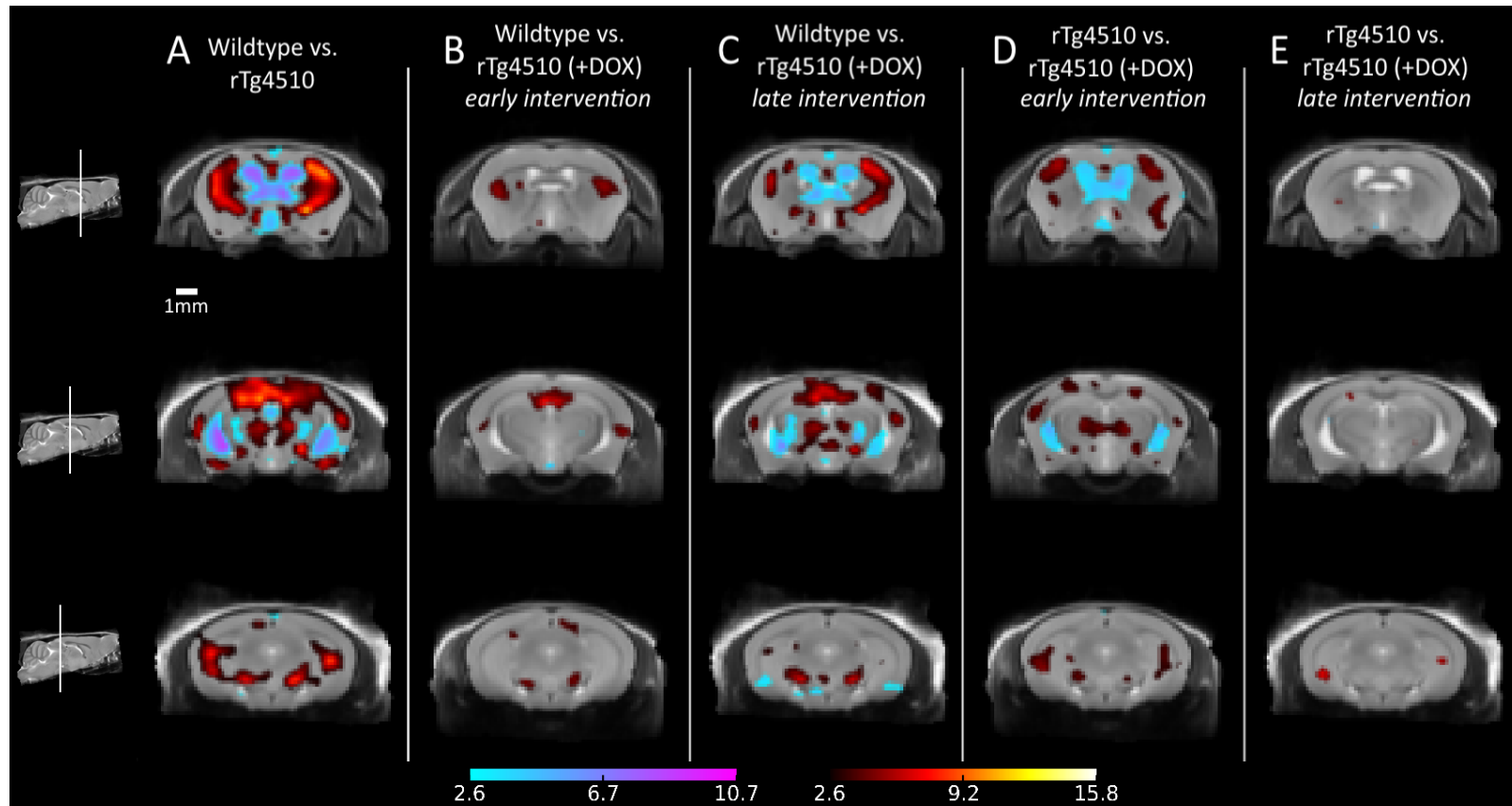
Figure 4.5 *Results from structural analysis at 7.5 months, showing TBM statistical results overlaid on representative coronal slices of the final group average images after 15 iterations of NRR. Red: regions where the rTg4510 brains are relatively locally smaller than the average; blue: rTg4510 brains are locally larger. Based upon FDR-corrected t-statistics (q=0.05).*

At 5.5 months (Figure 4.6), TBM detected comparable yet less widespread differences between the wildtype and early doxycycline-treated rTg4510 mice in the same regions implicated in Figure 4.5. In the comparison between the untreated rTg4510 mice and early doxycycline-treated rTg4510 mice (Figure 4.6C), no significant voxels survived FDR correction. TBM results at the baseline scan revealed negligible significant local differences between the rTg4510 mice and wildtype controls (data not shown).
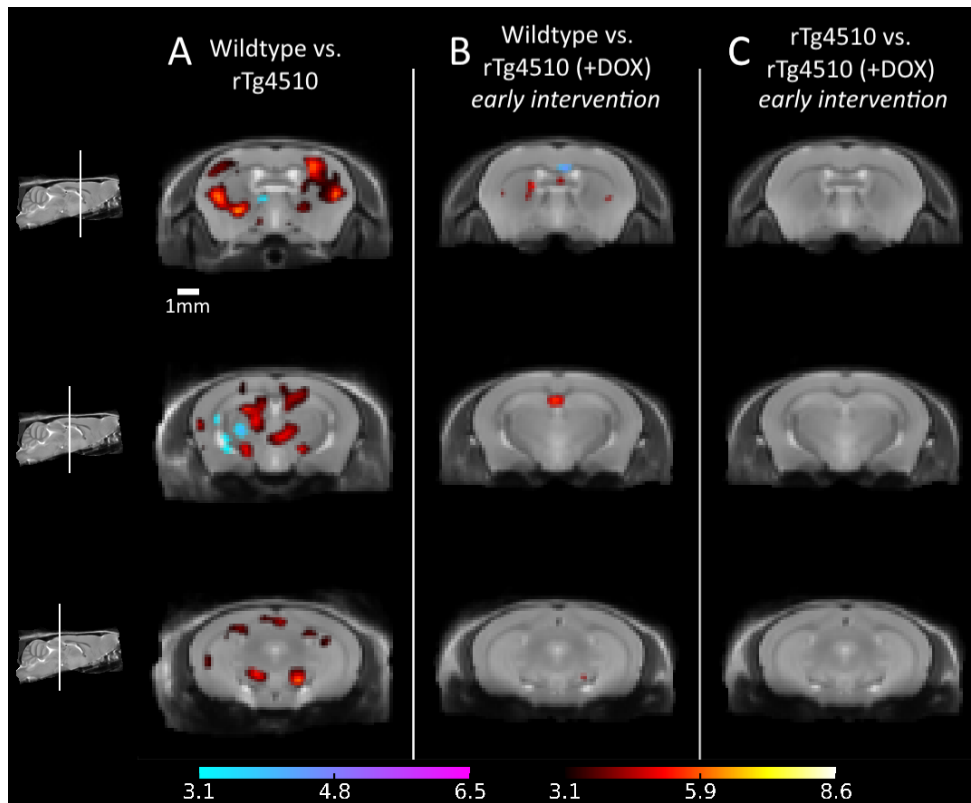
Figure 4.6 *Results from structural analysis at 5.5 months, showing TBM statistical results overlaid on representative coronal slices of the final group average image after 15 iterations of NRR. Red: regions where the rTg4510 brains are relatively locally smaller than the average; blue: rTg4510 brains are locally larger. Based upon FDR-corrected t-statistics (q=0.05).*

In order to quantify longitudinal volume differences between the transgenic mice and wildtype controls in the regions selectively vulnerable to high tau accumulation, my collaborators at the UCL Centre for Medical Image Computing also employed a fully automated atlas-based brain segmentation pipeline to measure absolute and normalised volume changes in the high ranked pathology regions across all timepoints. A sample

parcellated wildtype mouse brain can see seen in Figure 4.7. As well as investigating absolute volume alterations, normalized volume changes were explored by dividing the regional volume changes divided by the change in the whole brain volume (to account for gross differences in whole brain volume) (Figure 4.9).
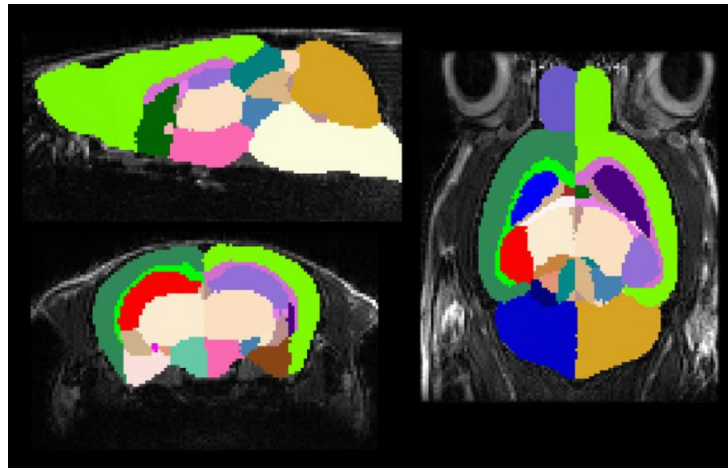
Figure 4.7 *Representative wildtype mouse with atlas-based parcellation results overlaid. The methodology segments the mouse brain into 40 different regions of interest (187).*

A significant reduction in absolute volume of the high ranked pathology regions within the untreated rTg4510 mice from 3.5 months of age compared to the wildtype controls was detected (p<0.001) (Figure 4.8A). The absolute volume of the high ranked pathology regions within the untreated rTg4510 mice continued to decline by a further 16.2% until the final imaging timepoint at 7.5 month (Figure 4.8A). The early treated rTg4510 mice suffered less atrophy compared to the untreated rTg4510 mice; the decline in volume was reduced to 6.3% owing to the suppression of the transgene (Figure 4.8A). Meanwhile, the absolute volume of the wildtype controls remained consistent from 3.5 months (82.1 mm3) to 7.5 months (83.8 mm3) indicating the volume changes were specific to the rTg4510 mice (Figure 4.8A). A similar trend was observed within the untreated rTg4510 mice in the late treatment study (Figure 4.8C). The volume of the thalamus, a region of low tau burden, was reduced in the rTg4510 mice compared to wildtype controls at 3.5 months. This echoed the result in the high tau burden regions, possibly indicating the effect of the transgene of brain morphology (Figure 4.10).
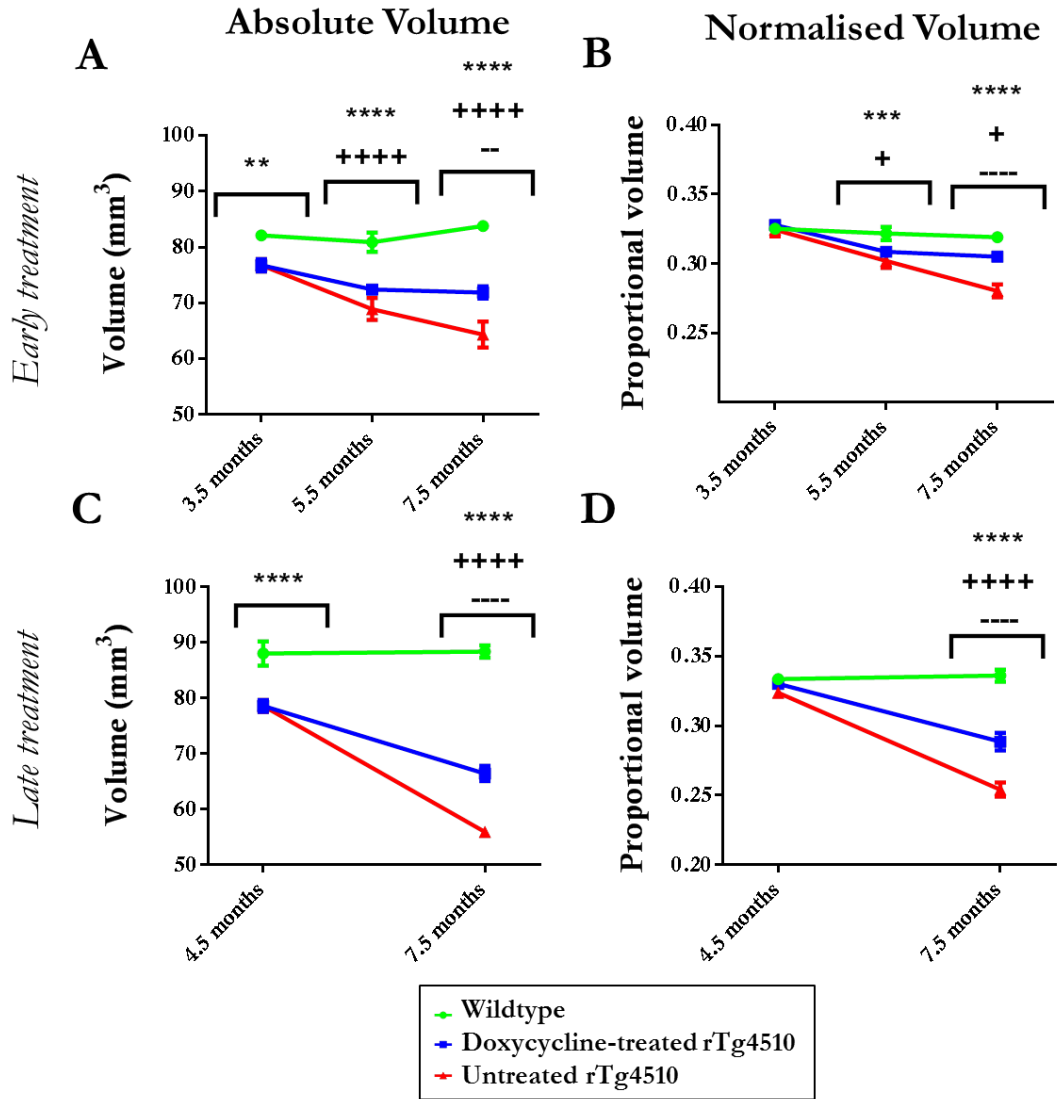
Figure 4.8 *Longitudinal volumetric changes in the high ranked pathology regions, extracted from the high resolution structural images. Early intervention: wildtype (n=10), untreated rTg4510 (n=10) and treated rTg4510 animals (n=10). Late intervention: wildtype (n=11), untreated rTg4510 (n=13) and treated rTg4510 animals (n=6). Hippocampal and cortical volumes were averaged in order to extract absolute and normalised volume changes in the high ranked pathology regions. The absolute volume changes within the high ranked pathology regions following (A) early and (C) late intervention are presented. In addition, the absolute volume changes were normalized to the TBV in order to extract the proportional volume changes following (B) early and (D) late intervention. A two-way ANOVA with a post-hoc Sidak multiple comparison was performed to identify significant differences between the groups. Statistically significant groups have been identified and highlighted. Error bars represent the SEM. Wildtype vs. untreated rTg4510s: ** = p≤0.01; *** = p<0.001; **** = p≤0.0001. Wildtype vs. treated rTg4510s: + = p≤0.05; ++++ = p≤0.0001. Treated rTg4510s vs. untreated rTg4510s: -- = p≤0.01; ---- = p≤0.0001.*

Figure 4.9 *TBVs for wildtype, rTg4510 and doxycycline-treated rTg4510 mice across all imaging timepoints. In order to account for the marked differences in brain volume between the mice cohorts, absolute volumes from the atlas-based parcellation were normalized to TBV in order to explore volumetric changes occurring disproportionately to alterations in brain volume. A two-way ANOVA with a post-hoc Sidak multiple comparison was performed to identify significant differences between the groups. Statistically significant groups have been identified and highlighted. Error bars represent the SEM. Wildtype vs. untreated rTg4510s: *** = p<0.001; **** = p≤0.0001. Wildtype vs. treated rTg4510s: ++ = p≤0.01; +++ = p≤0.001; ++++ = p≤0.0001. Treated rTg4510s vs. untreated rTg4510s: - = p≤0.05*

Figure 4.10 *Longitudinal volume changes in the thalamus, extracted from the high resolution structural images, following (A, B) early and (C, D) late doxycycline treatment. Results are shown for (A, C) absolute volume and (B, D) normalised volume. A two-way ANOVA with a post-hoc Sidak multiple comparison was performed to identify significant differences between the groups. Statistically significant groups have been identified and highlighted. Error bars represent the SEM. Wildtype vs. untreated rTg4510s: * = p≤0.05; ** = p≤0.01; **** = p≤0.0001. Wildtype vs. treated rTg4510s: + = p≤ 0.05; ++ = p≤ 0.01 +++ = p≤0.001. Treated rTg4510s vs. untreated rTg4510s: -- = p≤0.01; ---- = p≤0.0001.*

In order to uncover tau-specific volume changes, I also explored the normalised volume changes. Following normalisation of the absolute volumes to TBV at each timepoint, a significant volume loss was detected in the high ranked pathology regions of the untreated rTg4510 mice compared to wildtype controls at 7.5 months ($p < 0.0001$) (Figure 4.8B, D). Atrophy was detectable from 5.5 months within these mice ($p < 0.001$) illustrating the sensitivity of high resolution structural MRI to tau-specific morphological changes occurring in the rTg4510 mice (Figure 4.8B).

Following treatment with doxycycline, I observed significantly less atrophy in the treated rTg4510 mice when compared to the untreated rTg4510 mice at 7.5 months ($p < 0.0001$), following both early and late therapeutic intervention (Figure 4.8B, D). Interestingly, the atrophy within the mice treated from 3.5 months was significantly less than rTg4510 mice treated from 4.5 months: 7.0% and 12.4% volume loss respectively. These results suggest that earlier intervention was able to reduce atrophy to a greater extent.

Normalisation of the thalamus to TBV resulted in an expected (as this region suffers little tau pathology) increase in normalised thalamic volume within the rTg4510 mice compared to the wildtype controls (Figure 4.10B, D). This is due to normalisation with the decreasing TBV, leading to an apparent increase in thalamic volume over time.

4.4.3 Chemical exchange saturation transfer

Figure 4.11A shows the CEST results within the high ranked pathology regions of the rTg4510 mice following early intervention. A decrease in the APT signal was identified in the untreated rTg4510 mice relative to the wildtype controls at 7.5 months ($p < 0.01$).

Administration of doxycycline, following both early and late intervention, resulted in an increase in the APT signal towards wildtype values by 7.5 months (Figure 4.11). At this timepoint, the APT signal in the treated rTg4510 mice was not significantly different from the wildtype controls (Figure 4.11A, B). The early treated rTg4510 mice showed greater conservation: at this timepoint, both the treated rTg4510 mice and the wildtype controls were significantly different from the untreated rTg4510 mice ($p < 0.01$) (Figure 4.11A). This indicates that the APT signal may be sensitive to the suppression of pathological conformations of tau.
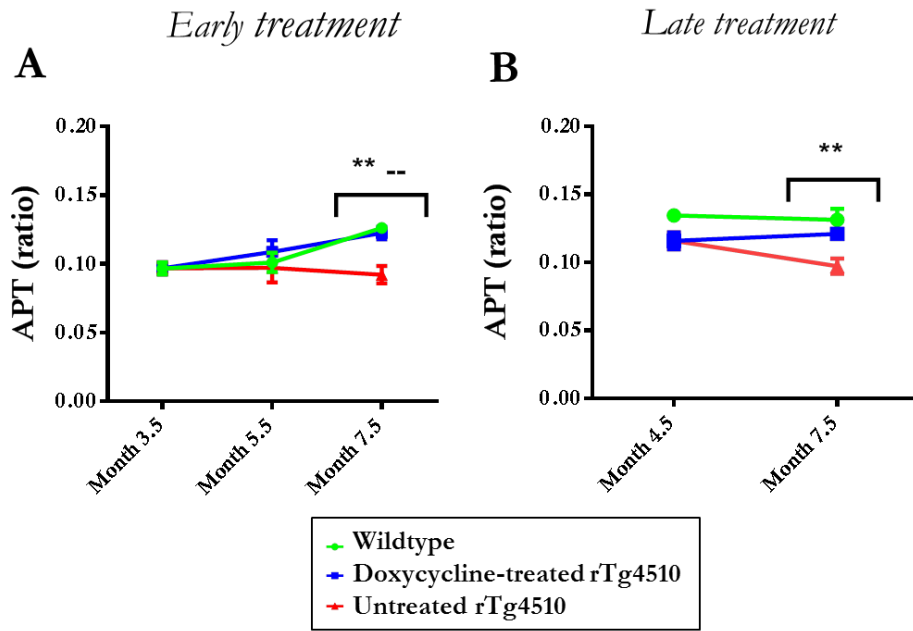
Figure 4.11 *Longitudinal CEST results from the high ranked pathology regions following (A) early and (B) late doxycycline treatment. A two-way ANOVA with a post-hoc Sidak multiple comparison was performed to identify significant differences between the groups. Statistically significant groups have been identified and highlighted. Error bars represent the SEM. Wildtype vs. untreated rTg4510s: * = p≤ 0.05; ** = p≤0.01.Treated rTg4510s vs. untreated rTg4510s: -- = p≤0.01.*

Within the thalamus, in the presence of low tau burden, the APT signal was not significantly different between the rTg4510 mice and wildtype controls (Figure 4.12). These results provide evidence in support of APT's sensitivity to tau-related pathology at later time points.
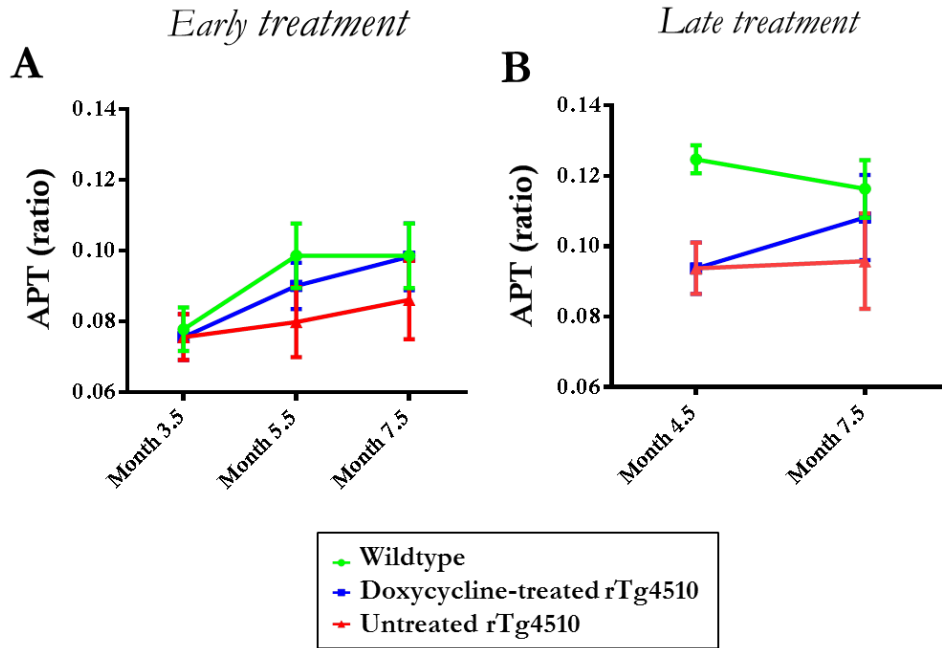
Figure 4.12 *Longitudinal CEST results from the thalamus – a region of low tau burden - following (A) early and (B) late doxycycline treatment. A two-way ANOVA with a post-hoc Sidak multiple comparison was performed to identify significant differences between the groups. No significant differences were identified between groups at any of the timepoints under investigation.*

4.4.4 Diffusion tensor imaging

DTI was employed to longitudinally investigate the microstructural changes in the grey and white matter of the rTg4510 mice. The results within the high ranked pathological grey matter tissues are shown in Figure 4.13.
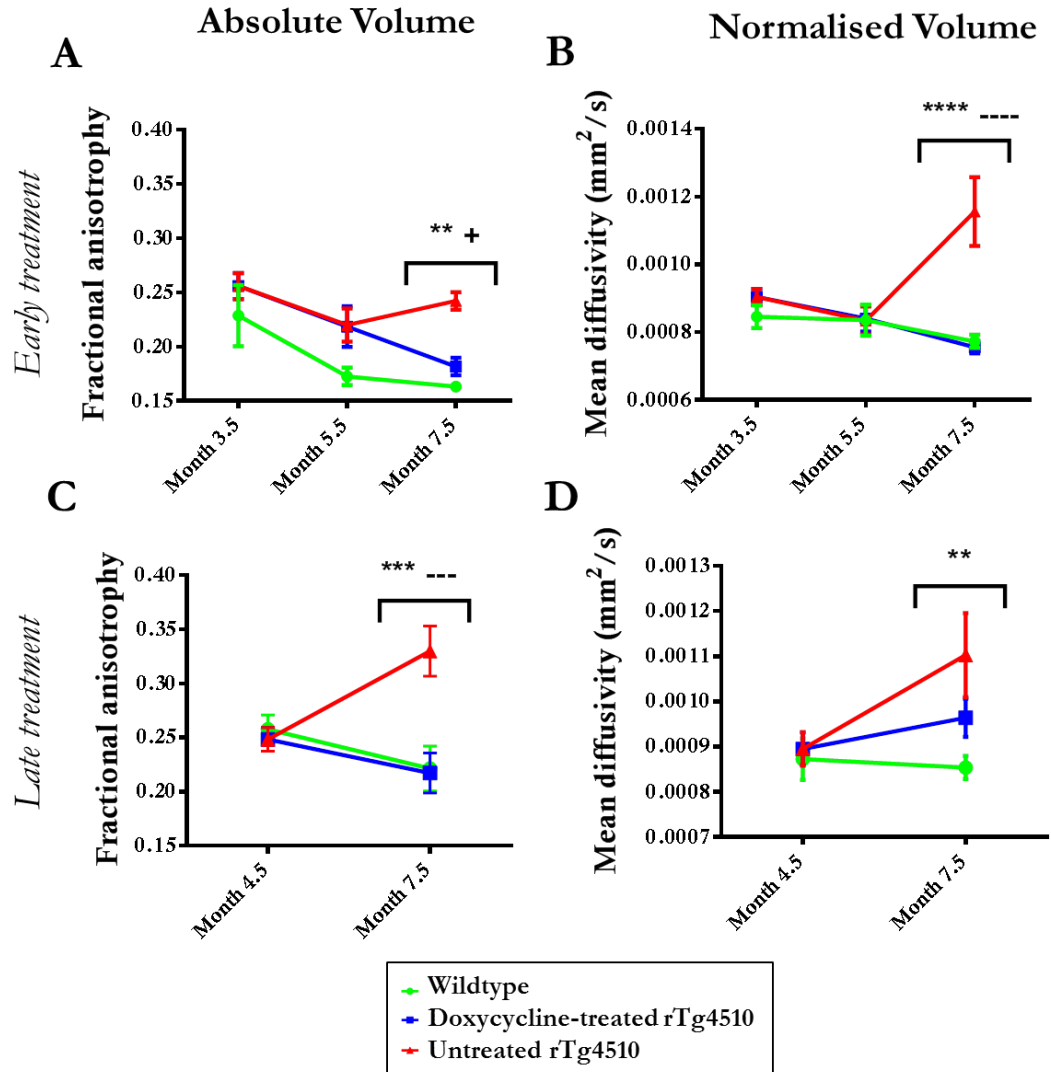
Figure 4.13 *Longitudinal (A, C) FA and (B, D) MD in the high ranked pathology regions following (A, B) early and (C, D) late doxycycline treatment. A two-way ANOVA with a post-hoc Sidak multiple comparison was performed to identify significant differences between the groups. Statistically significant groups have been identified and highlighted. Error bars represent the SEM. Wildtype vs. untreated rTg4510s: ** = p≤0.01; *** = p≤0.001; **** = p≤0.0001. Wildtype vs. treated rTg4510s: + = p≤0.05. Treated rTg4510s vs. untreated rTg4510s: --- = p≤0.001; ---- = p≤0.0001.*

At 7.5 months, the untreated rTg4510 mice exhibited increased FA and MD, with both parameters able to discriminate between the untreated rTg4510 mice and wildtype controls (Figure 4.13A-D). Interestingly, at earlier timepoints neither FA (Figure 4.13A, B) nor MD (Figure 4.13C, D) were able to distinguish between the rTg4510 mice and wildtype controls, suggesting that detectable changes in these DTI parameters occur downstream from the formation of tau lesions from 4 months.

Following early treatment with doxycycline, I observed no significant differences with control values of MD in the treated rTg4510 mice (Figure 4.13C, D). In this instance, MD readily discriminates between the treated and untreated rTg4510 mice (p<0.0001) as well as the untreated rTg4510 mice and wildtype controls (P<0.0001) at 7.5 months. Following late treatment, I saw a similar pattern of results (Figure 4.13C, D: 7.5 months). In particular, I observed good discrimination in FA between treated and untreated rTg4510 mice (p<0.001). In contrast the thalamus presented with comparatively few significant differences in DTI parameters between the cohorts in both longitudinal studies (Figure 4.14).

The RD results for the white matter region in the corpus callosum are shown in Figure 4.15. The findings of increased RD in the rTg4510 mice are consistent with previous findings in this model (*223*). The mean RD in the treated group was less than the untreated group at 7.5 months in both longitudinal studies and showed a trend towards wildtype values, however these differences were non-significant (Figure 4.15). Similarly to FA and MD (Figure 4.13, Figure 4.14), RD is not able to distinguish between the rTg4510 mice and wildtype controls at earlier timepoints, further reinforcing the observations that the DTI parameters may not be sensitive to early neuropathology in this model. Taken together, the pattern of FA, MD and RD results suggest that these DTI parameters are sensitive to more downstream events following suppression of the tau transgene.
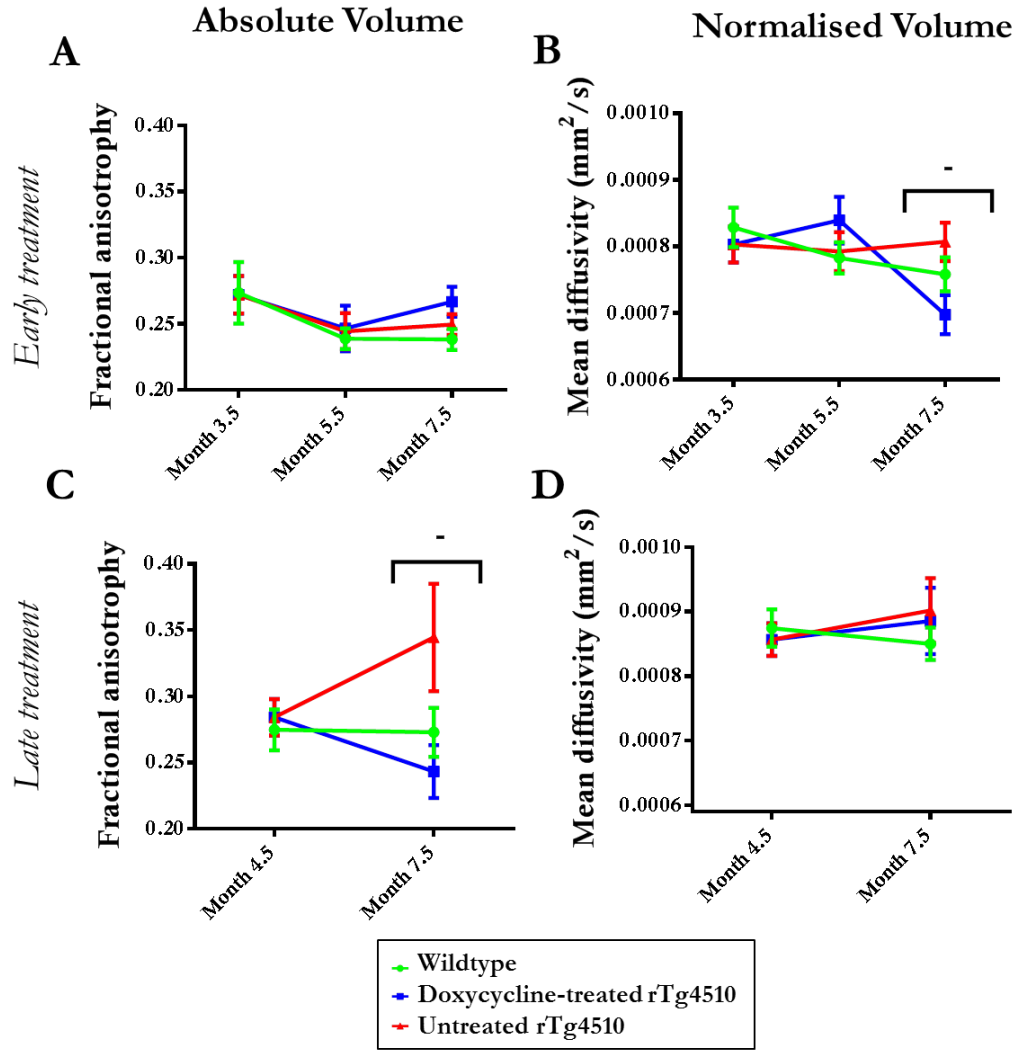
Figure 4.14 *Longitudinal (A, C) FA and (B,D) MD in the thalamus following (A, B) early and (C, D) late doxycycline treatment. A two-way ANOVA with a post-hoc Sidak multiple comparison was performed to identify significant differences between the groups. Statistically significant groups have been identified and highlighted. Error bars represent the SEM. Treated rTg4510s vs. untreated rTg4510s: - = p≤0.05.*
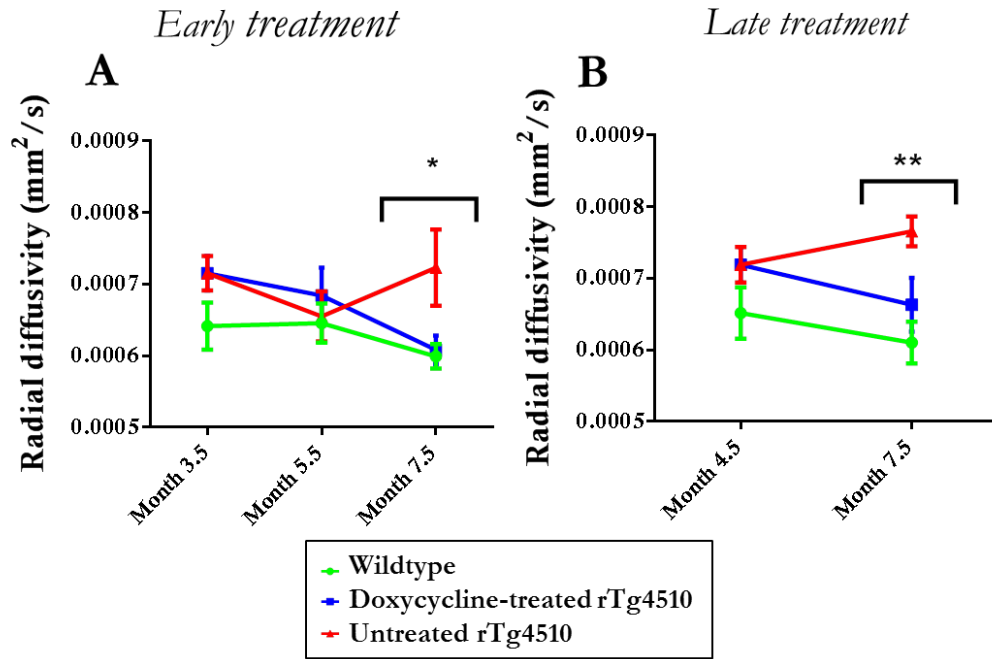
Figure 4.15 *Longitudinal RD in the corpus callosum following (A) early and (B) late doxycycline treatment. A two-way ANOVA with a post-hoc Sidak multiple comparison was performed to identify significant differences between the groups. Statistically significant groups have been identified and highlighted. Error bars represent the SEM. Wildtype vs. untreated rTg4510s: * = $p \leq 0.05$; ** = $p \leq 0.01$.*

4.4.5 Arterial spin labelling

ASL was employed to measure CBF in the rTg4510 mice. The results within the high ranked pathology regions, following early and late therapeutic intervention, are shown in Figure 4.16.

In the late treatment group, I detected significant elevation in CBF in the rTg4510 mice compared to the wildtype controls ($p<0.0001$) (Figure 4.16B: 4.5 and 7.5 months). Unexpectedly, this observation was not replicated in the early treatment group (Figure 4.16A). This discrepancy may be due to subtle differences in the concentration of isoflurane, a vasodilator, between the two animal cohorts (1.5%) (*224, 225*).
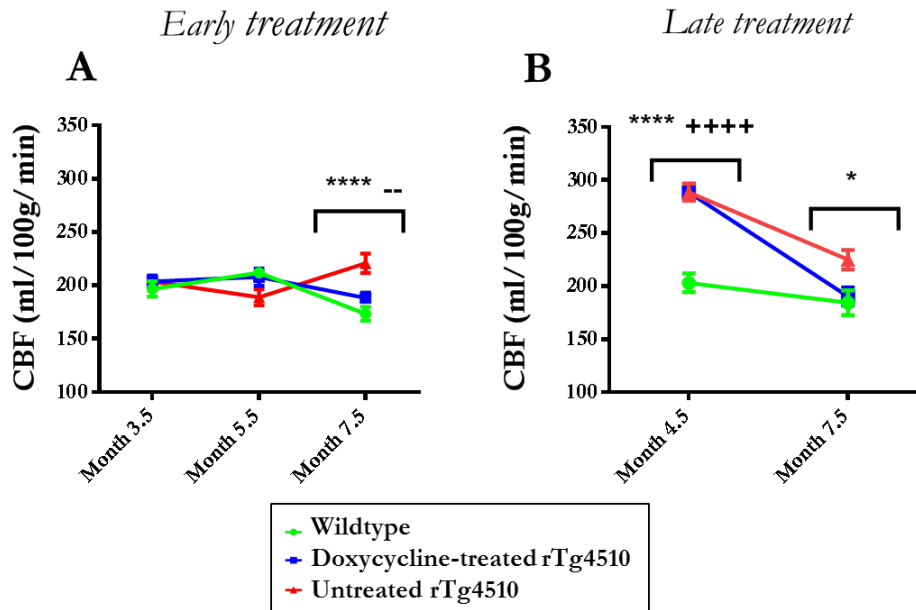
Figure 4.16 *Longitudinal CBF results from the high ranked pathology regions following (A) early and (B) late doxycycline treatment. A two-way ANOVA with a post-hoc Sidak multiple comparison was performed to identify significant differences between the groups. Statistically significant groups have been identified and highlighted. Error bars represent the SEM. Wildtype vs. untreated rTg4510s: * = p≤0.05; **** = p≤0.0001. Wildtype vs. treated rTg4510s: ++++ = p≤0.0001. Treated rTg4510s vs. untreated rTg4510s: -- = p≤0.01.*

I endeavoured to maintain consistency in the experimental set-up between imaging timepoints; this included executing the ASL sequence within the first 30 minutes of the imaging protocol, in order to reduce complications due to prolonged anaesthesia. Despite my best efforts, I believe that mis-calibration of the isoflurane vaporiser may have resulted in differences in the depth of anaesthesia. In order to investigate this hypothesis further, my collaborator at the UCL Centre for Advanced Biomedical Imaging acquired CBF measurements at increasing concentrations of isoflurane in a separate cohort of aged rTg4510 mice (9 months) and wildtype controls.
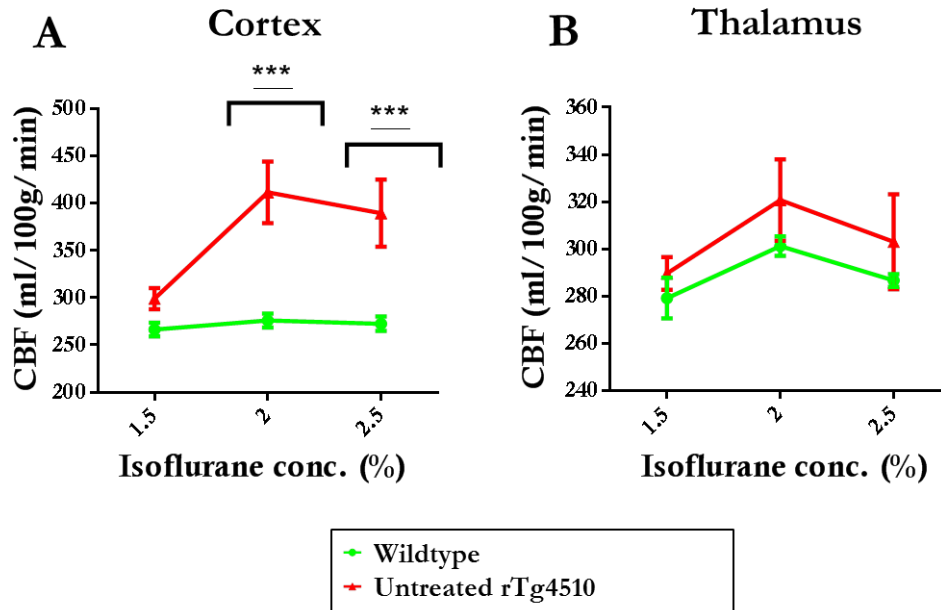
Figure 4.17 *CBF results within the (A) cortex and (B) thalamus at different concentrations of isoflurane. A two-way ANOVA with a post-hoc Sidak multiple comparison was performed to identify significant differences between the groups. Statistically significant groups have been identified and highlighted. Error bars represent the SEM. Wildtype vs. untreated rTg4510s: *** = p≤0.001.*

A marked increase in cortical CBF (high tau region) was observed when the isoflurane concentration was increased from 1.5 to 2% in the rTg4510 mice. This increase was not observed in the thalamus (low tau region) (Figure 4.17). These results support the hypothesis that CBF in the rTg4510 mice is dependent on the concentration of administered isoflurane, and may indicate that high ranked tau pathology regions are more vulnerable to isoflurane-driven hyperperfusion, as no significant increases in CBF were observed in the thalamus.

4.5 Discussion

As the incidence of Alzheimer's disease continues to rise to epidemic proportions, it is crucial that biomarkers of neurodegeneration are developed, to aid early diagnosis of the disease and facilitate drug development. The recent failure of several Phase III clinical trials targeting amyloid-β production or aggregation(*33*) has resulted in a surge of interest for tau-mediating therapies.(*226*) Tau plays an undeniable role in neurodegeneration; the spreading of tau pathology throughout the AD brain follows a hierarchical pattern which reflects the degree of cognitive impairment.(*227, 228*) In order to evaluate the efficacy of tau-targeting therapies, robust biomarkers which are sensitive to tau pathology are required. In this work, I report the first application of imaging biomarkers, including structural MRI, ASL, DTI and APT, in a longitudinal study of neurodegeneration in the rTg4510 mouse model of tauopathy. The rTg4510 mouse exhibits key cognitive and neuropathological features of the human condition, including early tau burden in the forebrain from 4 months, neuronal loss and marked atrophy within the forebrain (*114*). In addition, the rTg4510 mice provide an excellent platform to assess the sensitivity of the different MRI techniques, as the expression of tau can be effectively regulated with doxycycline.

In this work, I report the first application of multi-parametric MRI biomarkers, including structural MRI, ASL, DTI and APT, in a longitudinal study of neurodegeneration in the rTg4510 mouse model of tauopathy.

Histological evaluation of pathological tau revealed a distinct pattern of regional severity, with high deposition within the cortex and hippocampus, and milder affliction of the thalamus as previously observed in Chapter 3. Treatment with doxycycline dramatically reduced the amount of PG-5 positive neurons in all the regions analysed, through deactivation of the promoter within the transgene which drives tau expression and subsequent NFT formation (*114*). Although observed in both treatment groups the effect of doxycycline were more marked in the hippocampus and thalamus of the early (3.5 month) treatment group, suggesting that the transgene was repressed before the accumulation of significant tau pathology. These histological results illustrate the efficacy of the doxycycline intervention for reducing tau accumulation. I sought to exploit the dynamic range in tau accumulation, between early- and late- doxycycline treated and vehicle treated rTg4510 mice, and assess the sensitivity of MRI biomarkers to the development and suppression of pathological tau.

Structural MRI is now routinely employed in large-scale longitudinal studies of AD patients such as ADNI, which aims to identify early biomarkers and evaluate emerging AD intervention (*179*). It has been hypothesised that MR-detectable structural changes may precede cognitive impairment in AD, supporting the clinical utility of this technique for early diagnosis. In this work, I applied the previously optimised structural sequence in order to evaluate neurodegeneration in the rTg4510 mice. TBM was employed to detect morphological changes, in addition to atlas-based parcellation to explore regional volume differences. Both of these image processing techniques offers an unbiased estimation of brain atrophy, and eliminates the need for time-consuming manual methods for structural data analysis (*211*).

The TBM results identified gross structural changes within the rTg4510 brains, including extensive atrophy within the cortex. Gross morphometric changes in the late stage of the disease were previously described in Chapter 3, and substantiate my current imaging and histological findings (*157, 229*). These changes are markedly reduced following treatment with doxycycline, suggesting that structural MRI is sensitive to the suppression of pathological tau in this model. The atlas-based parcellation results provided quantitative regional volume estimates, with detectable atrophy occurring within the high ranked pathology regions of the rTg4510 mice from 3.5 months. However, this volume difference was also seen in the thalamus (low ranked pathology), indicating that this difference could be due to either neurodevelopmental effects of transgene expression during prenatal development, or brain alterations and compensation in response to the forebrain atrophy. Normalising the absolute volumes to TBV revealed a pattern of atrophy that is specific to tau pathology, and accounts for the early global changes in brain volume. The normalised volume data revealed deterioration of the high ranked pathology regions detectable at 5.5 months, proceeding the development of NFTs within the cortex from 4 months (*114*). I also observed a reduction in atrophy within rTg4510 mice treated with doxycycline; this was more apparent when treatment began at the earlier timepoint of 3.5 months. Normalising the absolute volumes to total intracranial volume instead of TBV may mitigate the proportional increases observed within tissues unaffected by tau pathology.

These results suggest that the presence of pathological tau underpins the key structural changes seen in this model. In addition to detectable volume losses within areas expressing high tau burden, the suppression of the tau transgene resulted in markedly

reduced atrophy, which correlates with the reduction of PG-5 positive cells in the high ranked pathology regions.

My findings support the application of structural MRI as a close correlate of tau pathology, where it has already garnered clinical acceptance (*230*). In addition, I believe that structural MRI may serve as a valuable biomarker for assessing therapies targeting the production or clearance of pathological tau and the associated neurodegeneration and volume loss.

CEST is a comparatively new technique for measuring the exchange water protons in bound and free states (*231*). The amide proton pool can be selectively saturated using an off-resonance RF pulse, permitting the APT signal to be calculated. APT imaging is more commonly used for imaging brain tumours (*232, 233*) owing to its sensitivity to changes in protein expression in malignant tissues (*234*). In this work, a reduction in the APT signal in high ranked pathology regions within the rTg4510 mice compared to wildtype controls was observed at 7.5 months. These changes may be caused by the presence of neuronal tau pathology, impairing the chemical exchange between the amide protons and water protons (*229*). No significant differences were observed within the thalamus, where tau pathology was notably mild, further supporting this interpretation.

While CEST aims to provide a direct measure of proton exchange, it is highly sensitive to changes in tissue pH. Acidification of the brain of AD patients has already been observed (*235*) and attributed to the accumulation of acidic metabolites and a breakdown in the brain's ability to maintain a constant internal pH. The decreased APT signal within the rTg4510 mice may therefore also reflect changes in tissue pH within the high ranked pathology regions. A separate study employing ^{31}P magnetic resonance spectroscopy would determine whether there was a pH change in the rTg4510 animals (*236*).

Isoflurane anaesthesia is not believed to alter tissue pH (*237, 238*), although the implications following prolonged anaesthesia have yet to be explored. In order to mediate any isoflurane-related changes in tissue pH, the CEST acquisition was performed at the beginning of the imaging protocol.

In addition to pH, the APT signal can also be influenced by the cellular water content, and the T_1 relaxation time of the bulk tissue water (*239*). It is also worth noting that

APT imaging is highly sensitive to B_0 and B_1 field in homogeneities, especially when applied to *in vivo* imaging data at high magnetic field strengths (*240*).

It is difficult to elucidate one underlying factor which is causing the APT signal changes in this model; regardless, these results illustrate the sensitivity of measures of APT to tau-related pathology in this model and may reflect neurodegenerative processes. In particular, it may serve as an important biomarker when assessing the efficacy of novel therapeutics targeting pH-sensitive pathways, such as neuronal transmitters (*44*).

DTI is increasingly being employed in longitudinal studies of AD (*241, 242*). It can offer heightened sensitivity to changes in grey and white matter integrity, which are not so readily detectable using structural MRI. It is believed that DTI changes may precede volume changes in AD, and therefore may represent an important early biomarker of the disease with enhanced sensitivity to early microstructural changes. (*243*)

RD is a valuable DTI parameter which reflects diffusion perpendicular to the primary direction in a voxel, which may reflect fibre orientation in the white matter. My observation of increased RD in the corpus callosum mimics the clinical picture (*244*) and has been previously observed in the rTg4510 mouse (*229*). Demyelination has been cited as a possible mechanism underpinning this change (*223, 245*). This is supported by previous work in the rTg4510 mouse, where electron microscopy revealed swollen unmyelinated processes in the corpus callosum from 4 months (*223*). No axial diffusivity changes have been observed in this model, suggesting that demyelination is occurring in the absence of axonal injury (*217*). Alterations in RD were not significantly different until the final imaging timepoint at 7.5 months; my observations therefore suggest that RD may be sensitive to downstream events proceeding the accumulation of pathological tau and unmyelinated processes from 4 months (*114*). Treatment with doxycycline marginally reduced the RD changes; however, there was no marked improvement in this parameter when treatment was commenced earlier.

Whilst DTI is traditionally used to characterise white matter structures, it can also be applied to fibre-rich grey matter structures such as the hippocampus.(*246*) FA and MD were extracted to investigate the high ranked pathology regions of the cortex and hippocampus. The observation of increased FA within the rTg4510 mice was unexpected, as this traditionally implies more intact axons. However, the phenomenon of increased FA in brain regions undergoing gross degenerative processes has

previously been observed (*247*), and may suggest increased disruption and loss of isotropic cells (*247*). Meanwhile, the observation of increased MD in the rTg4510 mice mimics the clinical condition (*248, 249*); this change is believed to indicate enlargement of the extracellular space, suggesting neurodegeneration is occurring (*249, 250*).

Similarly to the RD results, FA and MD in the high ranked pathology regions were only able to discriminate between the rTg4510 mice and wildtype controls at the final imaging timepoint. However, these parameters offered heightened sensitivity to the doxycycline treatment. Following early- and late-stage treatment, recovery of both FA and MD was observed, suggesting that the presence of pathological tau is underpinning these DTI changes. I observed greater recovery of MD following early treatment with doxycycline, suggesting that MD may be more sensitive to suppression of pathological tau.

While it has been claimed that microstructural changes detectable using DTI may precede structural changes,(*251*) my results do not support this hypothesis for this model. Increased FA, MD and RD in the rTg4510 mouse were only detectable at 7.5 months, in the presence of significant atrophy and tau burden at this timepoint. I therefore propose that the strength of DTI may not lie in its ability to discriminate between rTg4510 mice and wildtype controls; rather, it offers valuable information that may compliment the structural MRI results. This may be particularly beneficial when assessing therapeutic efficacy of treatments which target pathways for which DTI offers heightened sensitivity.

There is growing evidence supporting the role of CBF as a biomarker of AD (*252*). The vascular hypothesis for AD stipulates that underlying vascular factors such as hypertension, diabetes and obesity may substantially contribute to the development of AD pathogenesis (*253, 254*). Measurements of CBF therefore may represent an important biomarker in the early diagnosis of AD, and for evaluation of therapies which may produce a vascular response (*255*). CBF differences have already been observed in AD patients using ASL, with decreased perfusion in cortical regions affected by the disease.(*252*)

Previous observations in the rTg4510 mouse identified a distinct pattern of hyperperfusion in the cortical and hippocampal regions in an advanced stage of the pathology (*229*). In the late intervention group, I noted distinct hyperperfusion,

consistent with this previous work although this was not replicated in the early treatment group. To understand this further, the effects of the anaesthetic isoflurane in the rTg4510 mouse were investigated. I hypothesized that these discrepancies may be due to differences in the concentration of administered isoflurane, a volatile anaesthetic which causes a dose-dependent increase in CBF (*225*). This theory was supported by evidence of hyperperfusion at high concentrations of isoflurane.(*224*) Interestingly, when the mice were challenged with a higher concentration of isoflurane, the regions of high tau pathology responded with a marked increase in CBF; this was much less evident in the wildtype controls. Although it is unclear why this is the case, a recent work demonstrates that the rTg4510 mouse has increased cerebrovascular response (CVR) (*256*), which could suggest that elevated levels of blood CO_2 due to the reduced respiration rate that accompanies increased delivery of isoflurane, may result in the increased CBF. Similar results have recently been observed in a bigenic mouse model of AD, where increased CVR in response to hypoventilation was reported (*257*). Furthermore, the sensitivity of the rTg450 mouse to increased isoflurane concentration may be due to a breakdown in autoregulation (*258*), a mechanism which may be affected as a result of tau pathology, leading to vascular compensation and the increase in CBF, although the precise mechanism is still unknown (*256*).

A number of additional rodent studies have reported cortical hypoperfusion using ASL in conjunction with isoflurane anaesthesia at varying concentrations: 1-1.5% (*259*), 1.5-2% (*260*) and 2% (*261*). However, these studies all focus on models exhibiting amyloid pathology. In this study, the observation of hyperperfusion at high concentrations of isoflurane may be unique to the rTg4510 mouse, and reflect a tau-related effect. Despite the complexity surrounding CBF measurements, at higher concentrations of isoflurane complete discrimination of the rTg4510 mice from wildtype controls was observed. However, careful calibration of administered anaesthetic gases may be required in future studies in order to extract meaningful longitudinal CBF measurements in the rTg4510 mouse.

Previous work in the rTg4510 mouse at 8.5 months indicated that hyperperfusion and increased MD was detectable in regions of low tau pathology (the thalamus of the rTg4510 [mean NFT density = 2.3 cells/mm^2]). Thus these biomarkers were considered to be strong candidates for relatively early detection of tau-driven abnormalities in the cortex and hippocampus of the rTg4510. However, no differences in MD between the

wildtype and rTg4510 cohorts were detected in the high rank regions at 3.5, 4.5 or 5.5 months. Increased CBF at 4.5 months was observed in the late intervention study but this finding was not reproduced at 5.5 months in the early intervention study, likely owing to discrepancies in anaesthetic delivery between the two longitudinal studies.

4.6 Conclusion

This study demonstrates the value of non-invasive multi-parametric quantitative MRI for longitudinal assessment of tau pathology in the rTg4510 model, and monitoring distinct properties that reflect the biological responses to therapy in AD. The imaging protocol permits the acquisition of structural, ASL, DTI and CEST data in a longitudinal framework within the three hour anaesthesia tolerance of mice (*222*). Each of these techniques can be readily translatable to clinical studies, aided by ongoing efforts to standardise the sequences, enabling meaningful comparisons between sites (*262*). These diverse scans all offer complimentary information, and provide insight into different pathological mechanisms occurring within the disease process. The structural scans and analysis proved to be the earliest biomarker, in addition to offering the highest degree of sensitivity to the doxycycline treatment; however, over half of the imaging time is dedicated to the acquisition of the structural data, which should be considered upon interpretation. This data represents a platform for future longitudinal and therapeutic efficacy studies of novel therapeutic strategies that target varying aspects of the pathology time course in this model.

Chapter 5:   Is alive better than dead when investigating structural changes in transgenic mice using magnetic resonance imaging?

5.1   Aims

The preceding chapters have demonstrated the application of structural MRI for *in vivo* characterisation of the rTg4510 mouse and litter matched wildtype controls. Despite the growth of *in vivo* structural imaging to characterise mouse models of neuropathology, it is still not known whether it is best to scan a mouse alive or dead in order to maximise sensitivity to structural defects associated with disease models.

In this chapter, I have explored the trade-offs between *in vivo* and *ex vivo* imaging for morphometric characterisation of the rTg4510 mouse. I acquired structural images of the rTg4510 mice and wildtype controls *in vivo* before perfuse-fixing and scanning the same brains *ex vivo*. I also investigated cross-correlations between the TBM data and the histology.

I would like to acknowledge my collaborator Nick Powell at the UCL Centre for Medical Image Computing for developing the image processing software.

5.2   Introduction

Since Nature published the initial sequence of the mouse genome in 2002 *(263)*, there has been an exponential rise in the number of transgenic and targeted mice that have been engineered to deepen our understanding of the function of genes in human biology . An astonishing 99% of mouse genes have a homologue in humans, with great tracts of code appearing in the same order in the two genomes *(264)*. In fact, the laboratory mouse has now been hailed as the "experimental key to the human genome", partly because of the exquisite refinement with which it is possible to engineer human mutations and so model human disease. *(265)* Mice also breed well, do not appear to suffer from stress in captivity, and have a lifespan of approximately two – three years, making them a good model organism for phenotyping. Expanding our knowledge of

the operation and function of genes could ultimately lead to the development of improved and more selective therapies for the treatment of genetic diseases.

It has been estimated that to create a knock-out mouse for each of the 20,000 genes in the mouse genome, over 7 million animals will be needed to generate and characterize each of the knockout lines (*266*). This figure does not include knock-in and transgenic mice, all of which will also require characterisation in order to fully comprehend gene function.

In order to analyse increasingly complex phenotypes, robust and reproducible methods for phenotyping are required (*267*). Biochemical, behavioural, anatomical, physiological and pathological assays all contribute to understanding the true function of a gene (*268*).

Phenotyping at the macroscopic and microscopic level is traditionally carried out using histological methods. These techniques are useful for validating hypotheses and uncovering unexpected biochemical changes that accompany altered gene function. However, these techniques are terminal, invasive and limited by low throughput. Recently techniques for structural phenotyping have moved beyond the use of histology to embrace whole-body, high resolution methods of imaging. In recent years however, MRI has increasingly been employed for phenotyping transgenic mice, largely due to advances in MRI hardware and computer power, enabling sophisticated image processing techniques (*269*). Through a combination of high resolution MRI and automated computational analysis, the throughput and efficiency of the structural phenotyping of transgenic mice will significantly improve.

One of the key experimental decisions in the structural MRI of mouse neuroanatomy is whether to scan the mouse brain *in vivo* or *ex vivo* to maximise sensitivity to morphological changes with respect to wild-type controls. Imaging the animal post-mortem enables longer scan times, the use of contrast agents in high concentrations and limits motion. All of these factors can boost resolution, SNR and CNR, to support advanced computation approaches such as TBM. In addition, multiple brains can be imaged simultaneously using standard MRI hardware, thereby improving the throughput of data acquisition. Conversely, live animals do not suffer distortions and dehydration from fixation, which may disrupt the integrity of the tissues. Crucially, *in vivo* imaging permits longitudinal studies, where the same animal can be serially assessed to observe morphological and functional changes over time. This has been shown to

improve the statistical power of the results (*222*) as well as reducing the number of animals dedicated to imaging studies, compared to cross-sectional studies. *In vivo* imaging has particular relevance in preclinical drug studies, which are required before a candidate therapy can enter clinical trials.

In this chapter I have explored the sensitivity of *in vivo* and *ex vivo* structural imaging for detecting regions of structural changes in the rTg4510 mouse model of tauopathy (*114*). This mouse has been extensively characterized using *in vivo* structural MRI in the preceding chapters as well as within the literature, where gross atrophy of the forebrain regions has been observed (*157, 229*). In this chapter, I sought to investigate the morphological differences that can be detected in either *in vivo* or *ex vivo* structural MRI using an automated TBM pipeline for high throughput analysis of neuroanatomy in the mouse brain. TBM has previously been applied to a number of clinical disorders, including epilepsy (*270*) and Alzheimer's disease (*180, 271, 272*), and has recently been applied to both *in vivo* and *ex vivo* structural mouse brain data sets, as detailed in Chapter 3 (*154, 155, 194-202*).

As described in Chapter 4, the rTg4510 mouse offers a novel paradigm to support our investigation as the overexpression of tau can be inactivated by the administration of doxycycline. Therefore in addition to characterising the gross morphological differences between the transgenic and wildtype animals, I also sought to identify the structural changes occurring in a subset of doxycycline-treated rTg4510 mice using both *in vivo* and *ex vivo* structural MRI.

5.3 Methods

5.3.1 Transgenic animals

Generation of homozygous rTg4510 transgenic mice has been reported previously (*114*). rTg4510 mice were licensed from the Mayo Clinic (Jacksonville Florida, USA) and bred for Eli Lilly by Taconic (Germantown, USA). Mice were imported to the UK for imaging at the Centre for Advanced Biomedical Imaging, UCL, London. All studies were carried out in accordance with the United Kingdom Animals (Scientific Procedures) Act of 1986 and subject to review by the UCL internal ethics committee.

In this study, 11 female wildtype and 19 female rTg4510 litter-matched control mice were imaged both *in vivo* and *ex vivo* at 7.5 months of age. Of the 19 rTg4510 animals, 6 were fed with Doxycycline mixed chow from 4.5 months to suppress the overexpression of tau. These mice formed the 'late' intervention cohort, as described in Chapter 4.

5.3.2 Magnetic resonance imaging

All imaging was performed using a 9.4T VNMRS horizontal bore scanner (Agilent Inc.). The key differences between the *in vivo* and *ex vivo* are outlined in Table 5.1.

Table 5.1 *Summary of the key differences between in vivo and ex vivo imaging protocols.*

	In vivo	*Ex vivo*
Sequence	Fast spin echo	Gradient echo
Weighting	T_2-weighted	T_2*-weighted
Resolution	150 μm	40 μm
Imaging coil	Volume coil transmit/4 channel surface coil receive	Volume coil
Imaging time	1 h 30 mins	11 h 24 mins
No. of subjects imaged per acquisition	1	3
Averages	1	6
Contrast agent?	N	Magnevist

For *in vivo* imaging, mice were placed in an induction box before anaesthesia was induced using 2% isoflurane at 1 l/min in 100% O_2 Mice were subsequently positioned in a MRI-compatible head holder to minimise motion artefacts. Anaesthesia was maintained throughout imaging using 1.5% isoflurane at 1 l/min in 100% O_2 delivered via a nose cone g, which permitted spontaneous breathing of the mice. Core temperature and respiratory rate were monitored using a rectal probe and pressure pad respectively (SA instruments). Mice were maintained at ~37°C using heated water tubing and a warm air blower with a feedback system (SA instruments).

5.3.3 *In vivo* structural imaging

A 120 mm diameter imaging gradient set (SGRAD 205/120/HD/S, Agilent Technologies UK Ltd., Berkshire, UK) was used. A 72 mm birdcage RF coil was employed for RF transmission and a quadrature mouse brain surface coil (RAPID, Germany) was used for signal detection. Tuning and matching of the coil was performed manually. Shimming was performed across the mouse brain prior to image acquisition.

High resolution structural scans were acquired using the sequence optimised in Chapter 3. Briefly, a T_2-weighted, 3D FSE sequence was implemented with the following parameters: FOV = 19.2 mm × 16.8 mm × 12.0 mm; resolution = 150 μm × 150 μm × 150 μm; TR = 2500 ms, TE_{eff} = 43 ms, ETL = 4; NSA = 1. Total imaging time was approx. 1 h and 30 mins.

5.3.4 Perfusion fixation

The perfusion fixation protocol for the preparation of tissues for histological evaluation was previously described in Chapter 3.3.6. In this work, the protocol was adapted in order to prepare the brains for high resolution contrast-enhanced *ex vivo* scanning. Briefly, animals were terminally anaesthetised following *in vivo* scanning before being intracardially perfused through the left ventricle of the heart: first with 15 – 20 mL of saline (0.9%) and heparin; second with 50 mL of buffered formal saline (10%) doped with 8 mM Magnevist, at a flow rate of 3 mL per minute. Following perfusion, the animal was decapitated, defleshed, and the lower jaw removed. All brains were stored in-skull at 4 °C and soaked in buffered formal saline (10%) doped with 8 mM Magnevist for 9 weeks prior to *ex vivo* scanning (*140*).

5.3.5 *Ex vivo* structural imaging

An imaging gradient set with a 60 mm inner diameter (SGRAD 115/60/HD/S, Agilent Technologies UK Ltd., Berkshire, UK) was used. A 35L mm birdcage RF coil was employed for RF transmission and signal detection. Tuning and matching of the coil was performed manually.

A custom-build three brain holder was used to acquire high resolution *ex vivo* images of multiple brains simultaneously. A 3D GE sequence was implemented for structural imaging with the following parameters: FOV = 32 mm × 25 mm × 25 mm; resolution

= 40 μm × 40 μm × 40 μm; TR = 17 ms; TE = 4.54 ms; flip angle = 51°; NSA= 6. Total imaging time was 11 h 36 minutes (*140*).

Following *ex vivo* scanning, all brains were dispatched for histology.
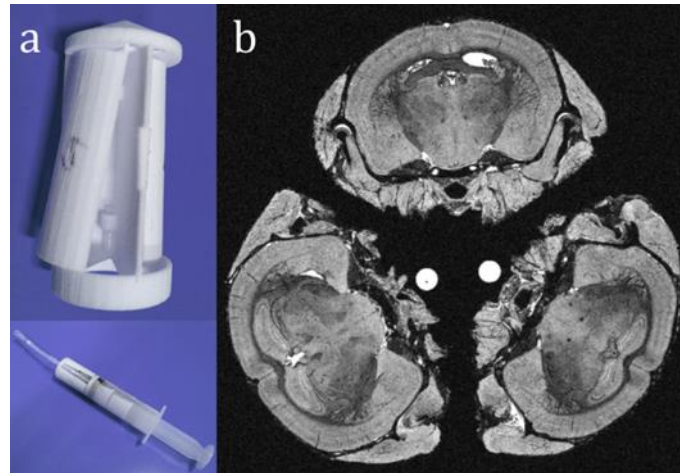
Figure 5.1 (A) *Custom 3D-printed three brain holder, which was engineered to fit inside a 50 mL syringe. (B) Representative MRI image, showing three brains scanned simultaneously. The hyperintense spheres are markers which aid identification of the brains in post-processing.*

5.3.6   Image processing

In vivo and *ex vivo* MR images were reconstructed using custom software written in MATLAB. As described in Chapter 3.3.8, a previously published calibration protocol (*165*) was used to adjust volume estimates to correct for scaling errors caused by the imaging gradients.

5.3.7   Tensor-based morphometry

TBM was performed by my collaborators at the UCL Centre for Medical Image Computing, using the methods previously detailed in Chapter 3.3.9. Briefly, the *in vivo* structural images were automatically oriented to a standard atlas space, non-uniformity corrected, skull-stripped and intensity-standardised. This was followed by 1 iteration of rigid registration, 4 iterations of affine registration and 15 iterations of non-rigid registration, to align equivalent voxels between subjects. The determinant of the Jacobian matrix was calculated at each voxel of the resulting deformation fields which

was subsequently smoothed, before statistics were performed at each voxel in order to compare groups. The resulting statistical parametric maps were corrected for multiple tests using the FDR (*169*); q=0.05).

5.3.8   Deformation maps

To measure the degree of local variability between *ex vivo* and *in vivo* images, my collaborators at the UCL Centre for Medical Image Computing registered each *ex vivo* brain to its corresponding *in vivo* counterpart, and calculated the mean positional distance (MPD) at each voxel, after resampling the resulting deformation fields into the *in vivo* brains' average space. The magnitude of the 3D vectors was calculated and the mean found over all N deformation fields, i:

$$MPD \ (voxel) = \frac{1}{N} \sum_{i=1}^{N} \sqrt{x_i^2 + y_i^2 + z_i^2}$$

where x, y, z are the vector components from the non-rigid registration only (excluding rigid and affine).

5.3.9   Signal-to-noise and contrast-to-noise ratio calculations

SNR and CNR were calculated as described previously, using Equation 3.2 and 3.3. Signal was taken from ROIs including: caudate putamen, cerebellum, corpus callosum, cortex, hippocampus, hypothalamus, olfactory bulb, midbrain and thalamus. The noise ROI was placed in a ghost-free region of background signal. Noise was defined as the SD of the background signal.

5.3.10   Histology and immunohistochemistry

Histology was performed by my collaborators at Eli Lilly. Brain samples were processed using a Tissue TEK® VIP processor (GMI Inc, MN USA). After processing, sections were embedded in paraffin wax to allow coronal brain sections to be cut. Serial sections (6 - 8μm) were taken using HM 200 and HM 355 (Thermo Scientific Microm, Germany) rotary microtomes.

Immunohistochemistry (IHC) was performed using a primary antibody for tau phosphorylated at serine 409 (PG-5; 1:500 from Peter Davies, Albert Einstein College

of Medicine, NY, USA) and the neuronal marker NeuN (1:500 from Millipore; MAB377). Following de-paraffinisation and rehydration of the tissue sections, antigen retrieval was performed using the Lab Vision PT module system (Thermo Scientific), where sections were heated to 100°C for 20 min in citrate buffer (TA-250-PM1X; Thermo Scientific). Slides were transferred to a Lab Vision Autostainer (Thermo Scientific) where the following incubations were performed: 10 min in H_2O_2 (0.3%); 30 min in normal goat serum (1:20; Vector Laboratories); 60 min in primary antibody; 30 min in biotinylated goat anti-mouse IgG (1:200, BA9200; Vector Laboratories); 30 min avidin-biotin complex solution (PK-7100; Vector Laboratories); 5 min in 3,3'-diaminobenzidine (SK-4105; Vector Laboratories). Apart from the last two steps, PBS with 0.05% Tween-20 (PBS-T) was used for diluting reagents and washes between steps. Sections were then counterstained with haematoxylin before dehydration and cover-slipping.

To quantify the density of PG-5 and NeuN positive neurons, stained sections were digitised using the Scanscope AT slide scanner (Aperio) at 20× magnification. Imagescope software (version 11.1.2.780; Aperio) was used to view the digitised tissue sections and delineate the boundaries of the cortex. PG-5 positive cells were manually counted within the delineated region and NeuN positive cells were quantified using a nuclear detection algorithm (Imagescope, version 11.1.2.780; Aperio); both were expressed as a percentage of the total area. These analyses were performed in a blinded fashion.

5.4   Results

5.4.1   Signal-to-noise and contrast-to-noise measurements

In order to explore quantitative differences in image quality between the *in vivo* and *ex vivo* images, SNR and CNR measurements were taken and averaged for 3 representative wildtype animals. Table 5.2 shows the mean SNR values for *in vivo* and *ex vivo* mouse brains.

I observed a significant increase in SNR of the *in vivo* images compared to the *ex vivo* images in 7 of the 9 regions under investigation, including: caudate putamen ($p \leq$ 0.001), corpus callosum ($p \leq$ 0.0001), cortex ($p \leq$ 0.01), hippocampus ($p \leq$ 0.0001), olfactory bulb ($p \leq$ 0.05), midbrain ($p \leq$ 0.01) and thalamus ($p \leq$ 0.01). Meanwhile, the

SNR *ex vivo* was significantly increased in the cerebellum ($p \leq 0.05$). However it is important to note that SNR is highly dependent on spatial resolution, so the increased SNR in the *in vivo* data is likely to be due to the greater voxel sizes of the *in vivo* data.

Conversely, I observed a three-fold increase in CNR between the grey (cortex) and white matter (corpus callosum) structures in the *ex vivo* images compared to CNR measured *in vivo* ($p \leq 0.01$).

Table 5.2 *Mean (± SD) SNR and CNR for in vivo and ex vivo wildtype mouse brains.*

Region	SNR		P value
	In vivo (n=3)	*Ex vivo* (n=3)	
Caudate putamen	14.4 ± 1.7	9.3 ± 1.1	≤0.001
Cerebellum	7.6 ± 0.9	11.4 ± 0.6	≤0.05
Corpus callosum	15.6 ± 0.6	4.2 ± 0.7	≤0.0001
Cortex	14.2 ± 1.4	10.0 ± 0.8	≤0.01
Hippocampus	19.3 ± 1.2	10.8 ± 0.8	≤0.0001
Hypothalamus	11.2 ± 1.2	11.5 ± 0.7	ns
Olfactory bulb	14.8 ± 1.9	10.9 ± 1.1	≤0.05
Midbrain	11.1 ± 1.2	6.9 ± 0.6	≤0.01
Thalamus	12.4 ± 1.5	7.8 ± 1.0	≤0.01
CNR	1.5	5.8	≤0.01

5.4.2   Total brain volumes

It has previously been reported that formalin fixation causes tissue shrinkage (*154, 222, 273*) which may be a confounder in our *ex vivo* MRI analysis, particularly if this shrinkage is inhomogeneous across structures. In order to investigate the changes in brain morphometry occurring due to formalin fixation, my collaborators at the UCL Centre for Medical Image Computing extracted TBVs for the *in vivo* and *ex vivo* mouse brain specimens using a previously published segmentation protocol (*211*).
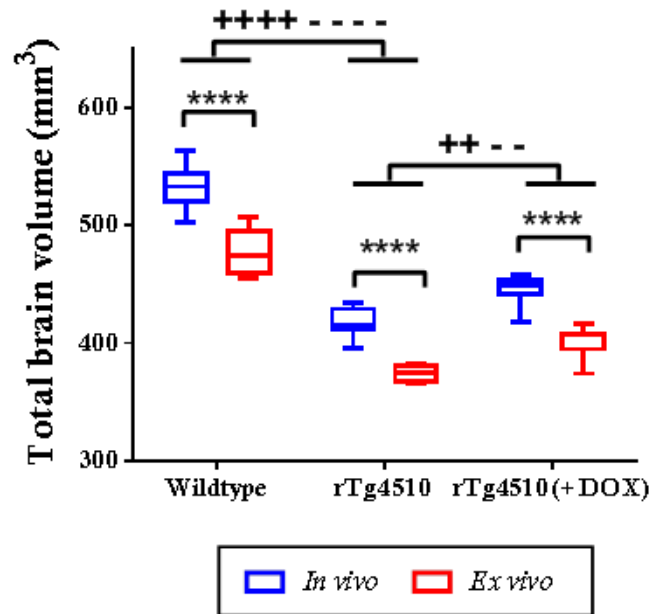
Figure 5.2 *In vivo and ex vivo TBVs for wildtype, rTg4510 and rTg4510(+DOX) animals. In vivo vs. ex vivo comparisons: **** = p ≤ 0.0001. In vivo TBV comparisons: ++ = p ≤ 0.01; ++++ = p ≤ 0.0001. Ex vivo TBV comparisons: - - = p ≤ 0.01; - - - - = p ≤ 0.0001.*

A significant reduction in *ex vivo* TBV in comparison to the corresponding *in vivo* TBV was observed (p ≤ 0.0001) (Figure 5.2). Tissue shrinkage in post-mortem specimens has been previously been observed and attributed to dehydration of the tissues (*274*). In this work, I stored the *ex vivo* brains in gadolinium-doped formalin for 9 weeks, to enable the contrast agent sufficient time to diffuse uniformly across the tissues (*140*). Despite this discrepancy in the *ex vivo* TBVs, I observed that the degree of shrinkage was consistent across the wildtype controls (10.3%), rTg4510 mice (10.4%) and doxycycline-treated rTg4510 mice (10.1%). I therefore do not anticipate tissue shrinkage to confound group comparisons of ex-vivo structural MRI data.

In addition to identifying significant shrinkage of the tissues during the fixation process, the TBV results identified gross differences in TBV of the wildtype mice when compared to the rTg4510 mice (p ≤ 0.0001) and the doxycycline-treated rTg4510 mice (p ≤ 0.01) (Figure 5.2). The differences were consistent between the *in vivo* and *ex vivo* TBV measurements: 21.3% volume loss within the rTg4510 cohort compared to wildtype controls, and 16.2% volume loss within the rTg4510 cohort compared to the doxycycline-treated rTg4510 cohort.

5.4.3 Deformation maps to estimate tissue shrinkage uniformity

The TBV results revealed a significant volume reduction in *ex vivo* TBV compared to the corresponding *in vivo* TBV (p ≤ 0.0001) (Figure 5.2). In order to further investigate the morphological differences between *in vivo* and *ex vivo* brain tissues at a voxel-wise level, my collaborators at the UCL Centre for Medical Image Computing registered the *ex vivo* mouse brains to their corresponding *in vivo* mouse brain template.

Figure 5.3 shows the mean distance moved by each voxel when aligning *ex vivo* images to in situ, *in vivo* images, from all three mouse cohorts. The greatest deformations were identified within structures located frontally and caudally in the mouse brain, including the brainstem and olfactory bulb. In these regions, displacements greater than 0.25 mm can be readily visualised. The brainstem was particularly vulnerable to disturbance; in this structure, displacements of 0.5 mm can be observed.

I observed deformations within the rostral aspect of the olfactory bulb; however, the displacements are markedly less than previous findings within this structure (*188*). By scanning the *ex vivo* specimens in the skull, I have minimised disturbances to this structure. The remaining brain structures, including the midbrain, hippocampus, thalamus and cortex, were relatively unaffected *ex vivo*; I attribute this preservation to keeping the brains in the skull for scanning, to prevent damage. It is notable that the cortical surface shows very few signs of systematic perturbation, suggesting high validity of *ex vivo* morphometric results in these structures.

Another possible cause of the apparent displacements seen in Figure 5.2 is the different sequences used for *in vivo* (FSE) and *ex vivo* (GE) acquisition. The latter may have induced some geometric distortion away from the bore isocentre, giving a similar pattern. However, the *ex vivo* brains were always aligned in the scanner bore so that their centres were aligned with the isocentre. Previous work by O'Callaghan et al. found gradient warp distortion was below 0.1 mm within ± 20 mm of the isocentre (35); the mouse skulls easily fit within this 40 mm window. Additionally, the displacements seen caudally appear predominately in the brainstem (rather than equally in the cerebellum), so it is more likely that physical distortion caused the dominant appearance here.
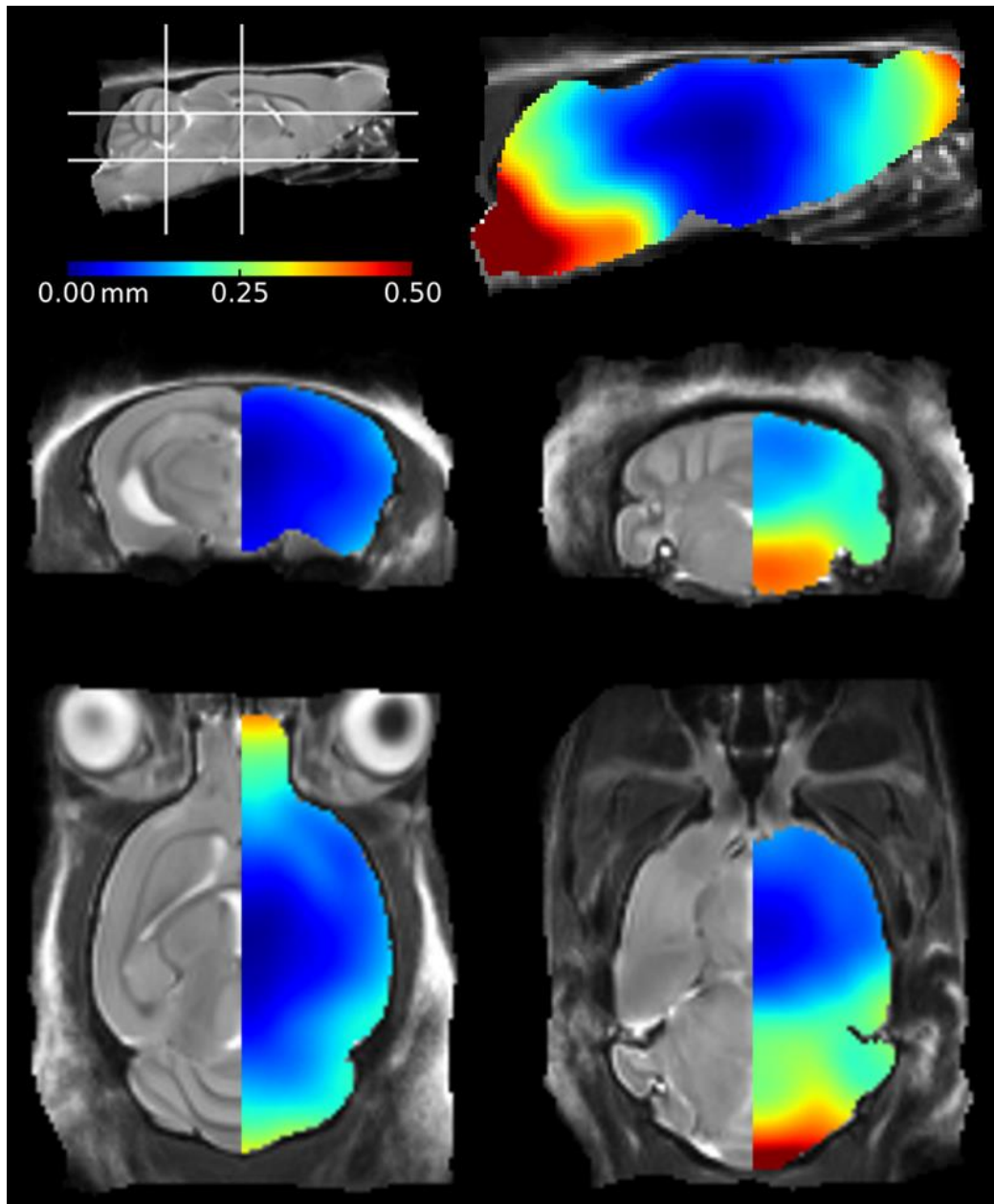
Figure 5.3 *Deformation maps showing local distortions of the ex vivo mouse brains in comparison to their in vivo mouse brain template. Deformations were calculated at a voxel-wise level. The colour bar illustrates the distance travelled by a voxel during registration of the ex vivo mouse brains to the in vivo atlas.*

5.4.4 Tensor-based morphometry

5.4.4.1 Unnormalized TBM results for the comparison between wildtype and rTg4510 mice

Figure 5.4 shows representative *in vivo* (Figure 5.4A, B) and *ex vivo* (Figure 5.4C, D) axial and coronal slices through the group average images after group-wise registration, with statistically significant voxels overlaid (FDR, q=0.05). Regions highlighted in red represent a significant local decrease in volume of rTg4510 group compared to the wildtype group, while regions highlighted in blue represent a significant increase in volume. I present un-normalized *in vivo* and *ex vivo* results (Figure 5.4A, C), in addition to results which have been normalized to TBV (Figure 5.4B, D) in order to account for global differences in TBV between the transgenic and wildtype mice (Figure 5.2). The *in vivo* TBM results have also been presented in Chapter 4; here, more slices are displayed in order to further explore the morphological changes detected in the *in vivo* and *ex vivo* data sets.

As discussed in Chapter 4, TBM applied to the unnormalized *in vivo* data identified extensive atrophy within the forebrain regions, including the cortex, caudate putamen, hippocampus and hypothalamus, as well as expansion of the lateral, third and fourth ventricles (Figure 5.4A).

The unnormalized *ex vivo* TBM results are shown in in Figure 5.4C. Good consistency was observed between the TBM results for the *in vivo* and *ex vivo* images for identifying morphological changes in this model, with a similar pattern of atrophy detected in both data sets. Interestingly, expansion of the lateral and third ventricles was visibly reduced in the *ex vivo* results (Figure 5.4Cii-iii). This may be due to collapse of the ventricular space during specimen preparation; a phenomenon which has previously been observed in *ex vivo* mouse brains (*188*).

5.4.4.2 Normalized TBM results for the comparison between wildtype and rTg4510 mice

The TBV results in Figure 5.2 highlighted the gross differences in brain volume between the rTg4510 mice and wildtype controls. In order to account for these differences and reveal local morphological changes which are disproportionately more

severe that the overall reduction in TBV, the TBM statistics were normalized to TBV. Figure 5.4 additionally shows the normalized *in vivo* (Figure 5.4B) and *ex vivo* (Figure 5.4D) TBM results.

Markedly fewer regions of expansion and contraction were observed in the normalized TBM results, in contrast to the corresponding unnormalized TBM results. The normalized *in vivo* TBM results identified atrophy within the rTg4510 mice which could be localised to the retrosplenial region of the cortex and thalamus (Figure 5.4Bii) as well as the caudate putamen (Figure 5.4Biii). These regions were implicated in the unnormalized *in vivo* TBM results (Figure 5.4A); these findings suggest volume loss occurring disproportionately to global TBV reduction within these regions.

The normalized *ex vivo* TBM results detected significant atrophy within the rTg4510 mice that could be localised to the somatosensory region of the cortex (Figure 5.4Dii). The CA1 region of the hippocampus was also identified (Figure 5.4Div). Interestingly, more voxels retained their significance in the normalized *in vivo* TBM results in comparison to the normalized *ex vivo* TBM results; this is likely to be due to the expansion and contraction correlating better with the TBV differences in the *ex vivo* mouse brains.
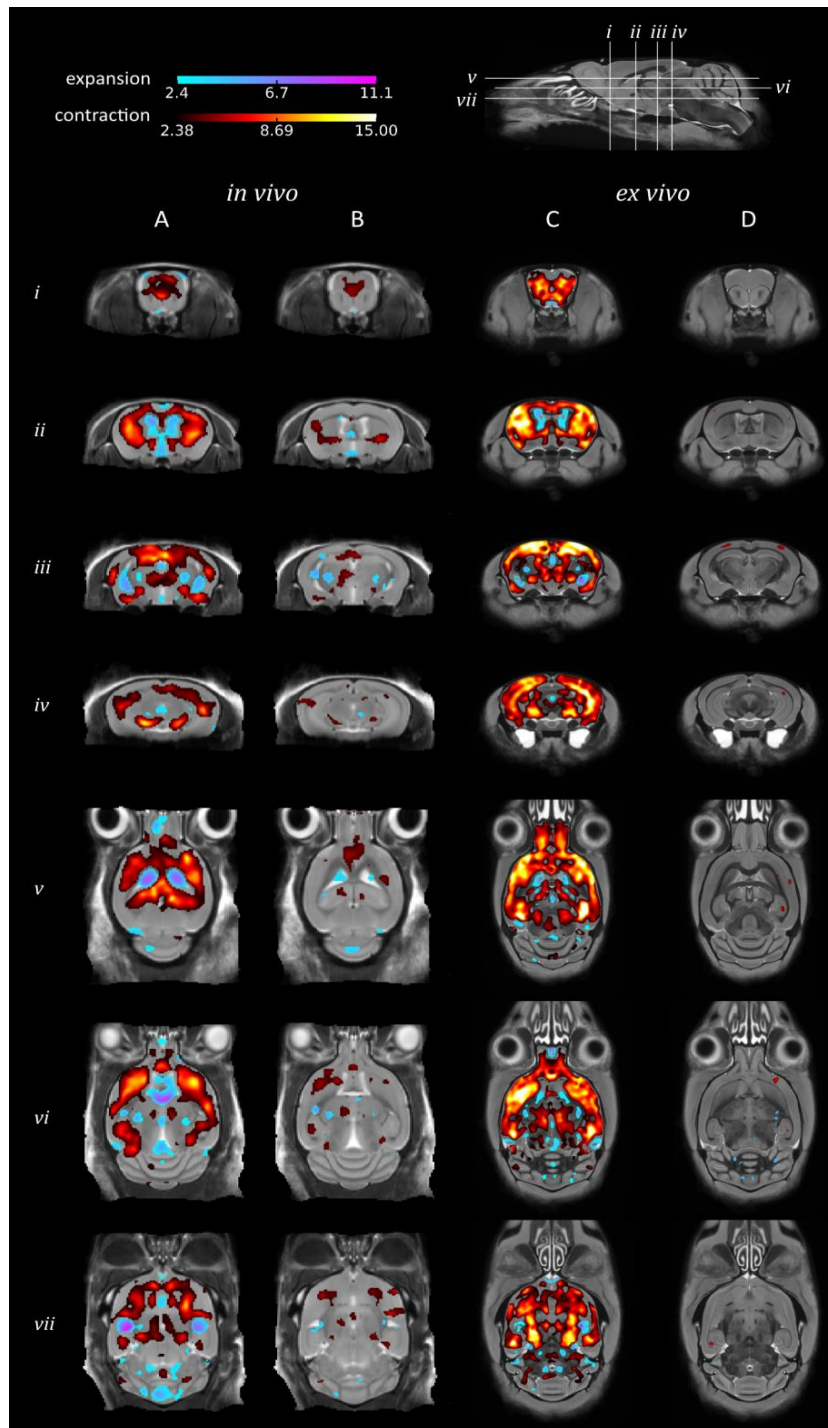
Figure 5.4 *TBM results for the morphological comparison between rTg4510 mice and wildtype controls. Results from in vivo (A, B) and ex vivo (C, D) structural analysis, showing TBM statistical results overlaid on representative axial and coronal slices of the final group average image after 20 iterations of NRR. I present unnormalized in vivo (A) and unnormalized ex vivo (C) TBM results in addition to normalized in vivo (B) and ex vivo (D) TBM results. Normalized TBM results were calculated by normalizing the TBM statistical results to TBV. Red: regions where the rTg4510 brains are relatively locally smaller than the wildtype controls; blue: rTg4510 brains are locally larger. Based upon FDR-corrected t-statistics (q=0.05).*

5.4.4.3 Unnormalized TBM results for the comparison between rTg4510 mice and doxycycline-treated rTg4510 mice

In order to investigate the sensitivity of *in vivo* and *ex vivo* imaging to more subtle structural changes, I sought to identify morphological differences between the doxycycline-treated and untreated rTg4510 mice. Figure 5.4 shows the unnormalized *in vivo* (Figure 5.4A) and *ex vivo* (Figure 5.4C) TBM results for the comparison between rTg4510 mice and doxycycline-treated rTg4510 mice. Regions highlighted in red represent a volume decrease in the rTg4510 mice compared to the doxycycline-treated rTg4510 mice; regions highlighted in blue represent a volume increase in the rTg4510 mice compared to the doxycycline-treated rTg4510 mice.

In contrast to the unnormalized results detailed in Figure 5.4A and C, I observed markedly reduced regions of expansion and contraction in the unnormalized *in vivo* and *ex vivo* TBM results (Figure 5.5A, C) due to the smaller morphological differences previously observed between the doxycycline-treated and untreated rTg4510 mice at this timepoint (previously described in Chapter 4.4.2).

The unnormalized *in vivo* TBM results identified small discrete clusters of significant voxels within the piriform area of the cortex (Figure 5.5Aii) and caudal slices of the hippocampus (Figure 5.5Aiv). I observed good correspondence between the unnormalized TBM results observed *in vivo* and those identified *ex vivo* (Figure 5.5B), with significant voxels identified in many of the same regions *ex vivo*. However, the *ex vivo* TBM results were significantly more widespread, with atrophy detected extensively throughout the cortex, caudate putamen and caudal hippocampal regions (Figure 5.5C). This may be due to the increased CNR of the *ex vivo* images (Table 5.2) which permits improved localisation of discrete morphological changes occurring between the rTg4510 and doxycycline-treated rTg4510 mice.

5.4.4.4 Normalized TBM results for the comparison between rTg4510 mice and doxycycline-treated rTg4510 mice

The TBV results identified significant differences in brain volume between the rTg4510 mice and the doxycycline-treated rTg4510 mice (p ≤ 0.01) (Figure 5.2). As detailed previously, the TBM statistics were normalized to TBV in order to reveal changes occurring disproportionality to the differences in brain volume.

Figure 5.5 shows the normalized *in vivo* (Figure 5.5B) and *ex vivo* (Figure 5.5D) TBM results for the comparison between rTg4510 mice and doxycycline-treated rTg4510 mice. In comparison to the unnormalized *ex vivo* TBM results (Figure 5.5B), many voxels retained their significance when normalized to TBV, suggesting the changes observed are occurring disproportionately to TBV differences. The observable alterations can therefore be attributed to the effects of doxycycline. Atrophy was detected in the CA1 region of the hippocampus (Figure 5.5Ci) and the somatosensory region of the hippocampus (Figure 5.5Cii).

Following normalization of the *in vivo* TBM results to TBV, all statistically significant voxels disappeared (Figure 5.5B). This finding suggests that the *in vivo* MRI study may have been underpowered to detect changes occurring disproportional to brain volume differences.
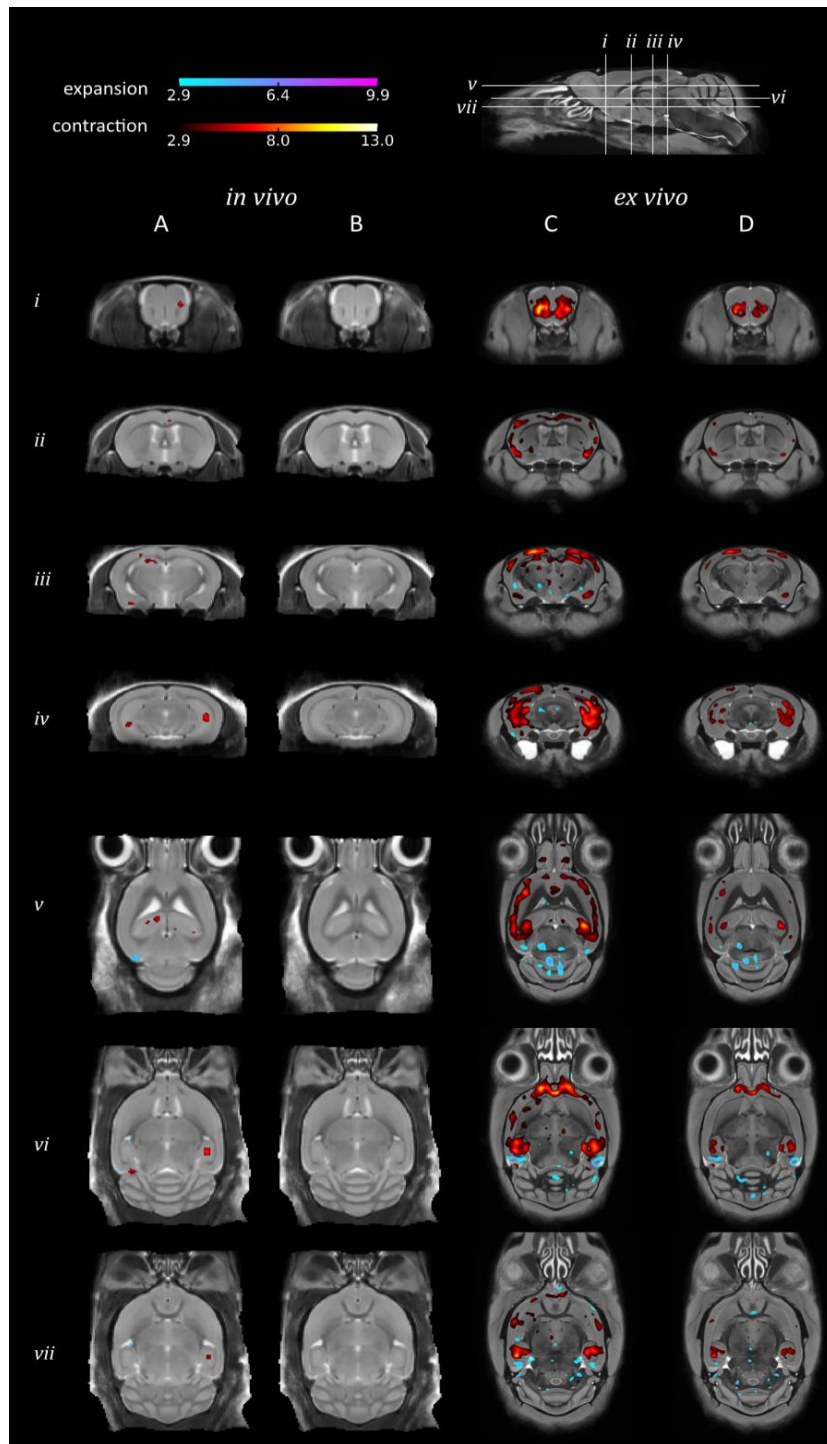
Figure 5.5 *TBM results for the morphological comparison between rTg4510 mice and doxycycline-treated rTg4510 mice. Results from in vivo (A, B) and ex vivo (C, D) structural analysis, showing TBM statistical results overlaid on representative axial and coronal slices of the final group average image after 20 iterations of NRR. I present unnormalized in vivo and ex vivo TBM results (A, B) and normalized ex vivo TBM results (C). Normalized TBM results were calculated by normalizing the TBM statistical results to TBV. Red: regions where the rTg4510 brains are relatively locally smaller than the treated rTg4510 brains; blue: rTg4510 brains are locally larger. Based upon FDR-corrected t-statistics (q=0.05).*

5.4.5 Immunohistochemistry to estimate cortical PG-5 and NeuN density

In order to corroborate the TBM findings with alterations occurring at the cellular level, quantitative immunohistochemistry was performed on each of the individual wildtype (n=11), untreated rTg4510 (n=13) and treated rTg4510 (n=6) mice following *ex vivo* imaging. My collaborators at Eli Lilly employed two stains: 1) NeuN, a neuronal marker, and B) PG-5, a marker for phosphorylated tau. Both neuronal loss and tau accumulation have previously been shown to correlate with structural MRI findings (*93, 97, 230*); in this work, I have used the histology results as a ground truth and identified regions where morphological changes identifiable using MRI were likely to be observed.

Figure 5.6A shows the regional distribution of NeuN positive neurons in a representative untreated rTg4510 mouse. The untreated rTg4510 mice showed a significant decrease in the density of NeuN positive cells in the cortex (mean NeuN density = 1099 ± 107.3 cell/mm^2) compared to wildtype mice (mean NeuN density = 1253 ± 131.3 cell/mm^2) ($p \leq 0.05$) (Figure 5.6B). These results are consistent with previous findings, and indicate severe neurodegeneration in this model (*114, 229*). Following treatment with doxycycline, I observed a significant increase in NeuN density in the treated rTg4510 mice (mean NeuN density = 1301 ± 44.89 cell/mm^2) compared to the untreated rTg4510 mice ($p \leq 0.01$) (Figure 5.6B). No significant differences were observed between NeuN cell densities in the treated rTg4510 mice compared to wildtype mice.

Figure 5.6C shows the regional distribution of PG-5 positive cells in a representative untreated rTg4510 mouse. Visual inspection of the slice section revealed high levels of PG-5 staining in the cortex and hippocampus. In agreement with previous findings in this model, I observed high levels of PG-5 positive cells in the cortex of the untreated rTg4510 mice (mean PG-5 density = 369.1 ± 39.11 cell/mm^2) (Figure 5.6C, D). No PG-5 positive cells were observed in the wildtype mice mean (Figure 5.6D). Following treatment with doxycycline, I observed a significant decrease in PG-5 positive cell density in the treated rTg4510 mice (mean PG-5 density = 268.6 ± 39.11 cell/mm^2) compared to untreated rTg4510 mice ($p \leq 0.001$) (Figure 5.6D).
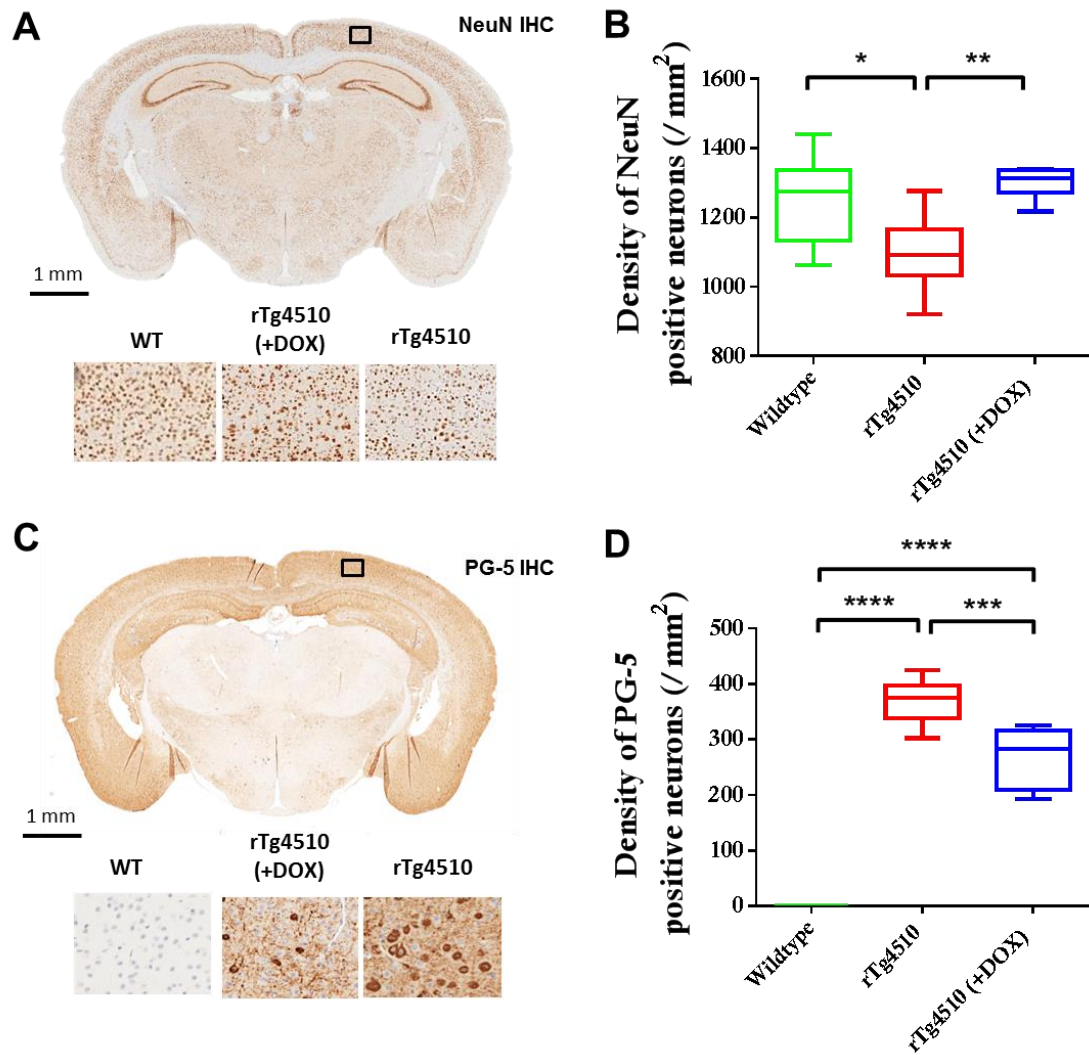
Figure 5.6 *Immunohistochemistry to estimate NeuN and PG-5 positive cell density in the cortex. Representative coronal slices illustrating the distribution of (A) NeuN and (C) PG-5 positive neurons in the cortex of an untreated rTg4510 mouse. Quantitative estimates of (B) NeuN and (D) PG-5 positive cell density in the cortex for each of the 7 wildtype, 10 untreated rTg4510 and 6 treated rTg4510 mice at 7.5 months of age. * = p ≤ 0.05; ** = p ≤ 0.01; *** = p ≤ 0.001; **** = p≤0.0001.*

5.4.6 Histological ranking to explore changes in NeuN staining

To further investigate whether the discrete volume changes detected using *ex vivo* TBM normalized to TBV reflected alterations at the cellular level, I explored whether the localized changes within the somatosensory region of the cortex (shown as statistically significant voxels in the TBM maps in Figure 5.4D) were mirrored in the NeuN staining.

Each NeuN slice section was manually delineated to identify the parietal (region 1), somatosensory (region 2) and auditory (region 3) regions of the cortex (Figure 5.7A). The degree and severity of NeuN disruption was assessed by semi-quantitative ranking by five independent and blinded raters (1, highly disrupted, to 5, no disruption).
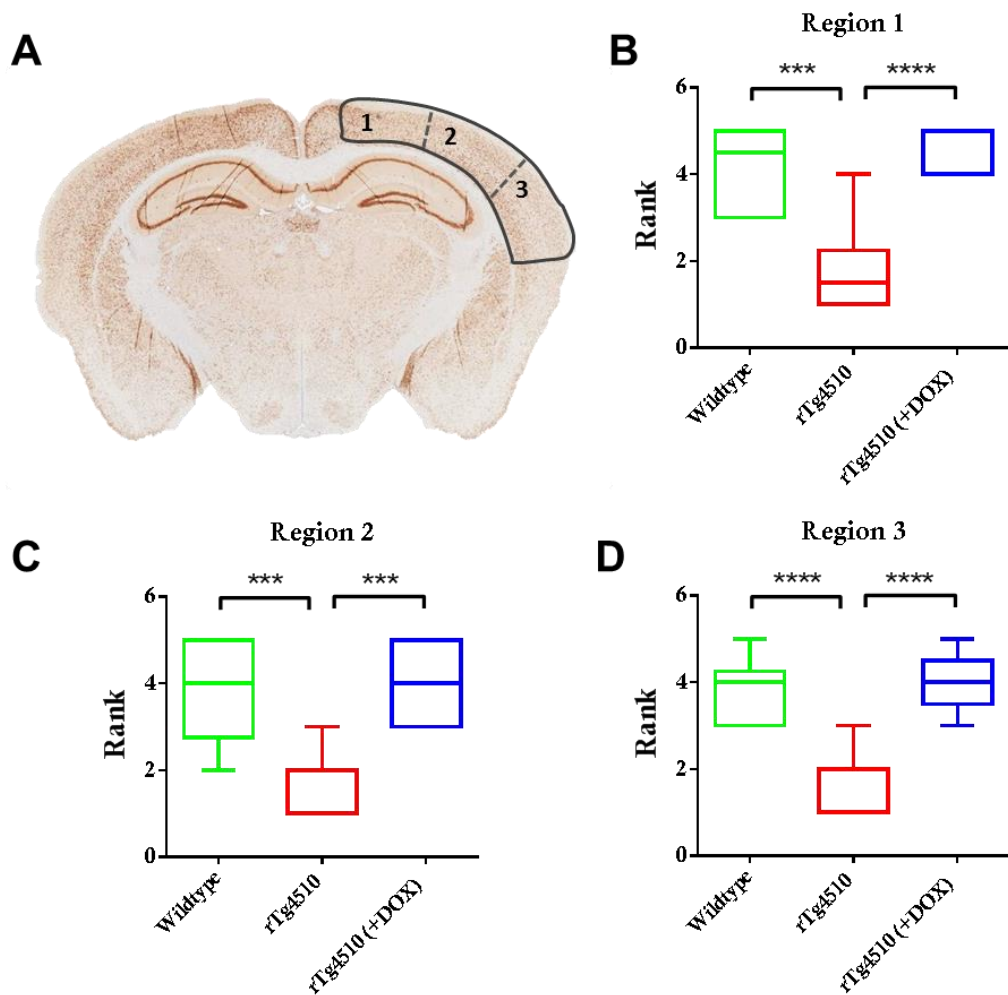
Figure 5.7 *Immunohistochemistry to estimate extent of NeuN disruption. Representative coronal slice illustrating the distribution of NeuN within the (1) parietal, (2) somatosensory and (C) auditory regions of the cortex. Modal ranking scores for each of the 7 wildtype, 10 rTg4510 and 6 rTg4510 (+DOX) animals at 7.5 months of age. *** = p≤0.001; **** = p≤0.0001.*

Significant disruption in NeuN staining in the rTg4510 mice compared to wildtype controls was observed in all regions under investigation: the parital (p ≤ 0.001), somatosensory (p ≤ 0.001) and auditory (p ≤ 0.0001) regions of the cortex (Figure 5.7B-D). A similar pattern of disruption was also observed between the rTg4510 and doxycycline-treated rTg4510 (Figure 5.7B-D). No significant differences in NeuN staining were observed between the treated rTg4510 mice and wildtype controls (Figure 5.7B-D).

These findings suggest that alterations in cell density may be underpinning the widespread cortical changes detected using TBM (Figure 5.4 and Figure 5.5). However, the somatosensory region of the cortex did not show increased NeuN disruption. These results therefore suggest there is no link between discrete (sub-cortical) disruption in NeuN staining, and the proportional volume changes observed in the normalized *ex vivo* TBM results.

5.5 Discussion

With increasing numbers of rodent neuroimaging studies employing automated analysis techniques to identify regions of structural change, it is important that the compromises between *in vivo* and *ex vivo* MRI are fully understood in order to maximise sensitivity to morphological differences. A number of studies have previously addressed the trade-offs associated with imaging *in vivo* and *ex vivo* mouse brains (*186, 188, 222*); in this chapter, I present the first application of TBM to both *in vivo* and *ex vivo* structural MRI for investigating morphological changes in the rTg4510 mouse model of tauopathy. In addition to characterising the gross morphological differences in the rTg4510 mice compared to wildtype controls, the ability to modulate the expression of the tau transgene with doxycycline introduced more subtle group differences in brain morphology to explore using *in vivo* and *ex vivo* MRI.

The T_2-weighted *in vivo* MRI images enabled visual identification of many structures of interest, including the hippocampus, caudate putamen and cortex. This was achieved in the absence of exogenous contrast agents such as manganese, which is frequently employed in *in vivo* studies of mouse neuroanatomy (*275, 276*). However, high doses of manganese are believed to produce neurotoxic effects (*277, 278*), which could confound longitudinal analysis by interfering with both normal healthy aging and disease

progression. In this chapter, I instead exploited the inherent differences in the T_1 and T_2 relaxation times to achieve adequate *in vivo* image contrast, as described in Chapter 3. Conversely, high resolution *ex vivo* MR images were acquired using a previously optimised protocol which employed the gadolinium-containing contrast agent Magnevist (*140*); the T_1-shortening effects of gadolinium enabled the acquisition of high resolution data sets within a feasible scan time (typically overnight to maximise the efficiency of scanner usage). The protocol was adapted to permit the acquisition of 3 *ex vivo* mouse brains simultaneously, which markedly improved throughput.

SNR and CNR measurements of the *in vivo* and *ex vivo* data sets allowed a quantitative assessment of image quality to support my investigation. Despite limits on scan time, the increasing availability of specialist hardware to support *in vivo* imaging studies permits the acquisition of *in vivo* data with sufficient SNR and CNR to perform voxel wise analyses. In the protocols applied here, SNR was significantly greater *in vivo* than *ex vivo* for 7 out of the 9 regions under investigation. The larger voxel size (150 μm^3 *in vivo* in contrast to 40 μm^3 *ex vivo*) of the *in vivo* acquisition and use of a surface coil will have been key contributors to the increased signal in ROIs.

Fixation of the *ex vivo* brain specimens results in dehydration and subsequent reduction of the relative proton density of tissues (*279*). This can cause a reduction in SNR in *ex vivo* images, although increasing the number of signal averages helped to mitigate this effect. Despite the lower SNR, *ex vivo* MRI experienced an increase in grey-white matter contrast compared to the *in vivo* images; this enhancement in CNR can be largely explained by the use of Magnevist. Despite the differences in the two protocols, *in vivo* and *ex vivo* imaging present different challenges and each protocol was optimised to mediate the unique demands of each.

In addition to comparison of the image signal quality, the main aim of this investigation was to explore the sensitivity of *in vivo* and *ex vivo* MRI to the morphometric changes occurring in the rTg4510 mouse. When investigating differences between the rTg4510 and wildtype mice, a similar bilateral pattern of atrophy *in vivo* and *ex vivo* was observed using TBM. Many of the same regions were identified as suffering volume loss, including the frontal cortical regions and caudal slices of the hippocampus. These regions are selectively vulnerable to NFT pathology and neuronal loss in this model, as depicted by the immunohistochemistry results. Conversely, expansion of the ventricles was underestimated in the *ex vivo* images, owing to collapse of the ventricular space

during formalin fixation. Whilst this doesn't appear to interfere with the findings in the rTg4510 mouse, if the model under investigation has a ventricular abnormality, this may not be observed so readily *ex vivo*.

When TBM was used to investigate more subtle structural changes, the benefits of *ex vivo* MRI became more apparent. A more extensive bilateral pattern of atrophy in the untreated vs. treated rTg4510 mice was detected in the e*x vivo* data sets, which could be localised to sub-regional structures: the anterior cingulate, somatosensory and piriform regions of the cortex, as well as the CA1 hippocampal subfield. The increased CNR of the *ex vivo* data sets is likely to enable the voxel-wise tests to highlight more extensive regions of difference between groups. In addition, the higher resolution afforded by *ex vivo* MRI permitted improved localisation of volume changes to sub-regional structures.

Although not as spatially extensive, the *in vivo* TBM results produced significant voxels which implicated the same sub-regional structures as the *ex vivo* results. It is possible that increasing the sample size *in vivo* would enable the detection of a more extensive pattern of atrophy. However the *in vivo* results were adequate to guide further histological evaluation into the underlying cellular changes underpinning these MR findings.

Within the normalized *ex vivo* TBM results, detection of significant atrophy was maintained in the somatosensory region of the cortex, in addition to the CA1 hippocampal subfield. This finding suggests that volume loss within these regions was occurring disproportionate to the global brain volume changes. No significant voxels were detected in the normalized *in vivo* TBM results. Despite this negative finding, in Chapter 3 I reported *in vivo* TBM findings in the rTg4510 mouse which had been normalized to TBV at 8.5 months. This earlier study consisted of 17 wildtype and 9 rTg4510 mice. I therefore hypothesise that the lack of sensitivity to discrete changes occurring disproportionately to the TBV differences is due to low animal numbers in each group. Increasing the sample size may increase the significance of the findings. A power calculation would confirm this hypothesis, and identify the minimum number of animals required to identify these changes for future studies.

I revisited the histology data to try and corroborate the TBM findings with alterations occurring at the cellular level. The somatosensory region of the cortex has been implicated in all of the TBM results as a region suffering from significant volume loss; I

sought to uncover whether this may reflect disruption in NeuN staining. The results from the user ranking did not reveal further NeuN disruption within the somatosensory region of the cortex when compared to its neighbouring cortical structures. This may be due instead to nearby deformations within the TBM results manifesting within that region.

I observed that the formalin fixation process causes an overall reduction in TBV of around 10%. Tissue shrinkage associated with formalin fixation is a widely accepted occurrence, yet the extent to which the tissues suffer differential distortion is still not fully known. A previous study identified 4.37% shrinkage in post-mortem wildtype mouse brains prepared for *ex vivo* MRI (*154*), markedly less than my observation of 10.3%. This discrepancy may be due to differences in the fixation protocol, such as time spent in fixative and the use of contrast agents. The authors also did not specify whether a calibration protocol was in place to estimate gradient scaling errors of the different imaging systems used for the acquisition of the *in vivo* and *ex vivo* data. An additional study reported no significant difference in *in vivo* and *ex vivo* TBVs in a cohort of Wistar rats (*280*); in this work, the post-mortem rat brains were scanned using different scanners located at different sites. This work was also published in the absence of a calibration protocol, and the authors did not provide details of the fixation protocol. In both cases, if discrepancies between the respective gradient sets were not accounted for, this may cause inaccuracies in the estimation of *ex vivo* tissue shrinkage. In this work, I adopted a previously published gradient calibration protocol (*165*) to calculate scaling errors which then used to correct the *in vivo* and *ex vivo* data, thus improving the brain volume estimates.

My observations of consistent whole brain shrinkage across the groups of wildtype, rTg4510 and doxycycline-treated rTg4510 mice suggest that this should not interfere with the TBM results, which rely on rigid and non-rigid registration algorithms to identify regions of expansion and contraction. In addition, the deformation maps identified minimum disruption to the cortical and central structures of the *ex vivo* mouse brains, which were of particular relevance in this work. The brain stem suffered the greatest deformations, as it is not protected from disturbance by the skull. A previous study identified similar disruption to the brain stem using a voxel-wise analysis (*188*); however, the authors reported additional disturbances in the dorsal cortical regions. These brains were removed from the skull prior to *ex vivo* imaging (*189*) which is likely

to have caused damage to the surface structures and subsequent local deformations. The olfactory bulb, cortex and cerebellum are particularly vulnerable to damage when extracting brains from the skull (*186*).

5.6 Conclusion

In this chapter, I have explored the compromises and trade-offs between *in vivo* and *ex vivo* MRI in conjunction with TBM for detecting regions of morphometry in transgenic mouse models. My findings support the utility of *in vivo* MRI, where atrophy was detected in regions known to be affected in this model. As demonstrated in Chapter 4, *in vivo* imaging permits longitudinal studies of neurodegeneration or neurodevelopment, which can offer novel insight into the mouse model under investigation. In addition, the data does not suffer from dehydration or distortion artefacts which can confound *ex vivo* studies. Furthermore I strongly advocate the use of a gradient calibration protocol in order to correct for gradient scaling errors and ensure accurate volume measurements (*165*).

I hope that this work will help support research groups working in the field of preclinical MRI, and shape their decision about the best way to image their transgenic mice.

Chapter 6: Application of *in vivo* MRI biomarkers to the J20 mouse model of Alzheimer's disease and the Tc1 mouse model of Down's syndrome: a single timepoint study

6.1 Aims

The preceding chapters have focused on the sensitivity of MRI biomarkers to tau pathology in the rTg4510 mouse model. This chapter aims to explore the relationship between genetics and neurodegeneration by applying clinically relevant biomarkers to novel mouse models of AD and DS.

In this work, I have been involved in the experimental set-up, acquisition of the imaging data and post-processing of the results. Following *in vivo* characterisation, I perfuse-fixed all of the mice in order to perform high resolution *ex vivo* structural imaging, before dispatching the tissues for histology. Furthermore, I investigated cross-correlations between the imaging parameters, as well as against histology.

I would like to acknowledge my colleagues and collaborators: Frances Wiseman and Susan Noy at the UCL Institute of Neurology who provided the animals used and performed histological sectioning and staining; and Nick Powell and Ma Da at the UCL Centre for Medical Image Computing for developing the image processing software.

6.2 Introduction

Down's syndrome (DS), or trisomy 21, is a genetic disorder caused by the presence of an extra copy of chromosome 21. Individuals with DS have a greater predisposition to early onset AD (*26*), widely believed to be due to the extra dosage of the *APP* gene. *APP* is an established risk factor gene for AD, with a number of mutations associated with familial forms of the disease (*281*). Crucially in the context of DS, the *APP* gene lies on chromosome 21, so individuals with DS have an additional copy of this gene. It is believed that the increased *APP* mRNA and protein expression, in conjunction with increased levels of amyloid-β results in early onset AD (*28*). However, is it likely that other disease-modulating genes lie on chromosome 21 which contribute to the

increased incidence of AD observed in DS individuals (*282*). Furthering our understanding of AD in individuals with DS may provide useful insights into the disease within the wider population.

Mouse models of DS are valuable tools for furthering our understanding of the significance of trisomy 21 and its relationship with AD. There are several mouse models of DS to choose from, each carrying various segments of chromosome 21. The *transchromic 1* (Tc1) mouse is an established model of DS which carries an almost-complete copy of human chromosome 21 but is not functionally trisomic for *APP* (*283*). The unique genetics of the Tc1 strain allow the study of the DS phenotype without the effects of *APP* trisomy. Several of the key features seen in the human DS condition are recapitulated in this mouse model, including altered heart development and behavioural changes (*283*). While initial characterisation of the Tc1 showed abnormalities in cerebellar neuronal density and skull morphology (*283*), there has since been no further investigation into additional cerebral defects in this mouse model.

In order to introduce AD pathology to the Tc1 DS mouse, my collaborators at the UCL Institute of Neurology bred the Tc1 DS mouse to the J20 mouse - an established model of AD (*104*). The J20 AD mouse overexpresses human *APP*, with two mutations which have been linked to familial forms of AD: the Swedish (*APP* KM670) and Indiana (*APP* V717F) mutations. The J20 AD mouse exhibits many key features of the human condition, including cognitive decline, neuronal loss and the build-up of amyloid plaques (*104*). By breeding the Tc1 DS mouse to the J20 AD mouse, progeny have been generated that carry chromosome 21 genes with mutant *APP*. This new DS-AD mouse, termed the Tc1*J20 mouse, permits the study of the DS phenotype in the presence of AD pathology, compared to AD pathology alone, to see if chromosome 21 genes modulate pathology when present in three copies to echo the early-onset AD seen in DS.

In this work, I have used multi-parametric MRI to characterise a cohort of Tc1, J20, Tc1*J20 and wildtype controls at 16 months, with the aim of investigating the relationship between genetics and the manifestation of AD neuropathology. The MRI biomarkers described in this study were chosen for their sensitivity to pathological mechanisms that have been implicated in neurodegenerative diseases. The use of identical MRI measurements across the different mouse strains permitted meaningful comparisons to be deduced. I used ASL to quantify CBF (*252*), MRA to evaluate

cerebral vasculature (*284*) and high resolution structural MRI (*93*) to evaluate morphological differences in these mice.

6.3 Methods

6.3.1 Animals

Generation of the Tc1 and J20 mice used in this study have been reported previously (2, 3). Tc1*J20 mice were generated by my collaborators at the UCL Institute of Neurology, by crossing Tc1 females with J20 males (Figure 6.1). In this study, two cohorts of animals were imaged. For initial characterisation, female Tc1 (n = 16), J20 (n = 14), Tc1*J20 (n = 9) and wildtype litter-matched controls (n = 22) were scanned aged 16 months. For further CBF characterisation, a separate cohort of male Tc1 (n= 5) and wildtype controls (n = 6) were scanned aged 6 months.
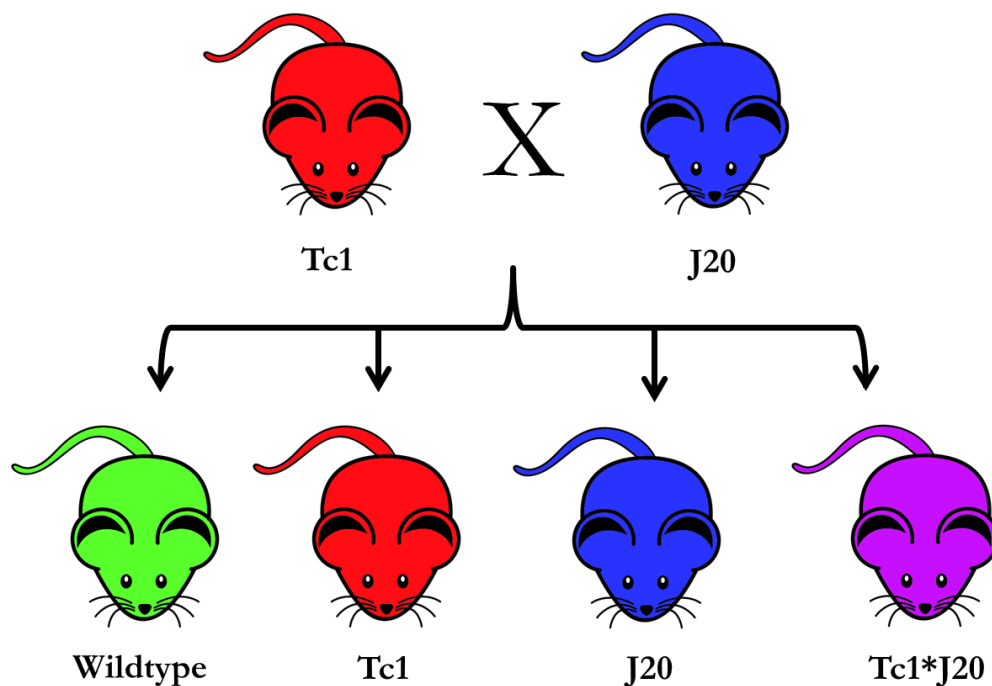
Figure 6.1 *Schematic showing generation of Tc1*J20 mice by crossing the Tc1 and J20 mice.*

All animals were bred at the Medical Research Council (MRC) Prion Unit (London, UK) and received on site 2 weeks prior to experimentation. All mice were kept in standard size mouse cages (29 × 18 × 13 cm; up to 5 per same sex groups) at 20°C to 26°C on a daily 12 hour light-dark cycle with ad libitum access to food and water.

All studies were carried out in accordance with the United Kingdom Animals (Scientific Procedures) act of 1986 and subject to approval by UCL's internal ethical review panel.

6.3.2   Magnetic resonance imaging

All imaging was performed with a 9.4T VNMRS horizontal bore scanner (Agilent Inc.).

For *in vivo* imaging, a 120 mm diameter imaging gradient set (SGRAD 205/120/HD/S, Agilent Technologies UK Ltd., Berkshire, UK) was used. A 72 mm birdcage RF coil was employed for RF transmission and a quadrature mouse brain surface coil (RAPID, Germany) was used for signal detection. Tuning and matching of the coil was performed manually. Shimming was performed across the mouse brain prior to image acquisition.

Mice were placed in an induction box before anaesthesia was induced using 2% isoflurane at 1 l/min in 100% O$_2$, Mice were subsequently positioned in a MRI-compatible head holder to minimise motion artefacts. Anaesthesia was maintained throughout imaging using 1.5% isoflurane at 1 l/min in 100% O$_2$ delivered via a nose cone g, which permitted spontaneous breathing of the mice. Core temperature and respiratory rate were monitored using a rectal probe and pressure pad respectively (SA instruments). Mice were maintained at ~37°C using heated water tubing and a warm air blower with a feedback system (SA instruments).

For *ex vivo* imaging, an imaging gradient set with a 60 mm inner diameter (SGRAD 115/60/HD/S, Agilent Technologies UK Ltd., Berkshire, UK) was used. A 35L mm birdcage RF coil was employed for RF transmission and signal detection. Tuning and matching of the coil was performed manually. A custom-build three brain holder was used to acquire high resolution *ex vivo* images of multiple brains simultaneously.

6.3.3   Arterial spin labelling

ASL was performed using the sequence previously described in Chapter 4.3.8. Briefly, a FAIR sequence (*218, 219*) with a 4-shot segmented SE EPI readout was implimented

with the following parameters: 5 slices, slice thickness = 1 mm, FOV = 20 × 20 mm, matrix size = 64 64, slice selective inversion pulse width = 12 mm, inversion time = 1500 ms, TE = 11 ms, TR = 3500 ms, 20 averages. A hyperbolic secant adiabatic inversion pulse was used with a bandwidth of 20 kHz for the FAIR labelling pulses (*220*). The splenium of the corpus callosum was used as a landmark for consistency of slice positioning between subjects. CBF maps were generated using the model described by Buxton *et al.* (*221*). In this work, T_1 maps were also acquired using an inversion recovery SE-EPI sequence for CBF quantification. CBF maps were generated by fitting the ASL images and T_1 maps to the model described by Buxton *et al.* (*221*). ROIs were manually drawn in the cortex, hippocampus and thalamus across two 1 mm thick slices and averaged, matching the regions that underwent histological analysis of amyloid-β burden.

6.3.4 Magnetic resonance angiography

High-resolution angiograms of the whole brain were acquired using a TOF MRA sequence. A 3D GE sequence was employed with the following parameters: TR = 40 ms; TE = 2.5 ms; FA = 40°; NSA = 2; matrix = 128 × 128 × 128; FOV = 15 mm × 15 mm × 20 mm; resolution = 117 μm × 117 μm × 156 μm.

6.3.5 Perfuse fixation

The perfusion fixation protocol was previously described in Chapter 3.3.6, in order to prepare the brains for histological evaluation. Following *in vivo* imaging, a subset of wildtype (n = 13), Tc1 (n = 15), J20 (n = 14) and Tc1*J20 (n = 8) were perfuse-fixed for high resolution *ex vivo* scanning and histological evaluation. The perfuse-fixation protocol for prepare post-mortem brain samples for contrast-enhanced *ex vivo* scanning was previously described in Chapter 5.3.4. Briefly, mice were terminally anaesthetised before being perfused through the left ventricle with 15 – 20 mL of saline (0.9%) followed by 50 mL of buffered formal saline (10%) doped with Magnevist (8 mM) at a flow rate of 3 mL per minute. Following perfusion, the animal was decapitated, defleshed, and the lower jaw removed. All brains were stored in-skull in buffered formal saline (10%) doped with Magnevist (8 mM) at 4°C for 9 weeks prior to *ex vivo* imaging.

6.3.6   High resolution *ex vivo* structural imaging

A 3D GE sequence was implemented for structural imaging with the following parameters: FOV = 32 mm × 25 mm × 25 mm; resolution = 40 µm × 40 µm × 40 µm; TR = 17 ms; TE = 4.54 ms; flip angle = 51°; NSA= 6. Total imaging time was 11 h 36 minutes (*140*).

Following *ex vivo* imaging, post-mortem brain samples were dispatched for histology.

6.3.7   Histology and immunohistochemistry

Histology was performed by my collaborators at the UCL Institute of Neurology. The brains were removed from the skulls and dissected down the midline with a scalpel to separate the left and right hemispheres. The blocks were placed in plastic cassettes and processed to wax overnight in a Leica ASP300S tissue processor. The processing was performed under vacuum, which involved dehydration through a graded series of alcohols, clearing in xylene followed by infiltration with paraffin wax. The blocks were sagitally orientated and embedded in fresh wax using a Leica embedding centre (EG1150H) and cold plate. The blocks of tissue were trimmed laterally from the midline by approx. 0.9-1.4mm to give a sagittal section of the hippocampal formation. 4μm thick sections were cut using a Leica RM2135 rotary microtome, dried overnight at 40°C before immunostaining for amyloid-β.

The sections were dewaxed in xylene, rehydrated through an alcohol series and washed in distilled water. The sections were then transferred to 98% formic acid for 8mins, followed by washing in distilled water. The sections were then loaded onto a Ventana XT automated stainer where they underwent a further 30min antigen retrieval procedure using Tris Boric acid EDTA buffer (pH9.0). The sections were incubated in a blocking solution prior to being stained for amyloid-β using a directly biotinylated mouse monoclonal IgG2b antibody from Sigma (SIG-39240). The antibody was raised to amino acid residues 17-24 of amyloid-β with the epitope between aa18-22 (VFFAE). This antibody has been reported to bind to abnormally processed isoforms, as well as precursor forms of amyloid-β. The sections were incubated with primary antibody at a concentration of 2µg/ml for 12hrs, followed by development of the staining using the Ventana DabMap kit. The sections were counterstained with haematoxylin, washed in distilled water, dehydrated, cleared and mounted in DPX prior to being microscopically assessed.

4G8 burden was quantified using ImageJ (*285*).

6.3.8 High resolution *ex vivo* structural image processing

Ex vivo MR images were reconstructed using custom software written in MATLAB. As described in Chapter 3.3.8, a previously published calibration protocol (*165*) was used to adjust volume estimates to correct for scaling errors caused by the imaging gradients.

6.3.9 Automatic structural parcellation

Atlas-based structural parcellation was performed by my collaborators at the UCL Centre for Medical Image Computing, using the methods previously described in Chapter 4.3.5. Briefly, images were automatically oriented to a standard atlas space, non-uniformity corrected, skull-stripped and intensity-standardised. The publicly available *ex vivo* mouse brain MRI atlas previously published by Ma et al. (*189*) was adopted for the framework. The atlas images were registered affinely to the imaging data, before the atlas masks were fused together to create a consensus brain mask for each animal's scan. This was followed by non-rigid registration of the atlas to the imaging data, before resampling of the structural labels to create the final parcellated images.

6.3.10 Tensor-based morphometry

TBM was performed by my collaborators at the UCL Centre for Medical Image Computing, using the methods previously detailed in Chapter 3.3.9. Briefly, the *in vivo* structural images were automatically oriented to a standard atlas space, non-uniformity corrected, skull-stripped and intensity-standardised. This was followed by 1 iteration of rigid registration, 4 iterations of affine registration and 15 iterations of non-rigid registration, to align equivalent voxels between subjects. The determinant of the Jacobian matrix was calculated at each voxel of the resulting deformation fields which was subsequently smoothed, before statistics were performed at each voxel in order to compare groups. The resulting statistical parametric maps were corrected for multiple tests using the FDR (*169*); q=0.05).

6.3.11 Magnetic resonance angiography image processing

Images were reconstructed using custom software written in MATLAB. A groupwise average angiography image was produced by registering the wildtype (n = 17), Tc1 (n = 14), J20 (n = 18) and Tc1*J20 (n = 8) angiography images together, using the TBM

protocol detailed in Chapter 3.3.9. This protocol was adapted for analysis of the angiography data: a mask was generated for the vasculature by thresholding the average image, and TBM stats were performed within this mask in order to constrain the region of interest and reduce the multiple testing problem.

6.4 Results

In this chapter, the influence of chromosome 21 genes on the AD phenotype has been investigated. By imaging the progeny of the Tc1 DS mouse and the J20 AD mouse, I explored whether deficits or alterations in the J20 mouse were exaggerated with the introduction of chromosome 21 genes compared to the J20 AD phenotype without the presence of chromosome 21 genes.

The highest levels of *APP* expression in the J20 AD mouse have been reported in the cortex and hippocampus; this is due to the PDGF-β promoter, which drives expression of *APP* within these regions (*104*). To align our MR measures with regions vulnerable to amyloid-β deposition, I took ROIs within the cortex and hippocampus. The thalamus, a region of low *APP* expression and low amyloid-β deposition, was selected as a control region.

6.4.1 Arterial spin labelling

ASL was employed to quantify CBF in the wildtype, J20, Tc1 and Tc1*J20 mice. Figure 6.2 shows the raw CBF maps for representative wildtype (Figure 6.2A), J20 (Figure 6.2B), Tc1 (Figure 6.2C) and Tc1*J20 (Figure 6.2D) mice.
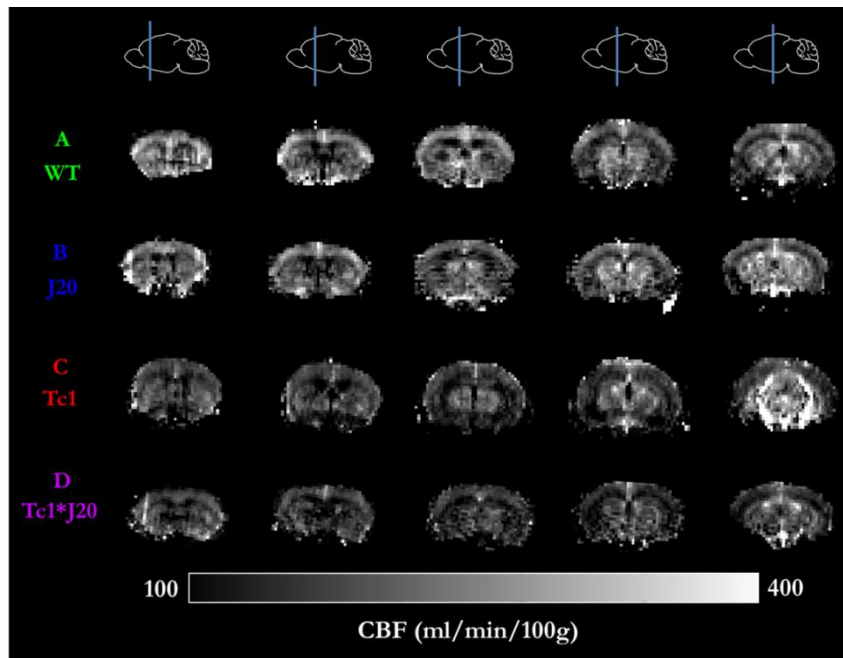
Figure 6.2 *CBF maps for representative (A) wildtype, (B) J20, (C) Tc1 and (D) Tc1*J20 mice.*

CBF was subsequently measured within ROIs within the cortex (Figure 6.3), hippocampus (Figure 6.4) and thalamus (Figure 6.5).

Figure 6.3 shows the CBF results within the cortex. I measured CBF within an ROI taken from the caudal and rostral cortex (Figure 6.3D); these measurements were subsequently averaged to investigate mean cortical perfusion.
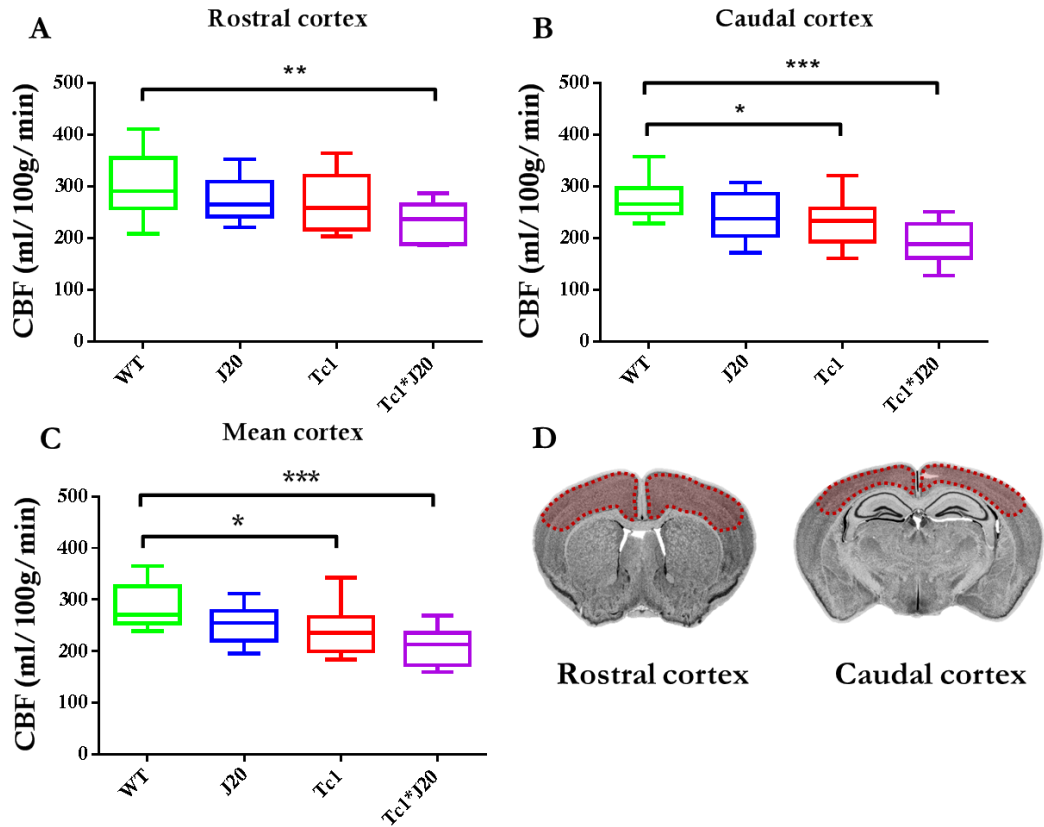
Figure 6.3 *CBF results from the 14 wildtype, 16 J20, 12 Tc1 and 7 J20*Tc1 animals 16 months in the (A) rostral cortex, (B) caudal cortex, and (C) the average of the two ROIs. (D) Cortical ROIs illustrated on slice sections taken from The Mouse Brain Library's Mouse Brain Atlas. A one-way ANOVA with a post-hoc Tukey multiple comparison was performed to identify significant differences between the groups. * = p≤0.05; ** = p ≤0.01; *** = p ≤0.001.*

The mean CBF within the rostral region of the cortex was significantly decreased in the Tc1*J20 mice compared to wildtype controls (p≤0.01) (Figure 6.3A). Within the caudal region of the cortex, I observed a similar decrease in CBF within the Tc1*J20 mice compared to wildtype controls (p≤0.001) (Figure 6.3B). Within this region, I also observed hypoperfusion within the Tc1 DS mice compared to wildtype controls (p≤0.05) (Figure 6.3B). When the caudal and rostral cortical measurements were combined, the CBF deficits within the Tc1 and Tc1*J20 mice retained significance compared to wildtype controls (p≤0.05 and p≤0.001 respectively).

Previously published CBF measurements taken from the J20 AD mice using ASL detected significant hypoperfusion in this model (*197*). Despite observing a significant

decrease in CBF within the caudal cortex of the J20 AD mice compared to wildtype controls (p ≤ 0.05), this significance did not survive Tukey multiple comparison correction (Figure 6.3B).

Mean cortical perfusion was found to be significantly lower in the Tc1*J20 mice (209.8 ± 38.67 ml/100g/min) compared to the J20 AD mice (253.9 ± 35.34 ml/100g/min) (p ≤0.05), however this alteration did not survive Tukey multiple comparison correction (Figure 6.3B).
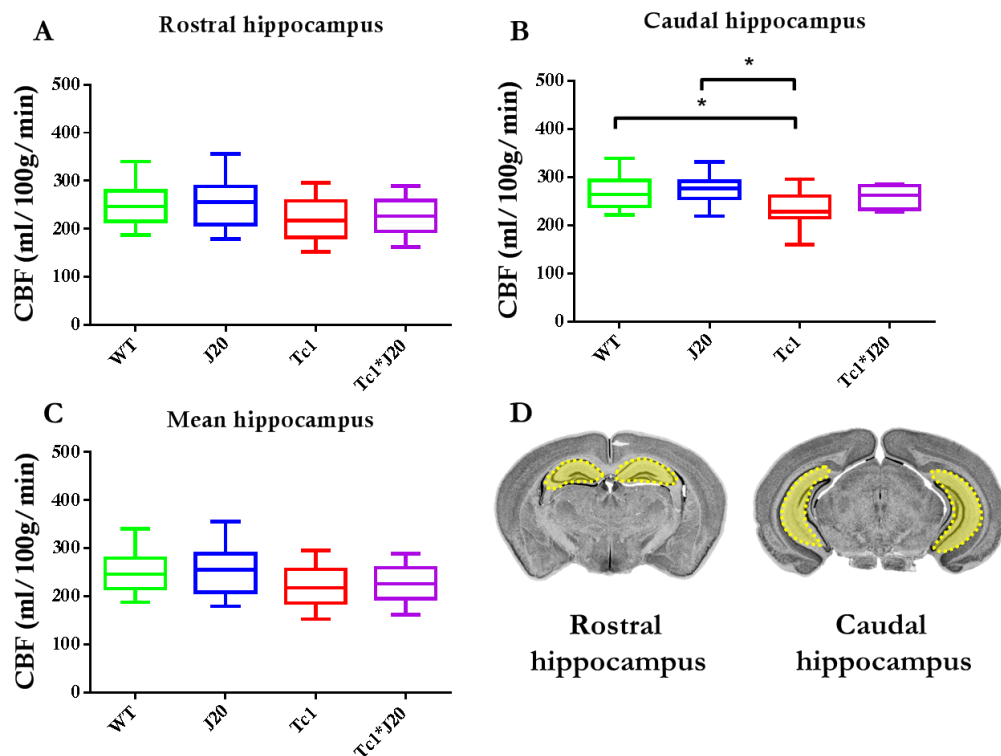
Figure 6.4 *CBF results from the 14 wildtype, 16 J20, 12 Tc1 and 7 J20*Tc1 animals 16 months in the (A) rostral hippocampus, (B) caudal hippocampus, and (C) the average of the two ROIs. (D) Cortical ROIs illustrated on slice sections taken from The Mouse Brain Library's Mouse Brain Atlas. A one-way ANOVA with a post-hoc Tukey multiple comparison was performed to identify significant differences between the groups. * = p≤0.05.*

Within the caudal region of the hippocampus, a significant decrease in CBF was detected in the Tc1 DS mice compared to wildtype controls (p≤0.05) (Figure 6.4B). CBF in the Tc1 DS mice was also significantly reduced in comparison to the J20 AD

mice (p<0.05). These alterations did not retain significance when combined with the measurements from the rostral region of the hippocampus (Figure 6.4C).
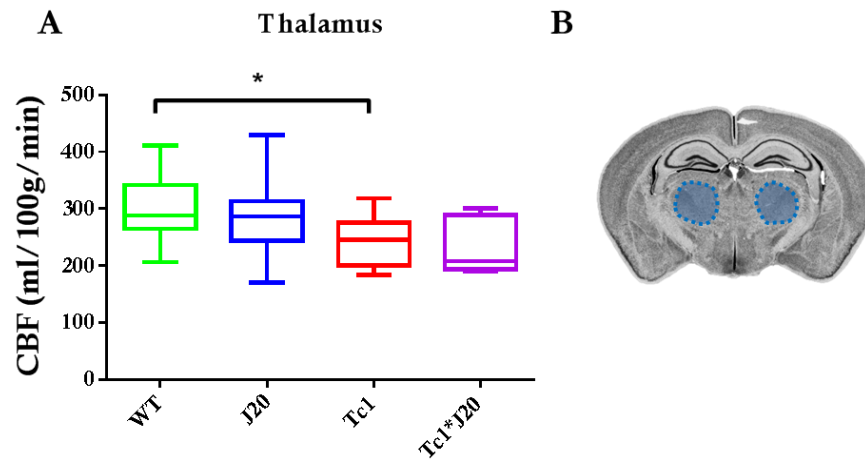
Figure 6.5 *CBF results from the 14 wildtype, 16 J20, 12 Tc1 and 7 J20*Tc1 animals 16 months in the (A) thalamus. (B) Thalamic ROI illustrated on slice sections taken from The Mouse Brain Library's Mouse Brain Atlas. A one-way ANOVA with a post-hoc Tukey multiple comparison was performed to identify significant differences between the groups. * = p≤0.05.*

Within the thalamus, a region of low *APP* expression (*104*), I observed hypoperfusion in the Tc1 DS mice compared to wildtype controls (p≤0.05) (Figure 6.5A). I also observed a significant decrease in CBF within the Tc1*J20 mice compared to wildtype controls (p ≤ 0.01), however this finding did not survive Tukey multiple comparison correction.

In order to elucidate whether the CBF deficits that I observed within the Tc1 mice were a neurodevelopmental or neurodegenerative abnormality, I imaged a separate cohort of young (6 month) Tc1 DS mice (n=5) and wildtype controls (n=6). Figure 6.6 shows the CBF maps for representative wildtype (Figure 6.6A) and Tc1 DS mice (Figure 6.6B). CBF measurements were taken from the same regions as detailed before.
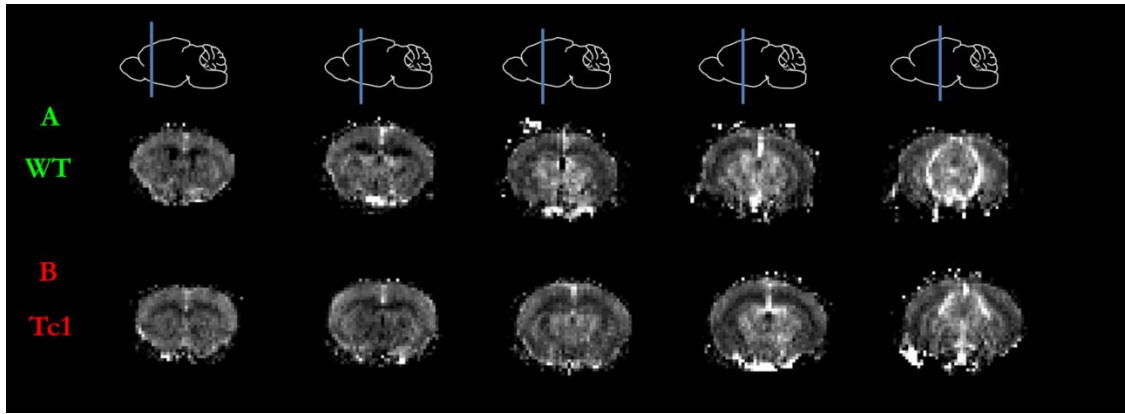
Figure 6.6 *CBF maps for a representative (A-E) wildtype and (F-J) Tc1 mice.*
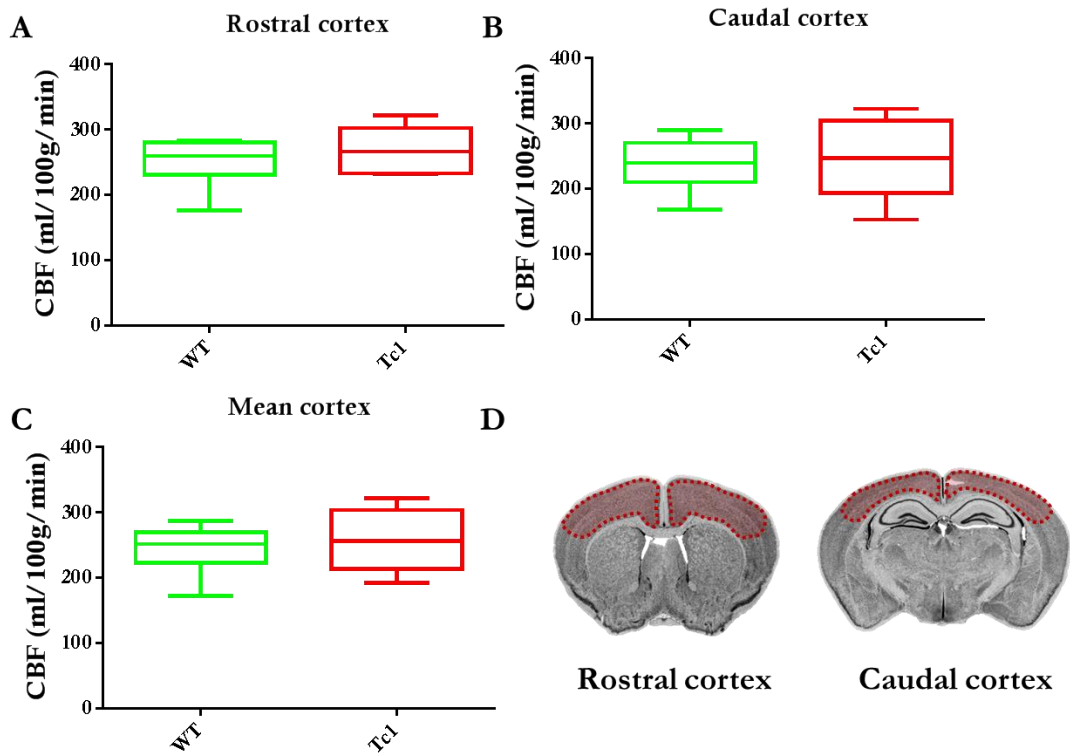
Figure 6.7 *CBF results from the 6 Tc1 and 6 wildtype animals at 6 months in the (A) rostral cortex, (B) caudal cortex, and (C) the average of the two ROIs. (D) Cortical ROIs illustrated on slice sections taken from The Mouse Brain Library's Mouse Brain Atlas. A t-test was performed to identify significant differences between the groups. No significant differences were found.*
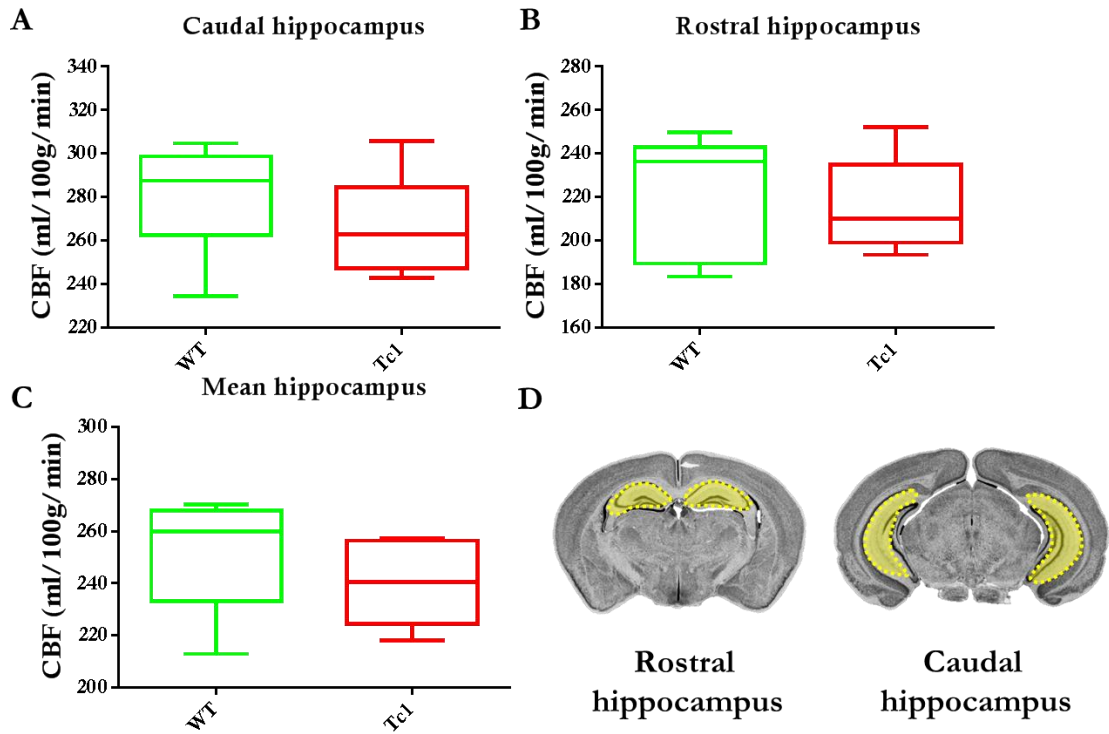
Figure 6.8 *CBF results from the 6 Tc1 and 6 wildtype animals at 6 months in the in the (A) rostral hippocampus, (B) caudal hippocampus, and (C) the average of the two ROIs. (D) Cortical ROIs illustrated on slice sections taken from The Mouse Brain Library's Mouse Brain Atlas. A t-test was performed to identify significant differences between the groups. No significant differences were found. No significant differences were found.*
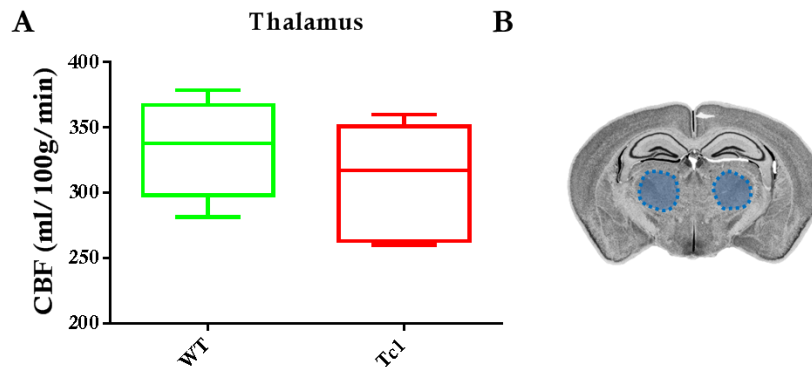
Figure 6.9 *(A) CBF results from the 5 Tc1 and 6 wildtype animals at 5-7 months in the thalamus. (B) Thalamic ROIs illustrated on slice sections taken from The Mouse Brain Library's Mouse Brain Atlas. A t-test was performed to identify significant differences between the groups. No significant differences were found.*

No differences in CBF were detected in any of the cortical regions (Figure 6.7), hippocampal regions (Figure 6.8), or the thalamus (Figure 6.9) at 5-7 months. These findings suggest that the CBF deficits I observed within the aged (16 month) cohort of Tc1 DS mice are due to an age-related decline in cerebral perfusion.

In order to investigate this hypothesis further, the CBF measurements from the 6 month and 16 month wildtype and Tc1 DS cohorts were combined to investigate age-related changes in perfusion within the mice.
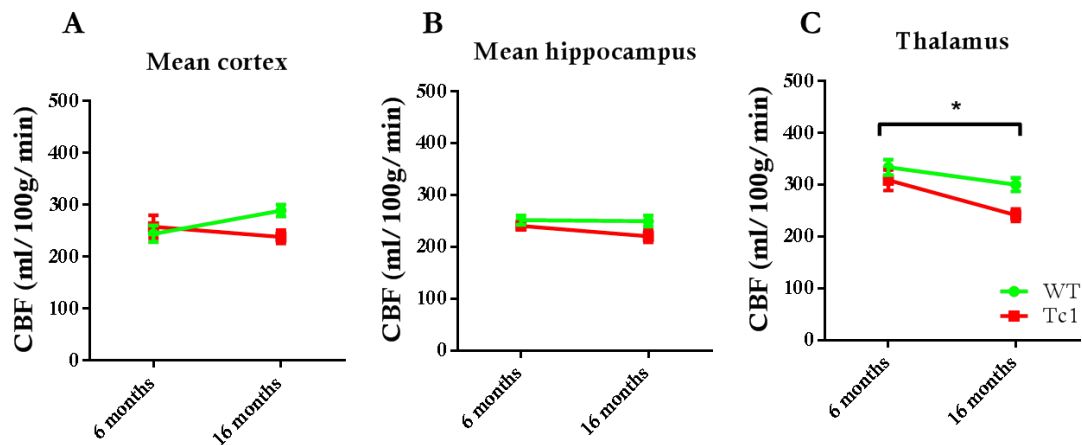
Figure 6.10 *Longitudinal CBF results from the cross-sectional wildtype and Tc1 animals at 6 months and 16 months in the (A) mean cortex, (B) mean hippocampus and (C) thalamus. A 2-way ANOVA with post hoc Sidak multiple comparison was performed to identify significant differences between CBF measurements taken at the different timepoints. 6 month Tc1 vs. 16 month Tc1: * = p < 0.05.*

Figure 6.10 shows the serial CBF analysis within the mean cortex (Figure 6.10A), mean hippocampus (Figure 6.10B) and the thalamus (Figure 6.10C). I observed a significant decrease in CBF within the thalamus of the Tc1 mice from 6 months to 16 months ($p \leq 0.05$), suggesting an age-related decline in perfusion within this region. However, no changes in CBF were detected within the mean cortex or hippocampus of the Tc1 mice.

6.4.2   Magnetic resonance angiography

MR angiograms were acquired in order to investigate vascular alterations in the wildtype, J20, Tc1 and Tc1*J20 mice. My collaborators at the UCL Centre for Medical Image Computing employed TBM in order to explore differences in vascular morphometry between the different cohorts of mice. Figure 6.11 shows the MIP of the

averaged angiograms for wildtype (n=17), J20 (n=18), Tc1 (n= 14) and Tc1*J20 (n=8) following 15 iterations of non-rigid registration.

Many of the major feeding vessels could be readily delineated and identified; vessel labels were adapted from previously published MR angiograms of the mouse brain (*286*). In order to explore morphological changes within the vasculature, the individual angiography images were registered together to create a groupwise average. An intensity threshold was applied, and TBM statistics were performed on the vascular network to identify regions of expansion and contraction.

The average groupwise MRA images are shown in Figure 6.12, with TBM statistics overlaid. TBM detected significant bilateral contraction of the ophthalmic artery, the azygus pericallosal artery and the anterior cerebral artery (Figure 6.12i-ii) in the Tc1 DS mice compared to wildtype controls. Unilateral vessel contraction was detected in the olfactory artery, with statistics localised to the left hemisphere (Figure 6.12i). Bilateral vessel expansion was detected in the posterior cerebral artery and the superior cerebral artery (Figure 6.12Aiii-iv), while unilateral changes were observed in the palatine portion of pterygopalatine. In addition, unilateral expansion of the olfactory artery of the J20 AD mice compared to the Tc1*J20 mice (Figure 6.12Bi) and unilateral expansion within the palatine portion of pterygopalatine (Figure 6.12iv) were detected. TBM did not detect any significant differences between the J20 AD mice and wildtype controls.
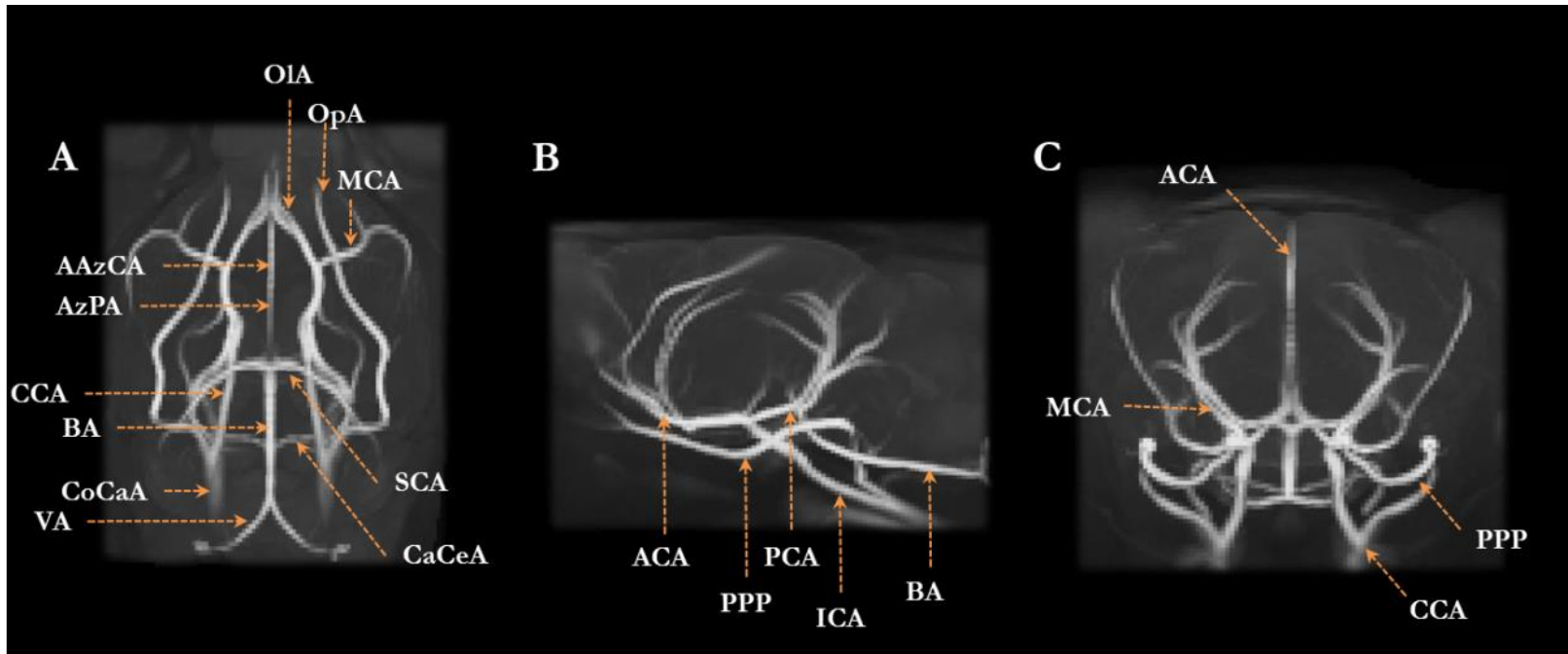
Figure 6.11 *Averaged time-of-flight MR angiograms for wildtype (n=17), J20 (n=18), Tc1 (n= 14) and Tc1*J20 (n=8) following 15 iterations of non-rigid registration. The MIPs are shown in (A) axial, (B) coronal and (C) sagittal orientations. AAzCA = Anterior azygos cerebral artery; AzPA = Azygos pericallosal artery; ACA = Anterior cerebral artery; BA = Basilar artery; CCA = Common carotid artery; CaCeA = Caudal cellebellar artery; CoCaA = common carotid artery; ICA = Internal carotid artery; MCA = Middle cerebral artery; OlA = Olfactory artery; OpA = Ophthalmic artery; PCA = Posterior cerebral artery; PPP = Palatine portion of pterygopalatine; SCA = Superior cerebellar artery; VA = vertebral artery.*
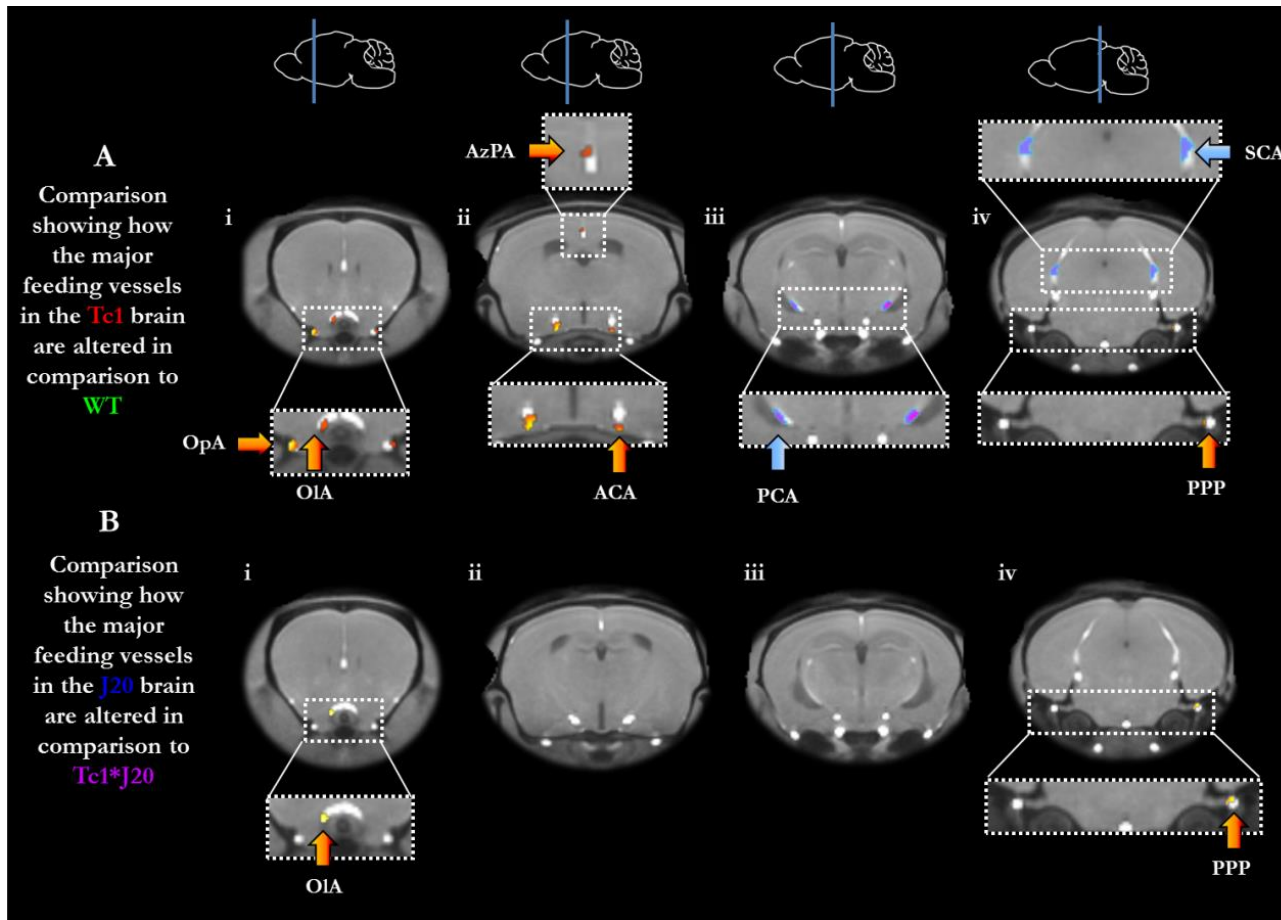
Figure 6.12 *MRA results showing statistically significant, FDR-corrected (q=0.05) t-statistics revealing local differences in vasculature. (A) Vessels in the Tc1 mice are significantly altered in comparison to the wildtype controls; (B) vessels in the J20 mice are significantly altered in comparison to the wildtype controls. Vessels highlighted in red represent a significant volume decrease, in the (A) Tc1 in comparison to wildtype controls and the (B) J20 in comparison to the Tc1*J20 mice. Vessels highlighted in blue represent a volume decrease. TBM results have been normalized to TBV to account for global volume differences between the groups. Arrows indicating regions of change have been coloured to correspond to expansion (blue) and contraction (red) of the vessel they are highlighting. OpA = ophthalmic artery; OlA = olfactory artery; AzPA = azygus pericallosal artery; ACA = anterior cerebral artery; PCA = posterior cerebral artery; PPP = Palatine portion of pterygopalatine; SCA = superior cerebral artery.*

6.4.3 High resolution *ex vivo* structural MRI

Following *in vivo* characterisation, a subset of wildtype (n = 13), J20 (n = 14), Tc1 (n = 15) and Tc1*J20 mice (n = 8) were perfuse-fixed and prepared for high resolution *ex vivo* imaging. My collaborators at the UCL Centre for Medical Image Computing employed atlas-based parcellation to explore regional volume differences between the cohorts of mice, and TBM to examine local morphological alterations.

TBVs were also extracted, to explore and control for overall differences in brain morphometry (Figure 6.13). The TBV results revealed a significant increase in brain volume of the Tc1 DS mice compared to wildtype controls (p≤0.001) (Figure 6.13). I also observed a significant increase in the brain volume of the Tc1 DS mice compared to the J20 AD mice (p≤0.05). Interestingly, I also noted that the mean TBV for the J20 AD mice was larger than the wildtype control values (494.7 ±32.53 mm^3 and 492.6 ± 21.27 respectively); a finding which has previous been observed in the J20 AD mouse at 6 months (*287*). However this observation was not significant.

The Tc1 animals also revealed a surprisingly high variance in TBV compared to the other animal groups under investigation. This is likely to be due to the mosaicism which the Tc1 exhibits – that is, not all cells in the model carry human chromosome 21 (*283*).
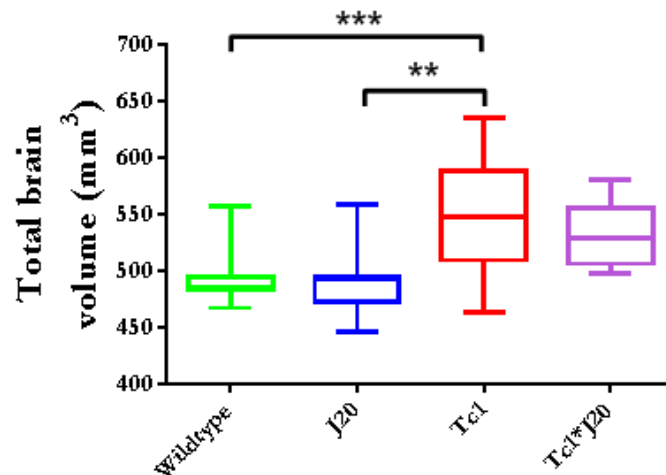
Figure 6.13 *Mean ex vivo TBVs for wildtype (n=13), J20 (n=14), Tc1 (n=15) and Tc1*J20 (n=8) mice.*
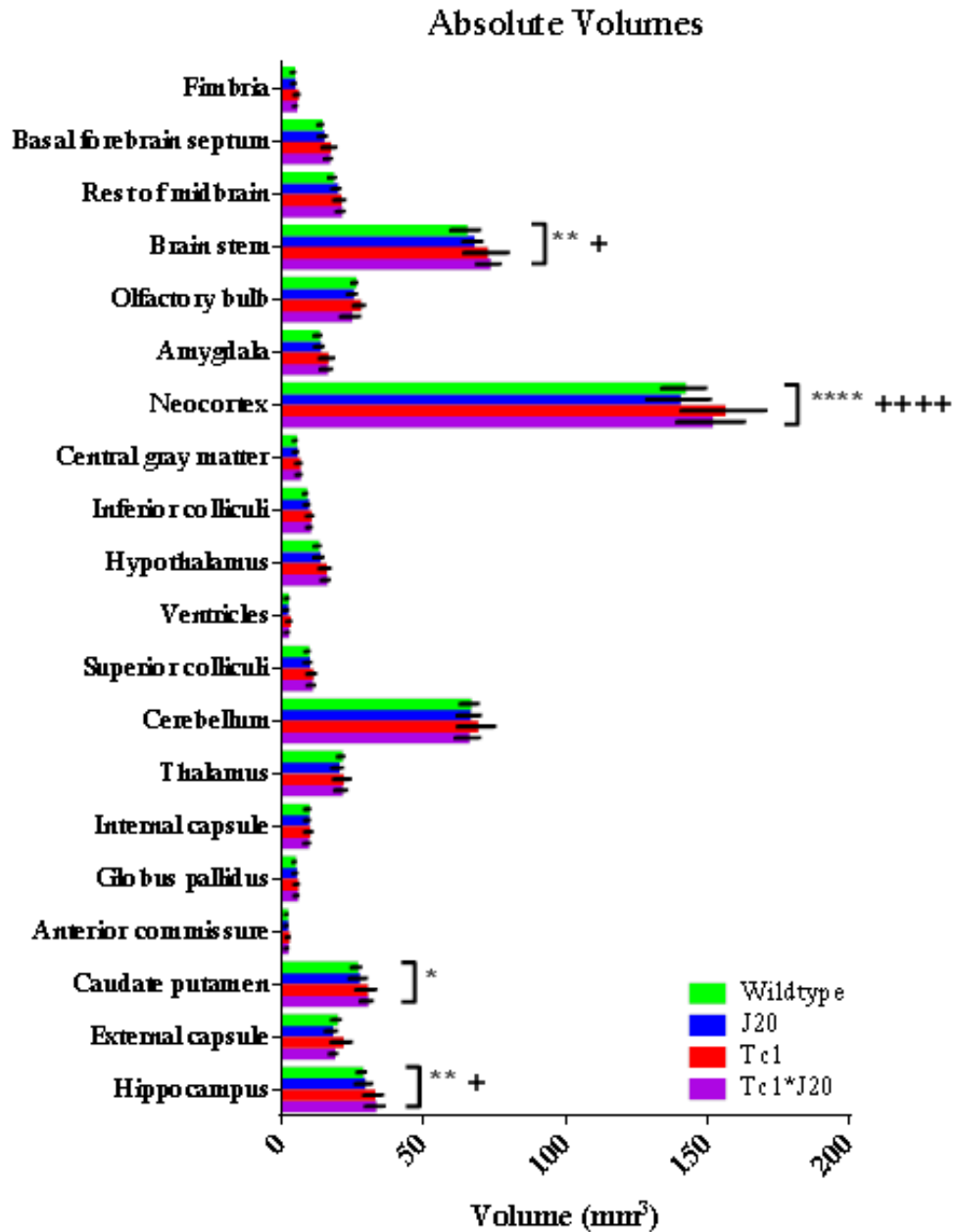
Figure 6.14 *Absolute volume results extracted from the ex vivo structural mouse brain images. A 2-way ANOVA with post hoc Sidak multiple comparison was performed. The results for comparisons between the wildtype and Tc1 mice, wildtype and J20, and J20 and Tc1*J20 are shown. wildtype vs. Tc1: * = p≤0.05; ** = p ≤0.01; **** = p≤0.0001. J20 vs. Tc1*J20: + = p≤0.05; ++++= p≤0.0001.*
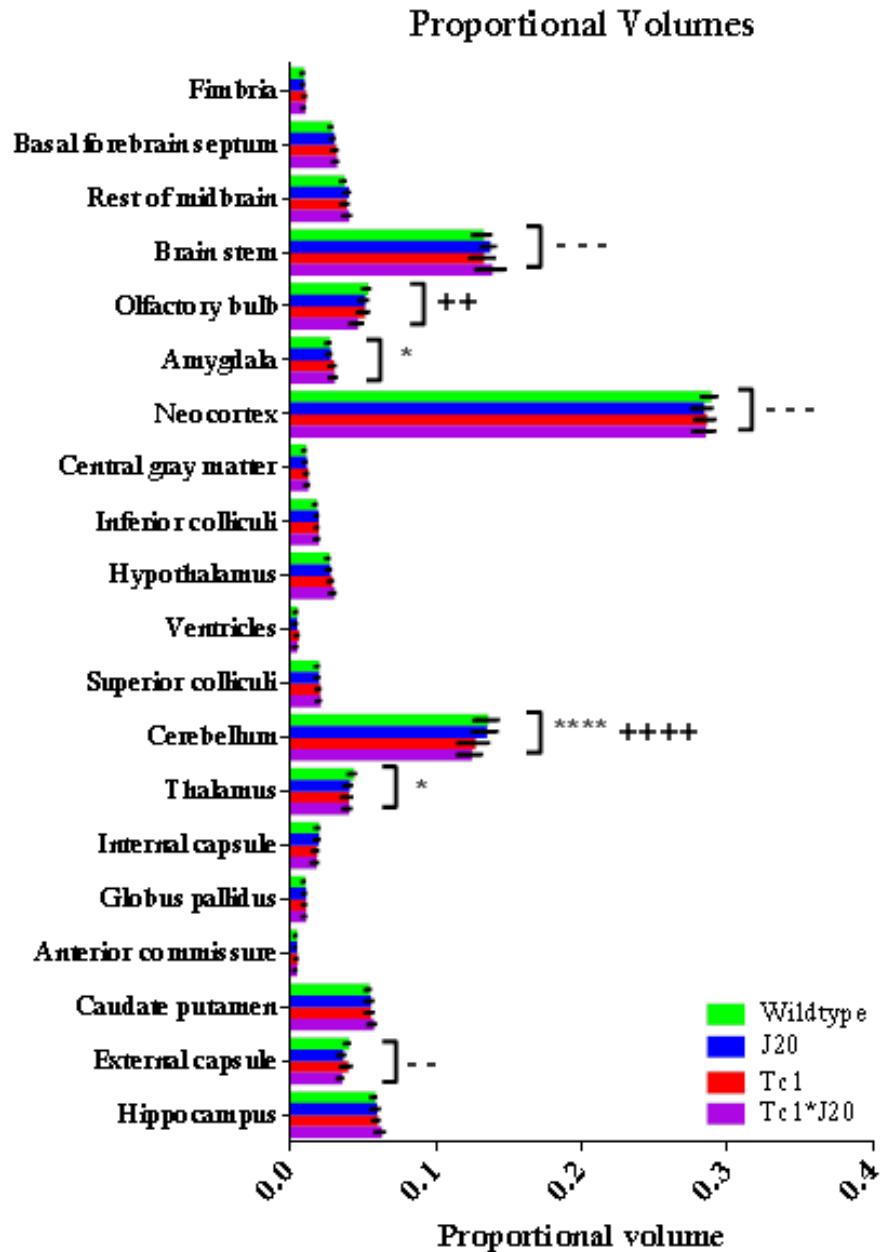
Figure 6.15 *Proportional volume results extracted from the ex vivo structural mouse brain images. The proportional volume changes were calculated by normalising the absolute regional volumes to the TBV (see Figure 6.13. A 2-way ANOVA with post hoc Sidak multiple comparison was performed. The results for comparisons between the wildtype and Tc1 mice, wildtype and J20, and J20 and Tc1*J20 are shown. wildtype vs. Tc1: * = p≤0.05; **** = p≤0.0001. wildtype vs. J20: -- = p ≤0.01; ---= p≤0.001. J20 vs. Tc1*J20: ++ = p ≤0.01; ++++= p≤0.0001.*

The atlas-based parcellation results are shown in Figure 6.14 and Figure 6.15. I have chosen to present the absolute regional volumes (Figure 6.14) in addition to the proportional brain volume changes (Figure 6.15), which were calculated by normalising the absolute volumes (Figure 6.14) to TBV (Figure 6.13).

The TBV results revealed a significant increase in brain volume of the Tc1 DS mice compared to wildtype controls ($p \leq 0.001$) (Figure 6.13). I also observed a significant increase in the brain volume of the Tc1 DS mice compared to the J20 AD mice ($p \leq 0.05$). Interestingly, I also noted that the mean TBV for the J20 AD mice was larger than the wildtype control values (494.7 $\pm$32.53 mm^3 and 492.6 $\pm$ 21.27 respectively); a finding which has previous been observed in the J20 AD mouse at 6 months (*287*). However this observation was not significant. In order to account for these differences, the absolute regional volumes (Figure 6.14) were normalized to TBV to calculate proportional volumes (Figure 6.15).

I did not detect any significance differences in absolute volumes of any of the individual brain structures in the J20 AD mice compared to wildtype controls (Figure 6.14). However, following normalization to TBV, a significant decrease in the proportional volumes of the neocortex ($p \leq 0.001$) and external capsule ($p \leq 0.01$) was detected (Figure 6.15). Atrophy within the cortex has previously been observed in AD patients and related to amyloid-β deposition (*288*); in addition, our findings are supported by previous work where cortical thinning has been observed in the J20 AD model (*197*). White matter alterations have previously been observed in AD patients, and may reflect demyelination and axonal loss in this model (*289*).

Interestingly, a significant increase in the proportional volume of the brain stem of the J20 AD mice compared to wildtype controls was observed (Figure 6.15). Hypertrophy of brain structures has previously been observed in this model and attributed to either an inflammatory response to the presence of amyloid-β, or a compensatory mechanism resulting in enlarged neurons (*287*). In the absence of *APP* overexpression, the observed enlargement of the brain stem may be due to disruption of these tissues during perfuse-fixation of the tissues. I took great care to reduce variability in the tissue preparation wherever possible, by perfuse-fixing all the brains myself using the same experimental protocol, and scanning the animal groups in a randomised way. However, the brain stem is particularly susceptible to disruption which may cause increased variability in the measurements (*189*).

A significant increase in the absolute volumes of the brainstem (p≤0.01), neocortex (p≤0.0001), caudate putamen (p≤0.05), and hippocampus (p≤0.01) was detected in the Tc1 DS mice compared to wildtype controls (Figure 6.14). Following normalization to TBV, these changes did not retain their significance, indicating that these observed regional increases were occurring proportionally to the increase in TBV in the Tc1 DS mice (Figure 6.13). The cerebellum and thalamus, however, were disproportionately smaller in the Tc1 DS mice compared to wildtype controls (p≤0.0001 and p≤0.05 respectively) while the amygdala was disproportionately larger (p≤0.1) (Figure 6.15). The cerebellum has previously been implicated in the Tc1 DS mouse, where decreased granule neurons have been observed.

Within the Tc1*J20 mice, no significant differences in absolute volumes were detected when compared to the J20 AD mice (Figure 6.14). However, following normalization to TBV, a significant decrease in the proportional volume of the olfactory bulb (p≤0.01) and cerebellum (p≤0.01) was observed (Figure 6.15); these regions presented as disproportionately smaller in the Tc1*J20 mice.

In addition to atlas-based parcellation, TBM was employed to identify local small discrete local volume differences which may not be detected when investigating whole brain structures (*287*). The TBM images show statistically significant, FDR-corrected (q=0.05) t-statistics revealing local structural differences between the brains of each group, controlling for TBV (Figure 6.13).
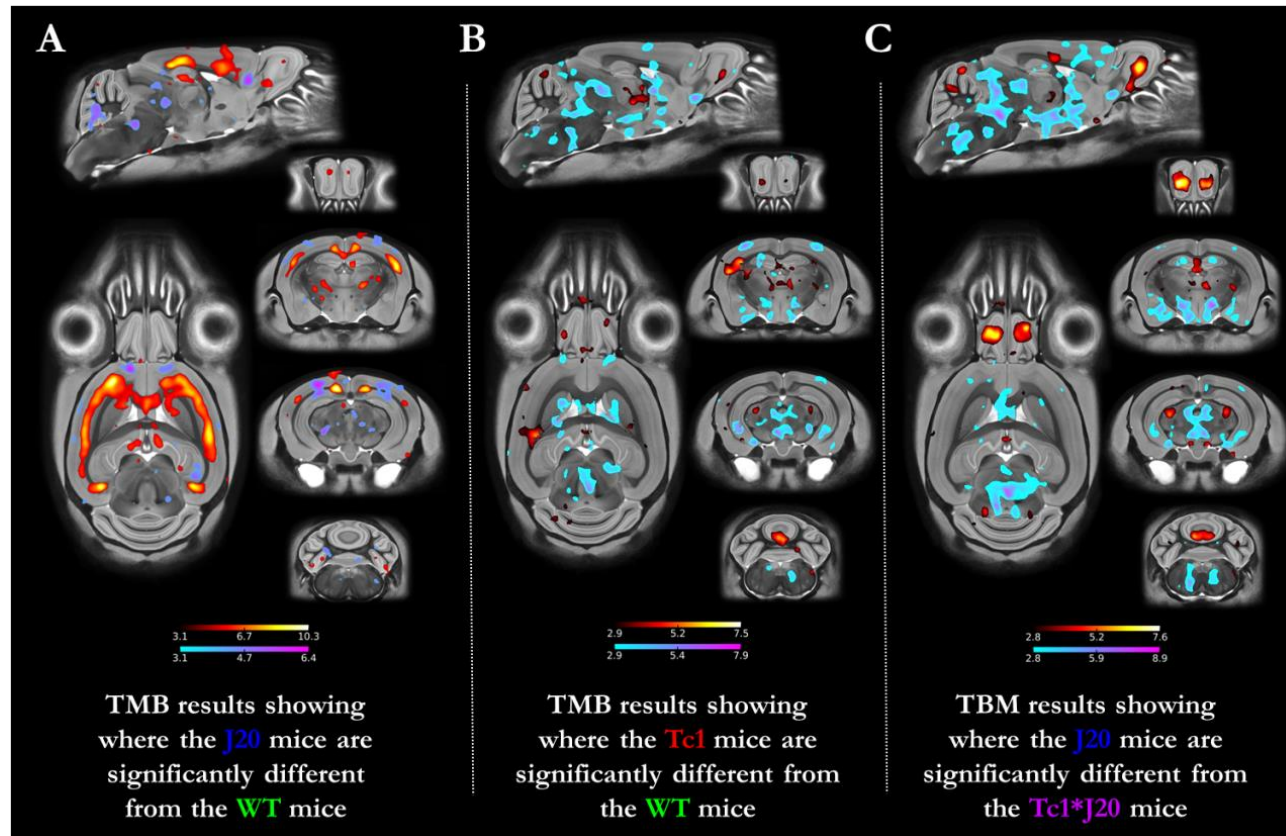
Figure 6.16 *Ex vivo TBM results showing statistically significant, FDR-corrected (q=0.05) t-statistics revealing local structural differences between the brains of the (A) J20 mice compared to wildtype controls, (B) Tc1 mice compared to wildtype controls, and (C) the J20 compared to Tc1*J20 mice. Regions highlighted in red represent a volume decrease, and regions highlighted in blue represent a volume increase. TBM results have been normalized to TBV to account for global volume differences between the groups (see Figure 6.13).*

TBM detected extensive bilateral contraction in the J20 AD mice compared to wildtype controls in multiple cortical regions including: the auditory, cingulate, motor, retrosplenial, somatosensory and visual areas of the cortex (Figure 6.16A). This is in agreement with Herbert et al. who identified increased cortical thinning in the J20 AD mouse (*197*) and is also reflected in our normalized parcellation results (Figure 6.16B). Interestingly, the cortical changes appeared to be localised to the deeper layers, such as the internal granular and pyramidal layers, and multiform layer. The superficial layers appeared unaffected. Atrophy was also observed in the cingulum bundle and corpus callosum – regions which have previous been implicated using voxel-wise analysis techniques (*197*). Volume loss within the CA1 hippocampal subfield, in the absence of any alterations within the CA3 region, was additionally observed. This finding is in good agreement with previous work, where neuronal loss was reported in the CA1 but not the CA3 hippocampal subfield (*290*). It also supports clinical AD findings, as neuronal loss is greatest in this region (*291*).

The Tc1 DS mice exhibited a marked pattern of expansion within the somatosensory and piriform regions of the cortex, with apparent preservation of all other cortical regions (Figure 6.16B). I observed additional expansion within the amygdala, midbrain and the CA1 hippocampal subfield. Atrophy was observed within the molecular and granular layers of the cerebellum, the olfactory bulb, thalamus and caudate putamen (Figure 6.16B). Decreased neuronal counts in the cerebellum have previously been observed in the Tc1 DS mouse and other mouse models of DS, which may be reflected in these structural changes (*283, 292*). Our atlas-based parcellation results also identified decreased cerebellar volume. The other regions implicated by TBM in Figure 6.16B have yet to be explored in the literature.

Figure 6.16C shows the morphological differences between the Tc1*J20 mice compared to the J20 AD mice. A similar yet more extensive pattern of contraction and expansion was detected as observed in Figure 6.16B including atrophy within the cerebellum and olfactory bulb. These regions were also implicated in the atlas-based parcellation results (Figure 6.15). Expansion of the cingulate, motor, somatosensory and auditory regions of the cortex, as well as the midbrain and the CA3 hippocampal subfield, were also observed.

In addition to atlas-based parcellation and TBM, I also scrutinised the unprocessed images for evidence of amyloid-β pathology. It has previously been reported that

amyloid-β plaques can be visualised using high resolution *ex vivo* MRI images in the form of discrete plaque-like hypointensities (*293, 294*). This has been attributed to the T_2 relaxation effect of iron which is contained with the plaque (*295*). Careful examination of our *ex vivo* MRI images did not reveal any hypointensities which could be attributed to plaque pathology. Subsequent histology was performed using Perl's Prussian blue, a stain used to detect the presence of iron within tissues. Perl staining was negative within the hippocampal and cortical tissues – regions vulnerable to plaque pathology in this mouse model – indicating that the plaque pathology in the J20 AD mice doesn't contain iron, or the iron levels are too low to be detected using Perl staining. The absence of iron staining within these regions may account for the absence of hypointensities in our *ex vivo* MRI images.

6.4.4 Histology and immunohistochemistry

Following high resolution *ex vivo* structural imaging, my collaborators at the UCL Institute of Neurology performed histology on a subset of wildtype (n=5), J20 (n=5), Tc1 (n=5) and Tc1*J20 mice (n=5). Immunohistochemistry was performed using the monoclonal antibody 4G8, which stains for amyloid-β.

Figure 6.17 shows sagittal slices stained using 4G8 for representative (A) wildtype, (B) J20, (C) Tc1 and (D) Tc1*J20. Consistent with the literature data, the J20 AD mice exhibited high 4G8 burden within the cortex and hippocampus (5.1 ± 2.8 % and 10.2 ± 3.5 % respectively) (Figure 6.17E-F) (*104, 296*). Negligible 4G8 staining was detected within the thalamus (7.2 ± 6.8 × 10^{-3} %) (Figure 6.17G).

Within the hippocampus, a significant increase in 4G8 burden of the J20 AD mice compared to the wildtype and Tc1 DS mice was observed (p≤0.0001) (Figure 6.17F). Despite observing a significant difference in 4G8 burden of the J20 AD mice compared to wildtype (p = 0.0049) and Tc1 DS mice (p = 0.0035) in the cortex, the significance did not survive Tukey multiple comparison correction (Figure 6.17E)

Similar to the J20 AD mice, the Tc1*J20 mice exhibited high 4G8 burden within the cortex and hippocampus (7.2 ± 5.5 % and 12.77 ± 2.5 % respectively), and low 4G8 burden within the thalamus (5.7 ± 4.3 x10^{-3} %). When compared with the J20 AD mice, a 40.0% increase in 4G8 burden within the cortex, and a 25.6% increase in 4G8 burden within the hippocampus were noted; however, this observation was not statistically significant.
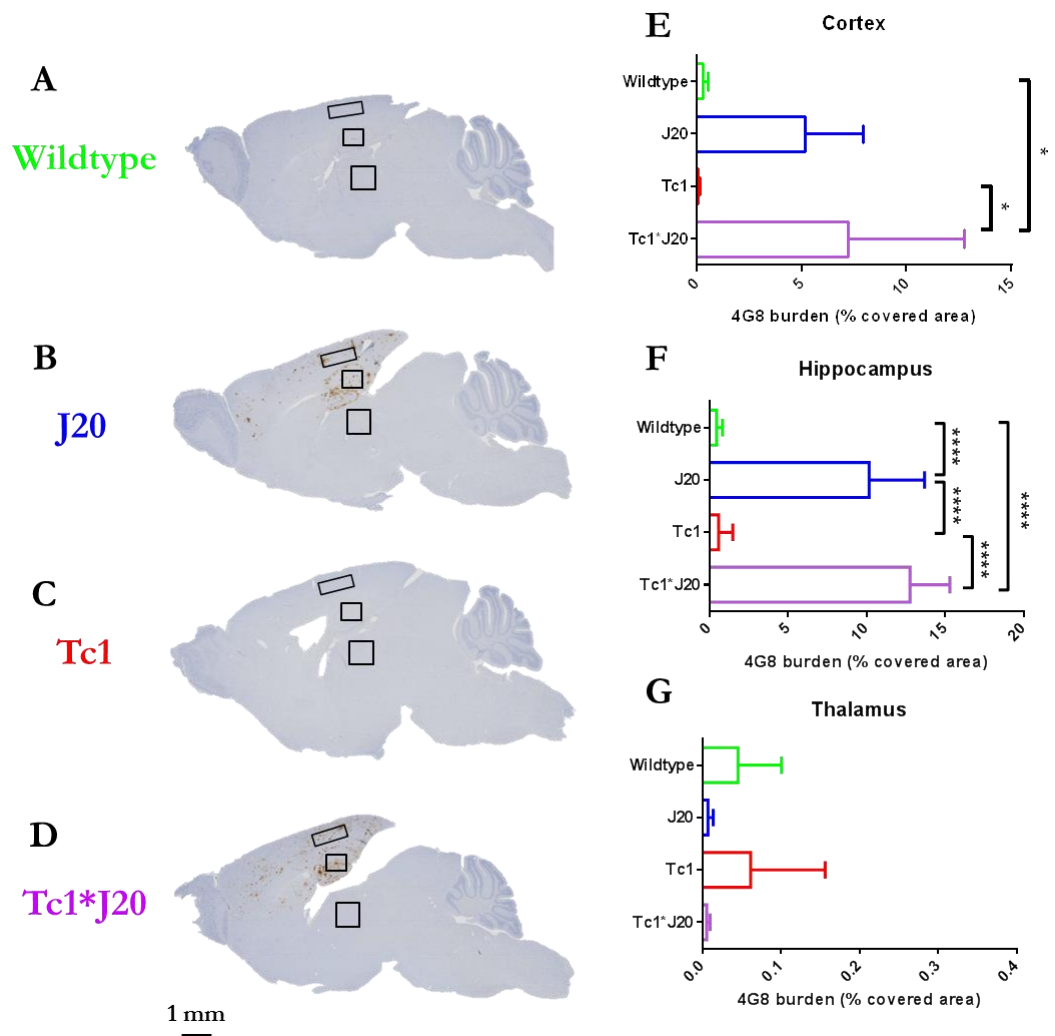
Figure 6.17 *Immunohistochemistry to estimate regional distribution of amyloid-β using the 4G8 antibody. Sagittal slices for representative (A) wildtype, (B) J20, (C) Tc1 and (D) Tc1*J20 mice, illustrating the distribution of amyloid-β, with visible accumulation in the cortex and hippocampus of the J20 and Tc1*J20 mice. Quantitative regional estimates of (E) cortical, (F) hippocampal and (G) thalamic 4G8 % burden for wildtype (n=5), Tc1 (n=5), J20 (n=5) and Tc1*J20 (n=5) mice. A one-way ANOVA with a post-hoc Tukey multiple comparison was performed to identify significant differences between the groups. * = p ≤ 0.05; **** = p ≤ 0.0001.*

6.5 Discussion

In spite of recent advances in our understanding of AD, the cause of the disease is yet to be fully understood. People with DS carry an increased risk of developing early onset AD, with 50 – 70% of DS individuals exhibiting symptoms of dementia before the age of 60 (*297*). Studying individuals with DS, and the onset and development of AD within this population, can offer unique insights into the pathogenesis of AD within the wider population. Triplication of the *APP* gene, which lies on chromosome 21, is believed to drive the development of AD by increasing the production of amyloid-β. Subsequent misfolding of amyloid-β results in the deposition of amyloid-β plaques – the classic neuropathological hallmark of AD, and believed by many to be the key causative agent in the disease (*24*). Indeed, DS individuals with partial trisomy of chromosome 21 resulting in *APP* disomy do not develop AD (*298*). However, it is believed that a number of other genes on chromosome 21 may contribute to the early onset of AD within DS (*282*).

In this work, I have characterised the J20 AD mouse, a model of amyloid plaque deposition, and the Tc1 DS mouse using MRI. In addition, the effects of chromosome 21 on AD pathogenesis have been introduced to the J20 AD mouse by breeding it with the Tc1 DS mouse – the progeny of which overexpress a mutant form of *APP* in the presence of chromosome 21 genes. The immunohistochemistry identified an increase in mean 4G8 staining within the cortex and hippocampus of the Tc1*J20 mice compared to the J20 AD mice; however this finding was not significant. I continued to probe for alterations in the MR parameters between these two mice cohorts, in addition to broader characterisation of the phenotypic differences in the J20 AD and Tc1 DS mice compared to wildtype controls.

In my analysis of the CBF data, I focused on the hippocampus and cortex as regions selectively vulnerable to amyloid-β pathology in the J20 AD model. These have been both previously reported (*104*), and replicated in our immunohistochemistry using the 4G8 stain for amyloid-β. The thalamus served as a control region without amyloid-β pathology. As the MRA and structural imaging sequences covered the whole brain, it was possible to implement automated atlas-based processing techniques, enabling the dissection of changes occurring globally.

ASL is an emerging MR biomarker of neurodegeneration, and is increasingly being applied to investigate regional CBF alterations in AD (*299*). A number of cortical regions have been reported to suffer hypoperfusion in AD, including the parietal and occipital lobes of the cortex, and the cingulate (*300*). The precise mechanisms underpinning these CBF alterations are not fully understood; however, they are believed to be associated with atrophy of neuronal tissues in regions vulnerable to AD neuropathology, as well as regions functionally connected to these degenerating tissues (*301*).

Previous work by Hébert et al. characterised a cohort of 6 month J20 AD mice using ASL, and identified hypoperfusion in subcortical regions including the somatosensory, entorhinal and piriform regions of the cortex (*197*). I observed reduced perfusion in the J20 AD mice within an ROI placed caudally in the caudal cortex (p ≤; this ROI encompasses the somatosensory region of the cortex, supporting Hérbert et al.'s previous findings. However, our results lacked the significance to survive correction for multiple comparisons. Hérbert et al. noted that, when the whole cortical CBF was measured, no significant differences were observed, and emphasised the importance of examining sub-regional changes which may be obscured when extracting global measurements (*197*). In our analysis, I focused on a caudal and rostral ROI placed within the cortex, and averaged these measurements to explore mean cortical perfusion; however, these ROIs may have been too large to capture any sub-regional changes occurring.

In contrast to the growing body of research into perfusion in AD, there are substantially fewer publications into CBF alterations in DS. To our knowledge, ASL has never been applied to a DS cohort – clinically or preclinically. A number of studies have employed single photon emission computed tomography (SPECT) to explore CBF in individuals with DS, and identified perfusion deficits similar to those seen in AD patients (*302, 303*). However, it is still unclear whether these alterations are present in the absence of AD neuropathology. Gokcora et al. reported patterns of hypoperfusion in a study of young non-demented DS individuals, and suggested these findings may reflect higher cortical dysfunction (*304*). Conversely, Deb et al. reported no CBF alterations in younger, non-demented DS individuals (*305*), indicating that blood flow deficits may be due to an age-related decline and accompany the descent into dementia.

Hypoperfusion was observed in the Tc1 DS mouse in all regions under investigation – the cortex, hippocampus and thalamus. This suggests a global reduction in CBF, although additional ROIs placed within more posterior and anterior slices of the brain are required to confirm this. These findings, in the absence of amyloid-β, are in agreement with Gokcora et al. and may reflect mental abnormalities or dysfunction (*304*). A follow-up study in younger Tc1 DS mice identified no deficits in CBF, suggesting age-related decline in perfusion. In the absence of *APP* triplication, these findings suggest that hypoperfusion in DS individuals may be related to trisomy of other chromosome 21 genes.

The Tc1 DS mouse exhibits a number of congenital heart defects which should also be considered when interpreting the CBF findings (*306*). These defects include perimembranous atrioventricular septal defect and ventricular septal defect which are also seen in the wider DS patient population.(*307*). Previous work exploring the relationship between cardiac output and CBF has found that cerebral autoregulation maintains CBF despite perturbations in systemic blood pressure associated with such cardiac abnormalities (*308*). Therefore, it is unlikely that our observations of hypoperfusion in the Tc1 DS mice relates to their cardiac defects.

The Tc1*J20 mice exhibited marked hypoperfusion within the cortex, to a greater extent than the Tc1 DS mice. These findings suggest that trisomy of chromosome 21 genes exacerbate the pathological processes, and may be related to the early-onset AD seen in the DS population.

There is mounting evidence implicating vascular alterations in clinical cases of AD (*309*). This includes a number of risk factors for AD which carry a vascular component, including diabetes (*310*) and atherosclerosis (*311*). In addition, depositions of amyloid-β around vessel walls are frequently observed in post-mortem AD brains – a condition called cerebral amyloid angiopathy (*309*).

MRA is a useful MRI technique for studying alterations within the artery vasculature, and permitted the study of differences in the morphology of large feeding arteries between the transgenic cohorts in this study. MRA is traditionally quantified manually, by visual inspection of whether the vessels appear altered within a transgenic cohort (*312*). However, it is possible to misinterpret flow artefacts as vascular alterations, including flow disturbances and signal voids (*313*). In this work, my collaborators at the

UCL Centre for Medical Image Computing registered the individual angiograms together to create an average atlas of the vasculature; this methodology provides a robust and unbiased framework for evaluating alterations in the cerebral vessels, and help mediate the confounding effects of flow artefacts as these are averaged out in the atlas (*312*). Visual inspection of the average vascular atlas revealed adequate contrast to detect many vessels previously identified by Kara et al. including branches of the cerebral and carotid arteries (*286*).

Previous work in other AD mouse models overexpressing mutant *APP* have reported deficits in the middle cerebral artery (*286, 314*); alterations which have also presented in clinical cases of AD (*315*). However these models also carried PSEN1 mutations, which are known to accelerate the deposition of amyloid-β and exaggerate the AD phenotype (*316*). In this study, I did not detect any alterations in the vasculature of the J20 AD mouse. In the absence of any significant CBF alterations, this finding was not unexpected. The 4G8 staining revealed cerebral amyloid angiopathy around the meningeal and parenchymal vessels in the brain, indicating amyloid-β pathology within the vasculature; however, the vessels implicated by the MRA results have yet to be investigated. The absence of any significant findings in the J20 AD mice, therefore, may be a shortcoming of the MRA sequence itself, which lacks the sensitivity to detect smaller arteriole and venous alterations. The use of an endogenous contrast agent may have improved vessel delineation and highlighted smaller changes occurring within the finer vascular structures (*317*).

The vascular alterations identifiable using MRA were markedly more extensive in the Tc1 DS model. Our observations of extensive vascular alterations within the olfactory, opthalamic, azygous pericallosal and anterior cerebral arteries may have arisen for a number of reasons, including narrowing or compression of the vessels, or reduced blood flow within these regions (*286*). Conversely, regions of artery expansion, including the posterior and superior cerebral arteries, suggest increasing flow or widening of the vessels.

Contraction of the olfactory artery may be related to the local volume decreases observed within the olfactory bulb of the Tc1 DS mice, although further work at earlier timepoints is required to determine whether this vascular alteration pre or proceeds the changes identified using TBM. This vessel was also implicated in the Tc1*J20 mice, with corroborative structural alterations in the olfactory bulb, supporting the abnormal

function of the olfactory artery in DS. I was unable to corroborate any of the other observed angiography alterations against the structural results, indicating high resilience of the Tc1 DS mice to alterations in the vascular.

Atrophy of the brain is a widely acknowledged occurrence in neurodegeneration, and structural changes identifiable using MRI are an accepted biomarker of AD (*98*). In this work, my collaborators at the UCL Centre for Medical Image Computing have employed two automated image processing techniques to characterise morphological differences between the mice cohorts.

Badhwar et el. have previously characterised the J20 AD mouse at 6 months using atlas-based structural analysis and identified significant volume increases in the 36 of the 64 structures under investigation, including the cortex and hippocampal subfields (*287*). Badhwar et al. attributed these unexpected findings to neuroinflammation in the absence of atrophy (*195*), and increased neurogenesis in response to *APP* overexpression (*318*). In addition, there is growing evidence in support of neuroinflammation as a major contributing factor in AD pathogenesis (*319*): gliosis has previously been observed within the hippocampus of the J20 AD mouse at 6 months (*290*); this is known to activate inflammatory processes and may be the underlying cause of the hypertrophy observed by Badhwar et al. (*290*). PET tracers targeting the 18 kDa translocator protein have been identified as promising biomarkers of microglial activation (*320*), and may shed light on neuroinflammation in the J20 AD mouse.

Our observation of atrophy within the cortex and CA1 hippocampal subfield at 16 months, following plaque deposition from 6 months (*104*) therefore represents downstream findings in this model. Badhwar et al. performed additional voxel-wise analysis and observed local atrophy within the corpus callosum and cingulum bundle – findings which were replicated in our TBM analysis. Alterations within these white matter regions may serve as a precursor to the widespread cortical atrophy that I observed at 16 months.

Atrophy within the olfactory bulb was also detected, a finding which has been observed within AD patients (*321*) and manifests clinically as difficulty identifying familiar odours using the *Brief Small Identification Test* (*322*). Previous work by Cao et al. in the J20 AD mouse found disrupted connectivity of the olfactory neuronal circuit (*323*) – deficits which may underpin our structural changes within the olfactory bulb.

Our TBM findings in the J20 AD mouse also identified marked atrophy occurring within the deeper cortical layers. This was unexpected, as it has been reported that the neurons of the deeper cortical layers are more resilient to the neurotoxic effects of amyloid-β deposition than the associated superficial neurons (*324*). Additionally, in clinical studies of AD patients, it has been reported that the superficial cortical layers are more vulnerable to plaque deposition (*325, 326*). Closer inspection of the distribution of 4G8 staining within the cortex of the J20 AD mice did not reveal increased specificity of the antibody for the deeper cortical layers, suggesting an alternative mechanism producing this unique pattern of changes, which at this stage remains unknown.

The Tc1 DS mouse presented with a pattern of TBM changes which mirror deficits previously observed within the DS population; this includes cerebellar alterations (*327*), which have been related to the motor disabilities observed in DS individuals (*328*). The Tc1 DS mice exhibited larger TIVs in comparison to the wildtype controls; this finding was unexpected, as reduced TBV has been reported in clinical studies of DS (*329*). It may be due to increased neurogenesis owing to trisomy of chromosome 21 genes. A large variation in the TBV measurements of the Tc1 DS mice was also observed; this is likely to be because the Tc1 DS mice are mosaic for chromosome 21, which is carried by different proportions of cells in different tissues (*283*).

TBM analysis uncovered atrophy within the olfactory bulb of the Tc1 DS mice – a finding which has not previously been discussed in the literature. Deficits within the olfactory bulb suggest impaired sense of smell in the Tc1 DS mouse – a finding which has previously been observed in DS individuals and attributed to AD-related changes within the DS population (*330*). A study of young DS adolescents did not identify any deficits in their ability to smell, further suggesting that this is an age-related decline in function (*331*). In the absence of AD neuropathology, our findings within the olfactory bulb suggest that deficits may be present in the DS population prior to the development of dementia. This, coupled with the vascular alterations within the olfactory artery, heavily implicate the olfactory bulb as a structure which is altered in DS.

The introduction of amyloid pathology in the Tc1*J20 mouse amplified the atrophy observed within the olfactory bulb, suggesting that the deficits within this structure are influenced by the combination of chromosome 21 genes and mutant *APP* overexpression.

6.6 Conclusion

In this chapter, I have used multi-parametric MRI to characterise the Tc1 DS mouse and the J20 AD mouse. Breeding these two mouse strains together produced the Tc1*J20 mouse, permitting the evaluation of AD-related changes both with and without *APP* trisomy.

Our MRI findings revealed previously unexplored alterations in the Tc1 DS mouse model; this includes cerebrovascular alterations and structural changes in the absence of *APP* trisomy. Further work is required to explore whether these are neurodevelopmental or age-related alterations. The J20 AD mouse has been extensively characterised in the literature; this includes a number of MRI studies. I have echoed previous findings, and also identified novel cortical specificity of brain atrophy which has not previously been described. Finally, the Tc1*J20 mouse revealed a number of amplified deficits, highlighting the influence of chromosome 21 genes on AD neuropathology. This work supports ongoing efforts to understand early onset AD within DS individuals, and may shed light on the role of genes other than *APP* which contribute to this increased risk.

Chapter 7: General discussion

According to the 2015 World Alzheimer report (*332*), there are an estimated 46.8 million people worldwide living with dementia at a total cost of more than $818 billion globally. With no known cure for this debilitating disease, a collaboration of scientists across the world is united in their efforts to identify the cause of AD, and develop effective disease-modifying therapies.

Mouse models of AD are valuable research tools, permitting the dissection of specific neuropathological events underpinning AD in highly controlled laboratory conditions. The most widely used AD mouse models are transgenic for human APP, and carry specific mutations associated with familial forms of the disease. These mice are reliable models of amyloid-β plaque formation; however they do not recapitulate the tau pathology in AD. In light of recent evidence in support of tau's primary role in the neurodegenerative cascade (*152*), mouse models expressing mutant human tau are increasingly being used to explore the degenerative effects of NFT pathology. Robust biomarkers of tau pathology are required in order to identify novel deficits in these mice, in addition to supporting preclinical trials of candidate therapeutics.

In Chapter 3, a sequence for high resolution *in vivo* mouse brain imaging was developed, for application in the rTg4510 mouse model of tauopathy. Scan parameters were carefully optimised for suitability for advanced image processing techniques; this included high resolution, isotropic voxels and whole brain coverage within a feasible *in vivo* imaging time of 90 minutes. It was found that a T_2-weighted sequence, with a TE of 43ms, would offer maximum contrast between the hippocampus and thalamus, whilst also retaining high contrast in the cortex and corpus callosum.

The optimised structural sequence was subsequently implemented in a single timepoint study of the rTg4510 mouse model of tauopathy. Gross morphological differences were readily detectable by eye in agreement with a previous study (*157*), while further analysis identified a negative correlation between hippocampal volume (manually segmented) and NFT density. These findings highlight the sensitivity of structural MRI to neurodegenerative alterations occurring in this mouse model, with potential application for *in vivo* evaluation of other mouse models of AD.

In order to ease the burden of time-consuming manual delineation of ROIs and reduce user bias, TBM was employed for global analysis of morphological alterations in the rTg4510 mice. A bilateral pattern of atrophy was detected in regions susceptible to NFT deposition including the cortex, caudate putamen and hippocampus. These results support the suitability of the optimised structural sequence for advanced image processing techniques, which will facilitate high throughput analysis of future studies of the rTg4510 mouse. As there is no limit to the number of mouse brain data sets that may be registered, potential applications of this technique includes quantitative analysis of large (>100) data sets, with increasing statistical power of the TBM results.

The development of this sequence laid the foundations for Chapter 4, where *in vivo* structural MRI was employed in a longitudinal study of neurodegeneration in the rTg4510 mouse. Atlas-based parcellation was employed alongside TBM for structural characterisation; this technique permitted the evaluation of absolute volume changes, in addition to those occurring disproportionately to TBV. The administration doxycycline to a subset of rTg4510 mice at discrete timepoints permitted the evaluation of two imaging paradigms: i) exploration of the longitudinal degenerative changes occurring in the rTg4510 mouse, and ii) assessment of the therapeutic impact of doxycycline. Additional biomarkers of AD neuropathology were recruited in order to explore their sensitivity to the accumulation and suppression of pathological tau. CEST, DTI and ASL were selected for their clinical translatability, in addition to their sensitivity to distinct pathological mechanisms implicated in AD.

The results showed that high resolution structural MRI, when used in conjunction with advanced image processing techniques, yielded the highest sensitivity to pathological changes occurring in this model. Atlas-based parcellation was able to discriminate between the rTg4510 mice and wildtype controls as early as 3.5 months, with tau-driven atrophy (inferred by the proportional volume results) detectable from 5.5 months in this model. Atrophy was greater reduced in animals treated with doxycycline from 3.5 months than from 4.5 months, highlighting the sensitivity of the structural MRI sequence to early therapeutic intervention. CEST, DTI and ASL provided insight into pathological mechanisms occurring within the disease process, and were also able to detect significant differences between treated and untreated rTg4510 animals as well as wildtype controls. These non-invasive MRI techniques offer insight into pathological

mechanisms underpinning AD that may be important when evaluating emerging therapeutics targeting one of more of these processes.

Despite the increasing application of structural MRI to mouse models of neurodegeneration, the pros and cons of scanning a mouse alive or dead have yet to be fully explored in the literature. Chapter 5 explores the trade-offs between *in vivo* and *ex vivo* MRI, and the suitability of structural data sets for TBM analysis.

It was observed that both *in vivo* and *ex vivo* MRI were able to detected a widespread bilateral pattern of severe atrophy in the rTg4510 mouse brain compared to wildtype controls at the 7.5 month timepoint; regions of atrophy were co-localised with neuronal loss and pathological tau accumulation demonstrated by immunohistochemistry. SNR measurements were greater in the *in vivo* data (likely primarily driven by the reduced spatial resolution), although CNR was greater in the *ex vivo* data sets; a finding that can be attributed to the strategic use of contrast agents during preparation of the *ex vivo* tissues. When TBM was employed to uncover differences in a cohort of doxycycline-treated rTg4510 mice, *ex vivo* MRI detected extensive alterations, more sensitive than our *in vivo* findings. However, this increase in sensitivity should be considered against the disadvantages of *ex vivo* MRI which include the effects of formalin fixation on tissues, and the inability to image the same animal longitudinally, prohibiting studies of neurodegeneration in the same mouse cohort. The disparity between our TBM findings from *in vivo* and *ex vivo* MRI, underlines the importance of appropriate study design, given the trade-off between the two imaging approaches. Through my exploration of these factors, I hope this work will help support research groups working in the field of preclinical MRI, and shape their decision about the best way to image their transgenic mice.

So far, the results chapters have focused on the sensitivity of structural and functional MRI techniques to tau pathology in the rTg4510 mouse. In the final results chapter, MRI techniques were employed to explore the role of genetics in AD, to uncover whether chromosome 21 genes other than *APP* influence the AD neuropathology seen universally among DS individuals.

The results in the J20 mouse echoed previous findings in this mouse model, which has been extensively characterised in the literature. Novel blood flow alterations were identified in the Tc1 DS mouse, in the absence of *APP* trisomy; this included marked

hypoperfusion in all regions under investigation: the cortex, hippocampus and thalamus. Additional alterations were observed within the vasculature of the Tc1 DS mouse, which were detected by generating a groupwise average of the MR angiograms - a novel approach to the analysis of such data sets. These findings further support the use of voxel-wise techniques for analysis of mouse brain MRI data, to detect statistically significant findings which may be difficult to detect using laborious manual methods.

By crossing the Tc1 DS mouse to the J20 AD mouse, the offspring developed characteristic amyloid-β plaques in the presence of additional chromosome 21 genes. The observed abnormalities in MRI biomarkers appeared to be exacerbated in the Tc1*J20 mouse, including CBF and histological assessment of plaque density, although none of these findings survived correction for multiple comparisons. Increasing the size of the Tc1*J20 cohort (n = 9) may have helped unambiguously demonstrate these differences.

7.1 Limitations

When interpreting the work presented in this thesis, a number of limitations must be taken into account when planning future studies. Firstly, it is important to consider that the work presented in Chapters 3, 5 and 6 is from late timepoint studies, where the pathology in these animals is fairly advanced. When planning these experiments, I chose an advanced timepoint in order to assess the sensitivity of the different imaging sequences to neuropathological alterations in the different models, and increase the likelihood of detecting significant correlations between histological assessment of NFT burden (which occur relatively late in the pathology) and imaging biomarkers. However, earlier timepoints are useful for investigating the sensitivity of imaging biomarkers to small discrete alterations occurring before the onset of gross neurodegeneration. This limitation has, to some extent, been addressed in Chapter 4, which describes the structural and functional changes occurring in the rTg4510 mouse from 3.5 months of age. It would be useful to characterise the J20 and Tc1 mice in a similar way, using multi-parametric MRI in a longitudinal study of neurodegeneration.

In addition, the studies presented in this thesis also only focus on the development and application of different MRI biomarkers which offer sensitivity to AD-related changes. For future studies, it would be beneficial to consider behavioural assessment of the

transgenic mice (e.g. with a Morris water maze, which is sensitive to CA1 hippocampal subfield damage) in conjunction with MRI assessment. In addition to offering an alternative insight into cognitive alterations in the transgenic animals under investigation, behavioural assessment more closely mimic the current clinical AD diagnostic criteria, which relies on neuropsychological testing.

It is also worth considering that the application of the multi-parametric MRI protocol is time-consuming, especially when performing longitudinal studies. Therefore, this protocol may not be feasible for groups with limited access to an MRI scanner.

In Chapter 5, I attempt to address an important question within the preclinical imaging community and explore the advantages and disadvantages of *in vivo* and *ex vivo* high resolution structural imaging of the mouse brain. I implement a fully optimised *in vivo* and *ex vivo* acquisition and analysis protocol respectively, in order to provide a meaningful comparison that is relevant to future studies of transgenic mice. Although I have not explored all possible methodological combinations when making this comparison (e.g. imaging time, different RF coils etc.), I hope that this work will provide a useful starting point for future structural imaging studies of the mouse brain.

7.2 Final conclusion

This thesis has demonstrated the development and implementation of *in vivo* MRI biomarkers to characterise mouse models of neurodegeneration. This work supports ongoing efforts to reduce the number of mice sacrificed for scientific endeavour, by implementing non-invasive imaging techniques and demonstrating their use in longitudinal studies.

References

1. A. Alzheimer, Uber eigenartige Krankheitsfalle des spateren Alters. *Journal of Neurology, Neurosurgery & Psychiatry* **4**, 356 (1911).
2. M. Graeber *et al.*, Rediscovery of the case described by Alois Alzheimer in 1911: historical, histological and molecular genetic analysis. *Neurogenetics* **1**, 73 (1997).
3. A. Goate *et al.*, Segregation of a missense mutation in the amyloid precursor protein gene with familial Alzheimer's disease. *Nature* **349**, 704 (1991).
4. R. Sherrington *et al.*, Cloning of a gene bearing missense mutations in early-onset familial Alzheimer's disease. *Nature* **375**, 754 (1995).
5. E. I. Rogaev *et al.*, Familial Alzheimer's disease in kindreds with missense mutations in a gene on chromosome 1 related to the Alzheimer's disease type 3 gene. *Nature* **376**, 775 (1995).
6. J. Hardy, D. J. Selkoe, The Amyloid Hypothesis of Alzheimer's Disease: Progress and Problems on the Road to Therapeutics. *Science* **297**, 353 (July 19, 2002, 2002).
7. S. G. Younkin, The role of Aβ42 in Alzheimer's disease. *Journal of Physiology Paris* **92**, 289 (1998).
8. M. Hutton, The Presenilins and Alzheimer's Disease. *Human Molecular Genetics* **6**, 1639 (September 1, 1997, 1997).
9. C. Reitz, R. Mayeux, Alzheimer disease: Epidemiology, diagnostic criteria, risk factors and biomarkers. *Biochemical Pharmacology* **88**, 640 (2014).
10. L. Bertram, R. E. Tanzi, Thirty years of Alzheimer's disease genetics: the implications of systematic meta-analyses. *Nat Rev Neurosci* **9**, 768 (2008).
11. J.-C. Lambert *et al.*, Genome-wide association study identifies variants at CLU and CR1 associated with Alzheimer's disease. *Nat Genet* **41**, 1094 (2009).
12. P. Hollingworth *et al.*, Common variants in ABCA7, MS4A6A/MS4A4E, EPHA1, CD33 and CD2AP are associated with Alzheimer's disease. *Nature genetics* **43**, 429 (2011).
13. D. J. Selkoe, Alzheimer's disease: genes, proteins, and therapy. *Physiological reviews* **81**, 741 (2001).
14. J. Gotz, L. M. Ittner, Animal models of Alzheimer's disease and frontotemporal dementia. *Nat Rev Neurosci* **9**, 532 (2008).
15. P. T. Francis, A. M. Palmer, M. Snape, G. K. Wilcock, The cholinergic hypothesis of Alzheimer's disease: a review of progress. *Journal of Neurology, Neurosurgery & Psychiatry* **66**, 137 (February 1, 1999, 1999).
16. D. M. Bowen, C. B. Smith, P. White, A. N. Davison, NEUROTRANSMITTER-RELATED ENZYMES AND INDICES OF HYPOXIA IN SENILE DEMENTIA AND OTHER ABIOTROPHIES. *Brain* **99**, 459 (1976).
17. P. Davies, A. J. F. Maloney, SELECTIVE LOSS OF CENTRAL CHOLINERGIC NEURONS IN ALZHEIMER'S DISEASE. *The Lancet* **308**, 1403 (1976).
18. R. Bartus, R. Dean, B. Beer, A. Lippa, The cholinergic hypothesis of geriatric memory dysfunction. *Science* **217**, 408 (July 30, 1982, 1982).
19. J. Birks, Cholinesterase inhibitors for Alzheimer's disease (Review). (2012).
20. S. Rountree *et al.*, Persistent treatment with cholinesterase inhibitors and/or memantine slows clinical progression of Alzheimer disease. *Alzheimers Res Ther* **1**, 7 (2009).

21. C. Berk, G. Paul, M. Sabbagh, Investigational drugs in Alzheimer's disease: current progress. *Expert Opinion on Investigational Drugs* **23**, 837 (2014/06/01, 2014).

22. K. L. Davis, R. C. Mohs, D. Marin, et al., CHolinergic markers in elderly patients with early signs of alzheimer disease. *JAMA* **281**, 1401 (1999).

23. A. Martorana, Z. Esposito, G. Koch, Beyond the Cholinergic Hypothesis: Do Current Drugs Work in Alzheimer's Disease? *CNS Neuroscience & Therapeutics* **16**, 235 (2010).

24. J. A. Hardy, G. A. Higgins, Alzheimer's Disease: The Amyloid Cascade Hypothesis. *Science* **256**, 184 (1992 Apr 10, 1992).

25. G. G. Glenner, C. W. Wong, Alzheimer's disease and Down's syndrome: Sharing of a unique cerebrovascular amyloid fibril protein. *Biochemical and Biophysical Research Communications* **122**, 1131 (1984).

26. D. M. A. Mann, M. M. Esiri, The pattern of acquisition of plaques and tangles in the brains of patients under 50 years of age with Down's syndrome. *Journal of the Neurological Sciences* **89**, 169 (1989).

27. K. E. Wisniewski, H. M. Wisniewski, G. Y. Wen, Occurrence of neuropathological changes and dementia of Alzheimer's disease in Down's syndrome. *Annals of Neurology* **17**, 278 (1985).

28. S. Ness *et al.*, Down's syndrome and Alzheimer's disease: towards secondary prevention. *Nat Rev Drug Discov* **11**, 655 (2012).

29. F. Mangialasche, A. Solomon, B. Winblad, P. Mecocci, M. Kivipelto, Alzheimer's disease: clinical trials and drug development. *The Lancet Neurology* **9**, 702 (2010).

30. K. Mullane, M. Williams, Alzheimer's therapeutics: Continued clinical failures question the validity of the amyloid hypothesis—but what lies beyond? *Biochemical Pharmacology* **85**, 289 (2013).

31. A. Serrano-Pozo, M. P. Frosch, E. Masliah, B. T. Hyman, Neuropathological Alterations in Alzheimer Disease. *Cold Spring Harbor Perspectives in Medicine:* **1**, a006189 (2011).

32. K. Herrup, The case for rejecting the amyloid cascade hypothesis. *Nat Neurosci*, 794 (2015).

33. E. Karran, M. Mercken, B. D. Strooper, The amyloid cascade hypothesis for Alzheimer's disease: an appraisal for the development of therapeutics. *Nat Rev Drug Discov* **10**, 698 (2011).

34. M. L. Garcia, D. W. Cleveland, Going new places using an old MAP: tau, microtubules and human neurodegenerative disease. *Current Opinion in Cell Biology* **13**, 41 (2001).

35. M. E. Murray *et al.*, Clinicopathologic and 11C-Pittsburgh compound B implications of Thal amyloid phase across the Alzheimer's disease spectrum. *Brain*, (2015-03-20 00:00:00, 2015).

36. H. Braak, E. Braak, Frequency of stages of Alzheimer-related lesions in different age categories. *Neurobiology of Aging* **18**, 351 (1997).

37. C. Duyckaerts, J. J. Hauw, Prevalence, incidence and duration of Braak's stages in the general population: Can we know? [2]. *Neurobiology of Aging* **18**, 362 (1997).

38. L. M. Bierer *et al.*, Neocortical neurofibrillary tangles correlate with dementia severity in Alzheimer's disease. *Arch Neurol* **52**, 81 (1995).

39. T. Gómez-Isla *et al.*, Neuronal loss correlates with but exceeds neurofibrillary tangles in Alzheimer's disease. *Annals of Neurology* **41**, 17 (1997).

40. M. G. Spillantini, M. Goedert, Tau protein pathology in neurodegenerative diseases. *Trends in Neurosciences* **21**, 428 (1998).

41. M. Hutton *et al.*, Association of missense and 5[prime]-splice-site mutations in tau with the inherited dementia FTDP-17. *Nature* **393**, 702 (1998).

42. M. S. Forman *et al.*, Frontotemporal Dementia: Clinicopathological Correlations. *Annals of Neurology* **59**, 952 (2006).

43. C. Reitz, Alzheimer's Disease and the Amyloid Cascade Hypothesis: A Critical Review. *International Journal of Alzheimer’s Disease* **2012**, 11 (2012).

44. R. Anand, K. D. Gill, A. A. Mahdi, Therapeutics of Alzheimer's disease: Past, present and future. *Neuropharmacology* **76, Part A**, 27 (2014).

45. C. M. Wischik, P. Bentham, D. J. Wischik, K. M. Seng, O3-04-07: Tau aggregation inhibitor (TAI) therapy with rember™ arrests disease progression in mild and moderate Alzheimer's disease over 50 weeks. *Alzheimer's & Dementia* **4**, T167 (2008).

46. K. R. Brunden *et al.*, Epothilone D Improves Microtubule Density, Axonal Integrity, and Cognition in a Transgenic Mouse Model of Tauopathy. *The Journal of neuroscience* **30**, 13861 (October 13, 2010, 2010).

47. Y. Matsuoka *et al.*, Intranasal NAP administration reduces accumulation of amyloid peptide and tau hyperphosphorylation in a transgenic mouse model of Alzheimer's disease at early pathological stage. *Journal of Molecular Neuroscience* **31**, 165 (2007).

48. T. Arendt *et al.*, Reversible paired helical filament-like phosphorylation of tau is an adaptive process associated with neuronal plasticity in hibernating animals. *Journal of Neuroscience* **23**, 6972 (2003).

49. W. F. Maragos, J. T. Greenamyre, J. B. Penney, A. B. Young, Glutamate dysfunction in Alzheimer's disease: an hypothesis. *Trends in Neurosciences* **10**, 65 (1987/02/01, 1987).

50. D. A. Butterfield, C. B. Pocernich, The glutamatergic system and Alzheimer's disease: Therapeutic implications. *CNS Drugs* **17**, 641 (2003).

51. J. A. Hardy, G. A. Higgins, Alzheimer's disease: the amyloid cascade hypothesis. *Science* **256**, 184 (1992).

52. P. T. Francis, Glutamatergic systems in Alzheimer's disease. *Int J Geriatr Psychiatry* **18**, S15 (2003).

53. L. Gasparini, A. Dityatev, Beta-amyloid and glutamate receptors. *Exp Neurol* **212**, 1 (2008).

54. K. Parameshwaran, M. Dhanasekaran, V. Suppiramaniam, Amyloid beta peptides and glutamatergic synaptic dysregulation. *Exp Neurol* **210**, 7 (2008).

55. M. P. Mattson, W. A. Pedersen, W. Duan, C. Culmsee, S. Camandola, Cellular and molecular mechanisms underlying perturbed energy metabolism and neuronal degeneration in Alzheimer's and Parkinson's diseases. *Ann N Y Acad Sci* **893**, 154 (1999).

56. W. Danysz, C. G. Parsons, Alzheimer's disease, β-amyloid, glutamate, NMDA receptors and memantine – searching for the connections. *British Journal of Pharmacology* **167**, 324 (2012).

57. R. Hellweg, Y. Wirth, W. Janetzky, S. Hartmann, Efficacy of memantine in delaying clinical worsening in Alzheimer's disease (AD): responder analyses of nine clinical trials with patients with moderate to severe AD. *International Journal of Geriatric Psychiatry* **27**, 651 (2012).

58. C. T. Loy, P. R. Schofield, A. M. Turner, J. B. J. Kwok, Genetics of dementia. *The Lancet* **383**, 828.

59. T. N. Tombaugh, N. J. McIntyre, The mini-mental state examination: a comprehensive review. *Journal of the American Geriatrics Society* **40**, 922 (1992).

60.   .   (https://www.nia.nih.gov/alzheimers/topics/diagnosis#how,   National Institute on Aging).

61.   S. Gauthier *et al.*, Mild cognitive impairment. *The Lancet* **367**, 1262.

62.   R. C. Petersen, Early Diagnosis of Alzheimer's Disease: Is MCI Too Late? *Current Alzheimer research* **6**, 324 (2009).

63.   C. R. Jack *et al.*, Hypothetical model of dynamic biomarkers of the Alzheimer's pathological cascade. *The Lancet Neurology* **9**, 119 (2010).

64.   C. Humpel, Identifying and validating biomarkers for Alzheimer's disease. *Trends in Biotechnology* **29**, 26 (2011).

65.   K. B. Rajan, R. S. Wilson, J. Weuve, L. L. Barnes, D. A. Evans, Cognitive impairment 18 years before clinical diagnosis of Alzheimer disease dementia. *Neurology* **85**, 898 (September 8, 2015, 2015).

66.   N. Fox, When, where, and how does Alzheimer's disease start? *The Lancet Neurology* **11**, 1017 (2012).

67.   R. A. Sperling *et al.*, Toward defining the preclinical stages of Alzheimer's disease: Recommendations from the National Institute on Aging-Alzheimer's Association workgroups on diagnostic guidelines for Alzheimer's disease. *Alzheimer's & Dementia* **7**, 280 (2011).

68.   K. Blennow, H. Zetterberg, Cerebrospinal fluid biomarkers for Alzheimer's disease. *Journal of Alzheimer's disease: JAD* **18**, 413 (2008).

69.   K. Blennow, H. Hampel, CSF markers for incipient Alzheimer's disease. *The Lancet Neurology* **2**, 605 (2003).

70.   N. Andreasen, K. Blennow, CSF biomarkers for mild cognitive impairment and early Alzheimer's disease. *Clin Neurol Neurosurg* **107**, 165 (2005).

71.   K. Buerger *et al.*, Differential diagnosis of Alzheimer disease with cerebrospinal fluid levels of tau protein phosphorylated at threonine 231. *Arch Neurol* **59**, 1267 (2002).

72.   N. H. Raskin, Lumbar Puncture Headache: A Review. *Headache: The Journal of Head and Face Pain* **30**, 197 (1990).

73.   S. Zhang *et al.*, (11)C-PIB-PET for the early diagnosis of Alzheimer's disease dementia and other dementias in people with mild cognitive impairment (MCI). *Cochrane Database Syst Rev* **23**, (2014).

74.   A. G. Vlassenko, T. L. S. Benzinger, J. C. Morris, PET amyloid-beta imaging in preclinical Alzheimer's disease. *Biochimica et Biophysica Acta (BBA) - Molecular Basis of Disease* **1822**, 370 (2012).

75.   W. E. Klunk *et al.*, Imaging brain amyloid in Alzheimer's disease with Pittsburgh Compound-B. *Annals of Neurology* **55**, 306 (2004).

76.   M. Biancalana, S. Koide, Molecular Mechanism of Thioflavin-T Binding to Amyloid Fibrils. *Biochimica et biophysica acta* **1804**, 1405 (2010).

77.   M. D. Ikonomovic *et al.*, Post-mortem correlates of in vivo PiB-PET amyloid imaging in a typical case of Alzheimer's disease. *Brain* **131**, 1630 (2008-06-01 00:00:00, 2008).

78.   C. R. Jack *et al.*, Brain beta-amyloid measures and magnetic resonance imaging atrophy both predict time-to-progression from mild cognitive impairment to Alzheimer's disease. *Brain* **133**, 3336 (2010).

79.   A. Forsberg *et al.*, PET imaging of amyloid deposition in patients with mild cognitive impairment. *Neurobiology of Aging* **29**, 1456 (2008).

80.   A. Nordberg, J. O. Rinne, A. Kadir, B. Langstrom, The use of PET in Alzheimer disease. *Nat Rev Neurol* **6**, 78 (2010).

81.   K. Herholz, K. Ebmeier, Clinical amyloid imaging in Alzheimer's disease. *The Lancet Neurology* **10**, 667 (2011).

82. D. T. Chien *et al.*, Early clinical PET imaging results with the novel PHF-tau radioligand [F18]-T808. *J Alzheimers Dis* **38**, 171 (2014).

83. N. Okamura *et al.*, Non-invasive assessment of Alzheimer's disease neurofibrillary pathology using 18F-THK5105 PET. *Brain* **137**, 1762 (2014-06-01 00:00:00, 2014).

84. P. T. Nelson *et al.*, Correlation of Alzheimer Disease Neuropathologic Changes With Cognitive Status: A Review of the Literature. *Journal of neuropathology and experimental neurology* **71**, 362 (2012).

85. O. James, M. Doraiswamy, S. Borges-Neto, PET Imaging of Tau Pathology: Towards an affirmative diagnosis of Alzheimer's and Tauopathies. *Frontiers in Neurology* **6**, (2015-March-9, 2015).

86. A. B. Rocher, F. Chapon, X. Blaizot, J. C. Baron, C. Chavoix, Resting-state brain glucose utilization as measured by PET is directly related to regional synaptophysin levels: A study in baboons. *NeuroImage* **20**, 1894 (2003).

87. R. Higdon *et al.*, A comparison of classification methods for differentiating fronto-temporal dementia from Alzheimer's disease using FDG-PET imaging. *Statistics in Medicine* **23**, 315 (2004).

88. P. Santens *et al.*, Differential Regional Cerebral Uptake of ^{18}F-Fluoro-2-Deoxy-*D*-Glucose in Alzheimer's Disease and Frontotemporal Dementia at Initial Diagnosis. *European Neurology* **45**, 19 (2001).

89. G. Chételat *et al.*, Mild cognitive impairment: Can FDG-PET predict who is to rapidly convert to Alzheimer's disease? *Neurology* **60**, 1374 (April 22, 2003, 2003).

90. W. Jagust, B. Reed, D. Mungas, W. Ellis, C. DeCarli, What does fluorodeoxyglucose PET imaging add to a clinical diagnosis of dementia? *Neurology* **69**, 871 (2007).

91. L. Mosconi *et al.*, Pre-Clinical Detection of Alzheimer's Disease Using FDG-PET, with or without Amyloid Imaging. *Journal of Alzheimer's disease : JAD* **20**, 843 (2010).

92. K. P. Willowson, E. A. Bailey, D. L. Bailey, A retrospective evaluation of radiation dose associated with low dose FDG protocols in whole-body PET/CT. *Australas Phys Eng Sci Med* **35**, 49 (2012).

93. G. B. Frisoni, N. C. Fox, C. R. Jack, P. Scheltens, P. M. Thompson, The clinical use of structural MRI in Alzheimer disease. *Nat Rev Neurol* **6**, 67 (2010).

94. E. S. C. Korf, L.-O. Wahlund, P. J. Visser, P. Scheltens, Medial temporal lobe atrophy on MRI predicts dementia in patients with mild cognitive impairment. *Neurology* **63**, 94 (July 13, 2004, 2004).

95. P. Vemuri, C. R. Jack, Jr., Role of structural MRI in Alzheimer's disease. *Alzheimers Res Ther* **2**, (2010).

96. M. Bobinski *et al.*, The histological validation of post mortem magnetic resonance imaging-determined hippocampal volume in Alzheimer's disease. *Neuroscience* **95**, 721 (1999).

97. J. L. Whitwell *et al.*, MRI correlates of neurofibrillary tangle pathology at autopsy: A voxel-based morphometry study. *Neurology* **71**, 743 (September 2, 2008, 2008).

98. C. R. Jack Jr *et al.*, Tracking pathophysiological processes in Alzheimer's disease: an updated hypothetical model of dynamic biomarkers. *The Lancet Neurology* **12**, 207 (2013).

99. C. R. Jack *et al.*, The Alzheimer's Disease Neuroimaging Initiative (ADNI): MRI Methods. *Journal of magnetic resonance imaging : JMRI* **27**, 685 (2008).

100. M. Tondelli *et al.*, Structural MRI changes detectable up to ten years before clinical Alzheimer's disease. *Neurobiology of Aging* **33**, 825.e25 (2012).

101. M. Ewers, R. A. Sperling, W. E. Klunk, M. W. Weiner, H. Hampel, Neuroimaging markers for the prediction and early diagnosis of Alzheimer's disease dementia. *Trends in Neurosciences* **34**, 430 (2011).

102. A. M. Hall, E. D. Roberson, Mouse models of Alzheimer's disease. *Brain Research Bulletin* **88**, 3 (2012).

103. D. Games *et al.*, Alzheimer-type neuropathology in transgenic mice overexpressing V717F beta-amyloid precursor protein. *Nature* **373**, 523 (1995).

104. L. Mucke *et al.*, High-Level Neuronal Expression of Aβ1–42 in Wild-Type Human Amyloid Protein Precursor Transgenic Mice: Synaptotoxicity without Plaque Formation. *The Journal of neuroscience* **20**, 4050 (June 1, 2000, 2000).

105. K. Hsiao *et al.*, Correlative memory deficits, Abeta elevation, and amyloid plaques in transgenic mice. *Science* **274**, 99 (1996).

106. C. Sturchler-Pierrat *et al.*, Two amyloid precursor protein transgenic mouse models with Alzheimer disease-like pathology. *Proc Natl Acad Sci U S A* **94**, 13287 (1997).

107. M. A. Chishti *et al.*, Early-onset amyloid deposition and cognitive deficits in transgenic mice expressing a double mutant form of amyloid precursor protein 695. *J Biol Chem* **276**, 21562 (2001).

108. B. T. Lamb *et al.*, Altered metabolism of familial Alzheimer's disease-linked amyloid precursor protein variants in yeast artificial chromosome transgenic mice. *Hum Mol Genet* **6**, 1535 (1997).

109. E. McGowan *et al.*, Aβ42 Is Essential for Parenchymal and Vascular Amyloid Deposition in Mice. *Neuron* **47**, 191 (2005).

110. L. Holcomb *et al.*, Accelerated Alzheimer-type phenotype in transgenic mice carrying both mutant amyloid precursor protein and presenilin 1 transgenes. *Nature Medicine* **4**, 97 (1998).

111. J. L. Jankowsky *et al.*, Mutant presenilins specifically elevate the levels of the 42 residue beta-amyloid peptide in vivo: evidence for augmentation of a 42-specific gamma secretase. *Hum Mol Genet* **13**, 159 (2004).

112. H. Oakley *et al.*, Intraneuronal beta-amyloid aggregates, neurodegeneration, and neuron loss in transgenic mice with five familial Alzheimer's disease mutations: potential factors in amyloid plaque formation. *J Neurosci* **26**, 10129 (2006).

113. J. Lewis *et al.*, Enhanced neurofibrillary degeneration in transgenic mice expressing mutant tau and APP. *Science* **293**, 1487 (2001).

114. K. Santacruz *et al.*, Tau suppression in a neurodegenerative mouse model improves memory function. *Science* **309**, 476 (2005).

115. S. Oddo *et al.*, Triple-transgenic model of Alzheimer's disease with plaques and tangles: intracellular Abeta and synaptic dysfunction. *Neuron* **39**, 409 (2003).

116. C. Andorfer *et al.*, Hyperphosphorylation and aggregation of tau in mice expressing normal human tau isoforms. *J Neurochem* **86**, 582 (2003).

117. R. E. Tanzi, The Genetics of Alzheimer Disease. *Cold Spring Harbor Perspectives in Medicine* **2**, (October 1, 2012, 2012).

118. M. C. Irizarry *et al.*, Aβ Deposition Is Associated with Neuropil Changes, but not with Overt Neuronal Loss in the Human Amyloid Precursor Protein V717F (PDAPP) Transgenic Mouse. *The Journal of neuroscience* **17**, 7053 (September 15, 1997, 1997).

119. M. C. Irizarry, M. McNamara, K. Fedorchak, K. Hsiao, B. T. Hyman, APPSw transgenic mice develop age-related A beta deposits and neuropil abnormalities, but no neuronal loss in CA1. *J Neuropathol Exp Neurol* **56**, 965 (1997).

120. O. Wirths, T. A. Bayer, Neuron Loss in Transgenic Mouse Models of Alzheimer's Disease. *International Journal of Alzheimer’s Disease* **2010**, 6 (2010).

121. K. Duff, F. Suleman, Transgenic mouse models of Alzheimer's disease: How useful have they been for therapeutic development? *Briefings in Functional Genomics & Proteomics* **3**, 47 (April 1, 2004, 2004).

122. L. Bertram, R. E. Tanzi, The current status of Alzheimer's disease genetics: What do we tell the patients? *Pharmacological Research* **50**, 385 (2004).

123. K. Duff *et al.*, Increased amyloid-[beta]42(43) in brains of mice expressing mutant presenilin 1. *Nature* **383**, 710 (1996).

124. L. Holcomb *et al.*, Accelerated Alzheimer-type phenotype in transgenic mice carrying both mutant amyloid precursor protein and presenilin 1 transgenes. *Nature Medicine* **4**, 97 (1998).

125. G. A. Elder, M. A. Gama Sosa, R. De Gasperi, Transgenic Mouse Models of Alzheimer's Disease. *The Mount Sinai journal of medicine, New York* **77**, 69 (Jan-Feb, 2010).

126. M. Sasahara *et al.*, PDGF B-chain in neurons of the central nervous system, posterior pituitary, and in a transgenic model. *Cell* **64**, 217 (1991).

127. P. Caroni, Overexpression of growth-associated proteins in the neurons of adult transgenic mice. *Journal of Neuroscience Methods* **71**, 3 (1997).

128. J. W. Gordon *et al.*, Regulation of Thy-1 gene expression in transgenic mice. *Cell* **50**, 445 (1987).

129. J. Boy *et al.*, Expression mapping of tetracycline-responsive prion protein promoter: Digital atlasing for generating cell-specific disease models. *NeuroImage* **33**, 449 (2006).

130. P. Tremblay *et al.*, Doxycycline control of prion protein transgene expression modulates priori disease in mice. *Proceedings of the National Academy of Sciences of the United States of America* **95**, 12580 (1998).

131. E. A. Asante, I. Gowland, J. M. Linehan, S. P. Mahal, J. Collinge, Expression pattern of a mini human PrP gene promoter in transgenic mice. *Neurobiology of Disease* **10**, 1 (2002).

132. K. E. Burgin *et al.*, In situ hybridization histochemistry of Ca2+/calmodulin-dependent protein kinase in developing rat brain. *J Neurosci* **10**, 1788 (1990).

133. L. Brocke, M. Srinivasan, H. Schulman, Developmental and regional expression of multifunctional Ca2+/calmodulin-dependent protein kinase isoforms in rat brain. *J Neurosci* **15**, 6797 (1995).

134. D. Stucht *et al.*, Highest Resolution In Vivo Human Brain MRI Using Prospective Motion Correction. *PLoS ONE* **10**, e0133921 (2015).

135. Nobelprize.org. (2015).

136. mri-q.com. (2014).

137. D. J. Dowsett, P. A. Kenny, E. R. Johnston, *The Physics of Diagnostic Imaging*. (Hodder Arnold, ed. 2, 2006).

138. D. W. McRobbie, ., et al., *MRI from Picture to Proton*. (Cambridge University Press, 2006).

139. G. A. Johnson *et al.*, Magnetic resonance histology for morphologic phenotyping. *Journal of Magnetic Resonance Imaging* **16**, 423 (2002).

140. J. O. Cleary *et al.*, Structural correlates of active-staining following magnetic resonance microscopy in the mouse brain. *NeuroImage* **56**, 974 (2011).

141. A. L. Alexander, J. E. Lee, M. Lazar, A. S. Field, Diffusion Tensor Imaging of the Brain. *Neurotherapeutics : the journal of the American Society for Experimental NeuroTherapeutics* **4**, 316 (2007).

142. D. S. Williams, J. A. Detre, J. S. Leigh, A. P. Koretsky, Magnetic resonance imaging of perfusion using spin inversion of arterial water. *Proceedings of the National Academy of Sciences* **89**, 212 (1992).

143. P. C. M. van Zijl, N. N. Yadav, Chemical exchange saturation transfer (CEST): What is in a name and what isn't? *Magnetic Resonance in Medicine* **65**, 927 (2011).

144. D. G. Gadian, *NMR and its Application to Living Systems.* (Oxford University Press, ed. 2, 1995).

145. J. A. Wells *et al.*, In vivo imaging of tau pathology using multi-parametric quantitative MRI. *NeuroImage* **111**, 369 (May 1, 2015).

146. H. Akiyama *et al.*, Inflammation and Alzheimer's disease. *Neurobiology of Aging* **21**, 383 (2000).

147. L. C. Fletcher *et al.*, Diagnosing Alzheimer's disease: are we any nearer to useful biomarker-based, non-invasive tests? *GMS Health Technol Assess* **11**, (2013).

148. A. Maruszak, C. Żekanowski, Mitochondrial dysfunction and Alzheimer's disease. *Progress in Neuro-Psychopharmacology and Biological Psychiatry* **35**, 320 (2011).

149. J. C. de la Torre, Alzheimer Disease as a Vascular Disorder. *Stroke* **33**, 1152 (April 1, 2002, 2002).

150. R. Models. (www.alzforum.com, 2015).

151. H. Braak, E. Braak, Neuropathological stageing of Alzheimer-related changes. *Acta Neuropathologica* **82**, 239 (1991/09/01, 1991).

152. V. M. Y. Lee, M. Goedert, J. Q. Trojanowski, in *Annual Review of Neuroscience.* (2001), vol. 24, pp. 1121-1159.

153. M. Ramsden *et al.*, Age-dependent neurofibrillary tangle formation, neuron loss, and memory impairment in a mouse model of human tauopathy (P301L). *J Neurosci* **25**, 10637 (Nov 16, 2005).

154. J. Zhang *et al.*, Longitudinal characterization of brain atrophy of a Huntington's disease mouse model by automated morphological analyses of magnetic resonance images. *NeuroImage* **49**, 2340 (2010).

155. J. C. Lau *et al.*, Longitudinal neuroanatomical changes determined by deformation-based morphometry in a mouse model of Alzheimer's disease. *NeuroImage* **42**, 19 (2008).

156. O. I. Alomair, I. M. Brereton, M. T. Smith, G. J. Galloway, N. D. Kurniawan, <italic>In vivo</italic> High Angular Resolution Diffusion-Weighted Imaging of Mouse Brain at 16.4 Tesla. *PLoS ONE* **10**, e0130133 (2015).

157. D. Yang *et al.*, Volumetric MRI and MRS provide sensitive measures of Alzheimer's disease neuropathology in inducible Tau transgenic mice (rTg4510). *NeuroImage* **54**, 2652 (2011).

158. F. Kara, F. Chen, J. Matysik, A. Alia, in *Proceedings of the International Society of Magnetic Resonance im Medicine.* (Quebec, Canada, 2011), vol. 3971.

159. Y.-T. Kuo, A. H. Herlihy, P.-W. So, K. K. Bhakoo, J. D. Bell, In vivo measurements of T1 relaxation times in mouse brain associated with different modes of systemic administration of manganese chloride. *Journal of Magnetic Resonance Imaging* **21**, 334 (2005).

160. R. C. G. van de Ven *et al.*, T1 relaxation in in vivo mouse brain at ultra-high field. *Magnetic Resonance in Medicine* **58**, 390 (2007).

161. R. A. Jones, S. Palasis, J. D. Grattan-Smith, MRI of the Neonatal Brain: Optimization of Spin-Echo Parameters. *American Journal of Roentgenology* **182**, 367 (February 1, 2004, 2004).

162. J. O. Cleary *et al.*, Cardiac phenotyping in ex vivo murine embryos using μMRI. *NMR in Biomedicine* **22**, 857 (2009).

163. Z. Ahmed *et al.*, A novel in vivo model of tau propagation with rapid and progressive neurofibrillary tangle pathology: the pattern of spread is determined by connectivity, not proximity. *Acta Neuropathologica* **127**, 667 (2014).

164. P. A. Yushkevich *et al.*, User-guided 3D active contour segmentation of anatomical structures: Significantly improved efficiency and reliability. *NeuroImage* **31**, 1116 (2006).

165. J. O'Callaghan *et al.*, Is Your System Calibrated? MRI Gradient System Calibration for Pre-Clinical, High-Resolution Imaging. *PLoS ONE* **9**, e96568 (2014).

166. J. G. Sled, A. P. Zijdenbos, A. C. Evans, A nonparametric method for automatic correction of intensity nonuniformity in MRI data. *IEEE Trans Med Imaging* **17**, 87 (Feb, 1998).

167. M. Jorge Cardoso *et al.*, STEPS: Similarity and Truth Estimation for Propagated Segmentations and its application to hippocampal segmentation and brain parcelation. *Medical Image Analysis* **17**, 671 (2013).

168. M. Modat *et al.*, Fast free-form deformation using graphics processing units. *Computer Methods and Programs in Biomedicine* **98**, 278 (2010).

169. C. R. Genovese, N. A. Lazar, T. Nichols, Thresholding of Statistical Maps in Functional Neuroimaging Using the False Discovery Rate. *NeuroImage* **15**, 870 (2002).

170. M. W. DiFrancesco *et al.*, Comparison of SNR and CNR for in vivo mouse brain imaging at 3 and 7 T using well matched scanner configurations. *Medical Physics* **35**, 3972 (2008).

171. J. Borg, E. Chereul, Differential MRI patterns of brain atrophy in double or single transgenic mice for APP and/or SOD. *Journal of Neuroscience Research* **86**, 3275 (2008).

172. C. Weiss *et al.*, Impaired Eyeblink Conditioning and Decreased Hippocampal Volume in PDAPP V717F Mice. *Neurobiology of Disease* **11**, 425 (2002).

173. N. Braakman *et al.*, Longitudinal assessment of Alzheimer's β-amyloid plaque development in transgenic mice monitored by in vivo magnetic resonance microimaging. *Journal of Magnetic Resonance Imaging* **24**, 530 (2006).

174. J.-K. Choi *et al.*, The effects of aging, housing and ibuprofen treatment on brain neurochemistry in a triple transgene Alzheimer's disease mouse model using magnetic resonance spectroscopy and imaging. *Brain Research* **1590**, 85 (2014).

175. O. Natt *et al.*, High-resolution 3D MRI of mouse brain reveals small cerebral structures in vivo. *Journal of Neuroscience Methods* **120**, 203 (2002).

176. J. P. Lerch, in *International Society for Magnetic Resonance in Medicine*. (Stockholm, Sweden, 2010).

177. I. McKeith *et al.*, Dementia with Lewy bodies. *The Lancet Neurology* **3**, 19 (2004).

178. F. Hentschel, M. Kreis, M. Damian, B. Krumm, L. Frölich, The clinical utility of structural neuroimaging with MRI for diagnosis and differential diagnosis of dementia: a memory clinic study. *International Journal of Geriatric Psychiatry* **20**, 645 (2005).

179. C. R. Jack *et al.*, The Alzheimer's disease neuroimaging initiative (ADNI): MRI methods. *Journal of Magnetic Resonance Imaging* **27**, 685 (2008).

180. X. Hua *et al.*, Tensor-based morphometry as a neuroimaging biomarker for Alzheimer's disease: an MRI study of 676 AD, MCI, and normal subjects. *NeuroImage* **43**, 458 (Nov 15, 2008).

181. X. Hua *et al.*, 3D characterization of brain atrophy in Alzheimer's disease and mild cognitive impairment using tensor-based morphometry. *NeuroImage* **41**, 19 (2008).

182.   M. Chupin *et al.*, Fully automatic hippocampus segmentation and classification in Alzheimer's disease and mild cognitive impairment applied on data from ADNI. *Hippocampus* **19**, 579 (2009).

183.   J. M. Redwine *et al.*, Dentate gyrus volume is reduced before onset of plaque formation in PDAPP mice: A magnetic resonance microscopy and stereologic analysis. *Proceedings of the National Academy of Sciences* **100**, 1381 (February 4, 2003, 2003).

184.   B. Delatour, M. Guégan, A. Volk, M. Dhenain, In vivo MRI and histological evaluation of brain atrophy in APP/PS1 transgenic mice. *Neurobiology of Aging* **27**, 835 (2006).

185.   K. Hayes *et al.*, Comparison of manual and semi-automated segmentation methods to evaluate hippocampus volume in APP and PS1 transgenic mice obtained via in vivo magnetic resonance imaging. *Journal of Neuroscience Methods* **221**, 103 (2014).

186.   A. E. Scheenstra *et al.*, Automated segmentation of in vivo and ex vivo mouse brain magnetic resonance images. *Mol Imaging* **8**, 35 (2009).

187.   D. Ma *et al.*, Automatic Structural Parcellation of Mouse Brain MRI Using Multi-Atlas Label Fusion. *PloS one* **9**, e86576 (2014).

188.   Y. Ma *et al.*, In vivo 3D digital atlas database of the adult C57BL/6J mouse brain by magnetic resonance microscopy. *Frontiers in Neuroanatomy* **2**, (2008-April-17, 2008).

189.   Y. Ma *et al.*, A three-dimensional digital atlas database of the adult C57BL/6J mouse brain by magnetic resonance microscopy. *Neuroscience* **135**, 1203 (2005).

190.   A. E. Dorr, J. P. Lerch, S. Spring, N. Kabani, R. M. Henkelman, High resolution three-dimensional brain atlas using an average magnetic resonance image of 40 adult C57Bl/6J mice. *NeuroImage* **42**, 60 (2008).

191.   N. Kovačević *et al.*, A Three-dimensional MRI Atlas of the Mouse Brain with Estimates of the Average and Variability. *Cerebral Cortex* **15**, 639 (May 1, 2005, 2005).

192.   M. Dhenain, S. W. Ruffins, R. E. Jacobs, Three-Dimensional Digital Mouse Atlas Using High-Resolution MRI. *Developmental Biology* **232**, 458 (2001).

193.   J. P. Lerch *et al.*, Cortical thickness measured from MRI in the YAC128 mouse model of Huntington's disease. *NeuroImage* **41**, 243 (2008).

194.   J. B. Carroll *et al.*, Natural history of disease in the YAC128 mouse reveals a discrete signature of pathology in Huntington disease. *Neurobiology of Disease* **43**, 257 (2011).

195.   S. Maheswaran *et al.*, Longitudinal regional brain volume changes quantified in normal aging and Alzheimer's APP-PS1 mice using MRI. *Brain Research* **1270**, 19 (2009).

196.   A. Badea, G. A. Johnson, J. L. Jankowsky, Remote sites of structural atrophy predict later amyloid formation in a mouse model of Alzheimer's disease. *NeuroImage* **50**, 416 (2010).

197.   F. Hébert *et al.*, Cortical atrophy and hypoperfusion in a transgenic mouse model of Alzheimer's disease. *Neurobiology of Aging* **34**, 1644 (2013).

198.   R. E. Mercer *et al.*, Regionally reduced brain volume, altered serotonin neurochemistry, and abnormal behavior in mice null for the circadian rhythm output gene Magel2. *American Journal of Medical Genetics Part B: Neuropsychiatric Genetics* **150B**, 1085 (2009).

199.   X. Yu *et al.*, Morphological and functional midbrain phenotypes in Fibroblast Growth Factor 17 mutant mice detected by Mn-enhanced MRI. *NeuroImage* **56**, 1251 (2011).

200. S. Spring, J. P. Lerch, M. K. Wetzel, A. C. Evans, R. M. Henkelman, Cerebral asymmetries in 12-week-old C57Bl/6J mice measured by magnetic resonance imaging. *NeuroImage* **50**, 409 (2010).

201. R. Verma *et al.*, Spatiotemporal maturation patterns of murine brain quantified by diffusion tensor MRI and deformation-based morphometry. *Proceedings of the National Academy of Sciences of the United States of America* **102**, 6978 (May 10, 2005, 2005).

202. B. J. Nieman *et al.*, Mouse behavioral mutants have neuroimaging abnormalities. *Human Brain Mapping* **28**, 567 (2007).

203. J. Ellegood, B. A. Babineau, R. M. Henkelman, J. P. Lerch, J. N. Crawley, Neuroanatomical analysis of the BTBR mouse model of autism using magnetic resonance imaging and diffusion tensor imaging. *NeuroImage* **70**, 288 (2013).

204. S. J. Sawiak, N. I. Wood, G. B. Williams, A. J. Morton, T. A. Carpenter, Voxel-based morphometry in the R6/2 transgenic mouse reveals differences between genotypes not seen with manual 2D morphometry. *Neurobiology of Disease* **33**, 20 (2009).

205. L. S. Cahill *et al.*, Preparation of fixed mouse brains for MRI. *NeuroImage* **60**, 933 (2012).

206. S. J. Teipel *et al.*, Automated detection of β-amyloid-related cortical and subcortical signal changes in a transgenic model of Alzheimer's disease using high-field MRI. *Journal of Alzheimer's disease : JAD* **23**, 221 (2011).

207. R. Radde *et al.*, Aβ42-driven cerebral amyloidosis in transgenic mice reveals early and robust pathology. *EMBO Reports* **7**, 940 (2006).

208. R. A. Stelzmann, H. Norman Schnitzlein, F. Reed Murtagh, An english translation of alzheimer's 1907 paper, "über eine eigenartige erkankung der hirnrinde". *Clinical Anatomy* **8**, 429 (1995).

209. R. Brookmeyer, E. Johnson, K. Ziegler-Graham, H. M. Arrighi, Forecasting the global burden of Alzheimer's disease. *Alzheimers Dement* **3**, 186 (2007).

210. P. Giannakopoulos *et al.*, Tangle and neuron numbers, but not amyloid load, predict cognitive status in Alzheimer's disease. *Neurology* **60**, 1495 (2003).

211. D. Ma *et al.*, Automatic Structural Parcellation of Mouse Brain MRI Using Multi-Atlas Label Fusion. *PLoS ONE* **9**, e86576 (2014).

212. S. Ourselin, A. Roche, S. Prima, N. Ayache, in *Medical Image Computing and Computer-Assisted Intervention–MICCAI 2000*. (Springer, 2000), pp. 557-566.

213. J. A. Wells *et al.*, In vivo imaging of tau pathology using multi-parametric quantitative MRI. *NeuroImage* **111**, 369 (2015).

214. P. van Zijl, N. N. Yadav, Chemical exchange saturation transfer (CEST): What is in a name and what isn't? *Magnetic Resonance in Medicine* **65**, 927 (2011).

215. P. G. Batchelor, D. Atkinson, D. L. G. Hill, F. Calamante, A. Connelly, Anisotropic noise propagation in diffusion tensor MRI sampling schemes. *Magnetic Resonance in Medicine* **49**, 1143 (2003).

216. D. Le Bihan *et al.*, Diffusion tensor imaging: Concepts and applications. *Journal of Magnetic Resonance Imaging* **13**, 534 (2001).

217. S. K. Song *et al.*, Dysmyelination revealed through MRI as increased radial (but unchanged axial) diffusion of water. *NeuroImage* **17**, 1429 (2002).

218. K. K. Kwong *et al.*, Dynamic magnetic resonance imaging of human brain activity during primary sensory stimulation. *Proc Natl Acad Sci U S A* **89**, 5675 (Jun 15, 1992).

219. S. G. Kim, Quantification of relative cerebral blood flow change by flow-sensitive alternating inversion recovery (FAIR) technique: application to functional mapping. *Magn Reson Med* **34**, 293 (1995).

220. J. A. Wells, B. Siow, M. F. Lythgoe, D. L. Thomas, The importance of RF bandwidth for effective tagging in pulsed arterial spin labeling MRI at 9.4T. *NMR Biomed* **25**, 1139 (2012).

221. R. B. Buxton *et al.*, A general kinetic model for quantitative perfusion imaging with arterial spin labeling. *Magn Reson Med* **40**, 383 (Sep, 1998).

222. J. P. Lerch *et al.*, Wanted Dead or Alive? The tradeoff between in-vivo versus ex-vivo MR brain imaging in the mouse. *Frontiers in Neuroinformatics* **6**, (2012-March-23, 2012).

223. N. Sahara *et al.*, Age-related decline in white matter integrity in a mouse model of tauopathy: an in vivo diffusion tensor magnetic resonance imaging study. *Neurobiology of Aging* **35**, 1364 (2014).

224. J. C. Drummond, M. M. Todd, M. S. Scheller, H. M. Shapiro, A Comparison of the Direct Cerebral Vasodilating Potencies of Halothane and Isoflurane in the New Zealand White Rabbit. *Anesthesiology* **65**, 462 (1986).

225. B. F. Matta, K. J. Heath, K. Tipping, A. C. Summors, Direct Cerebral Vasodilatory Effects of Sevoflurane and Isoflurane. *Anesthesiology* **91**, 677 (1999).

226. E. Giacobini, G. Gold, Alzheimer disease therapy[mdash]moving from amyloid-[beta] to tau. *Nat Rev Neurol* **9**, 677 (2013).

227. A. de Calignon *et al.*, Propagation of Tau Pathology in a Model of Early Alzheimer's Disease. *Neuron* **73**, 685 (2012).

228. H. Braak, E. Braak, Staging of alzheimer's disease-related neurofibrillary changes. *Neurobiology of Aging* **16**, 271 (1995).

229. J. A. Wells *et al.*, In vivo Imaging of Tau pathology using Multi-Parametric Quantitative MRI. *NeuroImage*, (2015).

230. C. R. Jack *et al.*, Antemortem MRI findings correlate with hippocampal neuropathology in typical aging and dementia. *Neurology* **58**, 750 (March 12, 2002, 2002).

231. J. Y. Zhou, J. F. Payen, D. A. Wilson, R. J. Traystman, P. C. M. van Zijl, Using the amide proton signals of intracellular proteins and peptides to detect pH effects in MRI. *Nature Medicine* **9**, 1085 (Aug, 2003).

232. C. K. Jones *et al.*, Amide proton transfer imaging of human brain tumors at 3T. *Magnetic Resonance in Medicine* **56**, 585 (2006).

233. J. Zhou, B. Lal, D. A. Wilson, J. Laterra, P. C. M. van Zijl, Amide proton transfer (APT) contrast for imaging of brain tumors. *Magnetic Resonance in Medicine* **50**, 1120 (2003).

234. J. Zhou *et al.*, Practical data acquisition method for human brain tumor amide proton transfer (APT) imaging. *Magnetic Resonance in Medicine* **60**, 842 (2008).

235. B. Fang, D. Wang, M. Huang, G. Yu, H. Li, Hypothesis on the Relationship Between the Change in Intracellular pH and Incidence of Sporadic Alzheimer's Disease or Vascular Dementia. *International Journal of Neuroscience* **120**, 591 (2010).

236. A. I. Hashim, X. Zhang, J. W. Wojtkowiak, G. V. Martinez, R. J. Gillies, Imaging pH and metastasis. *NMR in Biomedicine* **24**, 582 (2011).

237. R. Makaryus *et al.*, The metabolomic profile during isoflurane anesthesia differs from propofol anesthesia in the live rodent brain. *J Cereb Blood Flow Metab* **31**, 1432 (2011).

238. C. Constantinides, R. Mean, B. J. Janssen, Effects of Isoflurane Anesthesia on the Cardiovascular Function of the C57BL/6 Mouse. *ILAR journal / National Research Council, Institute of Laboratory Animal Resources* **52**, e21 (2011).

239. N. McVicar *et al.*, Quantitative tissue pH measurement during cerebral ischemia using amine and amide concentration-independent detection (AACID) with MRI. *J Cereb Blood Flow Metab* **34**, 690 (2014).

240.   P. Z. Sun, C. T. Farrar, A. G. Sorensen, Correction for artifacts induced by B0 and B1 field inhomogeneities in pH-sensitive chemical exchange saturation transfer (CEST) imaging. *Magnetic Resonance in Medicine* **58**, 1207 (2007).

241.   J. Acosta-Cabronero, S. Alley, G. B. Williams, G. Pengas, P. J. Nestor, Diffusion Tensor Metrics as Biomarkers in Alzheimer's Disease. *PLoS ONE* **7**, e49072 (2012).

242.   M. M. Mielke *et al.*, Regionally-specific diffusion tensor imaging in mild cognitive impairment and Alzheimer's disease. *NeuroImage* **46**, 47 (2009).

243.   C. E. Hugenschmidt *et al.*, Relating Imaging Indices of White Matter Integrity and Volume in Healthy Older Adults. *Cerebral Cortex* **18**, 433 (February 1, 2008, 2008).

244.   H. Huang *et al.*, Distinctive disruption patterns of white matter tracts in Alzheimer's disease with full diffusion tensor characterization. *Neurobiol Aging* **33**, 2029 (2012).

245.   S.-K. Song, J. H. Kim, S.-J. Lin, R. P. Brendza, D. M. Holtzman, Diffusion tensor imaging detects age-dependent white matter changes in a transgenic mouse model with amyloid deposition. *Neurobiology of Disease* **15**, 640 (2004).

246.   Y.-Y. Qin *et al.*, In vivo quantitative whole-brain diffusion tensor imaging analysis of APP/PS1 transgenic mice using voxel-based and atlas-based methods. *Neuroradiology* **55**, 1027 (2013/08/01, 2013).

247.   G. M. Kerbler *et al.*, Diffusion-weighted magnetic resonance imaging detection of basal forebrain cholinergic degeneration in a mouse model. *NeuroImage* **66**, 133 (2013).

248.   K. Kantarci *et al.*, Mild Cognitive Impairment and Alzheimer Disease: Regional Diffusivity of Water. *Radiology* **219**, 101 (2001/04/01, 2001).

249.   A. Cherubini *et al.*, Combined Volumetry and DTI in Subcortical Structures of Mild Cognitive Impairment and Alzheimer's Disease Patients. *Journal of Alzheimer's Disease* **19**, 1273 (2010).

250.   E. Sykova, Extrasynaptic volume transmission and diffusion parameters of the extracellular space. *Neuroscience* **129**, 861 (2004).

251.   T. den Heijer *et al.*, Structural and diffusion MRI measures of the hippocampus and memory performance. *NeuroImage* **63**, 1782 (2012).

252.   D. Wolk, J. Detre, Arterial spin labeling MRI: an emerging biomarker for Alzheimer's disease and other neurodegenerative conditions. *Curr Opin Neurol* **25**, 421 (2012).

253.   J. C. de la Torre, Is Alzheimer's disease a neurodegenerative or a vascular disorder? Data, dogma, and dialectics. *The Lancet Neurology* **3**, 184 (2004).

254.   A. Ruitenberg *et al.*, Cerebral hypoperfusion and clinical onset of dementia: The Rotterdam study. *Annals of Neurology* **57**, 789 (2005).

255.   I. Hajjar, K. Rodgers, Do angiotensin receptor blockers prevent Alzheimer's disease? *Current Opinion in Cardiology* **28**, 417 (Jul, 2013).

256.   J. A. Wells *et al.*, Increased cerebral vascular reactivity in the tau expressing rTg4510 mouse: evidence against the role of tau pathology to impair vascular health in Alzheimer/'s disease. *J Cereb Blood Flow Metab*, (2014).

257.   K. Govaerts, U. Himmelreich, F. V. Leuven, T. Dresselaers, in *International Society of Magnetic Resonance in Medicine*. (Milan, 2014).

258.   A. Gozzi *et al.*, A multimodality investigation of cerebral hemodynamics and autoregulation in pharmacological MRI. *Magnetic Resonance Imaging* **25**, 826 (2007).

259. A. Faure *et al.*, Impaired neurogenesis, neuronal loss, and brain functional deficits in the APPxPS1-Ki mouse model of Alzheimer's disease. *Neurobiol Aging* **32**, 407 (2011).

260. C. A. Massaad *et al.*, Mitochondrial Superoxide Contributes to Blood Flow and Axonal Transport Deficits in the Tg2576 Mouse Model of Alzheimer's Disease. *PLoS ONE* **5**, e10561 (2010).

261. C. Weidensteiner, F. Metzger, A. B. B. Bohrmann, B. Kuennecke, M. von Kienlin, Cortical hypoperfusion in the B6.PS2APP mouse model for Alzheimer's disease: Comprehensive phenotyping of vascular and tissular parameters by MRI. *Magnetic Resonance in Medicine* **62**, 35 (2009).

262. X. Golay, M. Guenther, Arterial spin labelling: final steps to make it a clinical reality. *MAGMA* **25**, 79 (Apr, 2012).

263. Initial sequencing and comparative analysis of the mouse genome. *Nature* **420**, 520 (2002).

264. J. L. Guénet, The mouse genome. *Genome Research* **15**, 1729 (December 1, 2005, 2005).

265. C. Gunter, R. Dhand, Human biology by proxy. *Nature* **420**, 509 (2002).

266. J. Qiu, Animal research: Mighty mouse. *Nature* **444**, 814 (2006).

267. H. Gates, A. M. Mallon, S. D. Brown, High-throughput mouse phenotyping. *Methods* **53**, 394 (Apr, 2011).

268. J. N. Crawley, Behavioral Phenotyping Strategies for Mutant Mice. *Neuron* **57**, 809 (2008).

269. P. McConville, J. B. Moody, B. A. Moffat, High-throughput magnetic resonance imaging in mice for phenotyping and therapeutic evaluation. *Current Opinion in Chemical Biology* **9**, 413 (2005).

270. S. S. Keller, N. Roberts, Voxel-based morphometry of temporal lobe epilepsy: An introduction and review of the literature. *Epilepsia* **49**, 741 (2008).

271. N. C. Fox *et al.*, Presymptomatic hippocampal atrophy in Alzheimer's disease. *Brain* **119**, 2001 (December 1, 1996, 1996).

272. N. C. Fox *et al.*, Imaging of onset and progression of Alzheimer's disease with voxel-compression mapping of serial magnetic resonance images. *The Lancet* **358**, 201 (2001).

273. R. J. Siegel, K. Swan, G. Edwalds, M. C. Fishbein, Limitations of postmortem assessment of human coronary artery size and luminal narrowing: Differential effects of tissue fixation and processing on vessels with different degrees of atherosclerosis. *Journal of the American College of Cardiology* **5**, 342 (1985).

274. C. H. Fox, F. B. Johnson, J. Whiting, P. P. Roller, Formaldehyde fixation. *J histochem Cytochem* **33**, 845 (1985).

275. A. P. Koretsky, A. C. Silva, Manganese-enhanced magnetic resonance imaging (MEMRI). *NMR in Biomedicine* **17**, 527 (2004).

276. X. Yu, Y. Z. Wadghiri, D. H. Sanes, D. H. Turnbull, In vivo auditory brain mapping in mice with Mn-enhanced MRI. *Nat Neurosci* **8**, 961 (2005).

277. D. Pan *et al.*, Revisiting an old friend: manganese-based MRI contrast agents. *Wiley interdisciplinary reviews. Nanomedicine and nanobiotechnology* **3**, 162 (2011).

278. M. Thuen *et al.*, Manganese-enhanced MRI of the rat visual pathway: acute neural toxicity, contrast enhancement, axon resolution, axonal transport, and clearance of Mn(2+). *J Magn Reson Imaging* **28**, 855 (2008).

279. T. M. Shepherd, P. E. Thelwall, G. J. Stanisz, S. J. Blackband, Aldehyde Fixative Solutions Alter the Water Relaxation and Diffusion Properties of Nervous Tissue. *Magnetic resonance in medicine : official journal of the Society of Magnetic Resonance in Medicine / Society of Magnetic Resonance in Medicine* **62**, 26 (2009).

280. I. Oguz *et al.*, Comparison of Magnetic Resonance Imaging in Live vs. Post Mortem Rat Brains. *PLoS ONE* **8**, e71027 (2013).

281. D. Scheuner *et al.*, Secreted amyloid β–protein similar to that in the senile plaques of Alzheimer's disease is increased in vivo by the presenilin 1 and 2 and APP mutations linked to familial Alzheimer's disease. *Nature Medicine* **2**, 864 (1996).

282. F. K. Wiseman *et al.*, A genetic cause of Alzheimer disease: mechanistic insights from Down syndrome. *Nat Rev Neurosci* **advance online publication**, (2015).

283. A. O'Doherty *et al.*, An Aneuploid Mouse Strain Carrying Human Chromosome 21 with Down Syndrome Phenotypes. *Science* **309**, 2033 (September 23, 2005, 2005).

284. T. Krucker, A. Schuler, E. P. Meyer, M. Staufenbiel, N. Beckmann, Magnetic resonance angiography and vascular corrosion casting as tools in biomedical research: application to transgenic mice modeling Alzheimer's disease. *Neurological research* **26**, 507 (2004/07/01, 2004).

285. M. D. Abràmoff, P. J. Magalhães, S. J. Ram, Image processing with ImageJ. *Biophotonics international* **11**, 36 (2004).

286. F. Kara *et al.*, Monitoring blood flow alterations in the Tg2576 mouse model of Alzheimer's disease by in vivo magnetic resonance angiography at 17.6 T. *NeuroImage* **60**, 958 (2012).

287. A. Badhwar, J. P. Lerch, E. Hamel, J. G. Sled, Impaired structural correlates of memory in Alzheimer's disease mice. *NeuroImage: Clinical* **3**, 290 (2013).

288. G. Chételat *et al.*, Relationship between atrophy and β-amyloid deposition in Alzheimer disease. *Annals of Neurology* **67**, 317 (2010).

289. P. S. Sachdev, L. Zhuang, N. Braidy, W. Wen, Is Alzheimer's a disease of the white matter? *Curr Opin Psychiatry* **26**, 244 (2013).

290. A. L. Wright *et al.*, Neuroinflammation and Neuronal Loss Precede Aβ Plaque Deposition in the hAPP-J20 Mouse Model of Alzheimer's Disease. *PLoS ONE* **8**, e59586 (2013).

291. M. J. West, P. D. Coleman, D. G. Flood, J. C. Troncoso, Differences in the pattern of hippocampal neuronal loss in normal ageing and Alzheimer's disease. *The Lancet* **344**, 769 (1994).

292. L. E. Olson *et al.*, Down syndrome mouse models Ts65Dn, Ts1Cje, and Ms1Cje/Ts65Dn exhibit variable severity of cerebellar phenotypes. *Developmental Dynamics* **230**, 581 (2004).

293. J. Zhang *et al.*, Detection of amyloid plaques in mouse models of Alzheimer's disease by magnetic resonance imaging. *Magnetic Resonance in Medicine* **51**, 452 (2004).

294. Y. Wadghiri, D. Hoang, T. Wisniewski, E. Sigurdsson, in *Amyloid Proteins,* E. M. Sigurdsson, M. Calero, M. Gasset, Eds. (Humana Press, 2012), vol. 849, pp. 435-451.

295. M. D. Meadowcroft, D. G. Peters, R. P. Dewal, J. R. Connor, Q. X. Yang, The effect of iron in MRI and transverse relaxation of amyloid-beta plaques in Alzheimer's disease. *NMR in Biomedicine* **28**, 297 (2015).

296. D. Z. Christensen, M. Huettenrauch, M. Mitkovski, L. Pradier, O. Wirths, Axonal degeneration in an Alzheimer mouse model is PS1 gene dose dependent and linked to intraneuronal Aβ accumulation. *Frontiers in Aging Neuroscience* **6**, 139 (2014).

297. F. K. Wiseman, K. A. Alford, V. L. J. Tybulewicz, E. M. C. Fisher, Down syndrome—recent progress and future prospects. *Human Molecular Genetics* **18**, R75 (April 15, 2009, 2009).

298. W. B. Zigman, I. T. Lott, Alzheimer's disease in Down syndrome: Neurobiology and risk. *Mental Retardation and Developmental Disabilities Research Reviews* **13**, 237 (2007).

299. C. E. Wierenga, C. C. Hays, Z. Z. Zlatar, Cerebral Blood Flow Measured by Arterial Spin Labeling MRI as a Preclinical Marker of Alzheimer's Disease. *Journal of Alzheimer's Disease* **42**, S411 (2014).

300. D. C. Alsop, W. Dai, M. Grossman, J. A. Detre, Arterial Spin Labeling Blood Flow MRI: Its Role in the Early Characterization of Alzheimer's Disease. *Journal of Alzheimer's disease : JAD* **20**, 871 (2010).

301. M. Lacalle-Aurioles *et al.*, Cerebral blood flow is an earlier indicator of perfusion abnormalities than cerebral blood volume in Alzheimer/'s disease. *J Cereb Blood Flow Metab* **34**, 654 (2014).

302. C. H. Kao *et al.*, Regional cerebral blood flow of Alzheimer's disease-like pattern in young patients with Down's syndrome detected by 99Tcm-HMPAO brain SPECT. *Nuclear Medicine Communications* **14**, 47 (1993).

303. E. Melamed, B. Mildworf, T. Sharav, L. Belenky, E. Wertman, Regional cerebral blood flow in down's syndrome. *Annals of Neurology* **22**, 275 (1987).

304. N. Gökçora, T. Atasever, N. İ. Karabacak, G. Vural, K. Gücüyener, Tc-99m HMPAO brain perfusion imaging in young Down's syndrome patients. *Brain and Development* **21**, 107 (1999).

305. S. Deb *et al.*, Alzheimer's disease in adults with Down's syndrome: the relationship between regional cerebral blood flow equivalents and dementia. *Acta Psychiatrica Scandinavica* **86**, 340 (1992).

306. L. Dunlevy *et al.*, Down's syndrome-like cardiac developmental defects in embryos of the transchromosomic Tc1 mouse. *Cardiovascular Research* **88**, 287 (2010).

307. S. B. Freeman *et al.*, Population-based study of congenital heart defects in Down syndrome. *Am J Med Genet* **80**, 213 (1998).

308. G. J. Bouma, J. P. Muizelaar, Relationship between cardiac output and cerebral blood flow in patients with intact and with impaired autoregulation. *J Neurosurg* **73**, 368 (1990).

309. J. De la Torre, T. Mussivand, Can disturbed brain microcirculation cause Alzheimer's disease? *Neurological research* **15**, 146 (1993).

310. A. Ott *et al.*, Association of diabetes mellitus and dementia: The Rotterdam Study. *Diabetologia* **39**, 1392 (1996/10/01, 1996).

311. A. Hofman *et al.*, Atherosclerosis, apolipoprotein E, and prevalence of dementia and Alzheimer's disease in the Rotterdam Study. *The Lancet* **349**, 151 (1997).

312. N. Beckmann, Probing cerebrovascular alterations in Alzheimer's disease using MRI: from transgenic models to patients. *Current Medical Imaging Reviews* **7**, 51 (2011).

313. R. M. Hoogeveen, C. J. G. Bakker, M. A. Viergever, Limits to the accuracy of vessel diameter measurement in MR angiography. *Journal of Magnetic Resonance Imaging* **8**, 1228 (1998).

314. N. El Tannir El Tayara, B. Delatour, A. Volk, M. Dhenain, Detection of vascular alterations by in vivo magnetic resonance angiography and histology in APP/PS1 mouse model of Alzheimer's disease. *Magn Reson Mater Phy* **23**, 53 (2010/02/01, 2010).

315. K.-I. Ishibashi *et al.*, Latent cerebral artery stenoses on magnetic resonance angiography in a patient diagnosed as probable Alzheimer disease. *Psychiatry and Clinical Neurosciences* **52**, 93 (1998).

316. D. R. Borchelt *et al.*, Accelerated amyloid deposition in the brains of transgenic mice coexpressing mutant presenilin 1 and amyloid precursor proteins. *Neuron* **19**, 939 (1997).

317. N. Beckmann, R. Stirnimann, D. Bochelen, High-Resolution Magnetic Resonance Angiography of the Mouse Brain: Application to Murine Focal Cerebral Ischemia Models. *Journal of Magnetic Resonance* **140**, 442 (1999).

318. K. Jin *et al.*, Enhanced neurogenesis in Alzheimer's disease transgenic (PDGF-APPSw,Ind) mice. *Proceedings of the National Academy of Sciences of the United States of America* **101**, 13363 (September 7, 2004, 2004).

319. F. L. Heppner, R. M. Ransohoff, B. Becher, Immune attack: the role of inflammation in Alzheimer disease. *Nat Rev Neurosci* **16**, 358 (2015).

320. C. Wu, F. Li, G. Niu, X. Chen, PET Imaging of Inflammation Biomarkers. *Theranostics* **3**, 448 (2013).

321. P. A. Thomann *et al.*, MRI-derived atrophy of the olfactory bulb and tract in mild cognitive impairment and Alzheimer's disease. *Journal of Alzheimer's disease: JAD* **17**, 213 (2008).

322. R. S. Wilson *et al.*, Olfactory Impairment in Presymptomatic Alzheimer's Disease. *Annals of the New York Academy of Sciences* **1170**, 730 (2009).

323. L. Cao *et al.*, Aβ alters the connectivity of olfactory neurons in the absence of amyloid plaques in vivo. *Nat Commun* **3**, 1009 (2012).

324. R. R. Romito-DiGiacomo, H. Menegay, S. A. Cicero, K. Herrup, Effects of Alzheimer's Disease on Different Cortical Layers: The Role of Intrinsic Differences in Aβ Susceptibility. *The Journal of neuroscience* **27**, 8496 (August 8, 2007, 2007).

325. R. C. Pearson, M. M. Esiri, R. W. Hiorns, G. K. Wilcock, T. P. Powell, Anatomical correlates of the distribution of the pathological changes in the neocortex in Alzheimer disease. *Proceedings of the National Academy of Sciences* **82**, 4531 (July 1, 1985, 1985).

326. T. Gómez-Isla *et al.*, Profound Loss of Layer II Entorhinal Cortex Neurons Occurs in Very Mild Alzheimer's Disease. *The Journal of neuroscience* **16**, 4491 (July 15, 1996, 1996).

327. J. D. Pinter, S. Eliez, J. E. Schmitt, G. T. Capone, A. L. Reiss, Neuroanatomy of Down's Syndrome: A High-Resolution MRI Study. *American Journal of Psychiatry* **158**, 1659 (2001/10/01, 2001).

328. U. Frith, C. D. Frith, SPECIFIC MOTOR DISABILITIES IN DOWNS SYNDROME. *Journal of Child Psychology and Psychiatry* **15**, 293 (1974).

329. E. H. Aylward *et al.*, MRI volumes of the hippocampus and amygdala in adults with Down's syndrome with and without dementia. *Am J Psychiatry* **156**, 564 (1999).

330. C. Murphy, S. Jinich, Olfactory dysfunction in down's syndrome. *Neurobiology of Aging* **17**, 631 (1996).

331. D. A. McKeown *et al.*, Olfactory function in young adolescents with Down's syndrome. *Journal of Neurology, Neurosurgery, and Psychiatry* **61**, 412 (1996).

332. "World Alzheimer Report: The Global Impact of Dementia" (2015).